AD NUMBER: AD0811530

LIMITATION CHANGES

TO:

Approved for public release; distribution is unlimited.

FROM:

Distribution authorized to U.S. Government agencies and their contractors; Export Controlled; 1 Nov 1966. Other requests shall be referred to Air Force Materials Laboratory, Wright-Patterson AFB, OH 45433.

AUTHORITY

AFML ltr dtd 29 Mar 1972

STRUCTURE OF VAPOR-DEPOSITED BORON FILAMENTS

M. L. Hammond
P. F. Lindquist
R. H. Bragg

Lockheed Missiles & Space Company

TECHNICAL REPORT AFML-TR-66-358

November 1966

Air Force Materials Laboratory
Research and Technology Division
Air Force Systems Command
Wright-Patterson Air Force Base, Ohio

NOTICES

When Government drawings, specifications, or other data are used for any purpose other than in connection with a definitely related Government procurement operation, the United States Government thereby incurs no responsibility nor any obligation whatsoever; and the fact that the Government may have formulated, furnished, or in any way supplied the said drawings, specifications, or other data is not to be regarded by implication or otherwise as in any manner licensing the holder or any other person or corporation, or conveying any rights or permission to manufacture, use, or sell any patented invention that may in any way be related thereto.

Qualified users may obtain copies of this report from the Defense Documentation Center.

This document is subject to special export controls and each transmittal to foreign governments or foreign nationals may be made only with prior approval of the Air Force Materials Laboratory, MAMS, Wright-Patterson Air Force Base, Ohio 45433.

Copies of this report should not be returned to the Research and Technology Division unless return is required by security considerations, contractual obligations, or notice on a specific document.

Form 1473

AFML-TR-66-358

(9) Summary technical rept, 1 Jul 65 - 1 Aug 66,

(6) STRUCTURE OF VAPOR-DEPOSITED BORON FILAMENTS

(20) M. L. Hammond
P. F. Lindquist
R. H. Bragg

Lockheed Missiles & Space Company

(18) (19) TECHNICAL REPORT AFML-TR-66-358

(11) November 1966

(12) 316 p.

Air Force Materials Laboratory
Research and Technology Division
Air Force Systems Command
Wright-Patterson Air Force Base, Ohio

(15) AF 33 (615)-3140
(16) AF-7351
(17) 735107

MK

(210 115) DE

FOREWORD

This report, entitled "Structure of Vapor-Deposited Boron Filaments," was prepared under Contract Number AF 33(615)-3140, Research to Study the Structure of Non-Crystalline Boron. The contact was initiated under Project No. 7351, Task No. 735107. The work was performed by the Materials Sciences Laboratory of the Lockheed Missiles & Space Company and was administered by the Air Force Materials Laboratory. Lt. L. D. Blackburn (MAMP) was Project Engineer until February 1966, at which time Lt. W. F. Stuhrke (MAMS) became Project Engineer. This report describes work done during the period 1 July 1965 through 1 August 1966. The manuscript was released by authors on 30 November 1966 for publication as an RTD Technical Report.

This research was conducted under the general supervision of Dr. R. H. Bragg with Dr. M. L. Hammond directing the program. The following personnel contributed to the research described in this report:

X-Ray Diffraction	– M. L. Hammond
	P. F. Lindquist
Electron Diffraction and Microscopy	– P. F. Lindquist
Metallography	– W. C. Coons
	A. R. Hansen

This technical report has been reviewed and is approved.

Charles T. Lynch

CHARLES T. LYNCH
Chief, Advanced Metallurgical Studies Branch
Metals and Ceramics Division
Air Force Materials Laboratory

ABSTRACT

This report describes the structure of boron filaments vapor-deposited at ~1150°C on a tungsten wire substrate. Production and specially prepared filaments were examined as were samples taken from the deposition chambers after a filament length was cooled there in place. Both the morphology and crystallographic structure of boron filaments are described. Boron deposited near 1150°C possesses a nodular structure typical of surface-nucleated, vapor-deposited material having a small crystallite size and no preferred orientation. The deposition process results in at least two types of structural defects: the incorporation of foreign particles in the boron sheath, which cause renucleated nodules and conchoidal fracture; and the occurrence of flat radial cracks, which produce longitudinal splitting having the appearance of cleavage cracking. The core of boron/tungsten filaments consists of an intimate mixture of tungsten borides with a crystallite size of approximately 0.1 μ. The boron sheath is composed primarily of 10 to 100 Å crystallites of α-rhombohedral boron with some tetragonal boron possibly present. Single- and poly-crystalline inclusions of both α- and β-rhombohedral boron, 100 to 10,000 Å in diameter, are scattered throughout the matrix. No evidence of stacking faults or dislocations was found in the microcrystalline matrix, but striations, unusual rel-rod effects, and anomalous missing reflections were noted in the larger crystallites. Large crystallites of both α and β boron were grown in the microcrystalline matrix by beam heating in the electron microscope. In many instances, unequivocal identification of the larger crystallites was made by observing several orders of certain reflections in the electron diffraction patterns.

CONTENTS

ILLUSTRATIONS

TABLES

Section 1 – INTRODUCTION

1.1 SCOPE OF PROGRAM

This research program was directed toward characterizing the crystallographic and metallurgical structure of the boron produced in continuous filaments. The program's primary emphasis was on the following:

- Characterizing the grain structure and substructure of boron filaments
- Characterizing the structural aspects of the nodular growth details of boron filaments
- Characterizing the crystallographic nature of the deposited boron

1.2 PROGRAM DIVISION

The program was divided into two parts: General Structure of Boron Filaments and Crystallographic Structure of Boron Filaments. In the first part of the program, different batches of Texaco Experiment, Inc. and United Aircraft Research production filaments were examined metallographically, by x-ray diffraction, and by transmission electron microscopy. In addition, boron filaments deposited under various conditions were studied with the above techniques, as were samples taken out of the deposition chambers at the end of a production run. Thus, the section on the general structure of boron filaments includes examination of various production filaments, filaments prepared under different conditions, and filaments at various stages in the production process.

The second part of the program concentrated on the crystallographic nature of boron filaments. This section is concerned primarily with theoretical and experimental considerations of the crystallographic features of boron filaments, as revealed by transmission electron microscopy and x-ray diffraction. Variations in crystal structure, nature of defects, and the effects of heat treatment on the structure of boron filaments were considered.

1.3 PROGRAM SUMMARY

1.3.1 General Structure of Boron Filaments

Boron filaments prepared by different production methods, at different deposition temperatures, and at different places in the production process have been examined. All production boron filaments were found to consist of a two-phase core of tungsten borides approximately 0.0007-in. in diameter with a sheath of vapor deposited boron 0.002-in. thick. The core structure cannot be resolved by light microscopy, but x-ray evidence is consistent with a boride crystallite size of approximately 0.1μ. The boron sheath or mantle consists of a nodular structure with major and minor nodules typical of surface nucleated, small crystallite size, vapor deposited materials. All the boron deposited between 870 and 1260° C has essentially the same crystallographic structure, regardless of substrate, and variations of deposition parameters within a broad range vary only the morphology.

Production filaments prepared by both Texaco Experiment, Inc. and United Aircraft Research Corp. were uniform over the entire filament length examined but considerable variation was possible for different batches of filaments. The Texaco material was characterized by:

- A strongly delineated major nodule structure with some filament lengths having a minor nodule structure as well
- A cusped ring structure; the cusps correspond to the major nodule structure and the chamber rings are the result of depositing in several chambers
- A lower resistance to chemical attack at the chamber ring interface which is related to the dominant growth mechanisms

The surface texture of the United Aircraft Research filament is similar to the Texaco material but there are two chamber rings with different morphologies. The United Aircraft filament is apparently built up in small waves and the entire structure has a chemical reactivity comparable to the chamber ring interfaces of the Texaco material.

All filaments exhibit two fracture modes: the flat, longitudinal mode which has the appearance of a cleavage fracture, and the conchoidal mode. The flat fracture mode is caused by flat radial cracks which form near the beginning of the deposition process and grow with the filament. These flat cracks are responsible for filaments splitting longitudinally. The conchoidal mode is simply a typical brittle fracture nucleated by defects, such as foreign particles and the core-sheath interface.

Filaments deposited at lower temperatures and shorter times tend to have a minor nodule structure while high temperatures tend to eliminate the minor nodules. The ratio of longitudinal to circumferential dimensions of the major nodules decreases with increasing deposition temperature, ranging from 1:1 to 1:3. This and other features can be incorporated into a nomenclature system for filaments which includes descriptions of the core structure, the sheath structure, and the dominant morphological features of the sheath.

The cores of all B/W filaments react to form various borides, depending upon the time and temperature of deposition. Expansions due to boride formation are probably responsible for the longitudinal cracks described above. The borides form by radial diffusion, and the expansion reaction probably occurs when the first boride to form reacts with the tungsten core to form another boride. Phase identification of the first boride has not been made because some kind of solid state transformation must occur on cooling to provide the intimate two-phase mixture of W_2B_5 and τ-$WB_2(WB_4)$ which is observed. This mixture is present in all the fully reacted B/W filaments examined in this study. The formula τ-$WB_2(WB_4)$ indicates only that the phases τ-WB_2 and WB_4 have essentially the same diffraction patterns and cannot readily be distinguished by x-ray diffraction.

A radial temperature decrease of less than 80° C from the core-sheath interface to the filament surface was estimated for 0.005-in. filaments. Thus, no structural gradient is likely to exist because of a large temperature difference; however, fluctuations in local temperature can cause the local variations of crystallite size and crystal structure which are observed.

During the deposition process, the filaments pass through several mercury seals. Quenching the filament in these seals does not appear to affect the structure of the filament, but the area of restarted growth is more susceptible to chemical attack. Foreign particles picked up in the radial cracks contribute to crack healing, cause the formation of re-nucleated nodules in the filaments, and are a source of stress concentrations which lower the filament fracture strength.

1.3.2 Crystallographic Structure of Boron Filaments

The crystallographic structure of boron in boron filaments was examined by polarized light microscopy, and x-ray and electron diffraction. Boron filaments deposited in the vicinity of 1150° C do not exhibit optical anisotropy even though filaments prepared by electric discharge at low temperature (~300° C) and by vapor deposition at high temperature (~1600° C) can be optically active. Because there are no reported cubic polymorphs of boron, the lack of optical activity indicates a crystallite size below the resolving power of the light microscope and a lack of preferred orientation.

The characteristic diffraction pattern from the boron sheath consists of six or seven broad halos. The three strongest halos can be observed quite easily by x-ray diffraction, but the others are usually found only in electron diffraction where the Lorentz-polarization factor is essentially constant. The electron diffraction technique has the additional advantage of sampling very small areas. Both electron and x-ray diffraction give equivalent data in terms of the number of halos observed, approximate relative intensities corrected for the Lorentz-polarization factor, and crystallite size. As-received filaments, filaments ground for 30 minutes in a B_4C mortar and pestle, and filaments thinned chemically or electrolytically give essentially the same diffraction patterns. The diffraction evidence obtained in this study is consistent with a small crystallite size (~30 Å) defect α-rhombohedral boron with some tetragonal boron possibly present. The halo intensity data definitely rule out a liquid-like amorphous structure.

No evidence of grain boundaries, dislocations, or stacking faults was found in transmission electron microscope studies of thinned or ground filament. The structure of vapor-deposited boron consists of a finely textured matrix with occasional embedded particles 100 – 10,000 Å in diameter. The occasional particles are usually identifiable as α- or β-rhombohedral boron and the matrix consists predominantly of defect α-rhomohedral boron with a crystallite size range of 10 – 100 Å. The crystallite size distribution was estimated from texture dimension measurements at very high magnification and by narrow beam diffraction experiments which examined areas as small as 200 Å × 200 Å. The halos were identified as α-rhombohedral boron with some tetragonal boron by comparing the halo positions with the powder patterns for the established boron polymorphs. Further proof for the presence of α-rhombohedral boron was obtained from beam heating experiments. Direct observation of recrystallization to form 1500 Å crystallites of α-boron was made and this reaction occurred at the lower temperatures developed during the beam heating. Further heating led to the formation of β-boron crystallites as well. Heating the filaments under a partial pressure of argon at 1050° C for 15 hours did not cause recrystallization or growth of the small crystallite matrix, but brought the intensity distribution of the halos into closer agreement with the α-boron powder pattern.

Long rel-rod effects were found for several orientations of pure, ground β-rhombohedral boron, in α- and β-boron crystallites (~1μ diameter) formed during deposition, and during beam heating. Accompanying these long rel-rod effects were consistently missing reflections which made indexing of the spot patterns very difficult. On occasion, some of these missing reflections were present but were much weaker than expected. Because of the large number of reflections and the unusual systematic extinctions, each indexing scheme had to be verified by checking both d-spacings and interplaner angles.

Section 2 – MATERIALS FOR PROGRAM

The following materials were obtained via Lt. L. D. Blackburn and Lt. W. F. Stuhrke of the Air Force Materials Laboratory:

- Two high-purity polycrystals of β-boron supplied by Leytess Metal and Chemical Corporation (material to be referred to as crystalline β-boron*)
- A 113-ft-long roll of Texaco Experiment, Inc. Run 071183 having a tensile strength of 478 ksi ± 1% as measured by Texaco Experiment – 416 ksi ± 25% by outside source (material to be referred to as Texaco-3)
- Sixty-eight 18-in. lengths of boron filament taken from one continuous length. Material supplied by Texaco Experiment, together with a table listing the tensile strength for each length (material to be referred to as Texaco-σ)
- Nineteen samples of specially prepared filaments from Astro Research (material to be referred to as Astro-A-16-)
- Two boron production tailings each consisting of a length of filament removed from the deposition chambers at the conclusion of a production run with the important parts of the deposition process, such as the ends of the deposition chambers, marked on the filament (material supplied by F. E. Wawner of Texaco Experiment, Inc.)

Other material acquired for this contract:

- A quantity of supposedly amorphous boron of unknown origin
- A 100-ft-long roll of boron filament from Texaco Experiment, Run 030273, Test 1333, Package No. 3 (material to be referred to as Texaco-6)
- One sample of α-boron 10 μ thick and 1 cm on a side, deposited on a silicon single crystal substrate (material supplied by E. T. Peters of Man Labs. Inc.)
- Samples of boron filament of unknown origin supplied through the LMSC Sunnyvale facilities (materials to be referred to as Texaco-1)
- A quantity of 99% "crystalline" boron from Shield-Alloy Corporation

---

*Throughout this report, when α- or β-boron is mentioned, it is understood that α- and β-rhombohedral boron is meant. The structure of α- and β-boron is discussed in Section 4. 1. 1.

- A sample of boron filament from United Aircraft Research having a filament strength of approximately 370 ksi
- A sample of reactive elemental boron powder prepared by flame pyrolysis (material purchased from Callery Chemical Corp.)

Section 3 – GENERAL STRUCTURE OF BORON FILAMENTS

3.1 INTRODUCTION

This section is concerned with general observations on the structure of boron examined by metallography, x-ray diffraction, and transmission electron microscopy. Experimental methods are described in detail. Production filaments prepared by Texaco Experiment, Inc. and United Aircraft Research were studied, as were filaments produced under various conditions of temperature and exposure time.

In addition, the growth of boron filaments was studied by examining samples taken from the deposition chambers after the filament had been allowed to cool in place. Each of these items is discussed in the following sections.

3.2 EXPERIMENTAL TECHNIQUES

3.2.1 Metallographic Preparation of Boron

Information regarding the preparation and etching of boron for microscopic study is quite meager. Ellis (Ref. 1) conducted studies to develop useful etches that would (1) clean the surfaces; (2) reveal crystal boundaries, twin planes and single crystal areas in polycrystalline material; (3) assist in sample orientation; and (4) assist in the study of crystal defects. No information was given regarding the mounting, grinding, and polishing procedures. The etchants proposed were H_2SO_4 at 300° C (570° F) for 10 min, and a mixture of 1 $Na_2B_4O_7$ to 1 KNO_3 by weight at 620° C (1148° F) for 1 min. While some details of microstructure were revealed by these etchants, the results were not considered sufficiently good for detailed microscopic study at high magnifications. Furthermore, etching in solutions at such high temperatures is quite difficult, inconvenient, and not always reproducible.

In this study of boron filaments, a combined polishing and etching procedure was developed which easily and very clearly revealed the structures of boron.

Procedure. So-called "amorphous boron" and crystalline β-rhombohedral boron are extremely hard, and it has been reported (Ref. 2) that boron will scratch sapphire. Thus, samples of boron must be mounted in a manner which will not unduly fracture the material, nor permit excessive rounding of the edges during polishing.

Mounting of filament cross sections is performed in the following manner:

1) A small hole, 11 to 13 mils in diameter, is drilled 1/8 in. off center through a 3/8-in. thick disk of linen-phenolic 3/4 in. in diameter. In addition, a much larger hole is drilled in the center to be used as a reference marker.

2) This hole is filled with finely ground, red bakelite and a length of boron filament is inserted about half way through the hole. Usually this must be performed under a stereomicroscope.

3) A layer of finely ground, red bakelite is placed on the bottom platen of the mounting mold, the linen-phenolic specimen configuration is gently placed on top of the bakelite layer, and the mounting mold sleeve is put in place around the entire assembly.

4) Additional ground bakelite is then added to cover the sample amply.

5) Unground bakelite is added to make a mount about 3/4-in. high.

6) Minimum pressure is applied to the mold (100 psi max) during the first 5 min of heat-up. After 5 min the pressure is increased slowly until maximum (4200 psi) is reached and the rest of the curing is then allowed to go to completion. When curing is finished (12–13 min total time starting with a cold heater) the specimen is allowed to cool for 10 min under pressure, at which time it can be removed.

7) The sample is ground on 120 or 240 grit SiC wet or dry paper until the specimen is revealed. Grinding is then performed on 600 grit until most of the chipping and spalling caused by the coarse grind is removed. It should be noted that because of the extreme hardness of the material, SiC will not grind a filament cross section flat.

8) Initial polishing is performed by inserting the specimen into a 240-gm weight and placing it on the dull surface side of slipper satin onto which 1μ diamond has been applied. Polishing proceeds until the sample is flat.

9) Final polishing can be performed in two ways:

   a. On "Microcloth" using a slurry of "Cer-Cre"* metallographic polishing abrasive to which a small amount of a 10% solution of chromic acid has been added (time of polish ~ 2–4 min).

   b. On "Microcloth" using a slurry of "Cer-Cre" metallographic polishing abrasive to which a small amount of an NaOH etch has been added (10 gm NaOH, 30 gm $K_3Fe(CN)_6$, 150 ml H_2O).

   Procedure (a) will lightly etch the tungsten boride core but will have no apparent chemical effect on the boron. Procedure (b) will severely attack and remove the core material, and have an etching effect on the boron. The degree of etching or attack of the boron will depend on the amount of the NaOH-$K_3Fe(CN)_6$ solution that is used.

The surfaces of boron filaments were photographed under oil immersion at 3000× to reveal surface texture.

3.2.2 X-ray Diffraction Techniques

The x-ray diffraction techniques are divided into two types: Debye-Scherrer techniques and diffractometer methods.

The Debye-Scherrer techniques consisted of mounting a sample filament at the center of either a 114.6 mm or 57.3 mm Debye-Scherrer camera and exposing with appropriate radiation, normally Ni-filtered CuKα radiation. In two instances, crystal monochromatized CuKα radiation was used to eliminate any uncertainty about contribution to the Debye-Scherrer patterns from unwanted radiations. The patterns obtained using crystal-monochromatized radiation had a clearer background but were

*Metallographic Supplies and Services, 565 Arastradero Rd., Apt. 204, Palo Alto, Calif.

not fundamentally different from those obtained using Ni-filtered Cu radiation. Therefore, to take advantage of the higher intensity, Ni-filtered Cu radiation was used in the Debye-Scherrer studies. The line positions on the Debye-Scherrer films were usually read with transparent d-spacing cards, but in some cases the broad peaks were scanned with a microphotometer. Precision film reading to 0.2° 2θ was used occasionally, as noted in appropriate sections of this report.

Boron filament samples for the diffractometer were prepared by placing three layers of filaments across a picture-frame sample holder which was notched to hold the filaments parallel to and symmetrically about the diffractometer axis. Boron powder samples were simply packed by hand in a holder 3 mm thick. Both point counting and step scanning methods were used to obtain the intensity data. The step scanned data were obtained through the courtesy of Dr. D. K. Smith of the Lawrence Radiation Laboratory on a Norelco diffractometer, and the point counted data were obtained on a General Electric XRD-5 diffractometer in the LMSC laboratories. Data were taken either with filtered Cu or CrKα radiation. The Cr radiation was used to obtain maximum resolution.

3.2.3 Electron Microscopy Techniques

Specimens of vapor-deposited boron filaments were prepared for transmission electron microscopy by two methods: grinding and direct thinning. The grinding technique was also used to study the structure of pure β-rhombohedral boron.

Grinding. The specimen to be ground was placed in a boron carbide mortar. Grinding was performed in pure ethanol, and the suspended particles were picked up on a pure carbon substrate. The ethanol evaporated quickly, and the specimen was immediately placed in the microscope. Grinding time was generally 30 minutes.

Thinning. The first attempts to thin the filaments directly were made by electropolishing. A length of filament, held by a pair of tweezers, was dipped in and out of a solution consisting of 10 gm NaOH, 100 ml H_2O, and 100 ml glycerine, using 20 vdc applied voltage. It was found that nearly all the current was conducted along the

boride core; when the core was eaten away, the current usually dropped about two orders of magnitude. Thinning was accelerated considerably at temperatures above 70° C, and the filaments usually thinned nonuniformly, the thinnest section occurring about 2 mm back from the tip.

During the course of the metallographic studies, it was discovered that the filaments could be thinned chemically at room temperature in a solution consisting of 10 gm NaOH, 35 gm $K_3Fe(CN)_6$, 150 ml H_2O, diluted 10:1 in H_2O. This solution dissolves the boride core almost immediately, and attacks the boron sheath at a slower rate. After this discovery, the electropolishing experiments were discontinued.

When lengths of filament were placed in a shallow dish containing the $K_3Fe(CN)_6$ solution, they were often found to split longitudinally. This splitting was very desirable in the preparation of thinned specimens for microscopy, since the core was completely removed and a flat strip of pure vapor-deposited boron remained.

The thinned filament specimens were removed from the solution just before complete dissolution, rinsed in distilled water, and transferred to a petri dish containing ethanol. A piece of thinned filament about 2 mm in length was sandwiched between two 75-mesh copper grids while still immersed in the ethanol, and the two grids were then lifted out of the ethanol, drained on filter paper, and mounted in the specimen holder. This technique was found to be very satisfactory for studying the structure of as-deposited filaments.

3.3 STRUCTURE AND PROPERTIES OF TUNGSTEN BORIDES

The primary purpose of this investigation was to study the crystallographic structure of boron in boron filaments. It has been shown by several investigators that boron filaments which are prepared on a tungsten wire substrate consist of a boron sheath and a core of tungsten borides. Therefore, the description of boron filaments cannot be complete without some information on the structure of these borides.

The structure of tungsten borides was first studied in detail by Kiessling (Ref. 3). This work and that of others has been reviewed by Samsanov (Refs. 4 and 5), Rudy and St. Windisch (Ref. 6) and Post (Ref. 7). Table 1, taken primarily from the summaries by Rudy (Ref. 6) and Samsanov (Ref. 4) gives the lattice constants, and calculated and observed density values.

In some of the initial examination of B/W filaments at Texaco Experiment, Inc. it was found that the observed diffraction lines from B/W filaments could not be indexed satisfactorily using the established crystal structure data (Ref. 8). The initial indexing led to the conclusion that normal production filament contained a core of W_2B_5 (a_o = 2.98Å, c_o = 13.87 Å), in accordance with the structure determined by Kiessling, and a new hexagonal phase WB_2 with a_o = 5.19Å, c_o = 6.31 Å. Table 2 (Ref. 8) shows the average d-values obtained by the Texaco researchers arranged according to their indexing. This phase will be termed the τ-WB_2 phase to distinguish it from the other reported WB_2 phases listed in Table 1.

Based on the appearance and splitting of certain diffraction lines, the Texaco study tentatively concluded that the reaction process starts with WB_2 with a small amount of δ-WB possibly present. After some fairly short reaction time, W_2B_5 forms and coexists with τ-WB_2 and the lines corresponding to δ-WB disappear. In a later paper, another WB_2 compound was reported by the Texaco workers (Ref. 9).

In summary, there are several tungsten borides which have been studied in the pure form or as mixed phases. The structural data based on compounds prepared by powder reaction or fusion agree fairly well; however, indexing the tungsten boride diffraction patterns obtained from boron filaments has not been adequately resolved. The indexing scheme proposed by the Texaco researchers is favored by the authors until more definitive studies are made. However, the chemical composition of τ-WB_2 is open

Table 1

STRUCTURE OF TUNGSTEN BORIDES

Phase	Structure	Lattice Parameters (Å)	Density gm/cc		Ref. or ASTM Card No.
			Calculated	Experimental	
γ-WB	Tetra.	a = 5.564 c = 4.740	10.7	16.0	6-0591
β-WB (High Temp)	Orthorh.	a = 3.19 b = 8.40 c = 3.07	16.0	15.3	6-0541
δ-WB (Low Temp)	Tetra.	a = 3.115 c = 16.93			6-0635
τ-WB_2	Hex.	a = 5.19 c = 6.31			8
WB_2	Hex.	a = 3.02 c = 3.05	14.15	9	9
WB_2	Hex.	a = 6.35 b = 8.24	13.6	13	4
W_2B_5	Hex.	a = 2.982 c = 13.87	13.1	11.0	6-0243
WB_4	Hex.	a = 6.34 c = 4.50	8.4	8.3	11
$WB_{\sim 12}$	Hex	a = 3.994 c = 3.174			12

Table 2

d VALUES OF THE CRYSTALLINE PATTERNS OBTAINED BY X-RAY DIFFRACTION[a]

I[b]	Observed[c]	HKiL[d]	W_2B_5		WB_2	
			I	Calculated (Å)	HKiL	Calculated (Å)
S	3.65				$10\bar{1}1$	3.66
W^+	3.46	0004	S	3.466		
W^+	3.14				0002	3.15
VS	2.59	$10\bar{1}0$	W^+	2 582	$11\bar{2}0$	2.598
M	2.54	$10\bar{1}1$	S	2.538		
VVW(Br)	2.25	$10\bar{1}3$	M	2.254		
W^+	2.12				$20\bar{2}1$	2.119
VS	2.005				$11\bar{2}2$	2.006
W(Br)	1.90	$10\bar{1}5$	M^+	1.890	$10\bar{1}3$	1.906
VW(Br)	1.73	0008	W	1.734		
W^+	1.64				$21\bar{3}1$	1.642
VW	1.58				0004	1.578
VW	1.535				$20\bar{2}3$	1.537
M(Br)	1.495	$11\bar{2}0$	S	1.491	$30\bar{3}0$	1.500
M	1.37	$11\bar{2}4$	S	1.370		
M(Br)	1.35				$11\bar{2}5$	1.349
W	1.325	$10\bar{1}9$	W^+	1.323		
W(Br)	1.30				$22\bar{4}0$	1.299
W	1.29	$20\bar{2}0$	W	1.291		
W	1.223	10110	W	1.222	$31\bar{4}1$	1.224
W^+	1.201				$22\bar{4}2$	1.201
VVW(Br)	1.173	$20\bar{2}5$	S	1.170		
VVW	1.13	$11\bar{2}8$		1.130		
M	1.087				$30\bar{3}4$	1.087
VVW(Br)	1.073				$31\bar{4}3$	1.073
W(Br)	1.019				$32\bar{5}1$	1.019
W	1.002				$22\bar{4}4$	1.003
VVW(Br)	0.9920				$40\bar{4}3$	0.99195
W	0.9820				$41\bar{5}0$	0.9818
W	0.9760	$21\bar{3}0$		0.9759		
M	0.9375				$41\bar{5}2$	0.9375

[a] Data taken from Ref. 8

[b] Intensities of the diffracted beam, I, are relative, corresponding to the following scale: VS, very strong; S, strong; M, medium; W, weak; VW, very weak; VVW, very,very weak; Br indicates that the observed lines were broad.

[c] d is the interplanar spacing in angstrom units.

[d] HKiL represents the Miller indices.

to question because, with the exception of one low intensity line at 4.48Å, the Chretian-Helgorsky WB_4 phase (Refs. 6, 11) has essentially the same diffraction peaks as that suggested for τ-WB_2. In this report, the diffraction pattern corresponding to τ-WB_2 and WB_4 will be ascribed to a phase labeled τ-$WB_2(WB_4)$ and not identified any further.

To facilitate indexing tungsten boride lines, Table 3 was prepared in which the various x-ray data are tabulated. These data were used to index the sharp diffraction lines observed from B/W filaments.

Note added in Proof – According to Wawner of Texaco Experiment, Inc.*, the phase τ-WB_2 probably has the chemical formula WB_6. Its hexagonal symmetry and lattice constants have been confirmed by Galosso et al. at United Aircraft Research (Ref. 21) but the chemical formula is still in doubt. One indication that the τ-WB_2 phase is a higher boride (say WB_6) is Wawner's observation (Ref. 8) that the τ-WB_2 phase will survive in boron filaments heated to ~3700 °F but the W_2B_5 phase is lost. The excess boron present would probably cause the formation of a higher boride.

3.4 OBSERVATIONS ON MISCELLANEOUS BORON AGGREGATES

Several different boron samples were obtained for examination in addition to the boron filaments. These samples are listed in Section 2.

The high purity crystals of β-boron were found to be large-grain boron polycrystals with fairly heavy twinning. To determine if any planes of easy cleavage existed, a crystal was struck with a hammer prior to mounting. Figure 1 is a low magnification photograph of a polished section of the β-boron polycrystal. Twinning, grain boundaries, and cracks are numerous. The cracks do not seem to follow any planes of easy cleavage, and curved fracture planes are common. Thus, curved or conchoidal fracture is possible even in crystalline β-boron. High magnification views of the β-boron polycrystal

*Private Communication with Frank Wawner, now at the Materials Science Department of the University of Virgina, Charlottesville, Va.

Table 3

DIFFRACTION DATA FOR TUNGSTEN BORIDES

d-Spacing in Å						
W[a]	γ-W_2B[b]	δ-WB[c]	β-WB[d]	τ-WB_2[e]	ϵ-W_2B_5[f]	WB_4[g]
		4.25 W	4.19 VS			4.48 VS
	3.96 W			3.66		3.66-S
					3.46 S	
		3.06 W	2.98 M	3.15		3.17 M
	2.78 S	2.74 S		2.60	2.58 W	2.59 VS
	2.37 S		2.48 S		2.54 S	
2.24 S	2.20 S	2.29 S			2.31 VW	
					2.25 M	
		2.13 S				
		2.12 W	2.14 S	2.12		2.11 M
	2.03 W		2.10 S	2.07		
				2.01		2.00 VS
	1.96 VW	1.91 M		1.91		1.90 M
	1.80 S				1.89 S	
	1.76 M	1.79 W	1.74 M		1.73 W	
1.58 W		1.61 VW	1.60 W	1.64		1.63 M
	1.51 VW	1.56 M	1.54 W	1.58		1.58 W
				1.54		1.53 W
		1.46 VS		1.50	1.49 S	1.49 W
	1.41 S	1.41 W	1.40 VS		1.44 VW	1.35 M
	1.39 VW	1.39 W				
		1.38 W			1.39 VW	
		1.35 W	1.37 W	1.35	1.37 S	
	1.33 S	1.34 M	1.34 W		1.32 W	1.32 M
	1.31 S					
1.29 M	1.30 S	1.29 M		1.30	1.29 VW	1.29M
			1.27 W		1.28 W	
	1.25 VW	1.25 M	1.24 M		1.25 VW	
					1.24 VW	
	1.20 VW	1.21 M		1.22	1.22 VW	
	1.19 W	1.20 W		1.20	1.21 VW	
1.12 VW						
			1.17 VW		1.17 S	
				1.08	.	
			1.11 W	1.07	.	
				1.00	.	
1.01 W				0.992	.	
				0.98	.	
0.92 VW				0.94	.	
0.84 W						
0.79 VVW						

(a) ASTM Card 4-0810

(b) ASTM Card 6-0591

(c) ASTM Card 6-0635

(d) ASTM Card 6-0541

(e) Ref. 8

(f) ASTM Card 6-0243

(g) Ref. 11

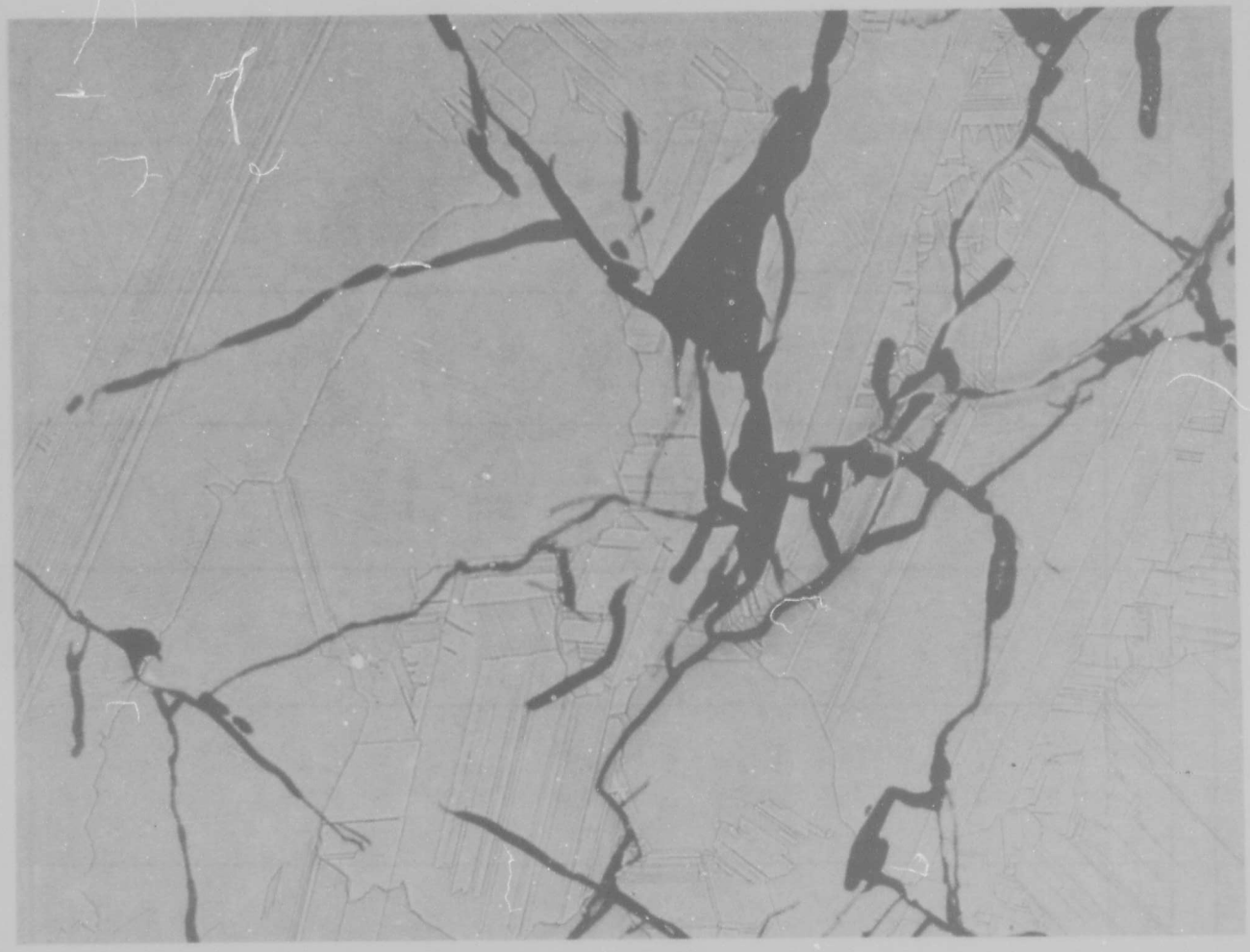

Fig. 1 Bulk, Fractured β-Boron Showing Twinning and Polycrystallinity. Black Lines are Partially Enlarged Cracks, Induced by Fracture and Widened by Etching. Polished and Etched Simultaneously. P-910; 150×.

are given in Fig. 2. Here, grain boundary and twin interactions are shown, as are possible dislocation etch pits. The β-boron showed definite optical anisotropy, as shown in Fig. 39 of Section 4.2.2 where the optical activity of boron filaments is discussed. Diffractometer scans and back-reflection Laue photographs of the boron polycrystals showed random intensity variations typical of a large-grain sample.

A diffractometer scan of the amorphous boron powder of unknown origin contained most of the diffraction peaks of β-rhombohedral boron. Because its diffraction pattern was different from that of boron filaments and its origin unknown, this sample of boron was not studied any further.

The sample of 10-μ thick α-boron deposited on Si was lost during an extraction attempt and hence no examination of the boron alone could be made. Preliminary diffraction patterns of the boron deposited on the Si showed only Si lines. Metallographic examination of the Shield-Alloy crystalline boron showed that it is extremely hard and consists of large grains. A second phase with a rectangular appearance was observed which is probably B_4C produced during arc-melting. The production methods of the Shield-Alloy boron were not available, and no further examination of this material was made, either.

Debye-Scherrer patterns obtained from Callery boron with Ni-filtered Cu radiation showed two broad maxima, one extending from 2.4 to 4.4Å and the other from 1.3 to 1.45 Å. The relevance of these data to the structure of vapor-deposited boron filaments is discussed in Section 4.3.1.

3.5 STRUCTURE AND PROPERTIES OF PRODUCTION BORON FILAMENTS

3.5.1 Material Examined

This section is concerned with the general structure of production boron filaments. The materials examined in this section are the production boron filaments Texaco-1, -3, -6, -σ, and a sample of United Aircraft Research production filament. The

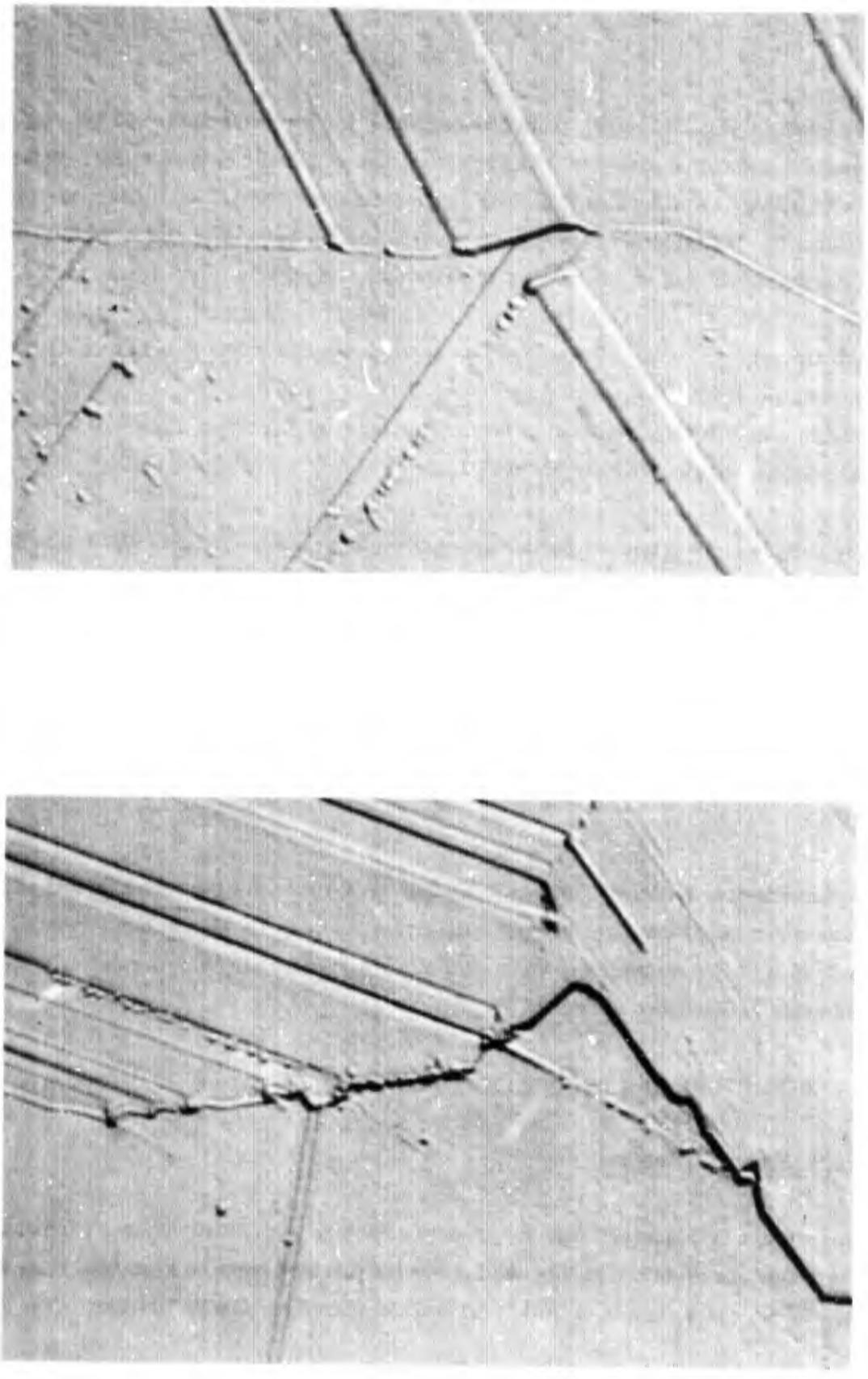

Fig. 2 Bulk β-Boron Showing Twinning, Grain Boundaries, and Possibly Dislocation Pits. Polished and Etched Simultaneously. P-890 and P-891; 3000×.

material referred to as Texaco-3 was divided into 10-ft segments and examined for structural variations along its length. The Texaco-σ filament segments were divided into three strength categories, as described below, and three samples in each category were examined to determine if general structural differences were responsible for the strength variations. The Texaco-1 and -3 and the United Aircraft filaments were examined for comparison.

3.5.2 Property Variations

All boron filaments have a variation in strength along their length, the quality control data frequently giving the average strength with some coefficient of variation. One set of samples (Texaco-σ) was supplied with tensile strength data at 18-in. intervals along the filament length. The tensile strength data for the 68 lengths of filament were plotted both as a frequency distribution and according to location in the original filament length. There was no correlation of high or low strength with position; the low strength values occurred at random along the entire filament length. Figure 3 shows the frequency distribution of strength. As may be seen, the strengths lie in three ranges: high (489 – 593 ksi), medium (387 – 489 ksi), and low (249 – 283 ksi) strength. This division of properties formed the basis of selecting samples from the Texaco-σ material. The predominance of high breaking strengths is typical of boron filaments and similar results have been reported by other investigators (Refs. 13 and 14). Wawner (Refs. 14 and 15) has shown that different defects are responsible for the different strength levels and he has characterized these different defects.

3.5.3 Metallographic Observations

The metallographic features of Texaco Experiment, Inc. and United Aircraft Research production filaments are described in this section. In addition, some examples of defects and fracture modes are given.

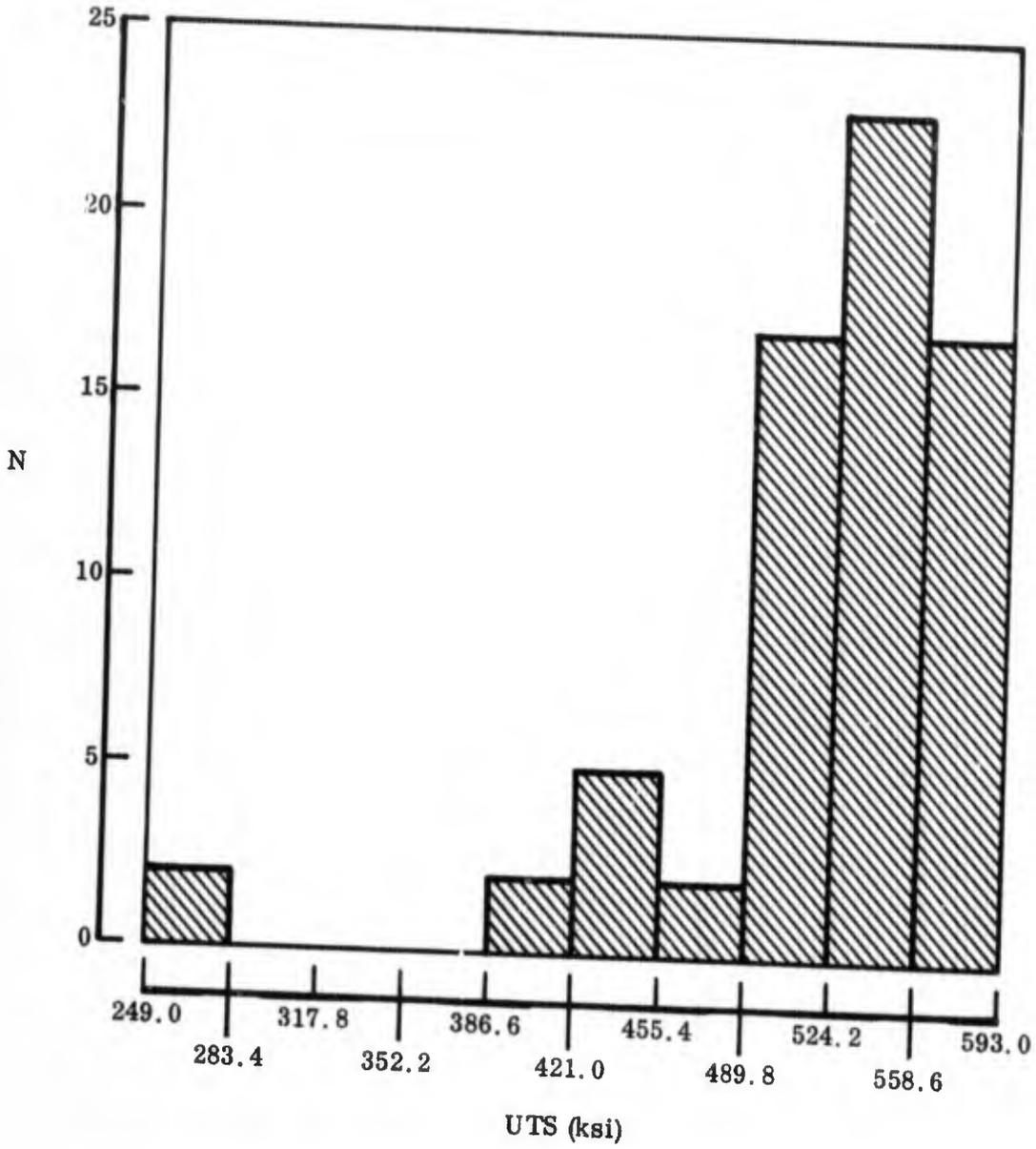

Fig. 3 Frequency Distribution of Strength in Texaco-σ Boron Filament

3.5.3.1 Texaco Experiment Production Boron Filaments

Figures 4 through 7 are photographs of various Texaco production filaments. The filaments are labelled Texaco-6, -1, and -3 to indicate the number of chamber rings, and the -σ denotes that breaking strength data were supplied with this particular filament length. The Texaco-6 and -1 filaments represent early efforts in the production of filaments.

The structure of Texaco-6, shown in Fig. 4, consists of relatively large major nodules with no minor nodules. The chamber rings in the cross section view show that the filament was produced in six deposition chambers. This cross section also shows cracks, which have been widened by etching, and the presence of radial lines, which correspond with the nodules in the surface photograph.

The Texaco-1 filament, shown in Fig. 5, differs considerably from the other filaments. It has no chamber rings; however, the cross section shows a wavy etching effect which is probably due to variations in structure which occurred because of variations in the local temperature and pressure. The surface of Texaco-1 contains both major and minor nodules; in general, the surface is quite rough.

The Texaco-3 filament was divided into 10-ft segments to determine the structural consistency along its length. Both surface and cross section examinations were made and no variations were noted along the entire 113-ft length. The surface and cross section views presented in Fig. 6 are quite representative of the Texaco-3 filament, this filament being representative of some of the production material made during 1965 at Texaco Experiment, Inc. The major nodules are readily apparent and there is a minor nodule structure with about six minor nodules in each major nodule. The cross section reveals differences in the chamber ring thicknesses with the thickness decreasing away from the center of the filament. The grainy texture in the outer ring probably indicates a greater degree of nucleation during its growth; the presence of a minor nodule structure may also indicate a higher nucleation rate.

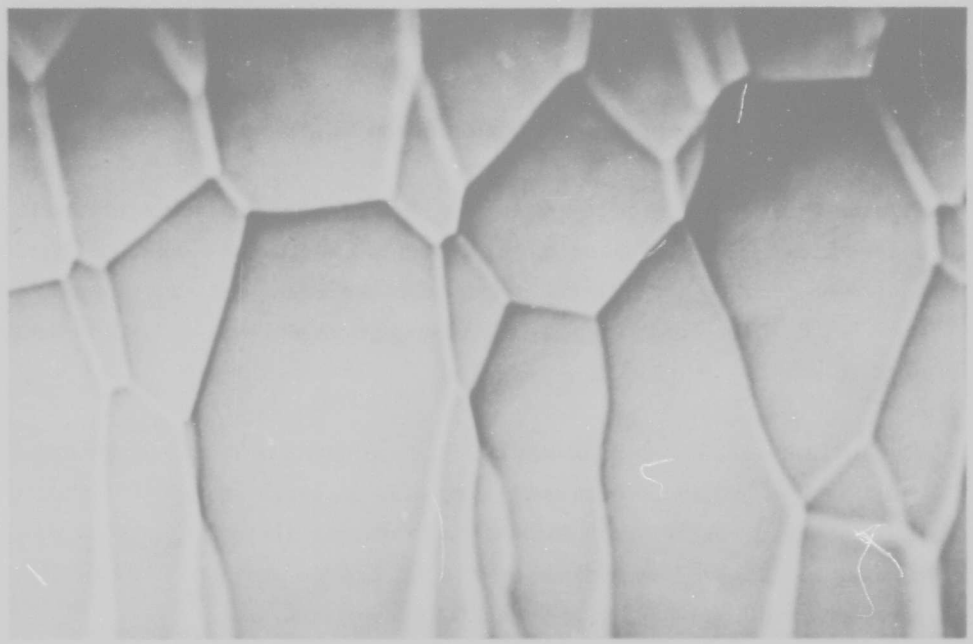

Fig. 4(a) Surface of Texaco-6 Filament. M9005, 3000×

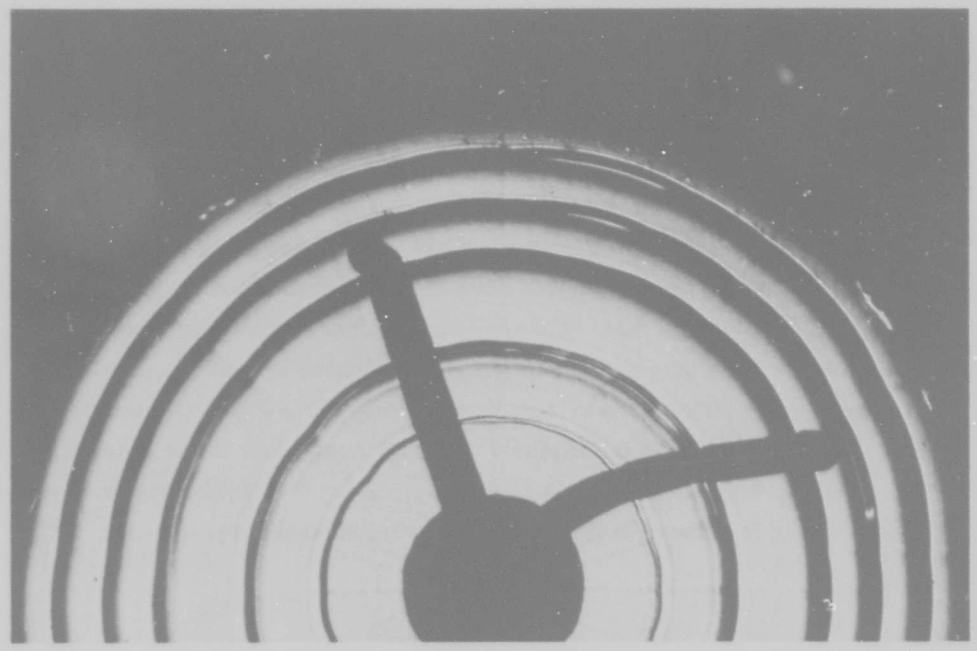

Fig. 4(b) Transverse Cross Section of Texaco-6 Filament. M9541, 1150×

Fig. 5(a) Surface of Texaco-1 Filament. M9013, 3000×

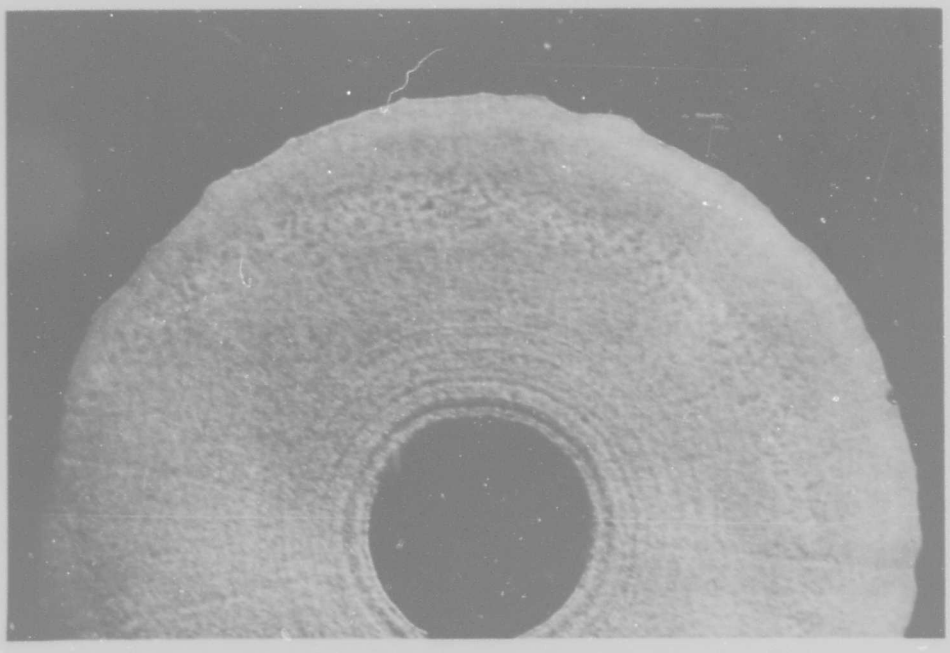

Fig. 5(b) Transverse Cross Section of Texaco-1 Filament. M9557, 1150×

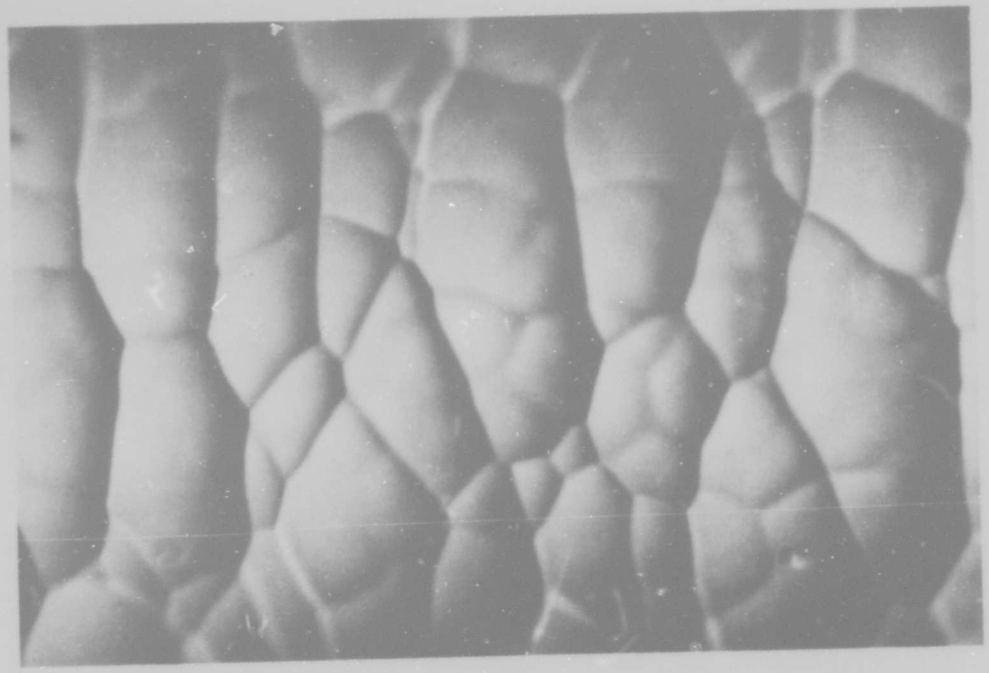

Fig. 6(a) Surface of Texaco-3 Filament. P1085, 3000×

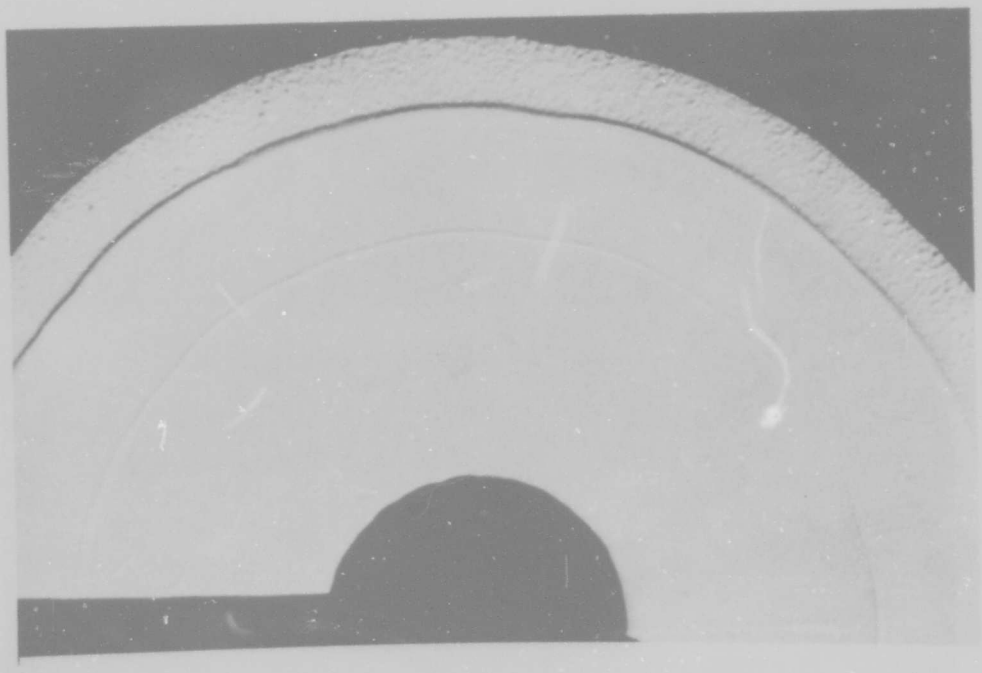

Fig. 6(b) Transverse Cross Section of Texaco-3 Filament. P1821, 2000×

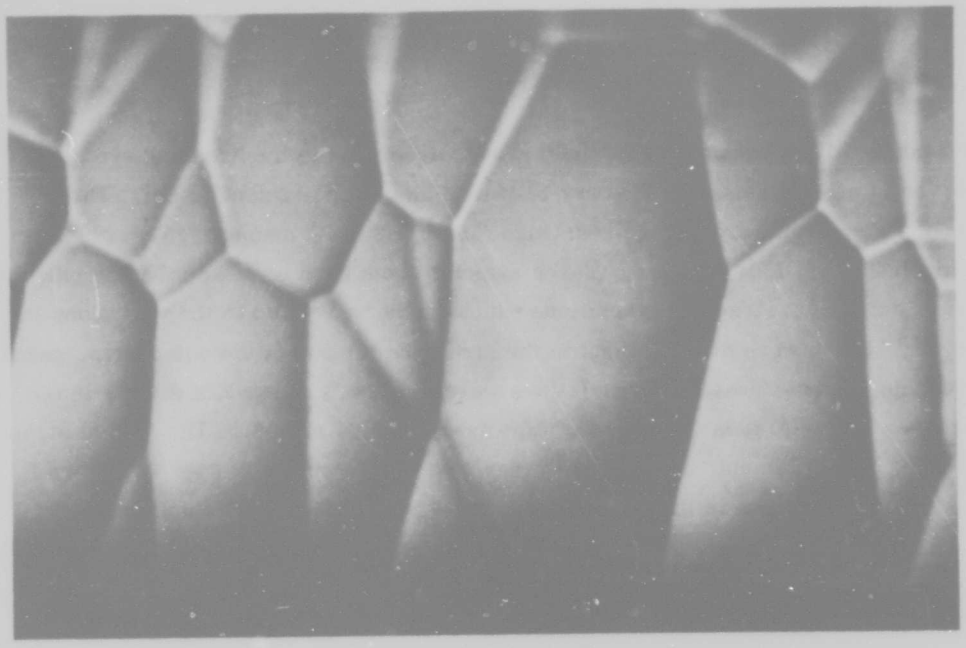

Fig. 7(a) Surface of Texaco-σ Filament. P1166, 3000×

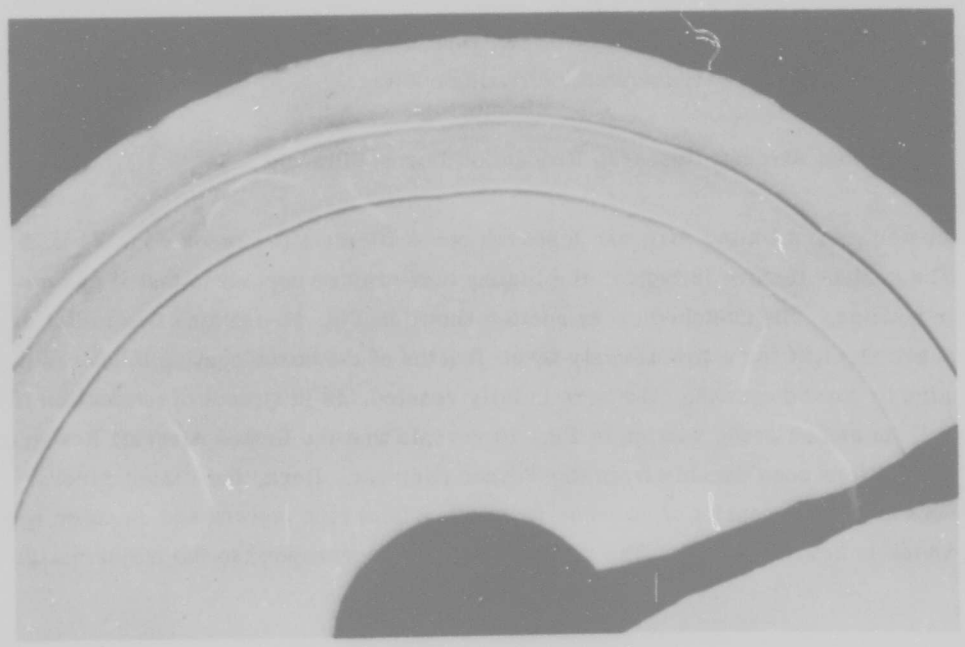

Fig. 7(b) Transverse Cross Section of Texaco-σ Filament. P1820, 2000×

The Texaco-σ filament was divided into groups according to the breaking strength observed in a 1-in. gage length every 18 inches along the filament length. Three strength categories were recognized: high (489 – 583 ksi), medium (387 – 489 ksi), and low (249 – 283 ksi) strength. Three samples from each of these strength categories were examined for structural variations which might be related to the variations in strength. There were no variations in the structure for any of the categories, and it was concluded that the strength variations were the result of random defects in the structure similar to those reported by Wawner (Refs. 14 and 15). The typical structure of the Texaco-σ filament, also prepared during 1965, is shown in Fig. 7. There is no minor nodule structure in this filament and the cross section etches uniformly flat across all three chamber rings. As will be demonstrated in Section 3.5.3.3 and 3.6, the lack of minor nodules is at least partly the result of higher deposition temperatures.

Figure 8 contains a high magnification view of the core of the Texaco-6 material; its structure is common to all production filament examined in this study. There are no sharp boundaries denoting different phases; however, all x-ray diffraction evidence indicates the presence of at least two phases, τ-$WB_2(WB_4)$ and W_2B_5. Photomicrographs shown in later sections demonstrate that the core is formed by radial diffusion with an additional phase transformation during cooling.

3.5.3.2 United Aircraft Research Production Boron Filament

The structure of a United Aircraft Research boron filament is presented in Figs. 9 and 10. The surface texture is typical of a higher temperature deposit in that it has no minor nodules. The unetched cross section shown in Fig. 9b contains two radial cracks which are straight for approximately three-fourths of the boron coating thickness before changing to curved cracks. The core is fully reacted, as is typical of production filaments. An etched cross section in Fig. 10 reveals that the United Aircraft Research filament differs considerably from the Texaco filament. Here, the United Aircraft filament is seen to consist of an inner ring with a faint ring pattern and an outer section which is heavily ringed. The radial lines again correspond to the major nodules

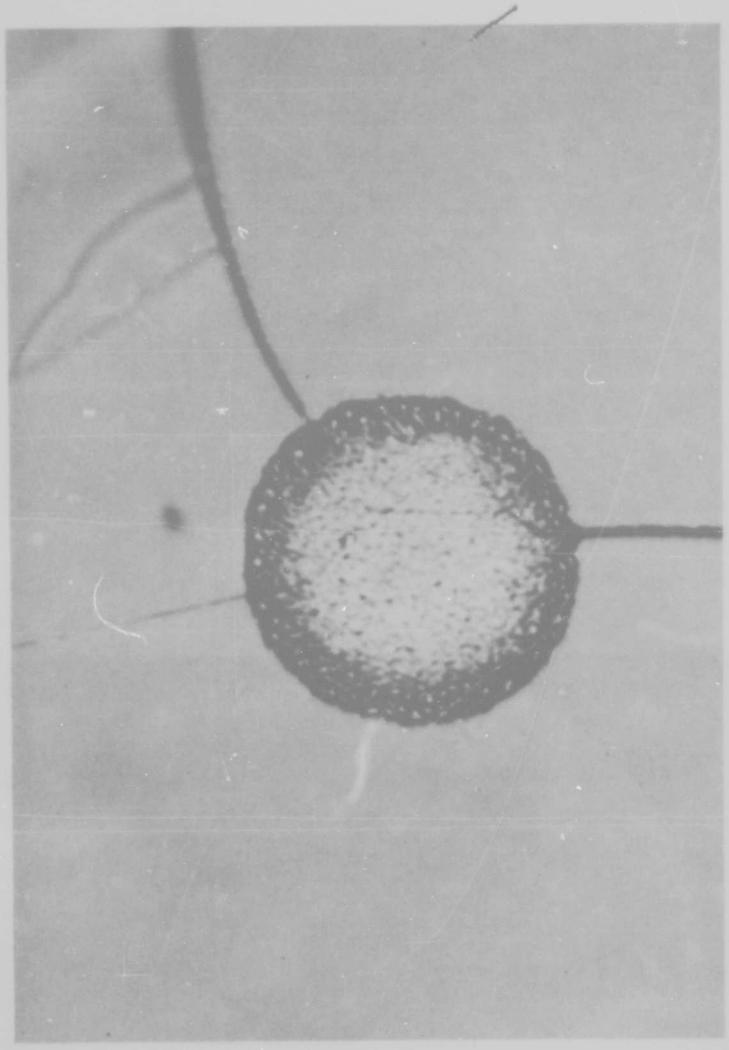

Fig. 8 Core Structure of Texaco-6 Boron Filament.
M8425, 3000×

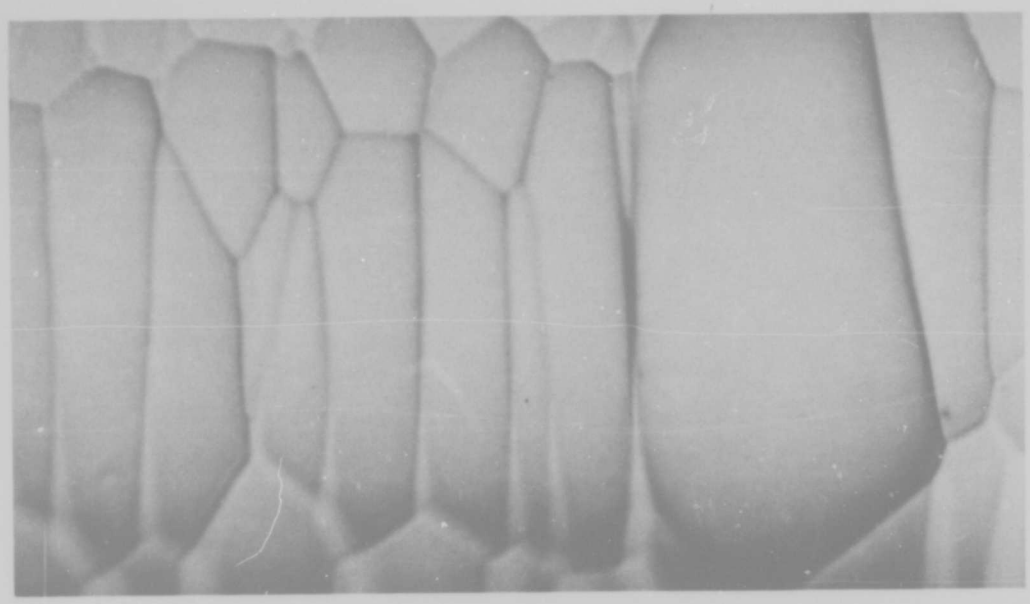

Fig. 9a Surface of United Aircraft Research Boron Filament. P4544, 3000×

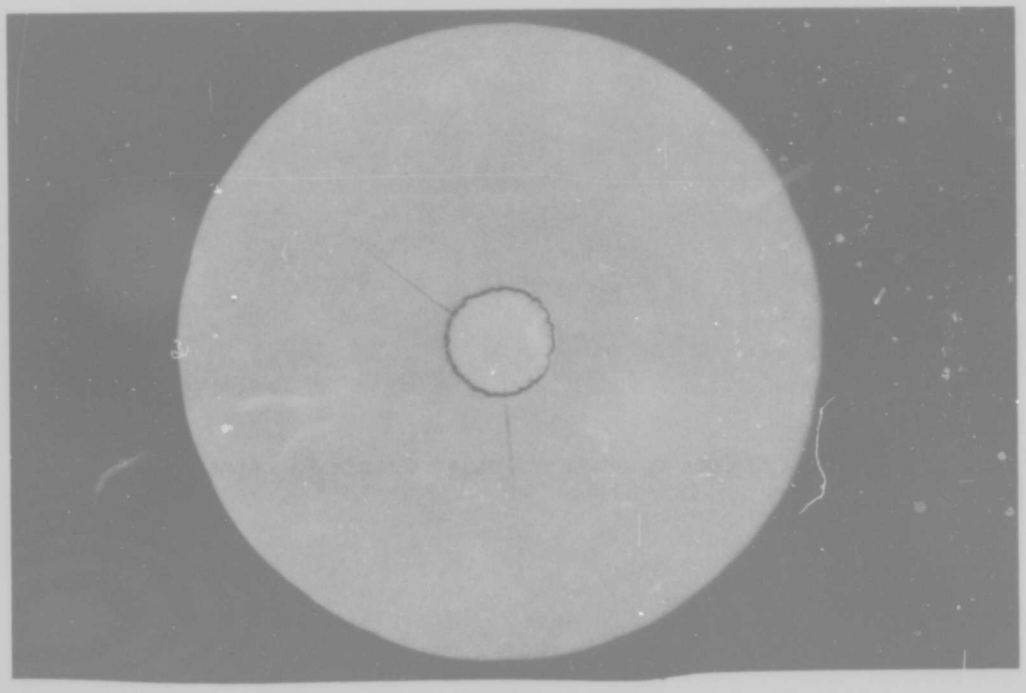

Fig. 9b Unetched Transverse Cross Section of United Aircraft Research Boron Filament. P2418, 1000×

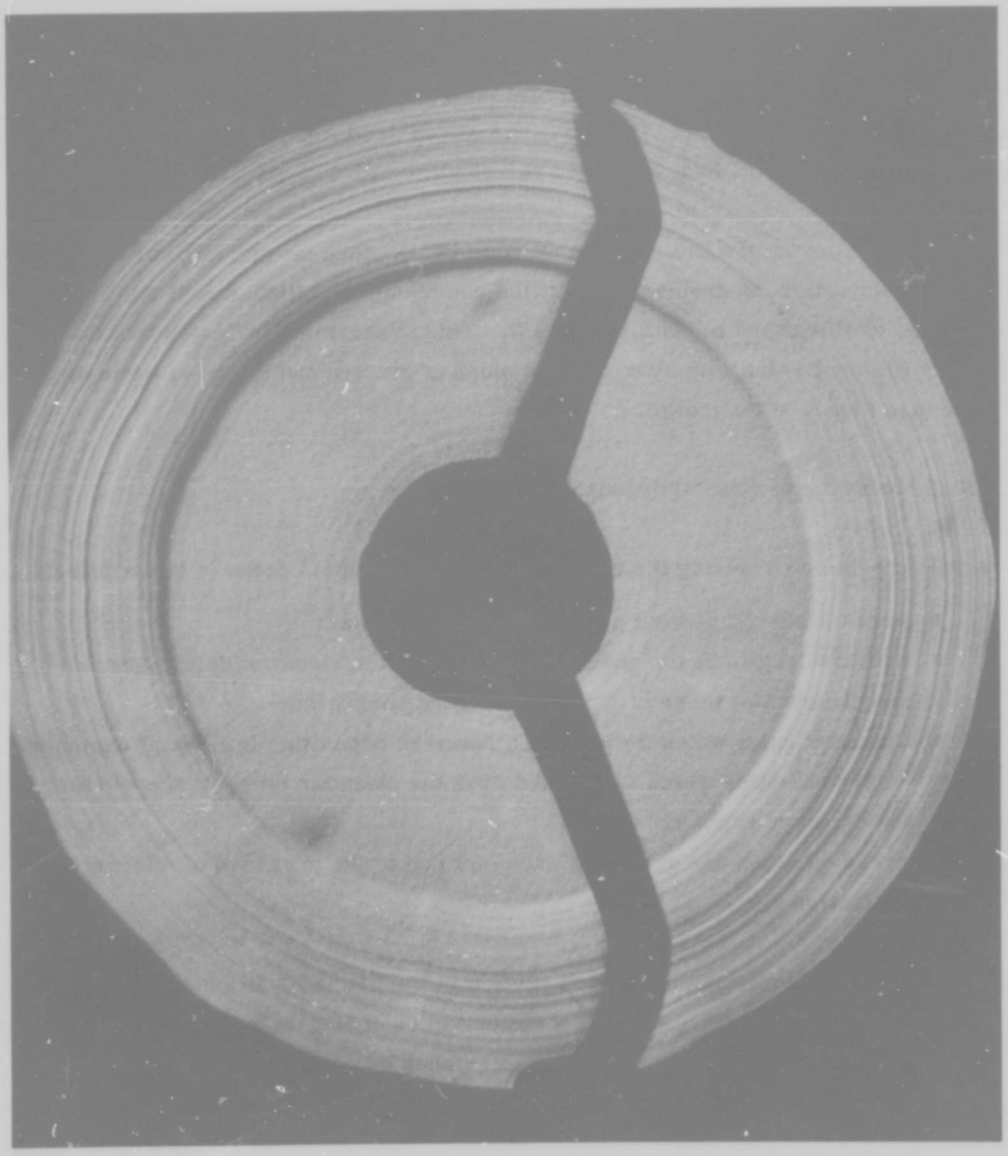

Fig. 10 Etched Cross Section of United Aircraft Research Boron Filament. P2614, 1550×

as is the case with the Texaco filament. The inner ring structure is apparently due to deposition at a fairly uniform rate while the second ring must be deposited at a much faster and less uniform rate. Gas pressure waves and local temperature variations probably account for the heavily ringed structure.

The etching action on the United Aircraft filament is more severe than for the Texaco material, but it is comparable to that at the chamber ring interfaces of the Texaco filaments, as discussed in Section 3.5.3.3. This observation indicates that the United Aircraft filament is built up by a process which is predominantly one of nucleation rather than steady state growth.

3.5.3.3 Defects and Fracture Modes

Several defects occur during the growth of boron filaments. Some of these defects are:

- Areas where nucleation predominates over growth
- Radial - longitudinal cracks which occur as the result of core expansion and differential thermal expansion during production
- Chamber rings which develop as a result of deposition in several chambers
- Solid impurities which are picked up at the chamber ring interfaces from the mercury seals
- Areas of excessive growth at one point due to the presence of a large nucleation site

Figure 11 shows a longitudinal tapered section in the Texaco-6 filament. The important features to be noted here are the cell structure in each ring-layer and the difference in the degree of etching at the chamber ring interfaces as compared with the central portions of the chamber rings.

A large nodule which formed by excessive growth is shown in Fig. 12. The nodule retains its continuity through all six chamber rings and this continuity of nodules is common, as shown in the cross section views of Figs. 4 – 7 and Fig. 12. Another

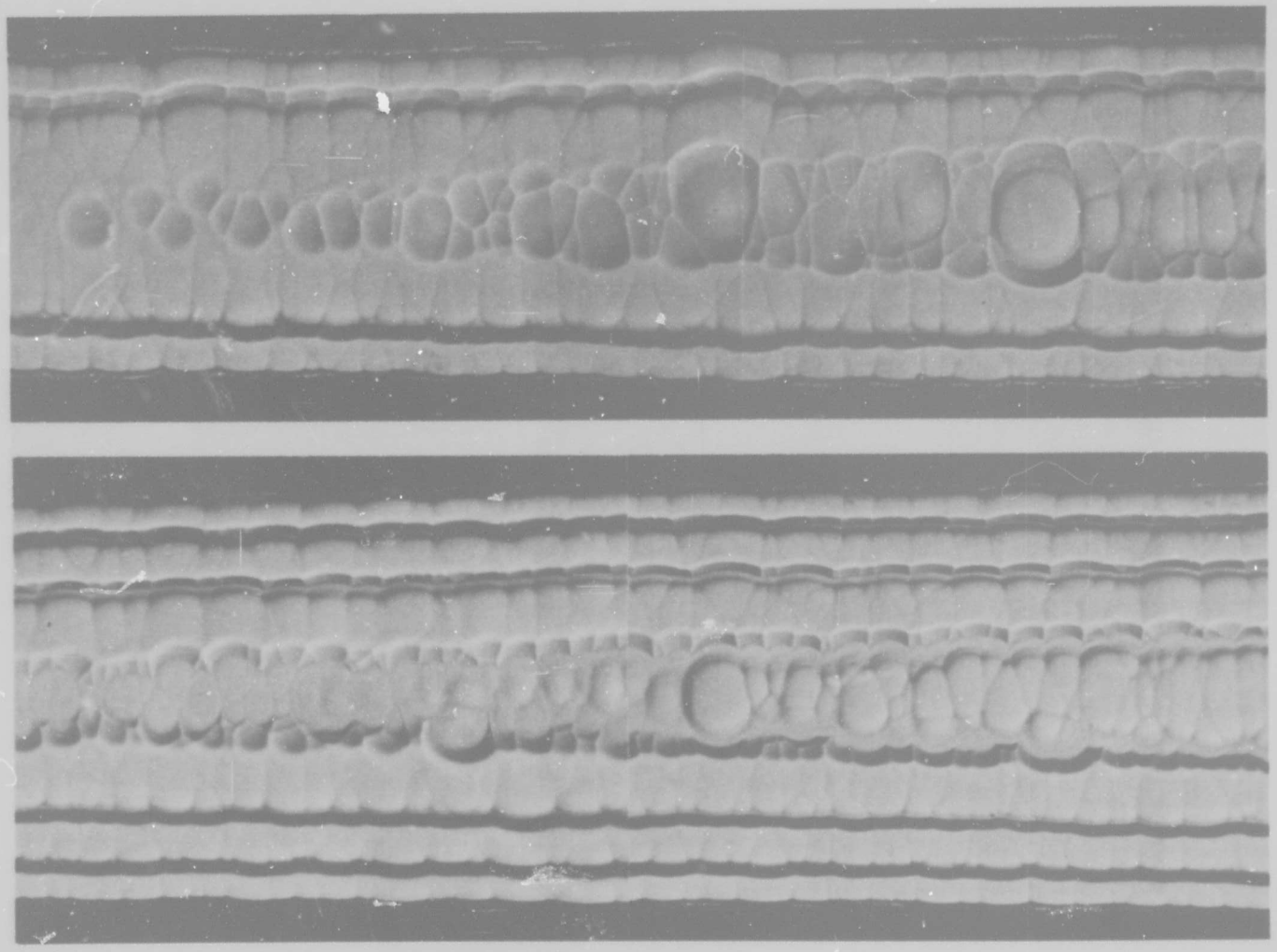

Fig. 11 Longitudinal Taper Section of Texaco-6 Filament. Details of Structure are Revealed on a Polished and Etched Cross Section. Composites of P-1101, P-1102, P-1090, and P-1088; 800×.

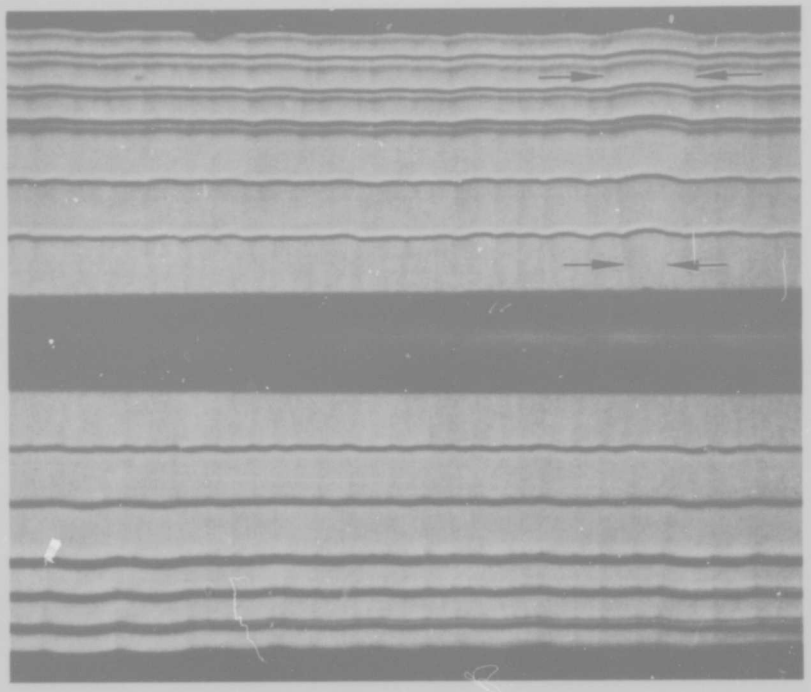

Fig. 12 Longitudinal Cross Section of Texaco-6 Filament. Core Removed During Polishing. Note Growth Continuity From Center to Outside as Indicated by Arrows. P-1104; 800×.

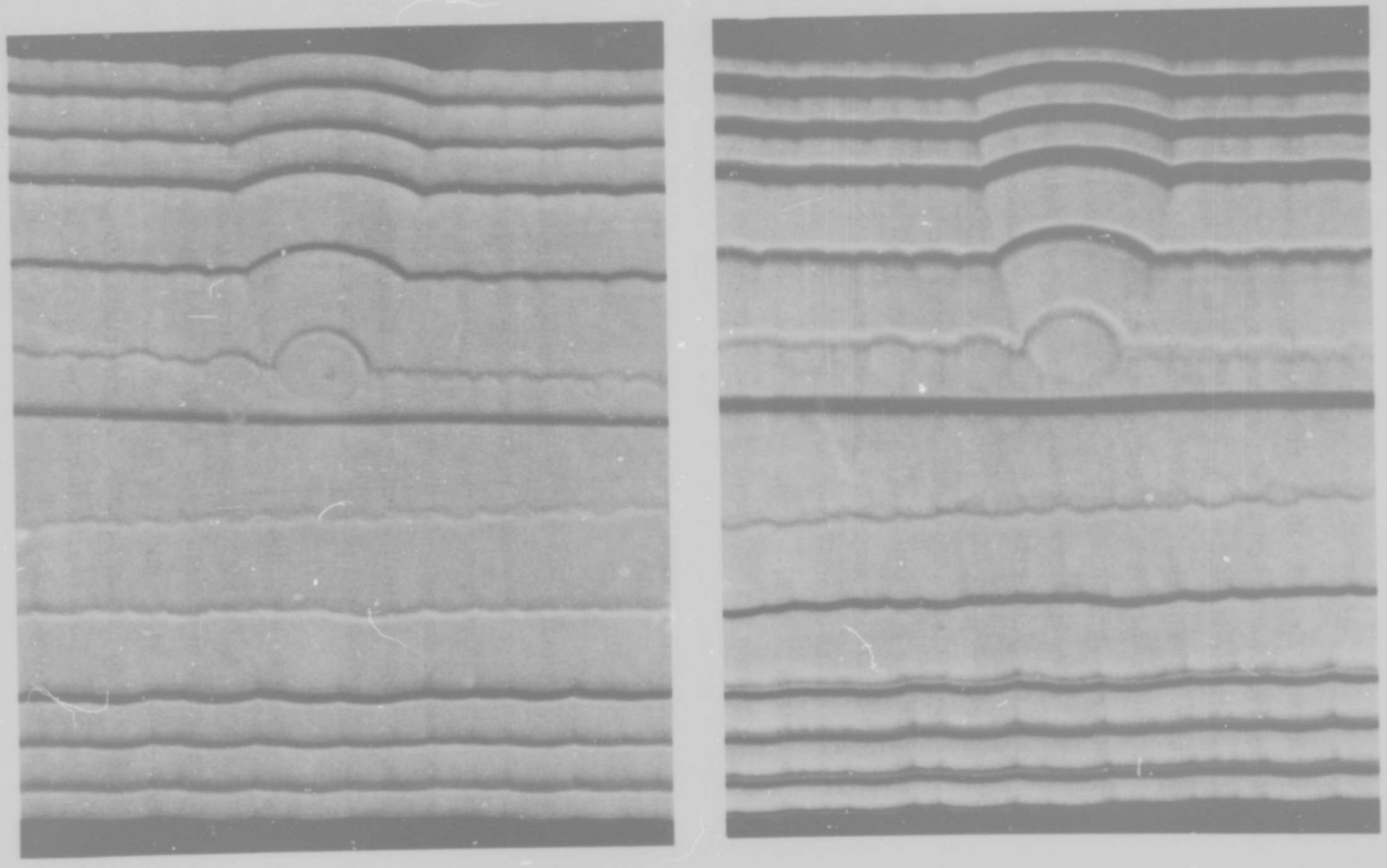

Fig. 13 Longitudinal Cross Section Near Center Showing Large Cone After Two Levels of Etching. Note Speck at Cone Origin (Left). Dark Line Near Center Is a Crack. P-1066 and P-1105; 1000×.

large nodule is shown in Fig. 13. Here, the foreign particle is visible in one photograph and has been removed by etching in the second photo. The method by which the nodule structure continues through the chamber rings is demonstrated quite clearly in these photographs. The original nodules occur as the result of surface roughness on the substrate, and Wawner (Ref. 14) has shown that a single scratch on a tungsten plate will produce a row of nodules when boron is vapor deposited onto the plate. As shown in Fig. 9, and elsewhere, the original tungsten wire is deeply scored with scratches from the wire drawing die, and each of these scratches results in a set of nodules by the mechanism described by Coffin (Ref. 16) and Diefendorf (Ref. 17). Nucleation occurs at closely spaced points over the entire surface, with the initial growth being microscopic and hemispherical. Interference of the microscopic spheres leads to a uniformly advancing surface which follows the contour of the substrate surface. Growth on a surface protrusion or foreign particle, as described by Coffin (Ref. 16) and Diefendorf (Ref. 17), produces abnormal nodules which are the result of radial growth away from the surface protrusion impinging on the growth from the flat portion of the substrate. The major boundary separating this abnormal nodule from the rest of the deposit is developed at the concavity surrounding the surface protrusion.

The development of a normal major nodule boundary is depicted schematically in Fig. 14. Uniform growth occurs until the thickness of the deposit is equal to the radius of the concavity. Impingement occurs with increasing growth, a major nodule boundary being formed at the center of the concavity. Uniform spacing and shape of the surface irregularities will lead to uniform major nodule structure, and reducing the severity of irregularities will reduce the surface curvature of the major nodules.

As will be shown in Section 3.6, minor nodules occur at the lower temperatures and longer exposure times. At the high temperatures, surface diffusion is rapid and the nodule will seek a minimum surface area. At the lower temperatures, slight local fluctuations such as gas-phase nucleation (Ref. 18) can promote nucleation at a few points on the major nodule surfaces and the lower surface diffusion rates will not permit these small protrusions to smooth out. The net result is a minor nodule structure within the major nodules.

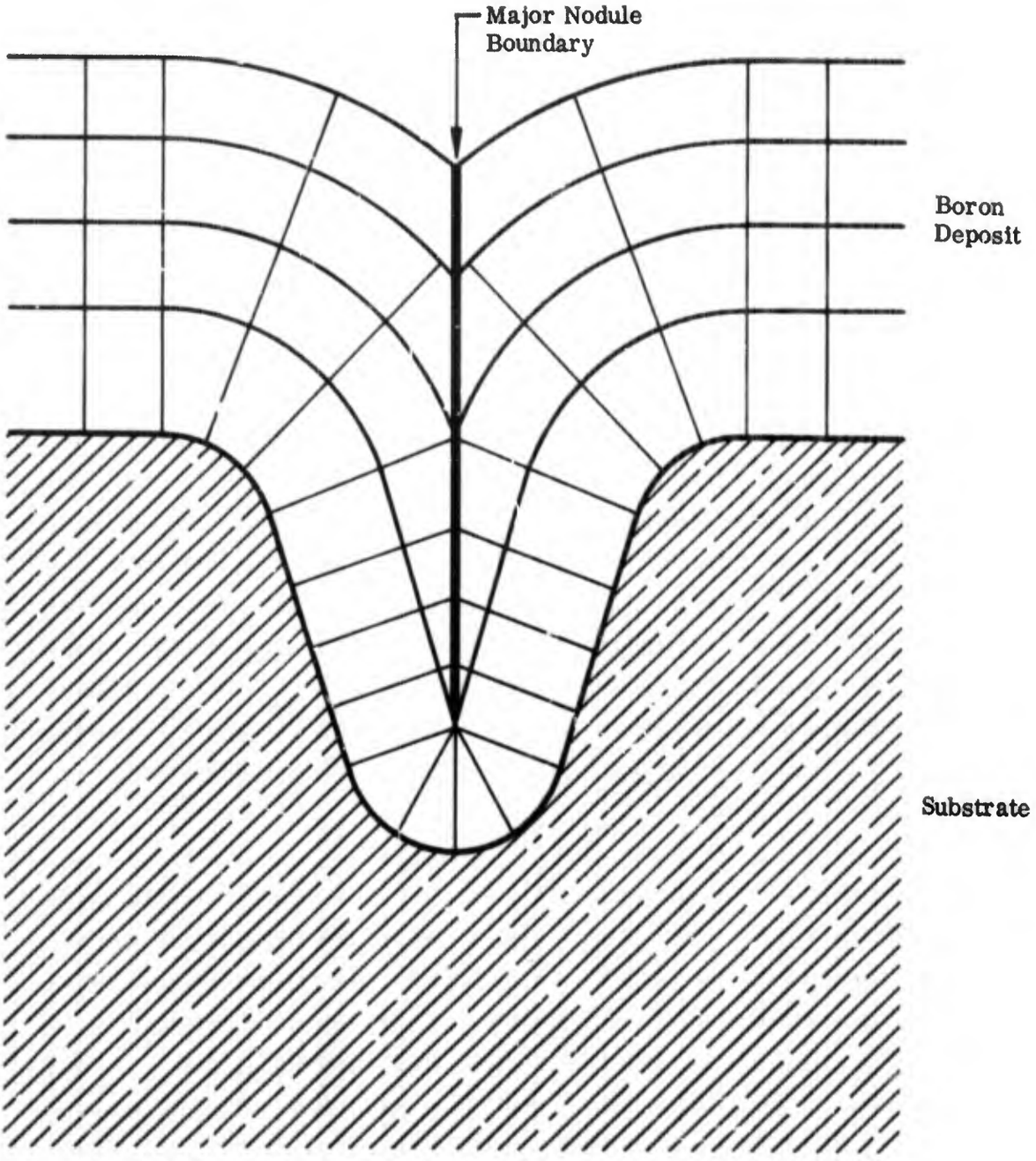

Fig. 14 Development of Major Nodule Boundary. (Major boundary forms at the center of a surface concavity by growth impingement)

The growth mechanisms described here apply equally well to all vapor deposited materials with a small crystallite size. Some examples are pyrolytic graphite, some forms of pyrolytic boron nitride, and silicon carbide filaments. In systems where large grains are formed, such as boron deposits at high temperature (Ref. 21), or metal deposits (Ref. 17), other factors determine the growth morphology.

Boron filaments do not seem to be capable of plastic deformation at room temperature; however, anelastic deformation near room temperature has been reported by Feingold et al. (Ref. 13) and at high temperatures by Hammond (Ref. 19). At least two modes of fracture at room temperature can be distinguished for boron filament: conchoidal fracture and apparent cleavage. Both of these modes are shown in Fig.15, which is a fractograph of a sliver taken from a filament broken by bending. The broad, flat fracture plane intersecting the core and lying parallel to its axis has the appearance of a cleavage fracture while the conchoidal fracture is evident from the specular reflection of light from the curved surfaces just below the depth of focus. As will be demonstrated in Section 3.7, the apparent cleavage fracture is the result of a crack which forms at the beginning of the deposition process and grows radially during most of the deposition process. The conchoidal fracture is typical of many brittle materials, including crystalline β-boron (see Section 3.4), and in boron filaments, it is generally nucleated by defects caused by foreign particles or by the boron-boride interface (Refs. 13, 14, 15, and 19).

The two modes of fracture are again seen in Fig. 16, which is a cross section of the Texaco-6 filament. The radial crack is perfectly straight and passes through the geometric center of the filament while the other cracks are not straight and do not necessarily pass through the center. The six chamber rings of Texaco-6 are visible in Fig. 16 and the increased chemical attack at the beginnings of the chamber rings is clearly shown. Continued etching of the cross section in Fig. 16, shown in Fig. 17, further indicates the enhanced chemical attack at the chamber ring interfaces and also reveals the presence of the radial line structure which corresponds to the major nodules. Finally, Fig. 18 demonstrates the effect of very heavy etching

M-7279

500×

Fig. 15 Fractograph of Boron Sliver from Boron Filament

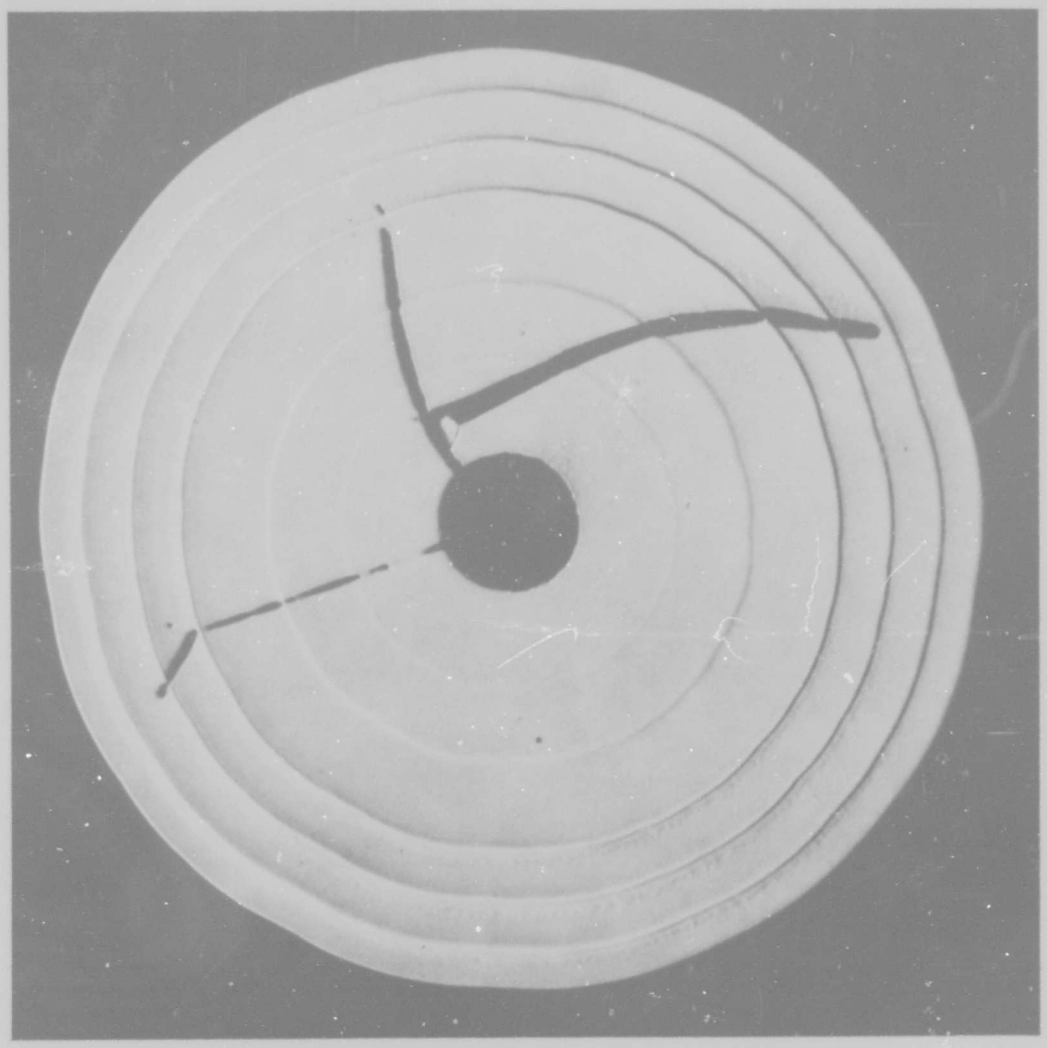

M-9011 1150×

Fig. 16 Cross Section of Texaco-6 Treated to Show Growth Rings

M-9012 1150×

Fig. 17 Same Cross Section as Fig.16 Treated to Show Radial Lines Associated With Inner Nodules

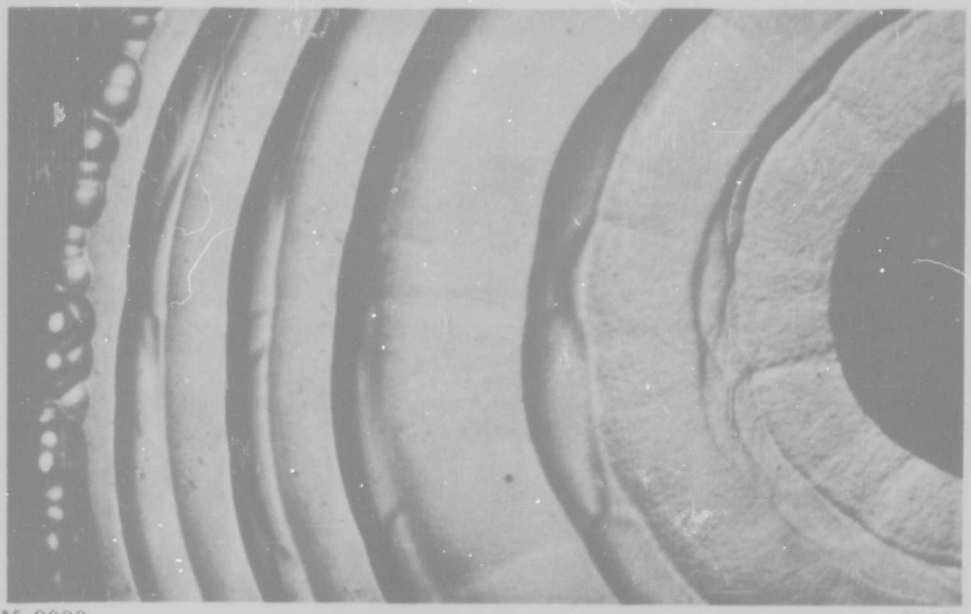

M-9000 2500×

Fig.18a Same Fiber as in Fig. 17 Treated to Show Nodular Growth Ring Surface. Bright Field

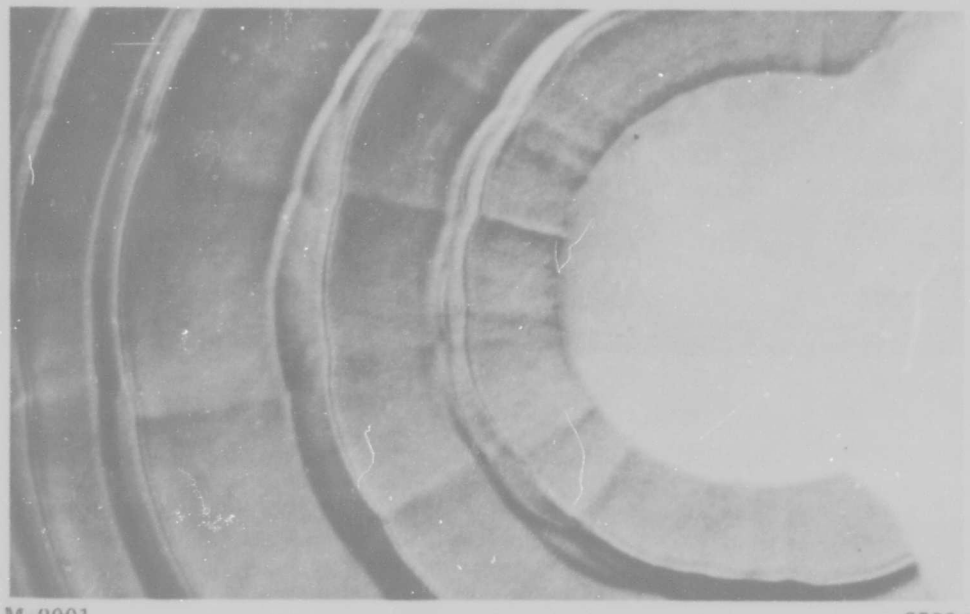

M-9001 2500×

Fig.18b Same Field as Fig. 18a. Polarized Light

on the chamber ring interface. This figure also demonstrates that boron filaments do not show optical anisotropy even though there are no cubic polymorphs of boron (Ref. 20). This lack of optical anisotropy is discussed further in Section 4.2.2.

3.5.4 X-ray Diffraction Observations

Debye-Scherrer films have been obtained from nine samples of the Texaco-σ material (three each of high, medium, and low strength), from eight samples of Texaco-3, taken at 10-ft intervals along the 100-ft length, and from one sample each of the Texaco-6 and -1 material. All the patterns were obtained with Ni-filtered Cu radiation in a 114.6 mm camera. Comparison of all the patterns showed that there are no significant differences among the samples and that the patterns are typical of boron filaments. Line widths of the boron halos were not measured, and the line widths of the boride lines were generally comparable to the instrumental broadening. The line breadths of the boride lines are thus commensurate with a boride crystallite size greater than 0.1μ, which compares favorably with the speckled structure in lightly etched cores observed at 3000×. The diffraction patterns were consistent with a mixture of W_2B_5 and τ-WB_2 (WB_4), as described in more detail in Sections 3.6 and 3.7.

3.5.5 Electron Microscopy

Electron microscope examinations were made on several production filaments; however, the interpretation of the data obtained from this portion of the study is best discussed later, in Section 4.4. In brief, the conclusions of that section are that all production filaments consist primarily of defect α-rhombohedral boron having crystallite sizes in the range 10 – 100 Å. Occasional small regions of large crystallite size α- and β-boron occur in the as-deposited filament, but their volume does not exceed a few percent of the total. The presence and distribution of the large crystallites is variable within a given filament, and no particular correlation was noted for the various filaments which were examined. It might be expected that the filaments deposited at higher temperatures would have a larger fraction of large crystallite size

material as compared to filaments deposited at lower temperatures; however, no evidence of this was found. The nature of transmission electron microscopy is such that only extremely small volumes of material are analyzed and small differences in material structure are difficult to discern if there is a wide variation within a given material. Some experiments to study the possibility of variations related to gross deposition parameters are suggested in Section 5.

3.5.6 Summary of Structure of Production Filaments

Samples of tungsten-core production filaments from Texaco Experiment, Inc. and United Aircraft Research were examined. In all cases, the tungsten core was fully reacted to form an intimately mixed two-phase region of τ-$WB_2(WB_4)$ and W_2B_5 with crystallite size greater than 0.1μ. The morphology of the boron sheath depended upon the production method, but the crystallographic nature of the boron seemed to be independent of the manufacturing method. All of the vapor-deposited filaments examined in this section lacked optical anisotropy under polarized light, and all had straight radial cracks which are related to the production process. The dominant features of the Texaco production filaments were:

- The high degree of uniformity of structure throughout a filament length
- The variation in strength brought about by random defects in the filament
- The wide range of morphologies produced under different conditions and in different production lengths
- The presence of growth nodules with and without minor nodules
- The presence of chamber rings caused by stopping and restarting the growth at mercury seals at the end of the deposition chambers
- The continuity of growth nodules across the chamber ring interfaces
- The cusped structure at the chamber ring interfaces and the radial lines revealed by polish-etch-buffing which correspond to the major nodule structure
- The strong chemical attack which occurs at the chamber ring interfaces
- The flat, longitudinal mode and the conchoidal mode of fracture

The United Aircraft Research boron filament was similar to the Texaco filaments except as viewed in transverse cross section. Instead of several chamber rings, the structure consisted of two rings, the inner ring having a normal appearance and the outer ring having a wavy texture. The growth nodules continue from the substrate to the filament surface, but the resistance to chemical attack is comparable to that at the chamber ring interfaces of the Texaco filament. This increased chemical attack led to the hypothesis that gas-phase nucleation occurred in the United Aircraft process while surface nucleation dominated in the Texaco process.

Electron microscopy demonstrated that boron deposited on W substrates in the vicinity of 1150°C consists primarily of α-rhombohedral boron with a crystallite size range of 10–100 Å. Occasional areas of large crystallite size α- and β-boron are also present and are the result of random fluctuations in the deposition conditions.

3.6 STRUCTURE OF BORON FILAMENTS DEPOSITED UNDER VARIOUS CONDITIONS

3.6.1 Material Examined

The production filaments described in the previous section were prepared under conditions which were optimized by observing mechanical properties. To study the effects of deposition parameters on the structure of boron filaments, nineteen samples of B/W filaments were acquired from Astro Research, Inc. which had been prepared under various temperatures and exposure times. Several 6-in. lengths of each filament type were supplied; Table 4 gives the sample designation and deposition conditions. The Astro sample number has been modified to include a number-letter combination which is related to the deposition parameters. The number increases with increasing temperature, the letter indicating the travel speed through the deposition chamber. This number-letter combination was used to identify the samples in the quarterly reports for this program.

Table 4

DEPOSITION CONDITIONS FOR SPECIALLY PREPARED ASTRO FILAMENTS[a]

Specimen Number	Speed (ft/sec)	Temperature (°C)
A16-1a	No Specimen	
15-2a	2/3	980
25-3A	2/3	1040
16-4a	2/3	1090
26-5a	2/3	1200
17-6a	2/3	1260
21-1b	2	870
12-2b	2	980
22-3b	2	1040
13-4b	2	1090
23-5b	2	1200
14-6b	2	1260
27-1c	6	870
18-2c	6	980
28-3c	6	1040
19-4c	6	1090
29-5c	6	1200
20-6c	6	1260
30[b]	2	1090
31[c]	2	1090

[a] Gas flow 1000 cm^3/min in all cases, BCl_3 concentration 40% except as noted

[b] BCl_3 concentration 30%

[c] BCl_3 concentration 67%

3.6.2 Property Variations

As expected, the properties of the Astro samples varied considerably from one set of conditions to another. In addition, there was some variation within batches A-16-12, -18, -19, -21, and -28, but other sets of these samples were supplied which were uniform within each sample type.

Mechanical properties were not available for the Astro samples; however, some indication of the mechanical properties can be inferred from the mechanical stability. Table 5 presents certain observations on the general mechanical integrity of the Astro filaments. More of each filament length was examined at Astro Research than at LMSC, and certain differences in the evaluation are reflected in the table. It is likely that these variations are due to the different lengths of filament examined in each case. Splitting occurred in all the Astro specially prepared filaments except for A16-21-lb, -18-2c, -28-3c and -19-4c. These filaments are four of the five smallest filaments which were prepared at the lowest values of temperature and exposure time.

3.6.3 Metallographic Observations

Specimens from each Astro Sample batch were studied optically. Surface textures were photographed at 3000X under oil immersion and transverse cross sections were photographed at 1000X and 3000X. Cross sections were prepared in the chromic acid polishing bath as described in Section 3.2 to preserve the core detail.

3.6.3.1 Surface Textures

The surface textures of the Astro samples are displayed in Fig. 19, together with their deposition parameters. Significant features to be noted are:

- Lower temperatures and longer exposure times tend to produce a minor nodule structure
- Higher temperatures tend to promote delineation of the major cone structure

Table 5

MECHANICAL STABILITY OF ASTRO SPECIALLY PREPARED FILAMENTS

Specimen Number	Broken As Received	Straight		Splitting Observed	
		Astro	LMSC	Astro	LMSC
A16-					
24-1a	yes	no	-	no	-
15-2a	yes	no	no	extreme	extreme
25-3a	yes	no	no	extreme	extreme
16-4a	yes	no	yes	yes	no
26-3a	yes	no	yes	yes	no
17-6a	yes	no	no	step	step
21-1b	yes	?	most	no	no
12-2b	no	no	most	step	no
22-3b	yes	no	most	yes	no?
13-4b	yes	no	most	yes	no?
23-5b	yes	yes	yes	step	step
14-6b	yes	no	no	yes	yes
27-1c	yes	?	yes	step	?
18-2c	yes	yes	yes	no	no
28-3c	yes	no	most	no	no
19-4c	no	no	no	no	no
29-5c	yes	no	no	yes	no
20-66	yes	no	yes	yes	yes
30	yes	no	most	yes	no?
31	yes	yes	yes	no	yes

- Combinations of high temperature and short exposure time can lead to the elimination of the minor nodule structure
- The minor nodules are nearly circular in shape while the ratio of the longitudinal to circumferential dimensions of the major nodules tends to be approximately 1:2.
- The ratio of longitudinal to circumferential dimension of the major nodules decreases with increasing temperature, ranging from 1:1 to 1:3

A method of describing boron filaments by their surface texture and other features is discussed in Section 3.6.3.4.

3.6.3.2 Transverse Cross Sections

Transverse cross sections of the Astro samples are shown in Fig. 20 at 500X as displayed; Table 6 contains the outer diameter and core diameters obtained from these and other photographs. Straight and curved cracks are present in nearly every cross section, and the cracks are of maximum width at the intermediate deposition temperatures. These cracks are not directly the result of sample preparation and it will be shown later that the straight, radial cracks are present in the filaments prior to handling. The curved cracks are fractures which can exist in the material prior to handling, which can be formed when a sample is broken off for mounting, or which can form during the mounting operation. The sources of the cracks are stresses due to volume changes during deposition, thermal expansion, volume changes occurring during cooling, and the presence of foreign particles occluded during deposition. The severity of the cracks reaches a maximum at the intermediate temperatures for all deposition conditions. At highest temperature, the core probably reacts very quickly, thereby minimizing the effects of volume change during deposition while the deposits made at the lowest temperatures are not sufficiently thick nor is the core sufficiently reacted to cause stresses greater than the fracture strength. Intermediate conditions lead to maximum stresses and largest cracks.

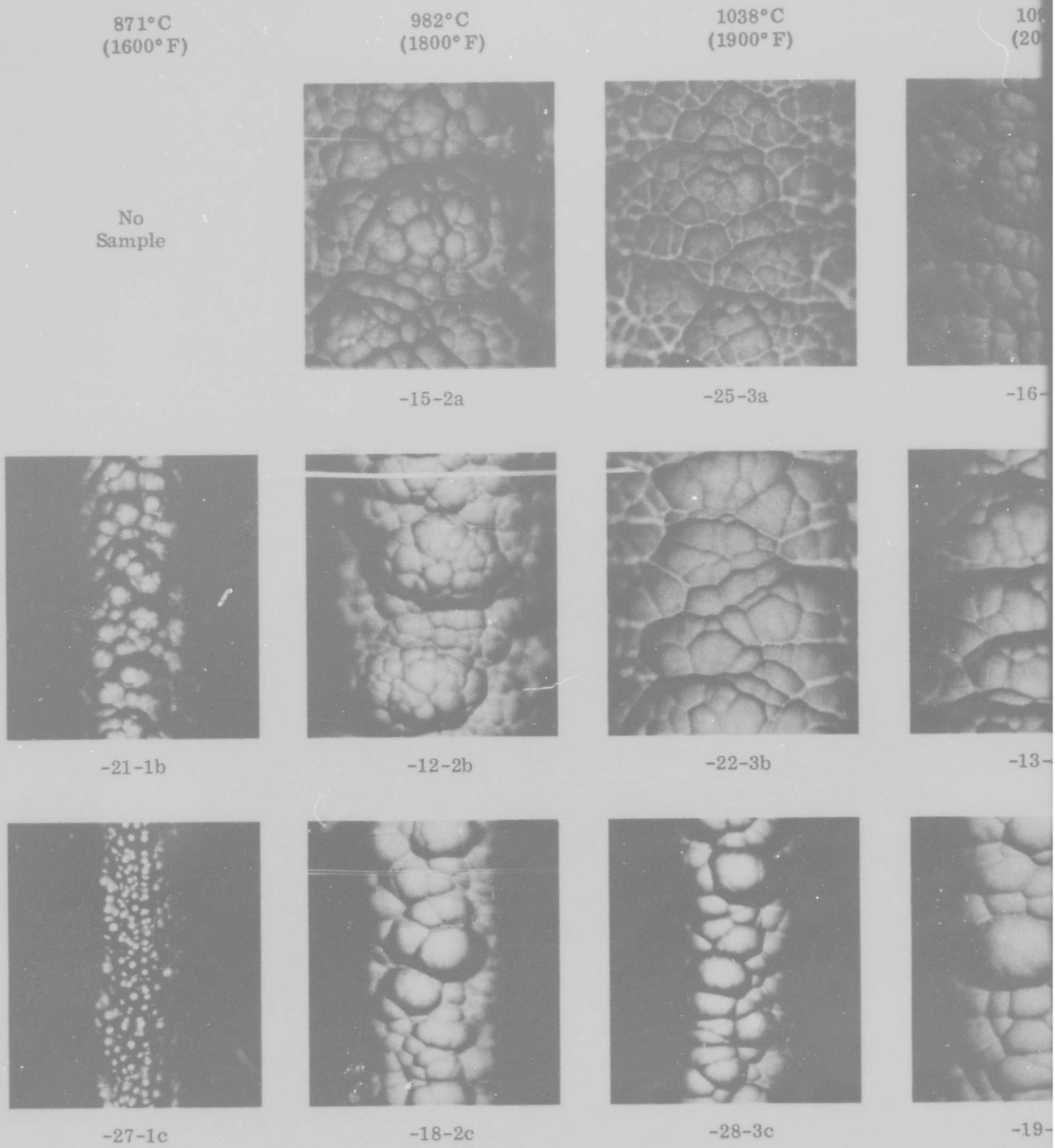

Fig. 19 Effect of Deposition Conditions on the Surface Texture of Boron Filaments. (Ast

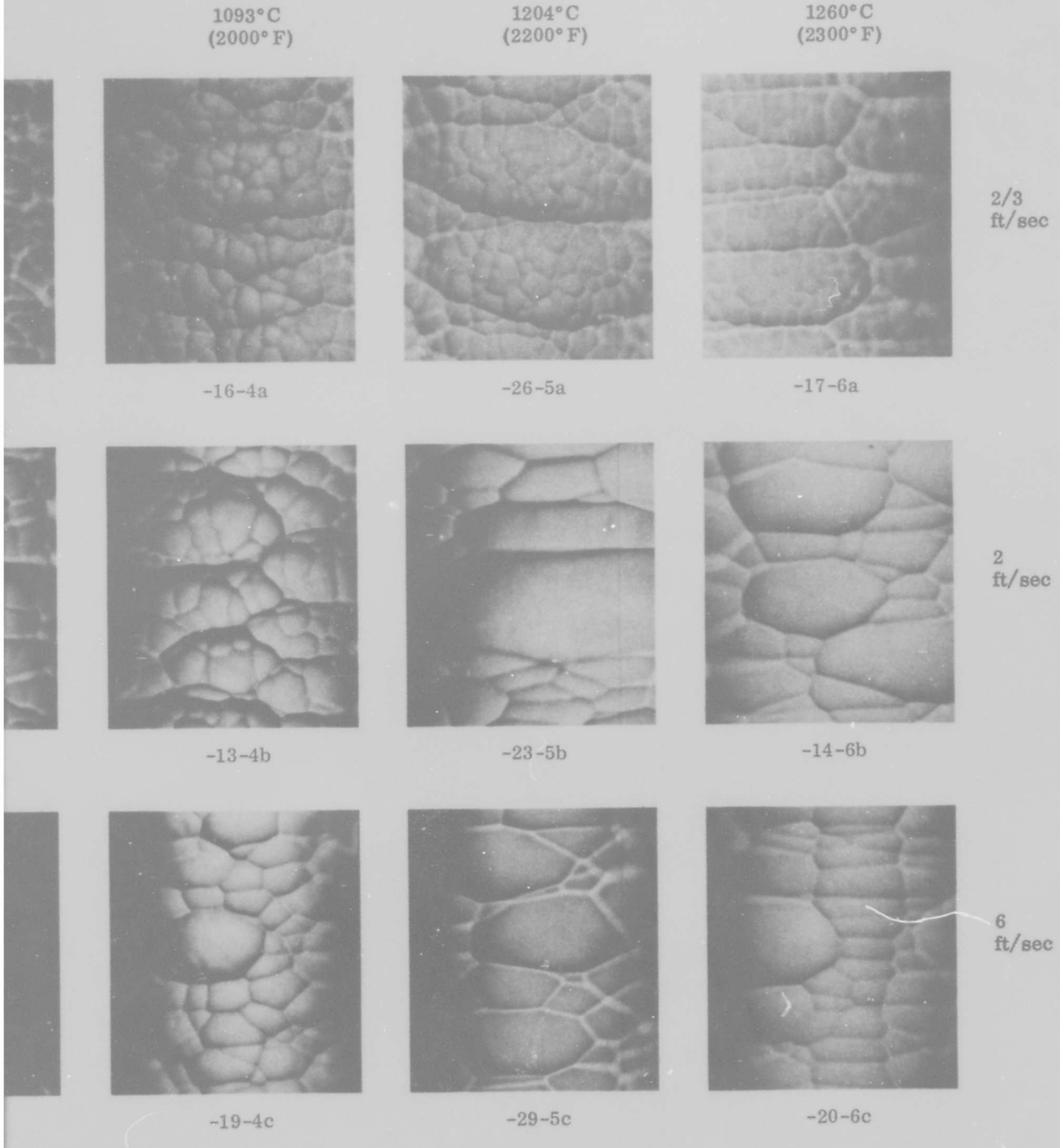

Boron Filaments. (Astro Material A-16-_) 3000×. Reduced 50% for reproduction

2

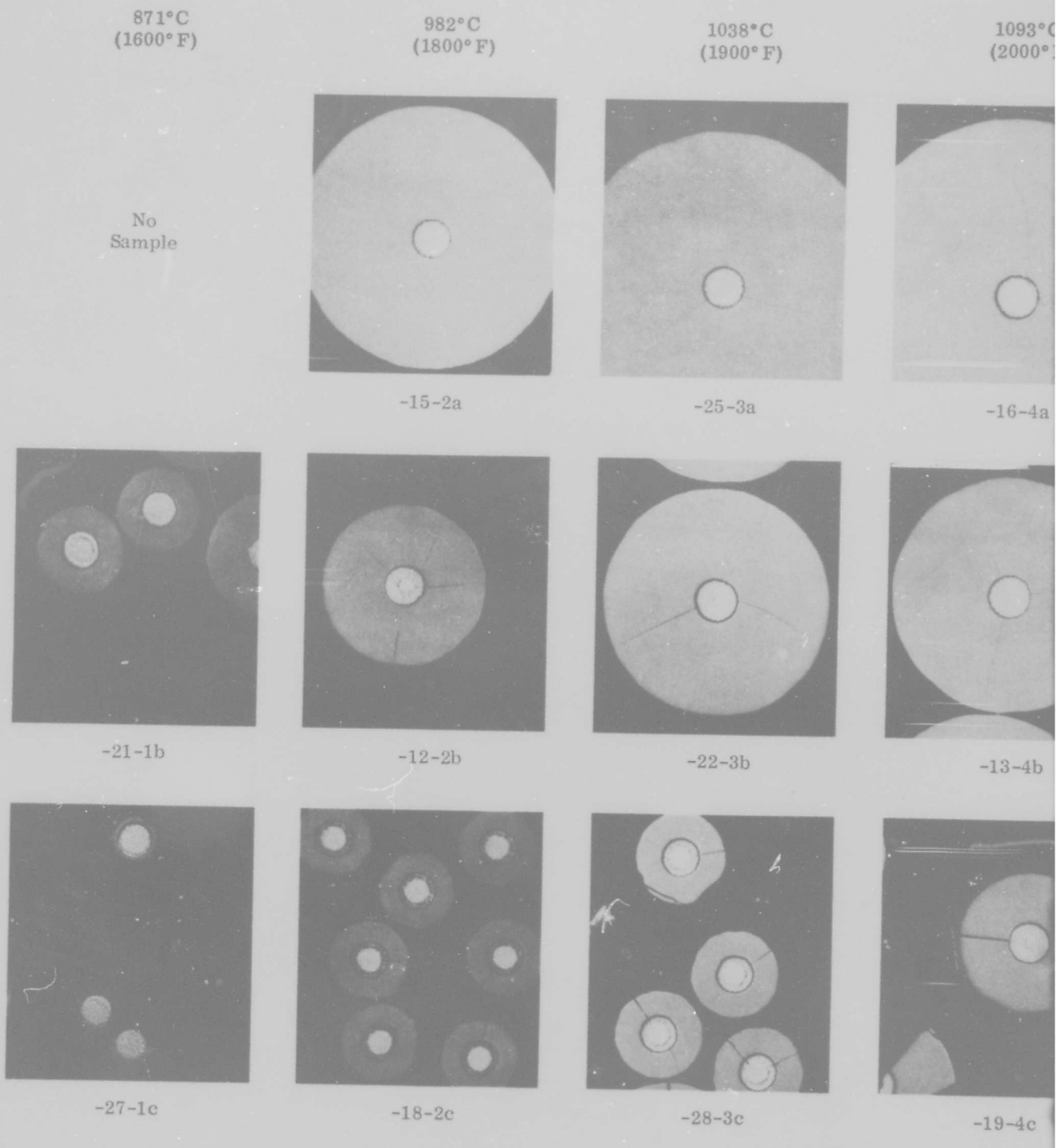

Fig. 20 Transverse Cross Sections of Boron Filaments Deposited Under Different Conditions. (As

	1093°C (2000° F)	1204°C (2200° F)	1260°C (2300° F)	
	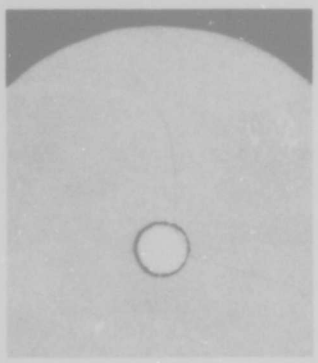	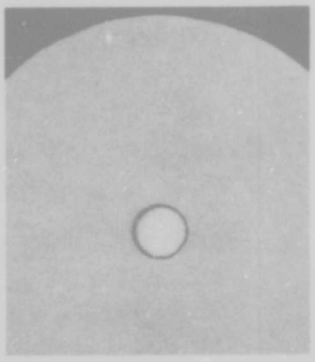	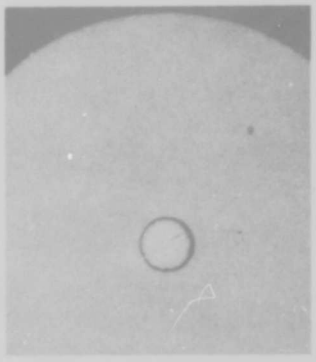	2/3 ft/sec
	-16-4a	-26-5a	-17-6a	
	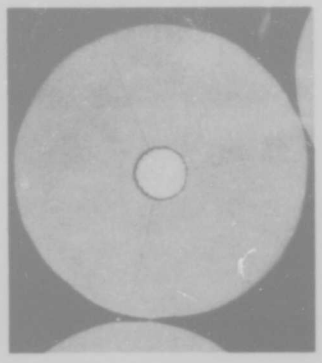	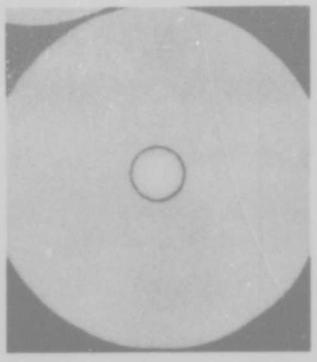	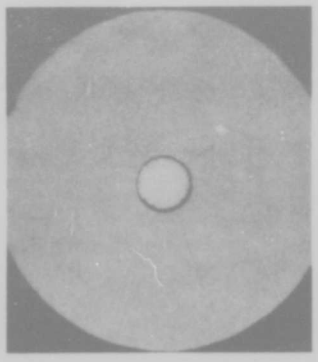	2 ft/sec
	-13-4b	-23-5b	-14-6b	
	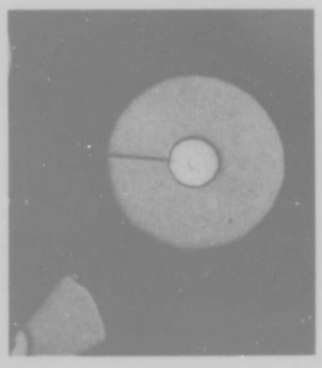	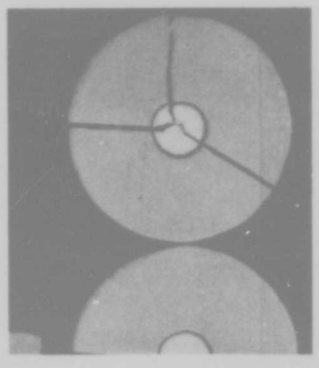	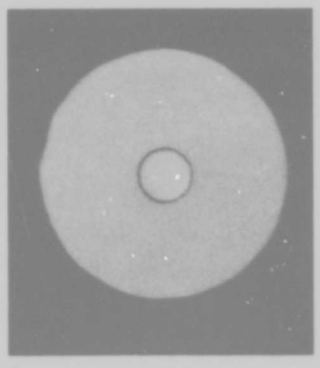	6 ft/sec
	-19-4c	-29-5c	-20-6c	

Different Conditions. (Astro Material A-16-_) 1000×. Reduced 50% for reproduction

2

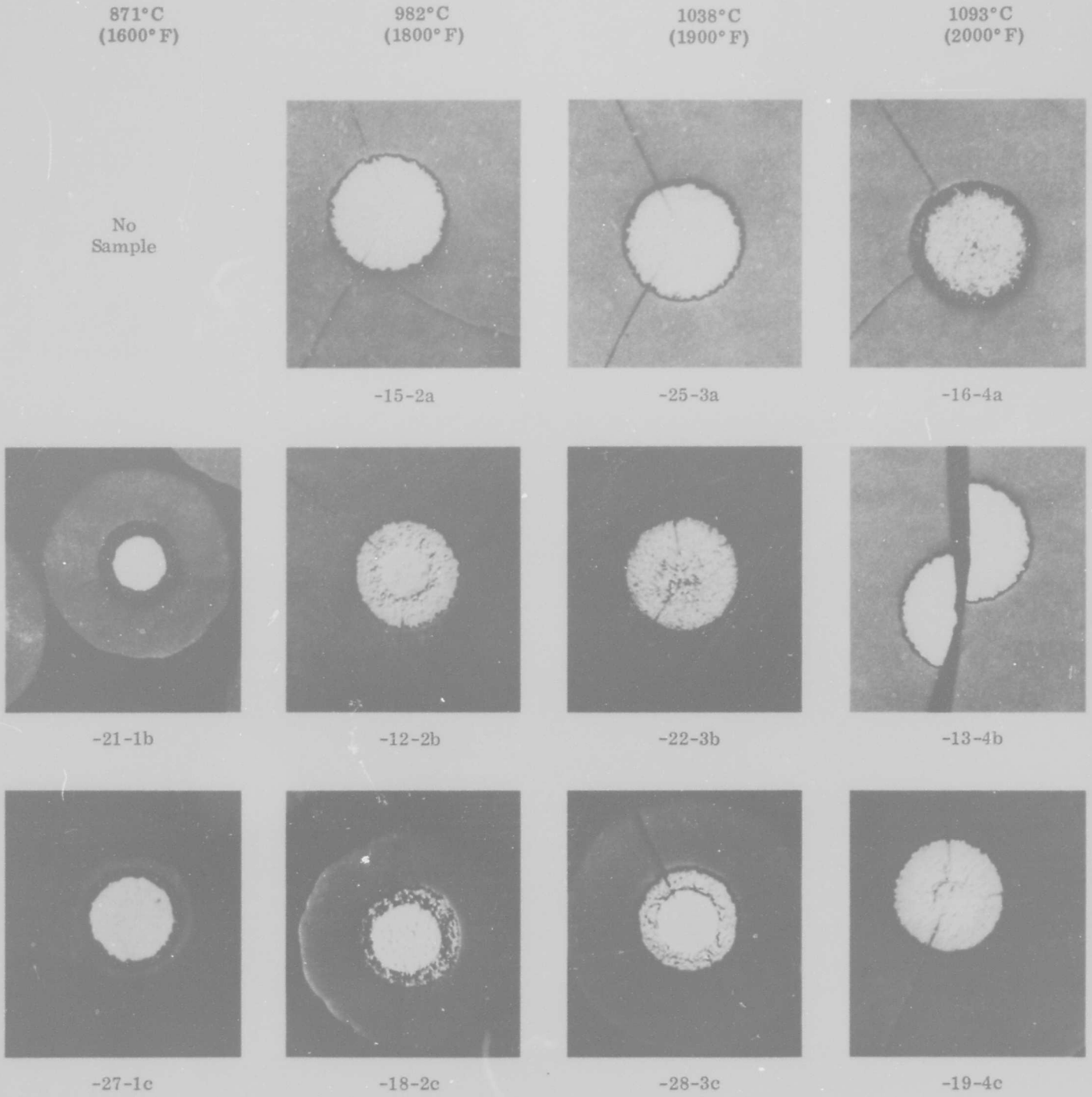

Fig. 21 Core Structures in Boron Filaments Deposited Under Different Conditions. (Astro Material A

	1093°C (2000°F)	1204°C (2200°F)	1260°C (2300°F)	
	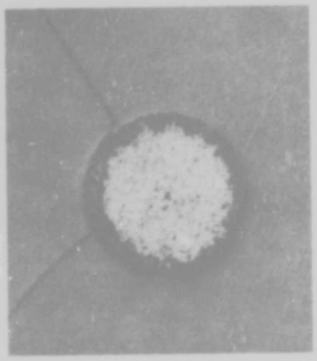	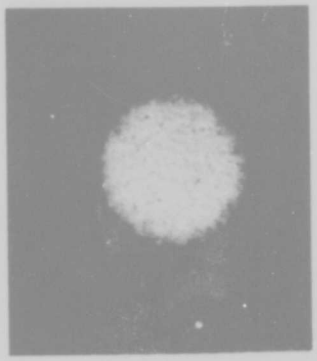	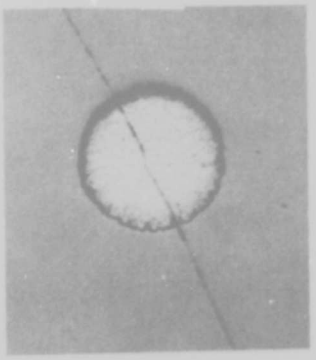	2/3 ft/sec
	-16-4a	-26-5a	-17-6a	
	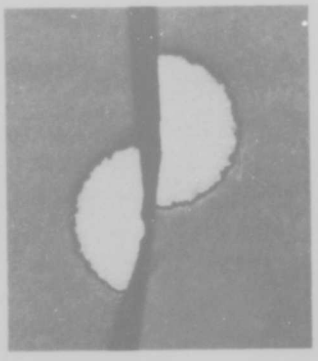	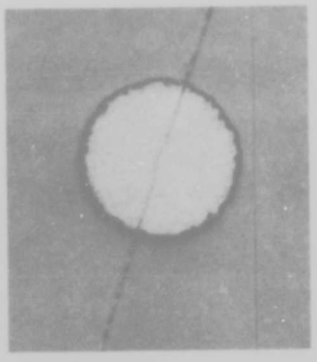	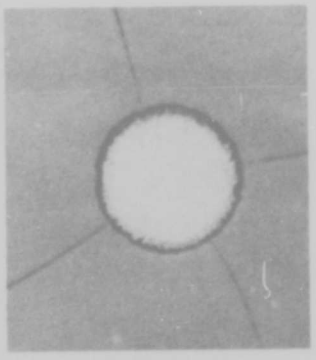	2 ft/sec
	-13-4b	-23-5b	-14-6b	
		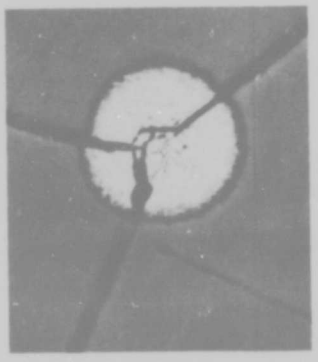	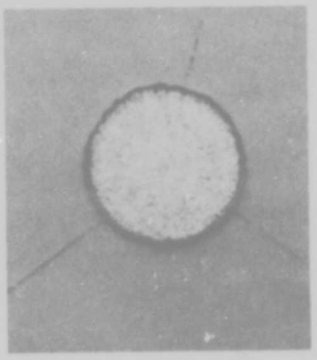	6 ft/sec
	-19-4c	-29-5c	-20-6c	

Different Conditions. (Astro Material A-16-_) 3000×. Reduced 50% for reproduction

2

Table 6

METALLOGRAPHIC FEATURES OF SPECIALLY PREPARED ASTRO FILAMENTS

Specimen Number A16-	Diameters				
	Plate[a]	Outer (μ)	Inner (μ)	Inner Inner (μ)	Crack Widths
1a					
15-2a	2520	104	16.7	–	Fine
25-3a	2371	134	16.3	–	Med
16-4a	2038	141	16.7	–	Med
26-5a	2130	137	167	–	Fine
17-6a	2363	147	15.3	–	Fine
21-1b	2043	35	11.0	7.3	Fine
12-2b	2036	64	14.7	6.7	Med
22-3b	2128	90	16.7	–	Med
13-4b	2417	93	16.7	–	Med
23-5b	2154	107	16.7	–	Fine
14-6b	2361	107	15.3	–	Fine
22-1c	2044	18	13.7	11.3	No
18-2c	2155	31	14.4	9.7	Fine
28-3c	2181	5	14.7	8.7	Med
19-4c	2040	56	16.7	4.3	Big
29-3c	2180	72	16.7	–	Big
20-6c	2368	79	16.7	–	Fine

[a]Metallography Photo Number

Table 7 gives the ratios of the outer diameters, corrected for the presence of the core, at each temperature relative to that for the shortest exposure time. The ratio of exposure times stands as 9:3:1 which differs considerably from the corrected diameter ratios. The growth rate apparently decreases with increasing diameter for all temperatures; the thicker the filament and/or the higher the temperature, the more pronounced the effect becomes.

3.6.3.3 Core Structure

The core structures of the Astro samples are shown in Fig. 21 at 1500X as displayed. The significant features of the core structure are:

- The radial cracks present in every sample except A16-27-1c
- The uniformity of the core structures for the 2/3 ft/sec travel speed
- The ringed structure for the lower temperature samples prepared at the faster travel times

By combining the x-ray diffraction observations with the core structures depicted in Fig. 21, a description of the core reaction process can be developed. All of the uniform cores gave diffraction patterns which could be explained by the presence of W_2B_5 and the Texaco WB_2 phase, called τ-WB_2 in this report, or its equivalent, WB_4 (Ref. 11). This indexing is described in Section 3.6.4.

For the 6 ft/sec travel speed, the core of the 870° C sample is mostly W with a thin outer core ring of δ-WB. There was no x-ray indication of another phase, but the outer core ring appears to be two phase. The core ot the 980° C sample consists of W, τ-WB_2(WB_4) and W_2B_5, the evidence of δ-WB having been covered by the other diffraction peaks. A radial crack has developed in the boron ring which extends into the core. The formation of this crack, which is a common occurrence in B/W filaments, is discussed in more detail in Section 3.7.2.3.

For the next higher temperature, 1040° C, some W still remains but the diffraction patterns of τ-WB_2(WB_4) and W_2B_5 are stronger. At 1090° C, the W is completely

Table 7

COMPARISON OF FILAMENT DIAMETERS FOR DIFFERENT DEPOSITION TEMPERATURES AND EXPOSURE TIMES

Relative Exposure Time	Corrected* Ratio of Diameter at x ft/sec to Diameter at 6 ft/sec					
	870° C	980° C	1040° C	1090° C	1200° C	1260° C
9	-	5.3	6.2	3.3	2.1	1.9
3	5.2	2.9	2.8	1.9	1.4	1.3
1	1	1	1	1	1	1

*Corrected Ratio = $\frac{\text{Diam. (x ft/sec)} - 14\mu}{\text{Diam. (6 ft/sec)} - 14\mu}$

reacted and a columnar structure of τ-WB_2(WB_4) and W_2B_5 remains. Above 1090° C, the core structure at the shortest exposure time becomes more uniform, and approaches the uniformity of the cores developed at the longer exposure times.

Because the outer core ring is two phase in all but sample A16-27-1c, the core development described above is not just a simple radial diffusion process. The W-B phase diagram, reported by Rudy and St. Windisch (Ref. 6) shows that all the boride phases have fairly narrow composition ranges with nearly vertical phase boundaries. Two solid state reactions are reported, a eutectoid reaction β-WB $\rightarrow$ δ-WB + W_2B_5 at 2100° C on cooling and a peritectoid reaction δ-WB $\rightarrow$ β-WB + W_2B_5 at 2170° C on heating. Although these solid state reactions occur at temperatures well above the maximum temperatures reached during the deposition process, they do show that solid state reactions occur in the W-B system.

Because diffusion in a binary system at constant temperature and pressure cannot result in the formation of a two phase region, the intimate mixture of two phases present in every core, but one, must have been formed by the decomposition of a single high temperature phase during cooling.

For this decomposition to occur without considerable mass transfer during cooling, the phase formed at temperature would have to lie between the compositions of the phases present at room temperature. This requirement rules out the reaction δ- or β-WB $\rightarrow$ τ-WB_2 + W_2B_5. The Rudy-St. Windisch phase diagram would suggest δ-WB $\rightarrow$ W_2B + W_2B_5 in filament cores; however, there is no strong x-ray evidence to prove the presence of W_2B in the filaments at room temperature. Two possibilities exist:

$$\varphi_1 \rightarrow \tau\text{-}WB_2 + W_2B_5$$

$$\varphi_1 \rightarrow W_2B_5 + WB_4$$

where φ_1 is the high temperature phase which decomposed on cooling. Since the τ-WB_2 and WB_4 phases have diffraction patterns which differ only in the position of one weak peak, it is not possible to conclude which of the phases is present at room temperature; the WB_4 phase is favored however because of the excess of B present. Because there are no reported phases between τ-WB_2 and W_2B_5 or between W_2B_5 and WB_4, the possibilities suggested above require that φ_1 be W_2B_5 with a solubility range which decreases rapidly with decreasing temperature. In that case, the two-phase appearance of the filament core can be explained by precipitation of either τ-WB_2 or WB_4 from the W_2B_5 on cooling.

3.6.3.4 Nomenclature for Boron Filament Structures

A description of boron filaments can be developed based on the core structure, the boron sheath structure, and the surface texture. It is sometimes convenient to have a quantitative designation for the structure of materials and such a designation scheme is presented here. A very complete nomenclature is first given but the simplified version presented later in this section is preferable because of its greater simplicity.

The designation can be in the form:

I(--)II(--)III(--)IV(--)

in which I(--) would given information on the core structure, II(--) would indicate the boron sheath structure, III(--) would give the dominant nodule type and IV(--) would indicate the nodule features. Thus, I(0.5 mil, WB_x, WB_y) would indicate a boron filament which was prepared on a 0.5 mil tungsten wire and now contains two borides, WB_x and WB_y. I(1.0 mil, SiO_2, Ni) would indicate a 1.0 mil SiO_2 core filament with a Ni coating for conductivity.

II(--) would give information on the general nature of the boron sheath and the diameter of the filament. For example, II(3 rings, micro-xtal, 4.0 mil) would indicate

three chamber rings, microcystalline boron (sometimes referred to as amorphous boron), with a 4.0 mil outer filament diameter. II(1, macro-xtal, 3.0) would indicate a single chamber ring with a well-defined grain structure such as occurs with depositions exceeding about 1400° C (Ref. 21).

III(--) describes the nodule type. Table 8 gives the various designations which might be used.

Table 8

NODULE TYPES USED TO DESIGNATE BORON FILAMENT STRUCTURE

Type Number	Description
III(A-)	Major Nodules Dominant
III(A1)	No Minor Nodules
III(A2)	Light Minor Nodule Delineation
III(A3)	Medium Minor Nodule Delineation
III(A4)	Heavy Minor Nodule Delineation
III(B-)	Minor Nodules Dominant
III(B1)	Large Minor Nodules
III(B2)	Small Minor Nodules
III(C-)	Lack of Nodular Structure

Finally, IV(--) would designate the nodule features such as

- Uniformity:
  U – Dominant nodules are uniform
  NU – Dominant nodules are nonuniform
- Ratio of longitudinal to circumferential dimensions of dominant nodules:
  >3/4 – high
  1/2 - 3/4 – medium
  <1/2 – low

- Number of minor nodules per major nodule
- Number of dominant nodules per cm in the longitudinal direction

Thus, IV(U, med., 7, 2000) indicates a uniform nodule size with a medium dimension ratio, 7 minor nodules per major nodule, and 2000 major nodules per cm of filament length.

Some samples of the Astro filaments, whose structures are given in Figs. 18 – 20, are described with this nomenclature in Table 9.

The nomenclature described above gives a complete description of boron filaments but it is rather cumbersome. A shorter form, following the same basic format, might be preferable. Thus, the designation I(W)II(1 ring, micro-xtal, 3.2 mil) III(Al)IV(NU, 0, 4000) is sufficient to describe sample Al6-20-6c for most purposes. Further abbreviations, e.g., using only the texture types given in Table 8, are also possible; the designations given in Table 8 are used frequently in this report.

The above system of nomenclature is adaptable to other filament structures by the simple addition of the sheath composition at the beginning of the designation. Some minor changes in the system to account for crystallite size and preferred orientation might also be required.

3.6.4 X-ray Diffraction

Rotating Debye-Scherrer patterns were obtained from all the Astro samples. The halo patterns in these Debye-Scherrer films were all the same; variations in the patterns were due to the presence of different tungsten boride peaks. To show the method of indexing the tungsten boride peaks, Tables 10, 11, and 12 give the observed peaks for each Astro sample. The peak positions are staggered somewhat so the emergence of peaks will be apparent. These diffraction patterns were indexed using the data presented in Section 3.5. Phases which were identified in each sample are noted at the bottom of each sample column. The line widths were generally consistent with a crystallite size of 0.1 μ or greater.

Table 9

NOMENCLATURE FOR SOME ASTRO FILAMENTS WHOSE STRUCTURES ARE PRESENTED IN FIGS. 18 – 20

Specimen Number A16-	Deposition Temp. (°C)	Nomenclature
27-1c	870	I (0.5 mil, W, δ-WB) II (1 ring, micro-xtal, 0.72 mil) III (B2) IV (U, High, - , 15000)
18-2c	980	I (0.5 mil, W, τ-WB_2, W_2B_5) II (1 ring, micro-xtal, 1.2 mils) III (A2) IV (NU, High, 6, 4000)
28-3c	1040	I (0.5 mil, W, τ-WB_2, W_2B_5) II (1 ring, micro-xtal, 1.4 mils) III (A2) IV (NU, Med, 6, 4000)
19-4c	1090	I (0.5 mil, W, τ-WB_2, W_2B_5) II (1 ring, micro-xtal, 2.2 mils) III (A1) IV (NU, Med, 0, 3000)
29-5c	1200	I (0.5 mil, τ-WB_2, W_2B_5) II (1 ring, micro-xtal, 3.0 mils) III (A1) IV (NU, Med, 0, 3000)
20-6c	1260	I (0.5 mil, τ-WB_2, W_2B_5) II (1 ring, micro-xtal, 3.2 mils) III (A1) IV (NU, Med, 0, 4000)

Table 10

BORIDE DIFFRACTION LINES IN ASTRO SAMPLES – PART A

d-Spacing in Å Specimen Number A16-				
-15-2a	-25-3a	-16-4a	-26-5a	-17-6a
3.50 A,W			3.65 W	3.60 A,W
			3.40 W	3.40 A,W
			3.18 W	3.20 VS
2.58 S			2.60 VS	2.56 VS
			2.45 VW	
			2.23 W	2.20 W
2.13 W				2.12 W
2.00 M			2.00 M	2.00 M
1.95 W			1.94 B,W	1.90 W
1.90 W				
1.75 B,W			1.75 B,W	
			1.65 W	1.65 VW
			1.53 VW	
			1.50 M	1.50 M
				1.37 M
			1.38 M	1.37 B
			1.36 M	
			1.33 W	
			1.30 W	1.30 W
			1.22 W	
1.20 W			1.20 W	1.20 W
			1.13 W	1.12 VW
			1.09 W	
1.01 W			1.03 VW	
0.98 B,W				0.98 B,W
0.94 B,W				
0.87 B,W			0.84 B,M	0.84 B,W
			0.80 B,W	0.79 B,W
Phases Present				
τ-WB_2 W_2B_5			τ-WB_2 W_2B_5	τ-WB_2 W_2B_5

S - Strong, M - Medium, W - Weak, A - Arced, B - Broad

Table 11

BORIDE DIFFRACTION LINES IN ASTRO SAMPLES -- PART B

d-Spacing in Å Specimen Number A16-					
-21-1b	-12-2b	-22-3b	-13-4b	-23-5b	-14-6b
		7.0 ? A			
		3.6 A	3.6 W	3.80 A	3.70 W
			3.4 W	2.50 M	3.50 W
		3.2 W	3.0 VW	3.10 W	3.20 VW
2.58 S	2.58 S	2.58 S	2.57 VS	2.60 VS	2.57 VS
				2.30 W	2.30 VW
2.22 W	2.23 A,M		2.22 VW	2.25 W	2.15 VW
	2.13 A,M	2.13 W	2.11 VW	2.10 W	
		2.00 M	2.00 M	2.00 M	2.00 M
	1.98 W	1.96 W	1.94 W	1.96 W,M,B	1.94 B,W
		1.90 W	1.90 W	1.90	1.90 B,W
		1.70 B		1.75 W	
1.56 M				1.65 W	1.64 VW
		1.50 M	1.50 W	1.50 M	1.50 M
	1.36 B,W	1.37 B,M	1.37 M	1.38 M	
1.33 M				1.36 M	1.36 W
				1.32 W	
1.30 W	1.28 B,W	1.30 W	1.29 W	1.29 W	1.30 W
1.27 W					
				1.20 M	1.20 VW
		1.19 W	1.18 B,W	1.17 W	
	1.11 VW			1.13 W	1.13 VW
		1.08 W			1.08 VW
				1.02 W	
1.01 W		1.01 W		1.01 W	
0.98 W	0.97 VW	0.98 M	0.98 VW	0.98 M	0.98 B,W
			0.94 VW		
		0.87 M	0.87 VW		
0.84 B,W	0.84 A	0.84 B			
0.79 B,W	0.79 B				
Phases Identified					
W W_2B_5	WB W_2B_5 τ-WB_2	WB τ-WB_2 (W_2B_5)	τ-WB_2 W_2B_5	τ-WB_2 W_2B_5	τ-WB_2 W_2B_5

Table 12

BORIDE DIFFRACTION PEAKS IN ASTRO SAMPLES – PART C

d-Spacing in Å Specimen Number A16-					
-27-1c	-18-2c	-28-3c	-19-4c	-29-5c	-20-6c
Asterism					
	VW 3.6 B				3.65 A,W
				3.5 W	3.42 A,M
	3.20 VW		3.25 A		3.10 VW
	2.59 S	2.60 A,M	2.58 S	2.60 VS	2.58 VS
		2.48 A,M			
2.22 A	2.20 A,W	2.22 A,W	2.25 VW	2.22 W	2.26 W
2.10 A		2.14 A	2.15 M	2.10 W	2.12 W
	2.00 M	2.00 W		2.00 M	2.00 M
		W			
	1.95 M	W	1.98 B,M	1.96 W	1.95 VW
		W			
	1.94 M	1.90 W		1.91 VW	
				1.88 W	1.89 M
	1.75 VW	1.75 A,W	1.76 W		1.74 VW
		1.65 VW		1.64 VW	1.65 W
1.57 A		1.60 A			
	1.50 M	1.50 M	1.50 M	1.50 M	1.50 M
	1.38 M	1.38 M		1.38 M	1.37 M
	1.37 M	1.35 M	1.36 M	1.36 VW	1.36 W
1.34 A					1.33 VW
	1.30 W	1.30 W	1.30 W	1.30 M	1.29 M
1.22 A					
	1.19 B,W	1.20 BW		1.20 M	1.20 M
				1.18 W	1.18 VW
1.12 A	1.13 B,W			1.13 W	1.13 W
				1.09 W	1.09 W
				1.02 W	
1.00 A		1.00 A,W		1.01 VW	1.02 W
	0.98 B,W	0.98 B,W	0.98 B,W	0.98 M	0.98 M
				0.94 W	0.94 M
0.912 A				0.93 W	0.93 W
				0.87 M	0.87 M
0.845 A		0.84 A	0.84 B,W	0.84 M	0.84 B,M
				W	
0.790 A		0.79 VW		0.80 B	0.79 B,W
Phases Identified					
W	W	W			
WB	τ-WB_2	WB			
	(WB)	τ-WB_2	τ-WB_2	τ-WB_2	τ-WB_2
	(W_2B_5)	W_2B_5	W_2B_5	W_2B_5	W_2B_5

S - Strong, M - Medium, W - Weak, VW - Very Weak, A - Arced
B - Broad

As may be seen, the presence of WB (ASTM cards 6-0635 and 6-0541) is difficult to establish, but the disappearance of W (ASTM card 4-0810) is quite evident. The phase W_2B_5 (ASTM card 6-0243) can be readily identified, but the structures and existence of W_2B (ASTM card 6-0591), τ-WB_2 (Texaco Expt., Ref. 8), WB_2 (Ref. 3), and WB_4 (Ref. 11) are by no means definitely determined. The τ-WB_2 and WB_4 phases have the same peak positions except for a 4.48 Å line of WB_4. The WB_2 phase reported by Woods et al. might be distinguished by its 3.05 Å line, but this peak was not observed in the Astro Debye-Scherrer patterns.

To specify the number of phases, the lines corresponding to τ-WB_2 and WB_4 were treated as belonging to one phase, designated τ-WB_2 (WB_4). Some preference might be given to WB_4 because of the presence of excess boron but the chemistry is somewhat arbitrary with the present information.* The identification of core phases in the Astro samples is discussed further in Section 3.6.3, and other core structures are described in Section 3.7.3.

3.6.5 Summary of Structure of Boron Filaments Deposited under Various Conditions

Filaments prepared with tungsten wire substrates covering the temperature range 870–1260° C for different exposure times were provided by Astro Research Corp. In all cases, the diffraction patterns of the boron were essentially the same, but the growth morphologies differed. The significant variations were:

- Lower temperatures and longer exposure times tend to produce a minor nodule structure
- Higher temperatures tend to promote delineation of the major cone structure
- Combinations of high temperature and short exposure time can lead to the elimination of the minor nodule structure
- The minor nodules are nearly circular in shape while the ratio of the longitudinal to circumferential dimensions of the major nodules tend to be approximately 1:2
- The ratio of longitudinal to circumferential dimensions of the major nodules decreases with increasing temperature, ranging from 1:1 to 1:3

*See note added in proof, Section 3.3

Nearly all the filaments were cracked or curved and the cracking was most severe at the intermediate temperatures. At a given temperature, the growth rate decreased with increasing filament diameter and this decrease was more pronounced the higher the temperature. The development of the core structure was followed fairly well, but better samples were available as described in Section 3.7. The core develops by radial diffusion but the intimately mixed two-phase region in the core can only be explained by postulating a solid state transformation on cooling.

A nomenclature system for filaments was devised which incorporates the core structure, the sheath structure, and the dominant morphological features of the sheath.

3.7 DEVELOPMENT OF BORON FILAMENT STRUCTURE DURING DEPOSITION

3.7.1 Material Examined

Two samples, each of which consisted of the filament length in the deposition chamber at the end of a run, were supplied by Texaco Experiment. These samples, to be called "tailings," were acquired to study the development of the boron filament structure during the deposition process. The samples came from Texaco Experiment Runs B5/3945 and B5/3946. The B5/3945 sample had approximately 15 inches missing from the beginning of the first deposition chamber; therefore, it was not examined systematically. Run B5/3946 had approximately 3 inches missing from the segment in the first deposition chamber, but there was sufficient material to systematically study the beginnings of the boron deposition process.

Figure 22 is a plot of the temperature profile in each deposition chamber during run B5/3946. The figure also shows the places where samples were taken for the study. Ten sections of the tailing were examined by light microscopy and by x-ray diffraction. In addition, theoretical considerations were given to the presence of a radial temperature gradient and to the nature of volume changes which could occur during deposition.

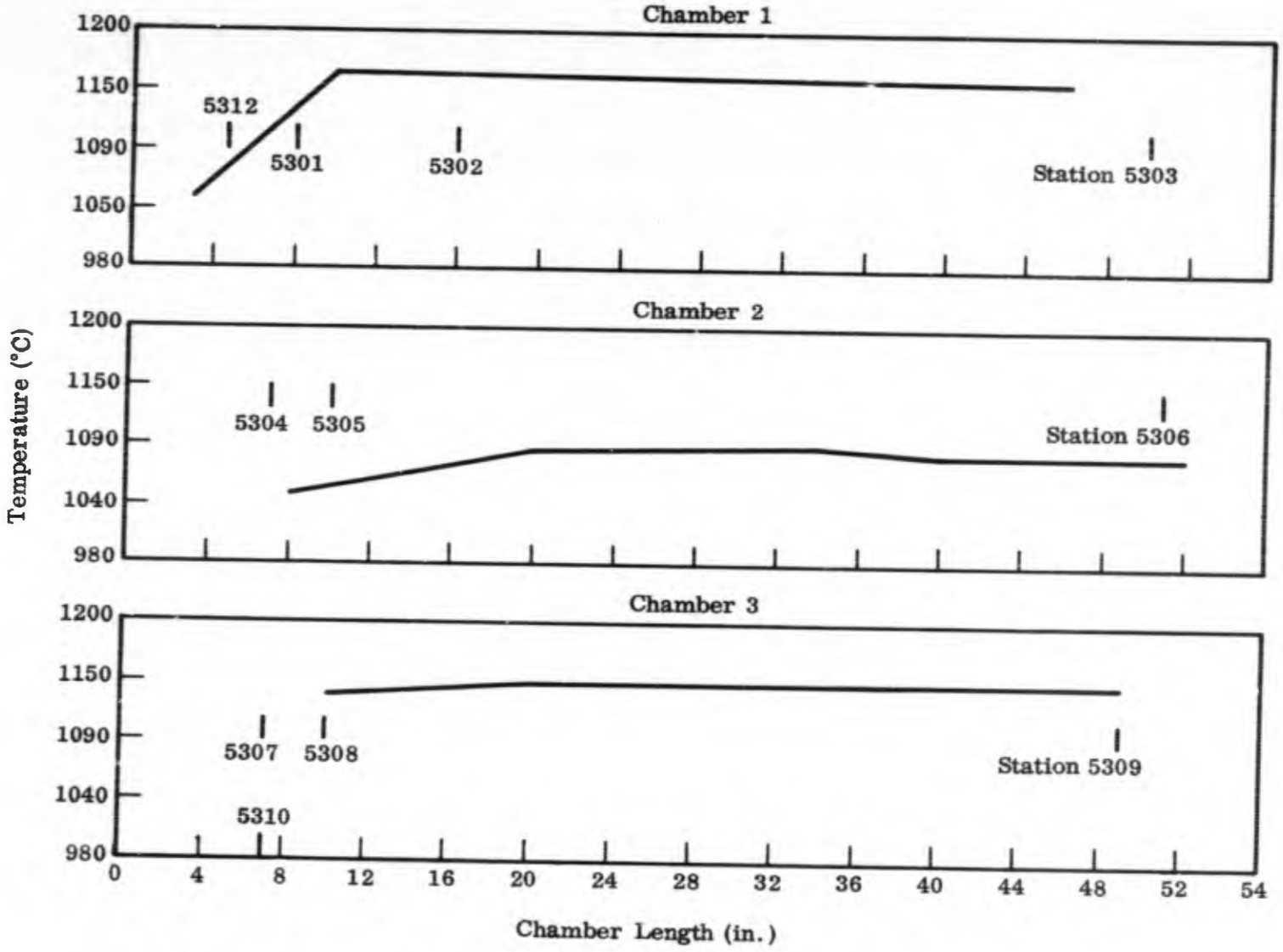

Fig. 22 Temperature Profile of Texaco Run B5/3946 With Sample Stations Noted (note lower temperature in Chamber 2)

3.7.2 Metallographic Observations

Samples of the tailing of run B5/3946 were taken, as shown in Fig. 22. The surface of each sample was examined at high magnification, and transverse cross sections were prepared using the chromic acid polishing baths as described in Section 3.2. Figures 23-38 contain selected photographs of the observed structures.

Figure 23 shows typical cross sections of the 1/2 mil tungsten wire present at Station 5312, at the beginning of the first deposition chamber. The temperature at this point is 1090° C, but no significant amount of B has been deposited.

Figure 24 gives the structure of the boron filament at Station 5301, 8 inches into the first deposition chamber where the temperature is approximately 1120° C. The surface texture is typical, being covered with rows of small nodules which will form major nodules when the filament is larger. The cross section reveals that the core is largely tungsten with a thick outer ring of borides identified in Section 3.7.3 as W_2B_5 and τ-$WB_2(WB_4)$. A very thin, faint ring exists between the two-phase boride ring and the tungsten core which has been identified as δ-WB. A crack has formed in the boron sheath and it extends into the two-phase boride ring. As will be seen in later photographs, this crack grows with the deposition of boron and is responsible for the apparent cleavage or longitudinal cracking which is frequently observed in boron filaments. The orgin of this crack is discussed in Section 3.7.5; more structural details are given in this and the following sections.

The structure at Station 5302 is shown in Fig. 25. The surface texture consists of major nodules without a minor nodule structure [Type III(A1), see Section 3.6.3.4]. The longitudinal crack is apparent in the surface view; it passes through nodules in a straight line with a slight spiral about the filament axis. Close examination of the crack shows that it is narrower in the center of the larger nodules than elsewhere. The cross section in Fig. 25 contains a tungsten core, surrounded by a δ-WB ring and a two-phase W_2B_5 - τ-$WB_2(WB_4)$ ring. The crack in the boron sheath persists and two more radial cracks have developed.

The structure at Station 5303 is given in Fig. 26. The surface texture is still of the III(A1) type, but some pitting has occurred on the nodule surfaces. The tungsten core has completely reacted to form a grainy δ-WB in the center and a two-phase W_2B_5 - τ-WB_2(WB_4) ring.

At Station 5304 (Fig. 27) the surface texture is essentially the same as at Station 5303. The cross section reveals that the δ-WB is almost completely consumed, leaving the two-phase region. One of the cracks in this cross section is no longer radial, but instead, it has a curved tip at the outer edge of the filament. This curved tip is a crack which has propagated through a bridge which formed over the end of the straight, radial crack. The filament section at Station 5304 was quenched in the mercury seal between the first and second deposition chambers but its structure is not different from that at Station 5303. The dark speckling in the core is etching stain and does not necessarily imply a significant difference in structure. The additional crack in this cross section could have been formed during quenching in the mercury,but a more likely explanation is that it formed during mounting. A high magnification view of the surface texture at Station 5304 in Fig. 28 shows a straight surface crack which passes through the major nodules. The slight curvature apparent at each nodule is the result of viewing a straight line passing along a curved surface.

The structure at Station 5305, at the beginning of the second deposition chamber, is shown in Fig. 29. The surface texture is still III(A1) with some pitting. In the cross section view, there is one radial crack which runs from near the filament axis out to the surface and one which ends near the outer surface in a curved portion. In addition, a third crack exists which is not straight. This curved crack probably occurred when the sample was broken away from the filament length while the straight cracks are due to filament growth and the lack of boron deposition inside the crack.

Figure 30 shows the structure at Station 5306, the end of the second deposition chamber. The surface texture is still III(A1) with pitting; the cross section shows a fairly uniform two-phase core of W_2B_5 and τ-WB_2(WB_4). Two straight cracks are present which do not go through to the filament surface, while a curved crack runs from the core to the surface.

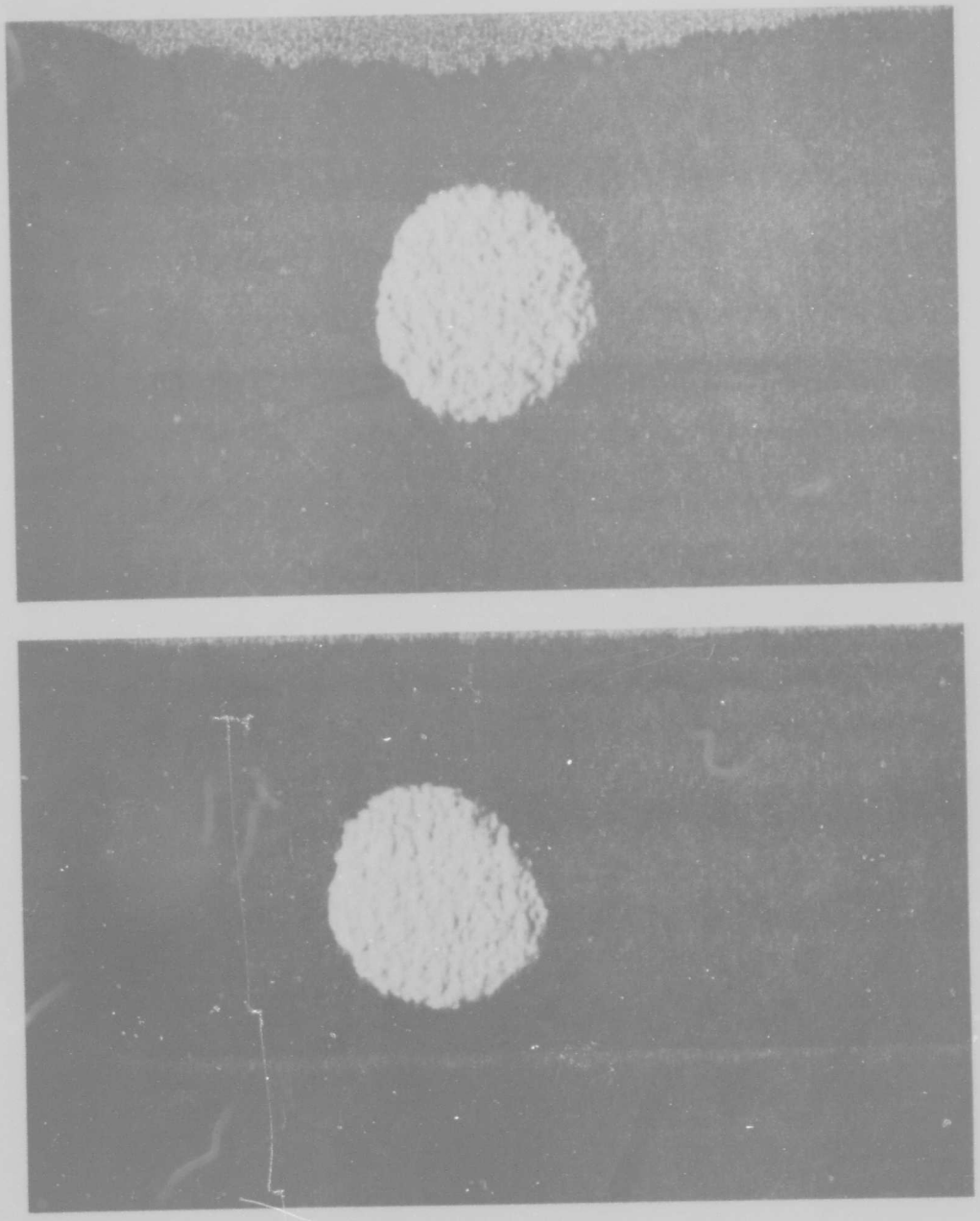

Fig. 23 Boron Filament at Station 5312, Beginning of First Deposition Chamber, 4-1/2 in. Into Process. (a) P3563, 3000×. (b) P3564, 3000×

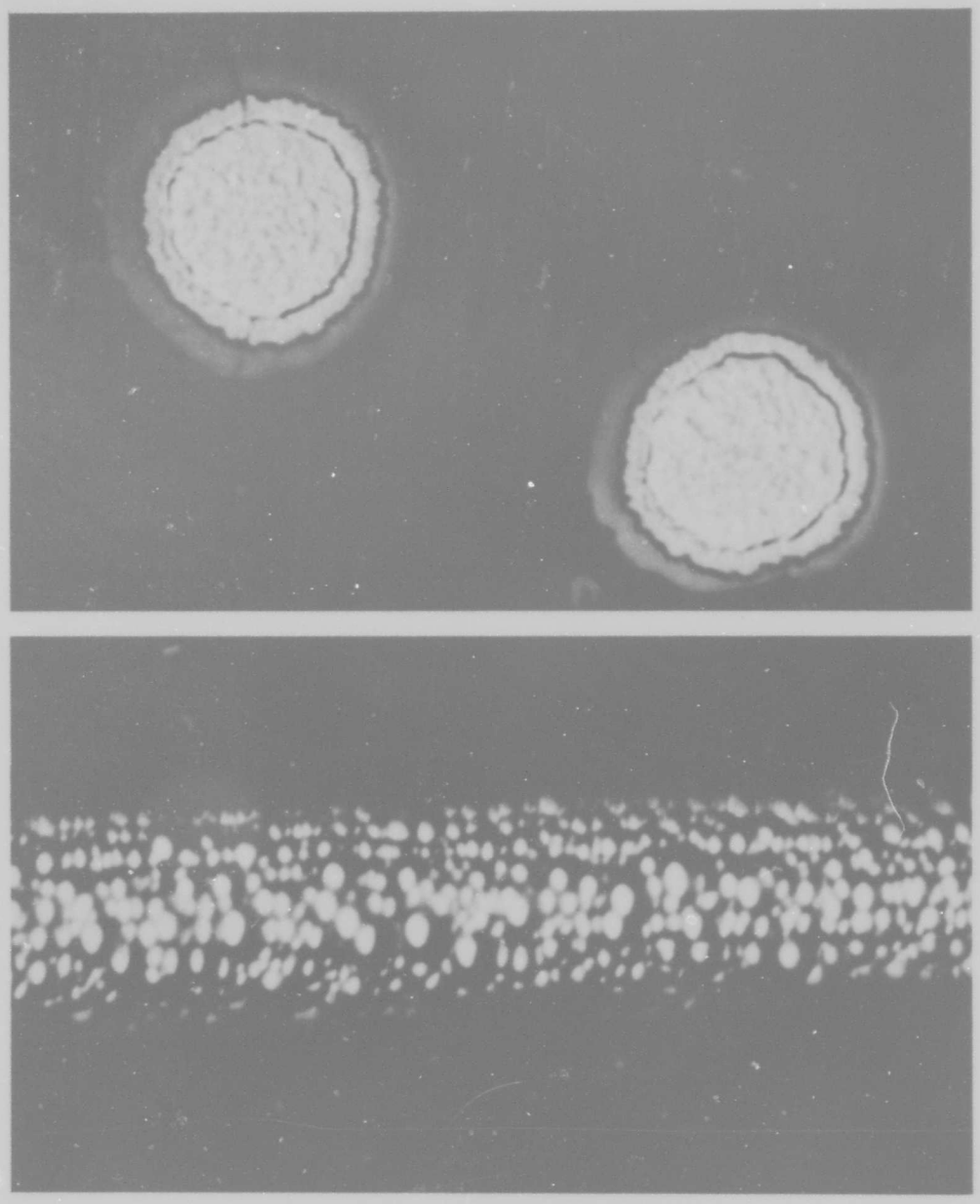

Fig. 24 Boron Filament at Station 5301, Beginning of First Deposition Chamber, 8 in. Into Process. (a) Cross section showing crack initiation, P3643, 3000×. (b) Surface texture, P3686, 3000×

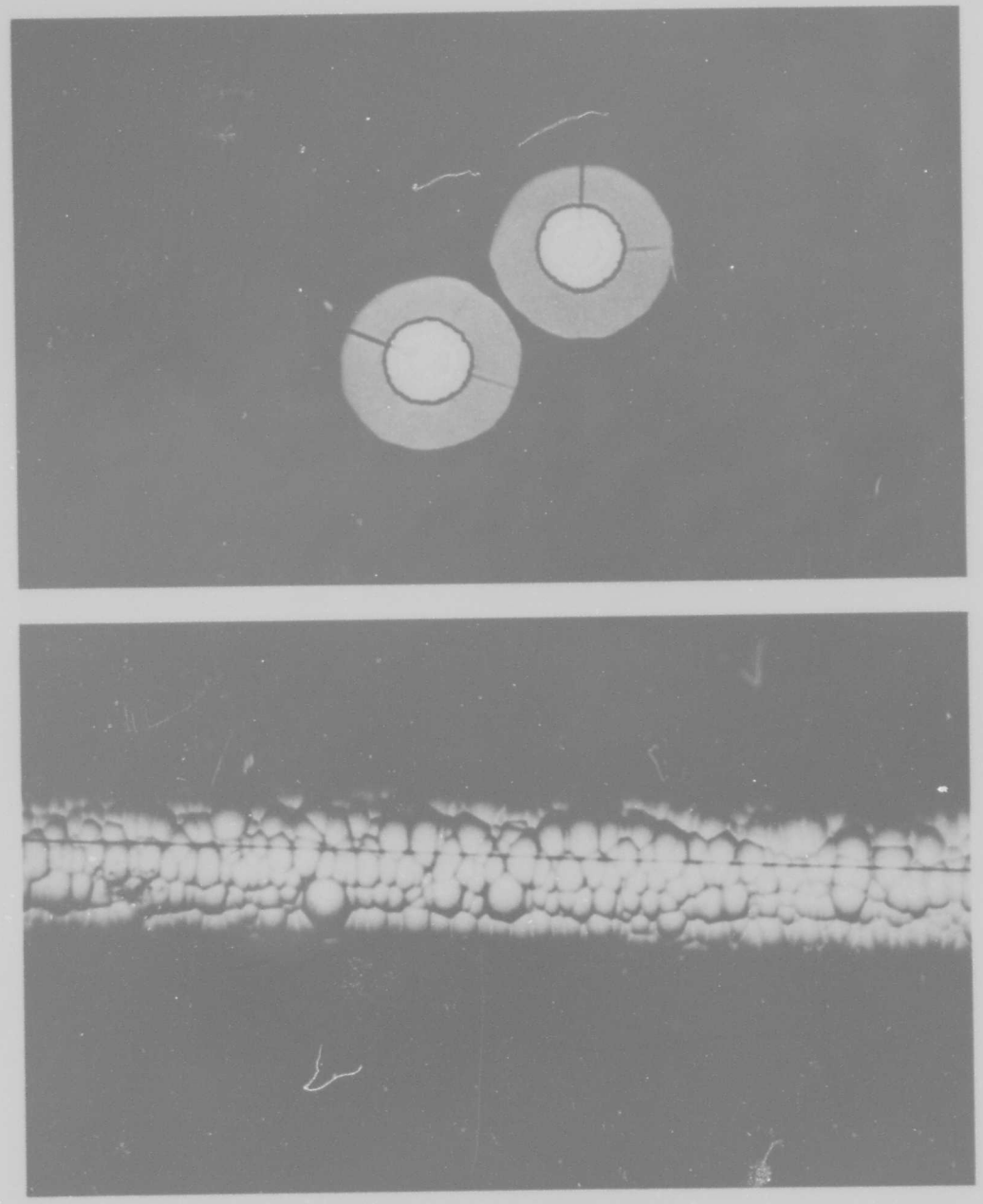

Fig. 25 Boron Filament at Station 5302, Middle of First Deposition Chamber, 16 in. Into Process. (a) Cross section showing continued crack growth. P3652, 3000×. (b) Surface texture showing longitudinal crack, P3689, 1000×

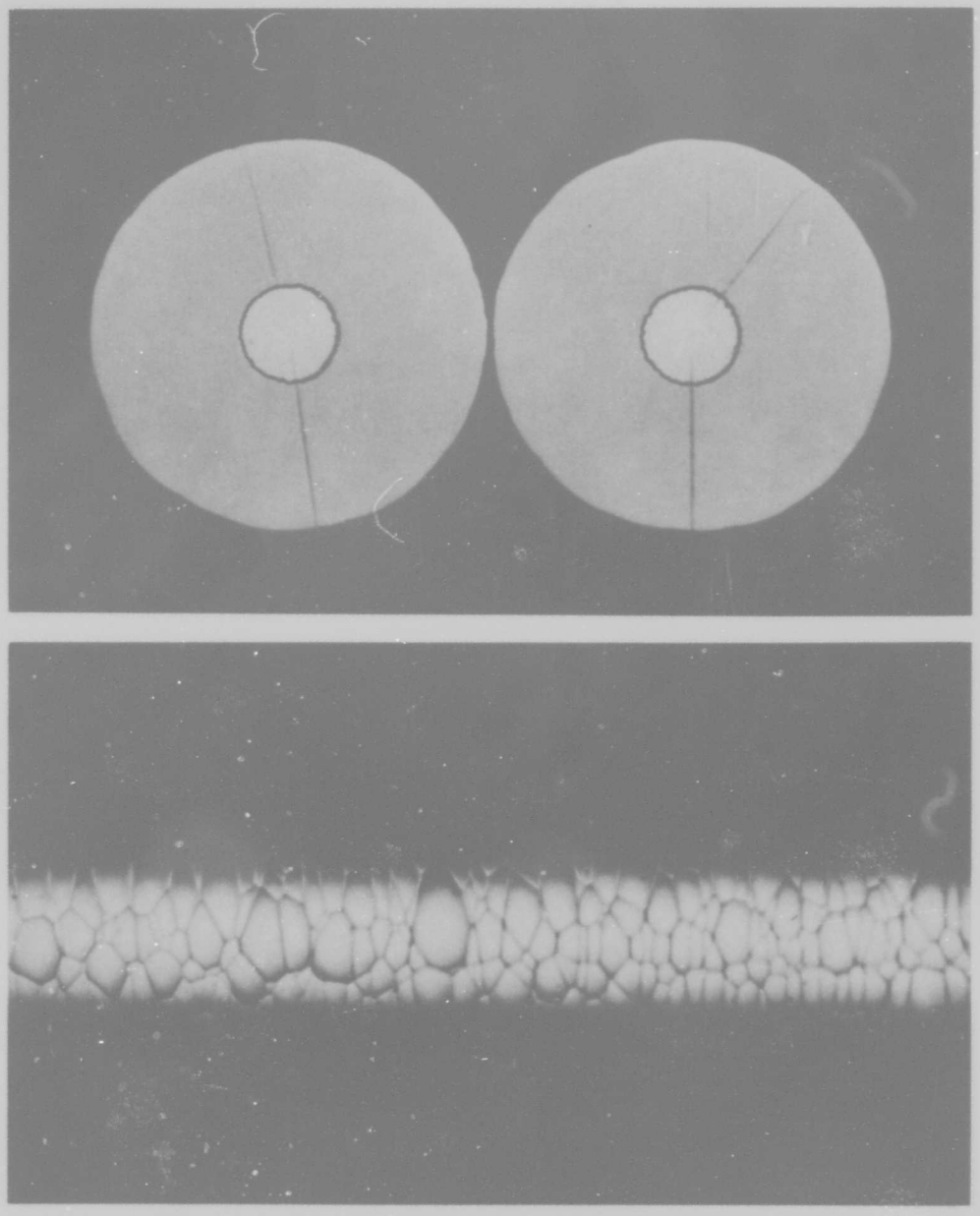

Fig. 26 Boron Filament at Station 5303, End of First Deposition Chamber, 50 in. Into Process. (a) Cross section showing continued crack growth. P3669, 1000×. (b) Surface texture showing pitting, P3670, 1000×

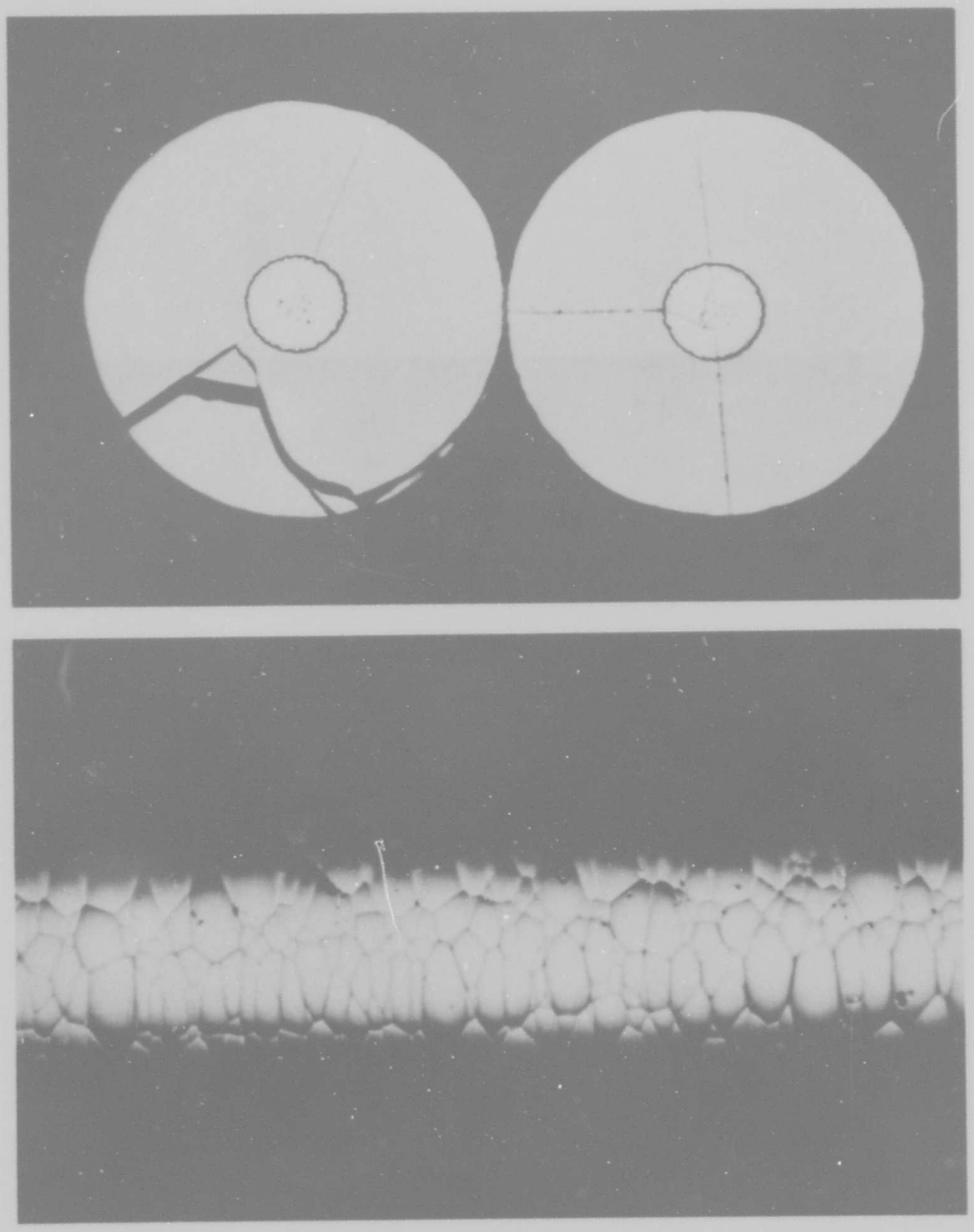

Fig. 27 Boron Filament at Station 5304, Mercury Seal Between First and Second Deposition Chambers, 57 in. Into Process. (a) Cross sections showing continued crack growth. P3671, 1000×. (b) Surface texture showing pitting. P3762, 1000×

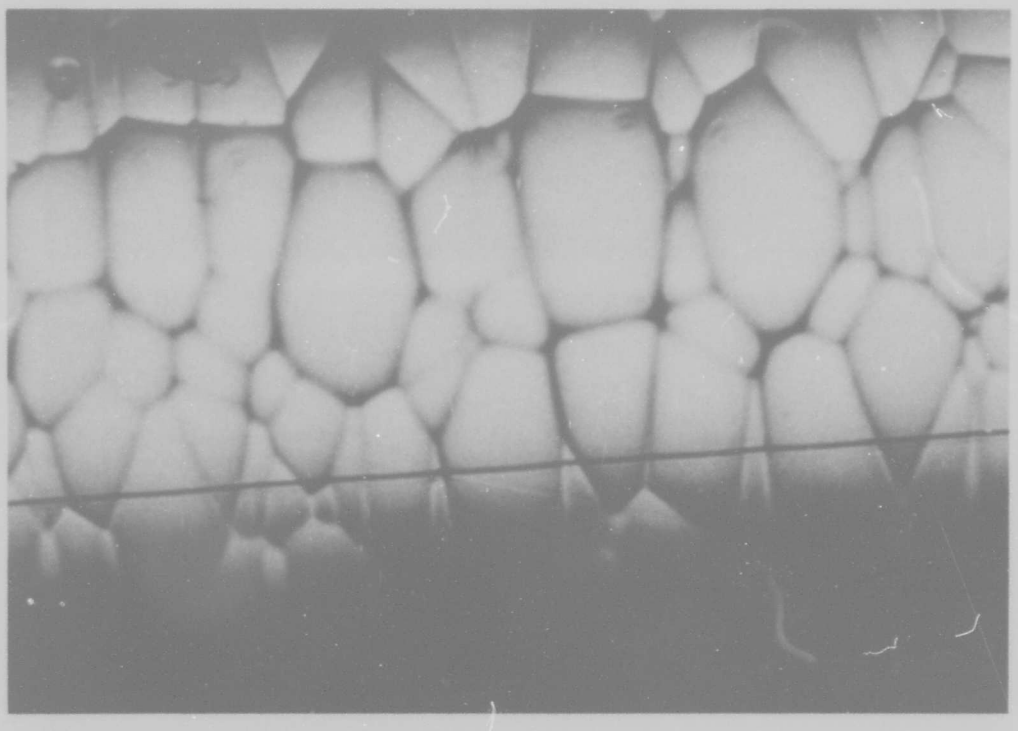

Fig. 28 Surface Texture With Longitudinal Crack at Boron Filament Station 5304, Mercury Seal Between First and Second Deposition Chambers, 57 in. Into Process. P3763, 3000×

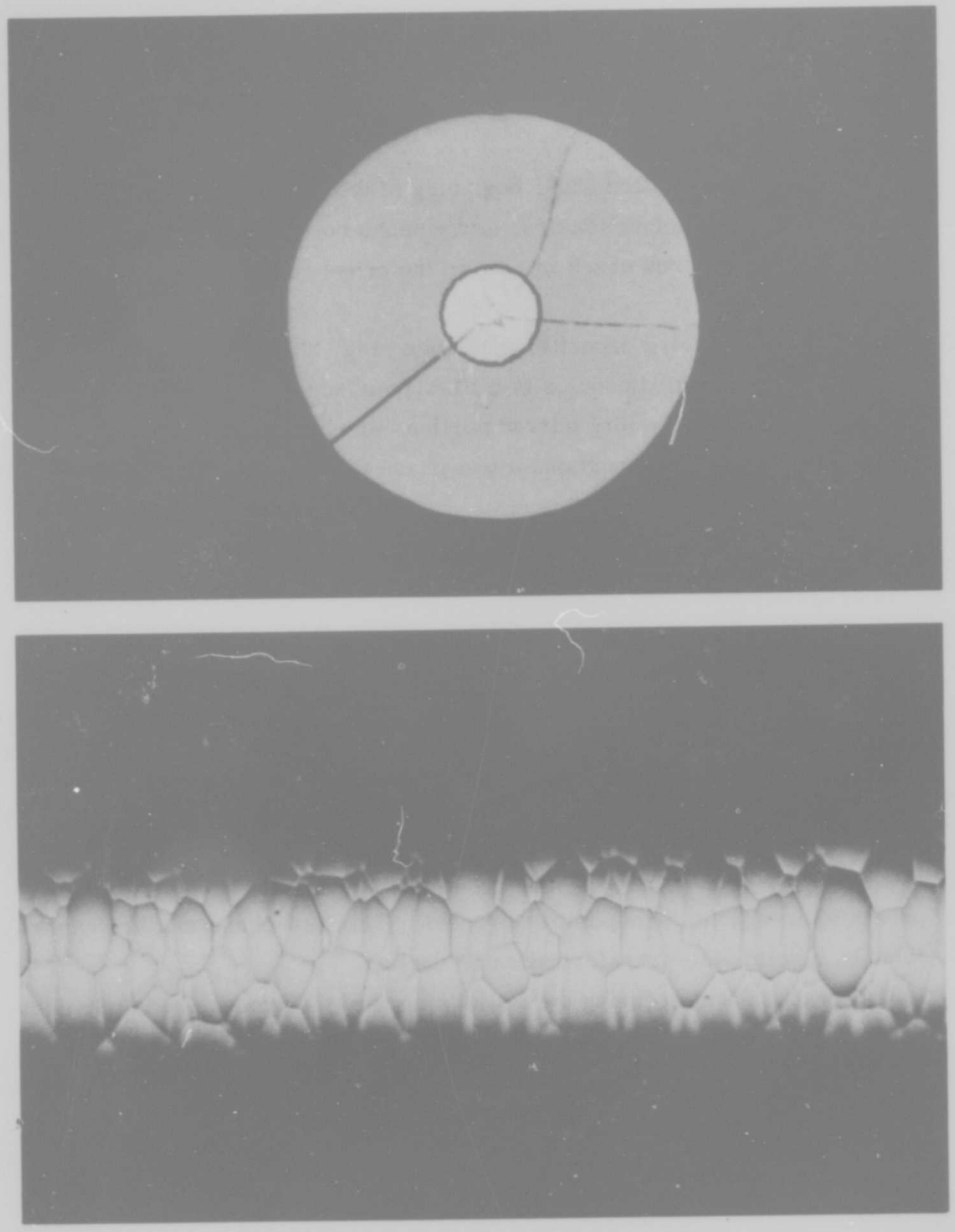

Fig. 29 Boron Filament at Station 5305, Beginning of Second Deposition Chamber, 60 in. Into Process. (a) Cross section showing continued crack growth. P3648, 1000×. (b) Surface texture showing pitting. P3765, 1000×

At Station 5307 (Fig. 31), in the mercury seal between the second and third deposition chambers, the structure is essentially the same as that at Station 5306. None of the cracks go through to the surface, and the dark speckling is a stain-etch effect.

In Fig. 32, the structure at Station 5308, beginning of the third deposition chamber, consists of a pitted III(A1) surface texture, a two-phase core, and bridged radial cracks. In addition, a nonradial, curved crack is seen in the cross section view.

At Station 5309, end of the third deposition chamber, Fig. 33, the surface texture is beginning to develop renucleated nodules in a III(A1) surface texture, and the ends of the straight, radial cracks have long curved portions which have propagated to the filament surface. The core still contains a two-phase mixture of W_2B_5 and τ-$WB_2(WB_4)$.

In the mercury seal at the end of the third deposition chamber, Station 5310, Fig. 34, the renucleated nodules persist in a III(A1) surface texture and the radial cracks have split ends near the filament surface. The core continues to be two-phase.

The series of photographs in Figs. 23–34 shows the general development of the structure of boron filaments. The dominant features which occur in this process are as follows:

- The core forms borides by radial diffusion with δ-WB, W_2B_5 and τ-$WB_2(WB_4)$ present in the initial stages after cooling.
- The W_2B_5 and τ-$WB_2(WB_4)$ phases occur together in a two-phase ring which persists throughout the deposition process. This two-phase mixture can only form by a solid state transformation on cooling.
- Radial cracks develop during the initial stages of the process and their presence is associated with the appearance of the δ-WB phase.
- The radial cracks continue to grow during the deposition process because the deposition rate inside the crack is negligible due to a lack of gas diffusion, while the deposition rates on each side of the crack are equal.
- The radial cracks go through the nodules undisturbed because the initial crack was straight and it passed through the early formed nodules. Equal growth rates on each side of the crack allowed the boron structure to continue to grow just as it started.

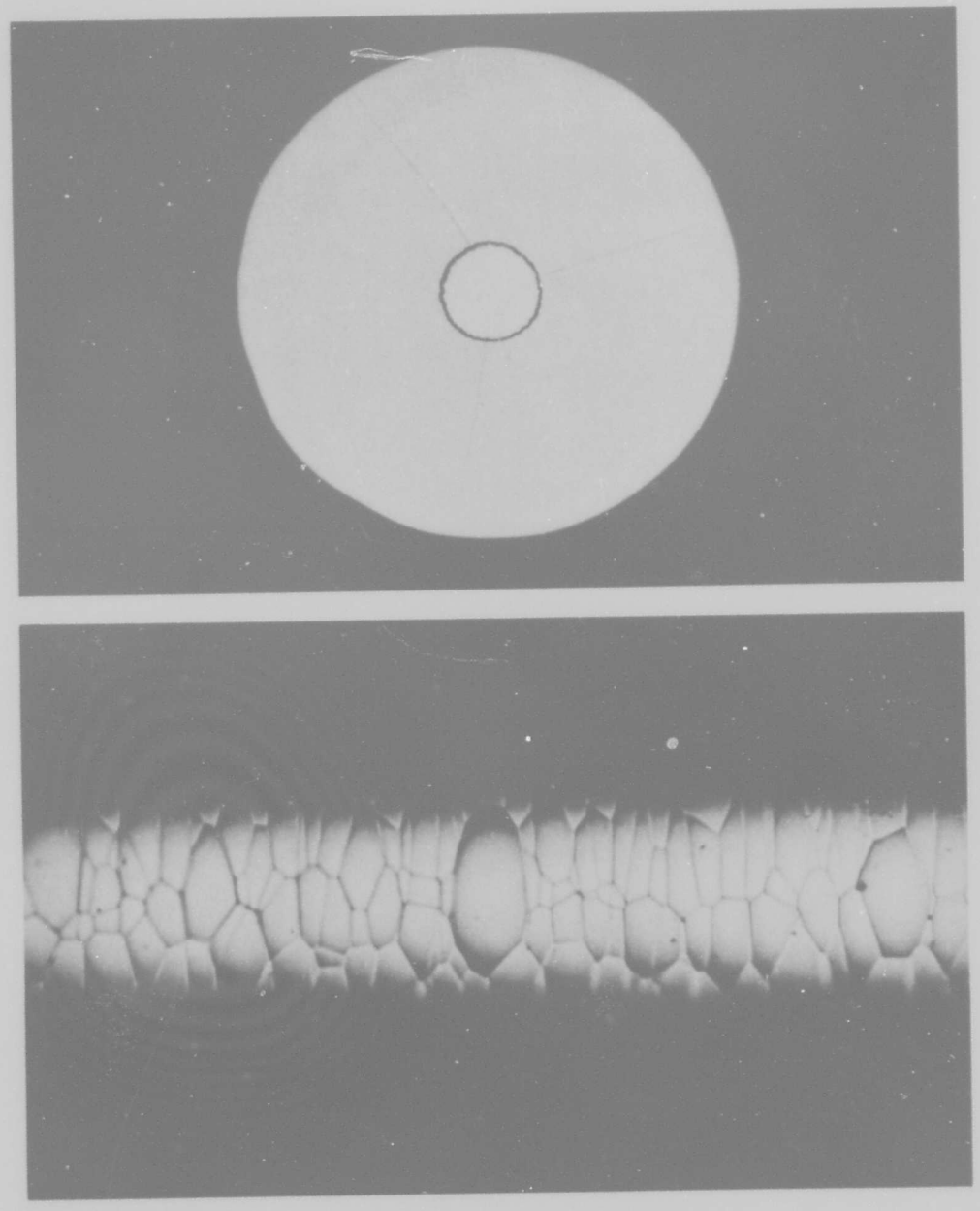

Fig. 30 Boron Filament at Station 5306, End of Second Deposition Chamber, 110 in. Into Process. (a) Cross section showing healing of longitudinal crack. P3673, 1000×. (b) Surface texture showing pitting. P3806, 1000×

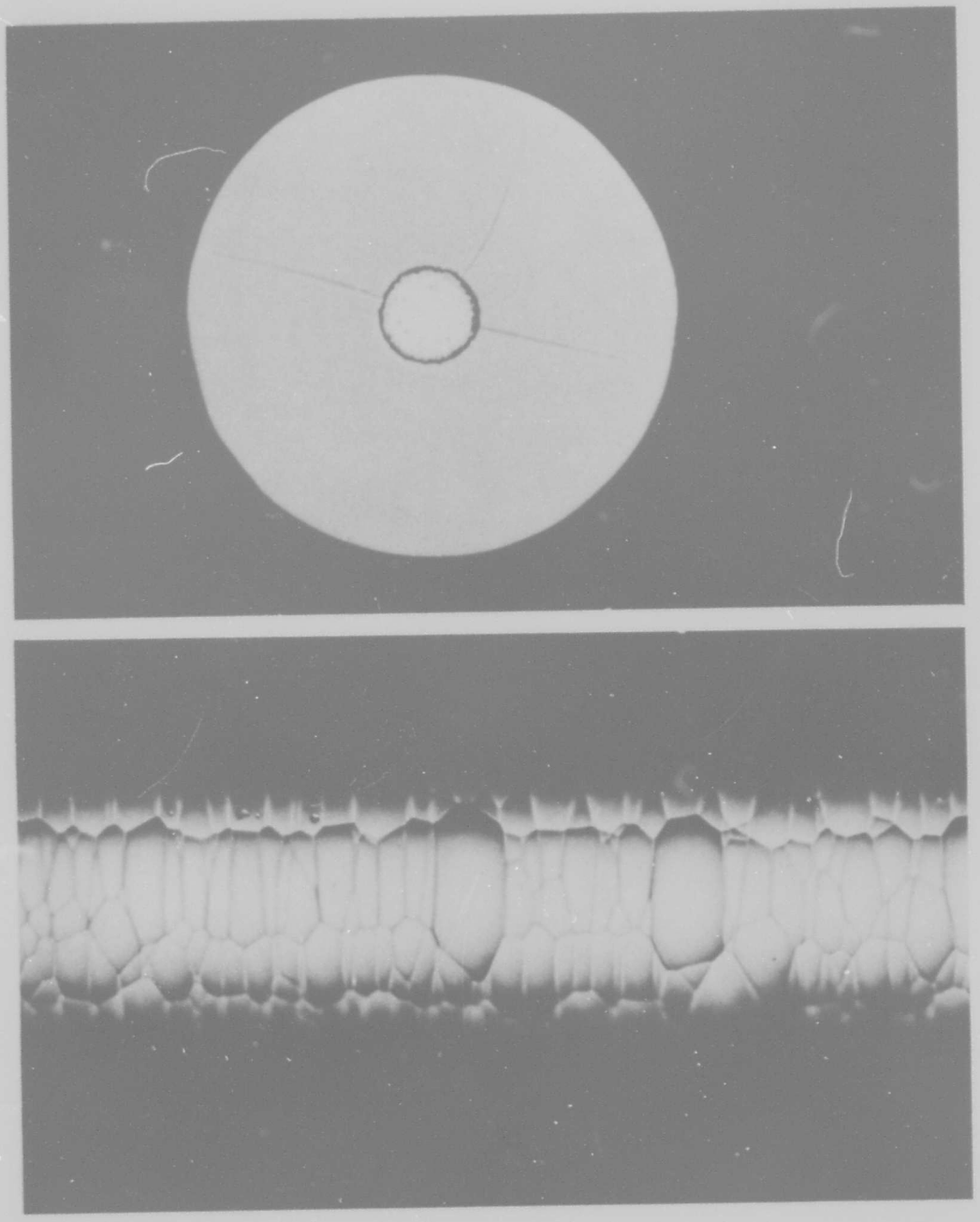

Fig. 31 Boron Filament at Station 5307, Mercury Seal Between Second and Third Deposition Chambers. (a) Cross section showing healed cracks. P3644, 1000×. (b) Surface texture. P3768, 1000×

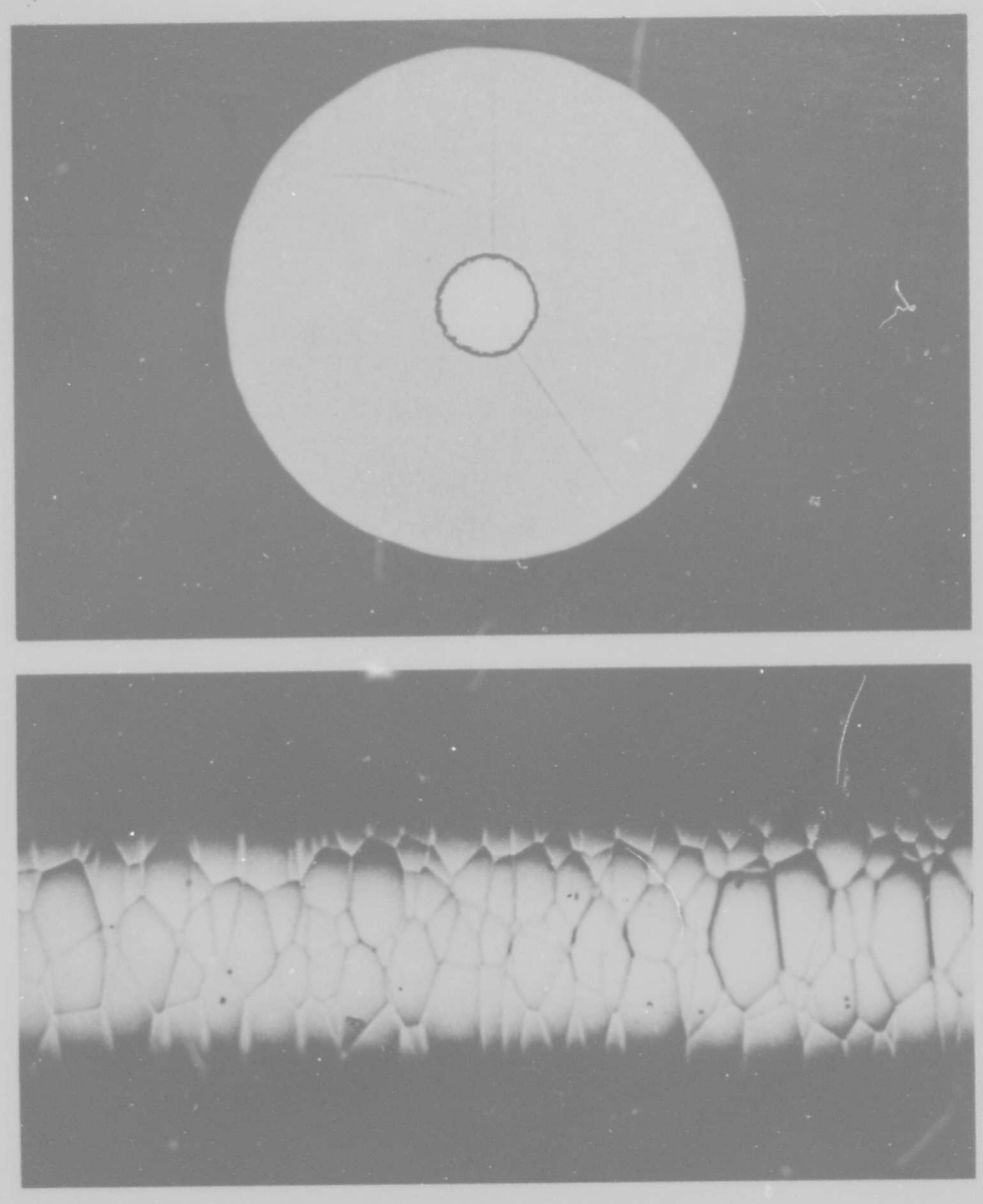

Fig. 32 Boron Filament at Station 5308, Beginning of Third Deposition Chamber, 120 in. Into Process. (a) Cross section showing healed cracks, P3654, 1000×. (b) Surface texture showing pits, P3809, 1000×

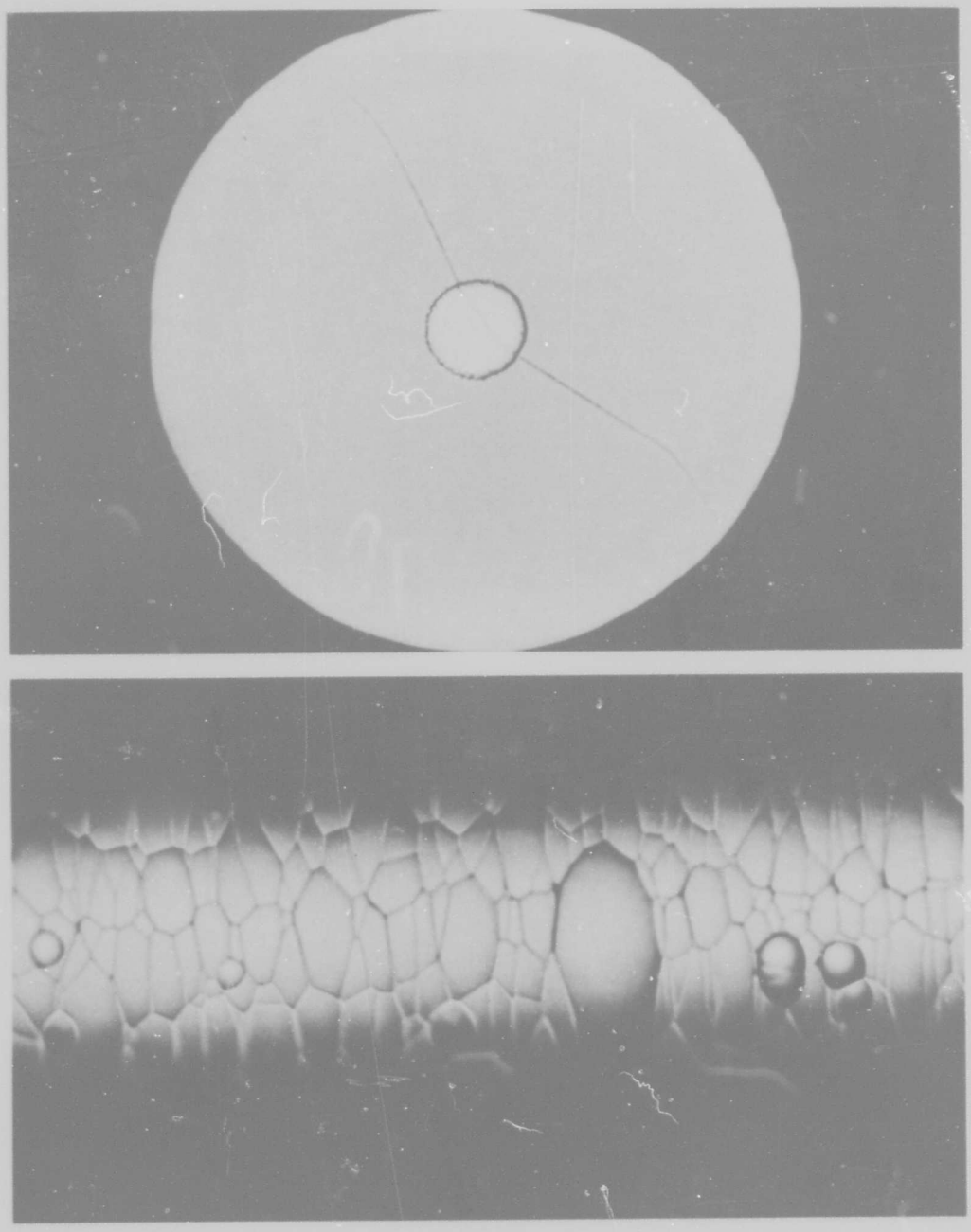

Fig. 33 Boron Filament at Station 5309, End of Third Deposition Chamber, 170 in. Into Process. (a) Cross section showing healed cracks, P3646, 1000×. (b) Surface texture showing renucleated growth nodules, P3812, 1000×

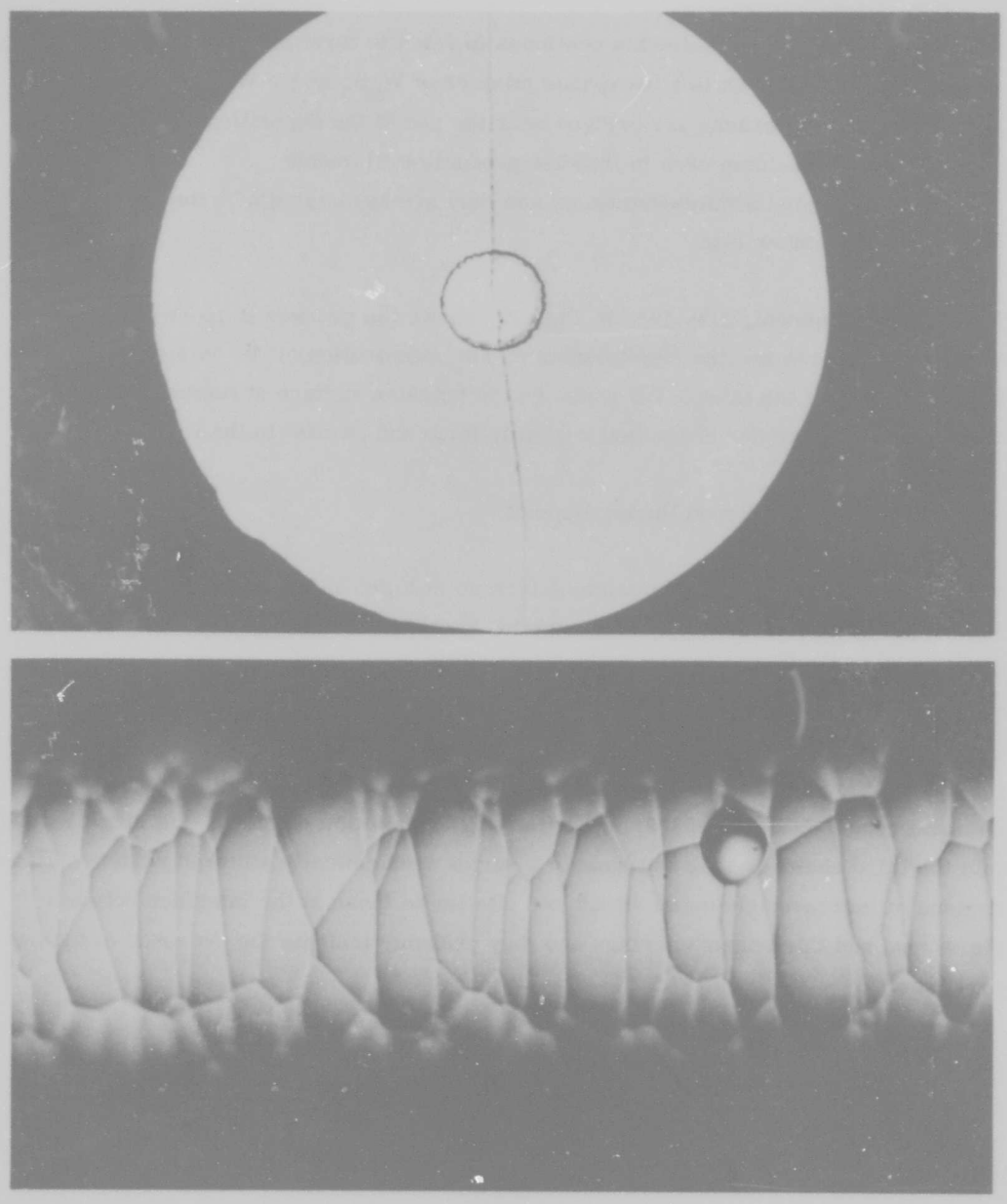

Fig. 34 Boron Filament at Station 5310, Mercury Seal at End of Third Deposition Chamber, 180 in. Into Process. (a) Cross section showing surface nodule and propagated crack. P3650, 1000×. (b) Surface texture showing renucleated nodules, P3918, 1000×

- The core of the filaments continues to react to form an apparently stable configuration which is a two-phase mixture of W_2B_5 and τ-$WB_2(WB_4)$.
- The radial cracks are bridged near the end of the deposition process so that they are seldom seen in finished production filaments.
- Renucleated nodules can occur and they are associated with the beginning of a chamber ring.

The core development, displayed in Fig. 35, shows the process in more detail. Significant features are the ring formation, the consumption of W to make borides, the appearance of the faint δ-WB phase on the tungsten surface at Station 5301, and the two-phase character of the last region to form and persist in the core.

3.7.2.1 Defects Developed During Deposition

Straight, radial cracks were a common feature in Figs. 23 – 34. These cracks are seldom seen in the surface of production filaments because they are bridged over near the end of the deposition process. Some details of the crack bridging in the second chamber ring are shown in Fig. 36. The cracks have been enlarged by the etch used to reveal the chamber ring interfaces. At Station 5308, beginning of the third deposition chamber, the crack is bridged about halfway through the second chamber ring. At Station 5309, end of the third deposition chamber, the crack extends into the third chamber ring and ends in a series of chemically attacked regions. These regions of increased chemical attack are similar to those at the interface between the second and third chamber rings and they probably indicate the presence of foreign particles.

More details of crack healing are shown in Fig. 37, Station 5310, the last mercury seal in the process. Foreign particles are present at the crack bridge as well as between the second and third chamber rings.

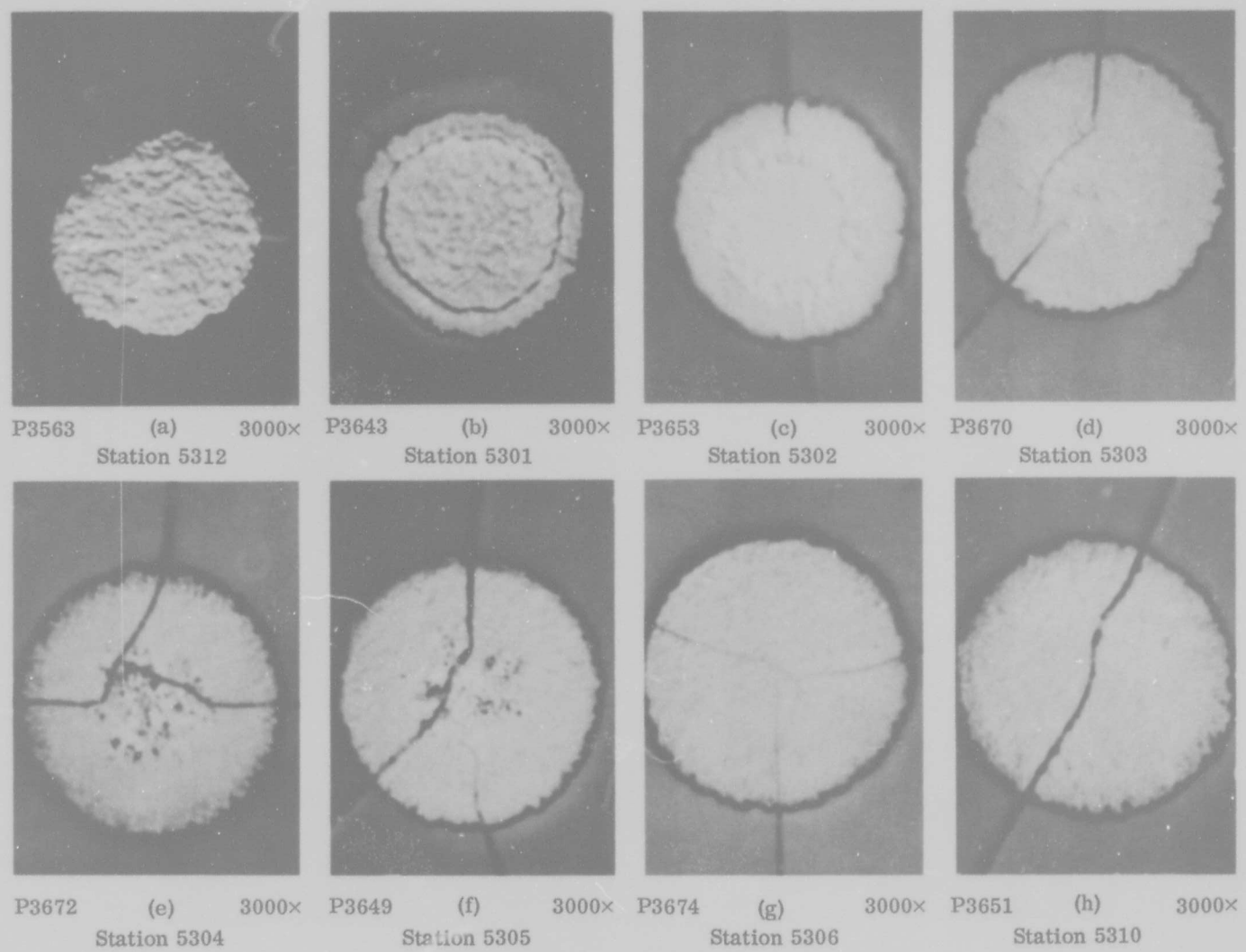

P3563 (a) 3000× Station 5312
P3643 (b) 3000× Station 5301
P3653 (c) 3000× Station 5302
P3670 (d) 3000× Station 5303
P3672 (e) 3000× Station 5304
P3649 (f) 3000× Station 5305
P3674 (g) 3000× Station 5306
P3651 (h) 3000× Station 5310

Fig. 35 Core Development During Growth of Boron Filament

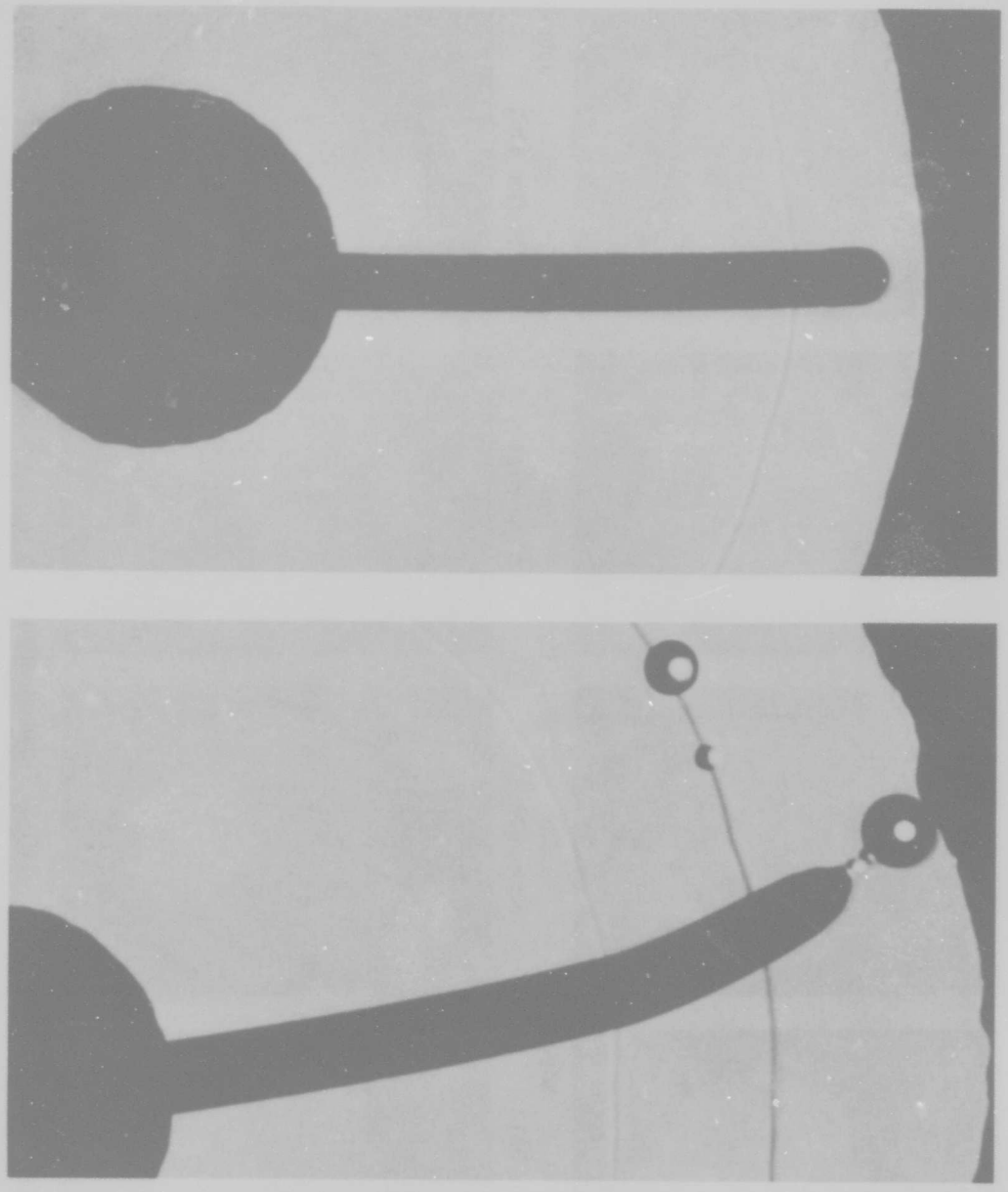

Fig. 36 Detail of Crack Healing (Crack Widened by Etching). (a) Filament at station 5308, beginning at third deposition chamber. P4140 3000×. (b) Filament at station 5309, end of third deposition chamber. P4142, 3000×

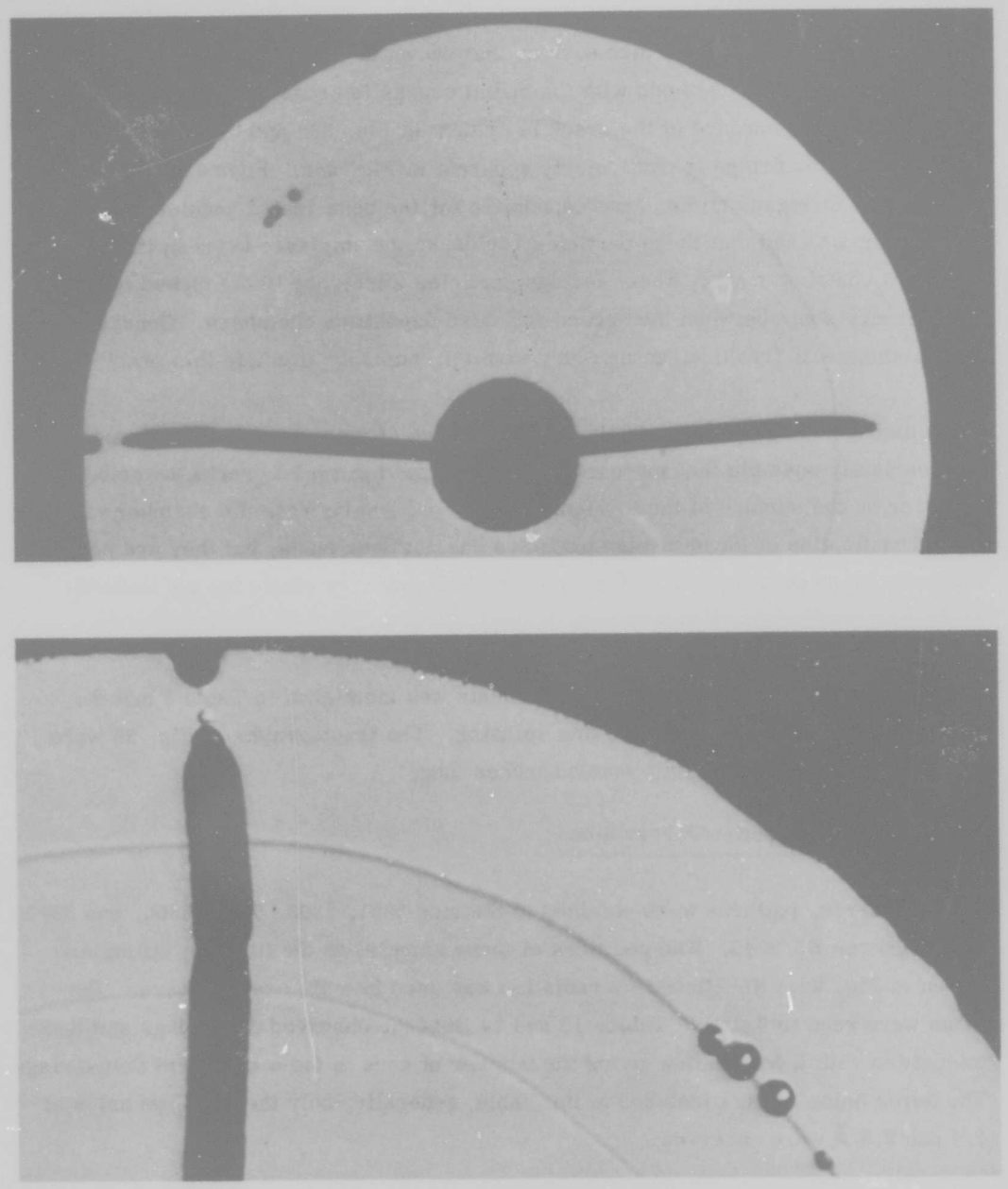

Fig. 37 Detail of Crack Healing at Station 5310, Last Mercury Seal in Process (a) Two cracks and defects between the second and third chamber rings, P4145, 1000×. (b) Crack tip detail. P4144, 3000×

It is evident that the straight, radial cracks present in Figs. 23 – 37 would result in the apparent cleavage fracture such as that shown in Fig. 15. Further evidence correlating this fracture mode with the radial cracks is presented in Fig. 38. The flat, cleavage appearance of the crack is evident in Fig. 38a and b, and the fracture across the crack bridge is particularly apparent in Fig. 38c. Figure 38 also demonstrates that foreign particles are responsible for the renucleated nodules shown in Fig. 33 and 34, and that these particles reside at the interface between the second and third chamber rings. These foreign particles were very likely picked up from the mercury seals between the second and third deposition chambers. Constantly replenishing with fresh, clean mercury would presumably alleviate this problem.

Some discussion has been made about the presence of mercury in boron filaments. It is certainly possible that mercury could be trapped in radial cracks described above or on the surface of the foreign particles present between the chamber rings. The identification of these foreign particles has not been made, but they are probably mercury compounds formed on the surface of the mercury where the hot filament enters the seal or where arcing occurs.

Severe longitudinal splitting of boron filaments was mentioned in Table 5 and the radial cracks are responsible for this splitting. The fractographs in Fig. 38 were taken from a longitudinal split several inches long.

3.7.3 X-ray Diffraction Observations

Debye-Scherrer patterns were obtained at Stations 5301, 5303, 5304, 5306, and 5309 of Texaco run B5/3946. The positions of these samples in the filament tailing are shown in Fig. 22. Ni-filtered Cu radiation was used in a 57.3 mm camera. The films were read to 0.2° 2θ; Tables 13 and 14 lists the observed d-spacings and their intensities with a designation giving the number of arcs in the nonuniform Debye rings. The boron halos are not included in this table; generally, only the first two halos at 4.4 and 2.5 Å were observed.

As noted previously, there is little to distinguish the diffraction patterns of all the reported borides taken together. Table 3 in Section 3.3 lists all the d-spacings of of the various borides and the difficulty of interpreting a Debye-Scherrer pattern from a partially reacted tungsten core is readily apparent.

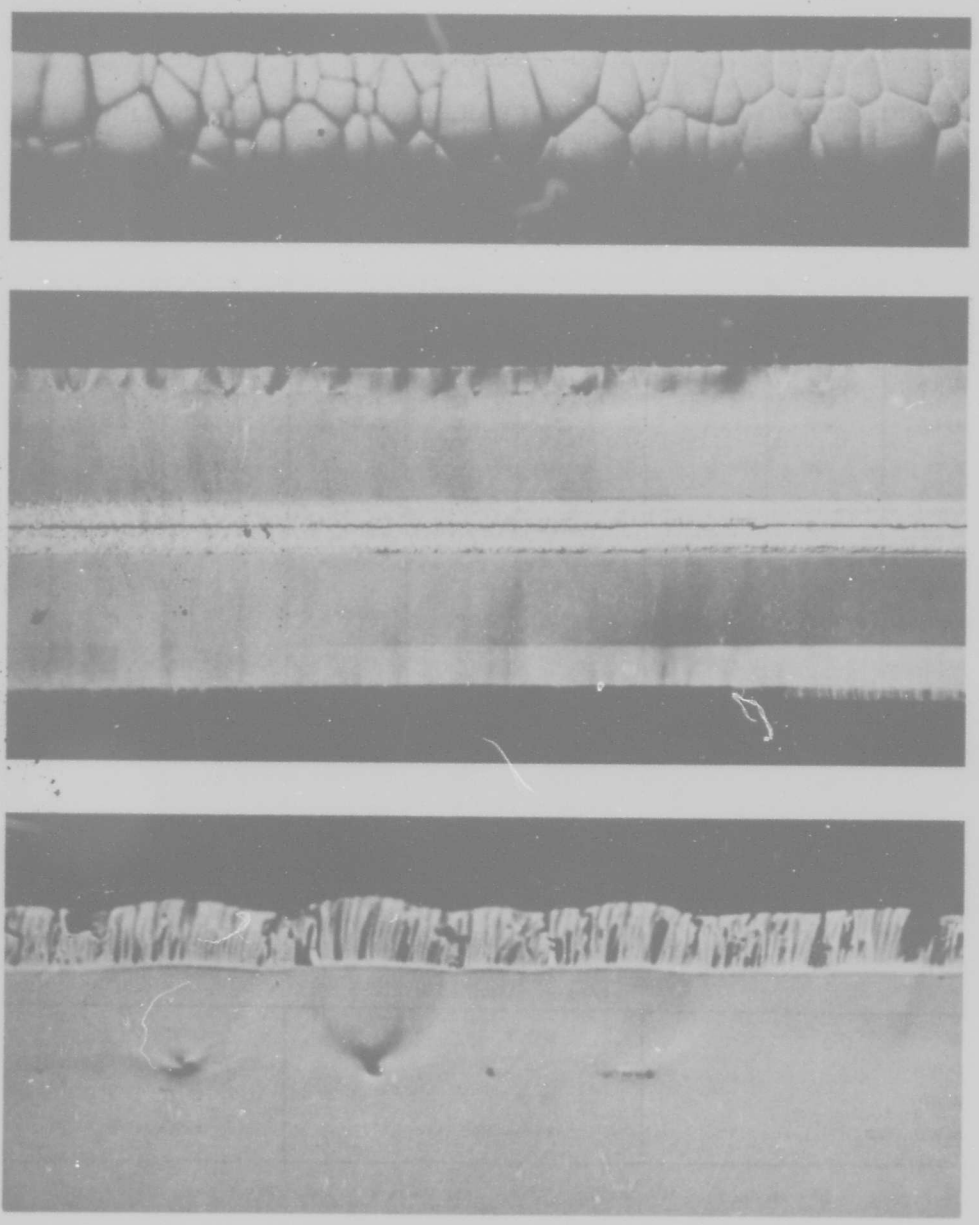

Fig. 38 Fractographs of Longitudinal Crack at Station 5310. (a) Surface texture, P3883, 1000×. (b) Crack plane showing substrate and renucleated cone structure, P3878, 500×. (c) Detail of sites for renucleation and crack morphology. P3877, 3000×

Table 13

TUNGSTEN BORIDE DIFFRACTION PEAKS FROM FILAMENT TAILING, PART 1

Station								
5301			5303			5304		
d-Spacing (Å)	Intensity	Number of Arcs	d-Spacing (Å)	Intensity	Number of Arcs	d-Spacing (Å)	Intensity	Number of Arcs
3.64	VW	2-Br[a]	3.67	M	2-Br	3.70	M	2-Br
3.40	W	4-Br	3.45	M	4-Br	3.45	M	4-Br
3.10	VW		3.16	W	2-Br	3.16	W	2-Br
			2.85	VW				
2.74	VW		2.74	VS		2.76	VW	
2.58	S		2.58	S		2.58	S	
2.25	arc	6-Sh[b]	2.25	VW		2.26	W	
2.13	M	2-Br.	2.14	M	2-Br	2.14	M	2-Br
2.00	W	2-Br	2.00	S		2.01	S	
1.93	arc	10-Sh	1.96	W	10-Sh	1.92	M	
			1.89	M				
1.74	VW	2-Br	1.74	W		1.74	VW	
			1.64	W		1.64	VW	
1.58	arc	2-Sh	1.57	W		1.57	VW	
1.50	M		1.49	M		1.50	S	
1.37	M		1.37	S		1.37	S	
1.34	M		1.34	M		1.35	W	
			1.32	W				
1.29	arc	6-Sh	1.29	M		1.29	M	
1.26	VW		1.25	VW		1.26	VW	
			1.22	VW		1.22	VW	
			1.20	W		1.20	W	
			1.17	VW		1.17	VW	
1.11	arc	6-Sh	1.13	W		1.13	W	
			1.10	VW		1.10	VW	
Phases Identified								
W			δ-WB			δ-WB		
δ-WB								
W_2B_5			W_2B_5			W_2B_5		
τ-$WB_2(WB_4)$			τ-$WB_2(WB_4)$			τ-$WB_2(WB_4)$		

S - Strong, M - Medium, W - Weak, VW - Very Weak,

[a] 4-Br = Four Broad Arcs

[b] 6-Sh = Six Sharp Arcs

Table 14

TUNGSTEN BORIDE DIFFRACTION PEAKS FROM FILAMENT TAILING, PART 2

Station 5306			Station 5309		
d-Spacing (Å)	Intensity	Number of Arcs	d-Spacing (Å)	Intensity	Number of Arcs
3.64	M	2-Br	3.70	S	2-Br
3.45	M	4-Br	3.48	S	4-B
3.14	M		3.16	S	2-V Br
2.56	S		2.60	M	
2.41	VW		2.39	VW	
2.25	W		2.25	W	
2.11	W		2.12	M	
2.065	VW	2-Br	2.00	S	
2.00	S				
1.92		4-Sh			
1.89	M		1.89	M	
1.73	VW		1.74	VW	
1.635	W		1.64	W	
1.57	VW				
1.52	VW		1.54	VW	
1.49	S		1.50	S	
1.37	S		1.37	S	
1.35	M		1.35	M	
1.32	W		1.32	W	
1.29	M		1.29	M	
1.25	VW		1.26	VW	
1.22	VW		1.22	VW	
1.20	W		1.20	M	
1.17	VW		1.17	W	
1.125	W		1.13	M	
1.08	W		1.08	M	
1.07	VW		1.07	VW	
Phases Identified					
δ-WB W_2B_5 τ-$WB_2(WB_4)$			W_2B_5 τ-$WB_2(WB_4)$		

Sample 5301 yields definite evidence of W, W_2B_5 and either τ-WB_2 or WB_4. Because there is virtually nothing in the diffraction patterns to distinguish τ-WB_2 from WB_4, the phase is designated τ-$WB_2(WB_4)$. The transverse cross section in Fig. 23 reveals the presence of a very faint ring next to the tungsten core which could be responsible for the 10 or so spots at 1.93 Å in the Station 5301 diffraction pattern. These specks cannot belong to W_2B_5 or τ-$WB_2(WB_4)$ because the rest of their lines are continuous; thus, the choice lies between γ-W_2B and WB(δ or β). Many of the strong lines of γ-W_2B are missing from the 5301 pattern; these missing lines are the 2.37, 1.80, 1.41, 1.33, 1.31, and 1.30 Å strong peaks. On the other hand, the 2.74, 2.29, 2.13, and 1.91 Å strong peaks of δ-WB are possibly present in the 5301 pattern and the 10 specks observed in the 1.93 Å line correspond to strong line for δ-WB and a very weak line for γ-W_2B. The absence of the strong 2.48 Å line of β-WB leads to the conclusion that the minute ring next to the tungsten core in Fig. 22 consists of δ-WB. If that is the case, then the ring next to the boron sheath must contain two phases: W_2B_5 and either τ-WB_2 or WB_4.

The W is consumed in sample 5303 and the δ-WB is nearly gone in sample 5304. In sample 5306, the 2.74 Å line of δ-WB has disappeared and only a few specks remain of the 1.92 Å line of δ-WB. In sample 5309, both δ-WB lines have disappeared, leaving a pattern which can be easily attributed to W_2B_5 and either τ-WB_2 or WB_4.

3.7.4 Temperature Gradient in Boron Filaments

Because boron filaments are prepared by resistively heating a tungsten wire substrate, there exists the possibility of a radial temperature gradient in the filament which could result in a structure gradient. An analysis of the problem of radial heat flow in composite cylinder by Dolton and Schneider (Ref. 22) is given in Appendix A and their results form the basis of the following discussion.

Assuming steady state with thermal properties not a function of temperature, the temperature drop across the mantle, ΔT, is related to the thermal and geometrical properties of the system (Appendix A) by

$$\frac{4K_m \Delta T}{\dot{q}_m r_m^2} = 2\left(\frac{r_c}{r_m}\right)^2 \left(\ln \frac{r_m}{r_c}\right)\left(\frac{\dot{q}_c}{\dot{q}_m} - 1\right) - \left(\frac{r_c}{r_m}\right)^2 + 1 \qquad (1)$$

where

K_m = thermal conductivity of the mantle

$\dot{q}_m$ = rate of heat generation per unit volume in the mantle

$\dot{q}_c$ = rate of heat generation per unit volume in the core

r_m = radius of the mantle

r_c = radius of the core

For boron filaments, r_c/r_m is approximately 0.1; substituting this ratio into Eq. (1) yields

$$\Delta T \cong \frac{\dot{q}_m r_m^2}{4K_m}\left[1 + 0.046\left(\frac{\dot{q}_c}{\dot{q}_m}\right)\right]$$

The ratio $\dot{q}_c/\dot{q}_m$ for boron filaments at temperature should be between 0.01 and 1. For this range of $\dot{q}_c/\dot{q}_m$

$$\Delta T \cong \frac{\dot{q}_m r_m^2}{4K_m}$$

Taking

$$r_m = 2.5 \times 10^{-3} \text{in.} = 6.3 \times 10^{-3} \text{ cm}$$

$$\dot{q}_m = 10 \text{ W/linear in.} = 0.5 \times 10^6 \text{ W/in.}^3$$

$$= 8 \times 10^3 \text{ cal/cm}^3 \text{ sec}$$

$$K_m = 0.01 - 0.001 \text{ cal/cm sec } ^\circ\text{C}$$

then

$$\Delta T = \frac{8 \times 10^3 (6.3 \times 10^{-3})^2}{4K_m} = \frac{8 \times 10^{-2}}{K_m}$$

For $K_m = 0.01 \text{ cal/cm}^3 \text{ sec}$, $\Delta T \cong 8^\circ\text{C}$

and for $K_m = 0,001 \text{ cal/cm}^3 \text{ sec}$, $\Delta T \cong 80^\circ\text{C}$

If the above values are correct, this analysis demonstrates that the radial temperature gradient is not as important as might be supposed. However, the radial temperature gradient, thermal fluctuations due to local high deposition rates, and hot spots due to inclusions in the mantle and inhomogeneities in the substrate all lead to local temperature increases which can result in the small areas of large crystallite boron which are observed.

3.7.5 Volume Changes During Deposition

During the formation of boron filaments with a tungsten wire substrate, the tungsten wire reacts with the boron to form tungsten borides by a radial diffusion process. Although the phases present at temperature are not well known (see Section 3.3), it

is of benefit to consider the possibility of volume change occurring during the boriding of the tungsten core. The simple case of one compound forming can be treated by simple geometrical arguments and Karlak (Ref. 22) has treated the general case. The general treatment is given in Appendix B.

Consider first the simple case, in which a deposit of boron of radius r_B is deposited around a cylinder of tungsten of radius r_W, and the system then reacts to form a core with one compound of stoichiometric formula WB_k with radius r_C. The number of tungsten atoms remains constant; therefore

$$\gamma'_W \pi r_W^2 \ell = \gamma'_C \pi r_C^2 \ell$$

where ℓ is unit length, γ'_W is the molar density of W (mols/cm^3) found by dividing the density ρ (gm/cm^3) by the atomic weight M (gm/mol), γ'_C is the molar density of the compound WB_k and r_C is the radius of the compound formed. Similarly for the boron atoms

$$\gamma'_B \pi \ell \left(r_C^2 - r_W^2\right) = k \gamma'_C \pi \ell \left(r_C^2\right)$$

The stoichiometry of the compound, assuming no volume changes, is given by the ratio

$$\nu = \frac{N_B(V_C)}{N_W(V_C)} = \frac{\gamma'_B \left(r_C^2 - r_W^2\right)}{\gamma'_W r_W^2}$$

Using the constant volume condition $r_C^2 = \gamma'_W r_W^2 / \gamma'_C$

$$\nu = \frac{\gamma'_B}{\gamma'_C} - \frac{\gamma'_B}{\gamma'_W} \qquad (2)$$

For $\nu > k$, the compound requires fewer boron atoms than were consumed in its formation so an expansion of the boron sheath must occur. For $\nu < k$, more boron atoms are needed than are available, and the boron sheath must contract to maintain contact around the interface between the compound and the boron.

Karlak's analysis (Appendix B) is based on the ratio (R) of the volume consumed to the volume of new compound formed. Thus, for a reaction of the form

$$aA + bB \rightarrow cC$$

$$R = \frac{V_A + V_B}{V_C} \tag{3}$$

and

$$R = \frac{\gamma_A + \gamma_B}{\gamma_C}$$

where V_i is the total volume of chemical species i, and γ_i is the molar volume of species i times the number of moles of i involved in the reaction.

For the reaction

$$A + kB \rightarrow AB_k$$

Karlak's simple expression (Eq. 3) becomes

$$R = \frac{1/\gamma'_A + k/\gamma'_B}{1/\gamma'_B}$$

$$R = \frac{\gamma'_C}{\gamma'_A} + \frac{k\,\gamma'_C}{\gamma'_B} \tag{4}$$

An increase in volume will correspond to $R > 1$, no change to $R = 1$, and a shrinkage corresponds to $R < 1$.

Calculations based on Eqs. (2) and (4) are given in Table 15. The compounds $WB_{0.5}$, δ-WB and WB_4 all cause a volume expansion, if they occur between the W and B phases, and this expansion could easily account for the radial cracking which propagates by the growth mechanism discussed in Section 3.7.2. The density of δ-WB has not been determined and the value of 14 gm/cc was estimated from the values for W_2B and β-WB.

The situation is more complex than presented in the above analyses. First, the precursor to the W_2B_5 – τ-WB_2(WB_4) mixture is not known, nor are its molar volume and nature of phase transformation known. Second, the formation of the borides proceeds first with the formation of the precursor phase, followed by the appearance of δ-WB. Assuming that the precursor is W_2B_5, the reaction to form δ-WB is

$$WB_{2.5} + 1.5\ W \rightarrow 2.5\ \delta\text{-WB}$$

and

$$R = \frac{\gamma_W + \gamma_{WB_{2.5}}}{\gamma_{WB}}$$

$$R = \frac{1.5/\gamma'_W + 1/\gamma'_{WB_{2.5}}}{2.5/\gamma'_{WB}}$$

$$R = 0.60 < 1.0$$

The result of this reaction is a net expansion which also could be responsible for the radial crack which is present near the beginning of the deposition and seems to be associated with the appearance of δ-WB.

Table 15

VOLUME CHANGES DURING BORIDE FORMATION

Compound	Calculated Density ρ(gm/cm^3)	Mole. Wt. (M)	Atomic Density[a] γ'(mol/cm^3)	γ'_B/γ'_C	ν[b]	k[c]	Volume Change[d]	γ'_C/γ'_A	$k\,\gamma'_C/\gamma'_B$	R[e]	Volume Change[d]
W	19.3	184	0.105	2.3 (γ_B/γ_W)	–	–					
$WB_{0.5}$	10.7	195	0.055	4.4	2.1	0.5	+	0.52	0.12	0.64	+
δ-WB	14[f]	200	0.070	3.4	1.1	1.0	+	0.68	0.29	0.97	+
β-WB	16.0	200	0.080	3.0	0.7	1.0	-	0.76	0.32	1.08	-
τ-WB		206									
WB_2	14.2	206	0.069	3.5	1.2	2.0	-	0.66	0.57	1.23	-
ϵ-$WB_{2.5}$	13.1	211	0.062	3.9	1.6	2.5	-	0.59	0.51	1.20	-
WB_4	8.3	227	0.037	6.5	4.2	4.0	+	0.35	0.58	0.91	+
B	2.35	10.8	0.240	–	–	–	-	–	–	–	

(a) $\gamma' = \rho/M$

(b) ν = mols B consumed/mols W at constant volume

$$\nu = \frac{\gamma_B}{\gamma_C} - \frac{\gamma_B}{\gamma_W}$$

(c) k = stoichiometric ratio in compound WB_k

(d) Volume change: (+) net expansion
(-) net contraction

(e) R = Corrected molar volume ratio

$$R = \frac{\gamma'_C}{\gamma'_A} + \frac{k\gamma'_C}{\gamma'_B}$$

(f) Estimated

In summary, there are several phases which would cause a net expansion of the filament and produce the radial cracking and longitudinal splitting which is common to B/W filaments. Also, there are several secondary reactions between phases which could also produce the radial cracking. There are not sufficient density nor phase equilibrium data to adequately treat this problem, but there is sufficient evidence to suspect that volume changes occurring during the formation of tungsten borides are responsible for the straight radial cracks which form. Observing the flexure of a flat tungsten sheet reacting with boron on one side would indicate the nature of the volume changes.

3.7.6 Summary of Development of Boron Filament Structure During Deposition

The tailings of filament production runs were examined systematically to observe the development of the filament structure. The temperature profile, provided by Texaco Experiment, Inc., showed a fairly uniform central temperature with a decrease of several hundred degrees F in about 6 inches at the end of each deposition chamber where the filament passes through mercury seals.

Initially, boron is deposited on the tungsten wire. Next, a boride phase is formed which is the precursor of the intimate two-phase mixture of W_2B_5 and τ-WB_2(WB_4). This two-phase mixture persists throughout the deposition process and eventually occupies the entire core volume. The phase δ-WB forms between the precursor phase and the tungsten core, and its formation is probably the source of the radial cracks which are responsible for the flat fracture mode and longitudinal splitting. The crack developed at this early stage continues to grow during deposition because the growth rate on each side is equal and limited gas diffusion prevents growth inside the crack. This crack is bridged late in the deposition process and it then can fracture conchoidally through the bridge. Because of the bridging, these radial cracks are seldom seen in finished production filaments. These processes are depicted in Figs. 24–39.

In the samples examined, the nodule structure was type III(A1), a large major nodule structure with no minor nodules (see Section 3.6.3.4). Quenching in the mercury

seals does not cause obvious changes in the morphology but the areas of restarted growth have a much lower resistance to chemical attack. Renucleated nodules grow on foreign particles picked up at the mercury seals between the deposition chambers. Bridging of the radial cracks can be promoted by foreign particles and the regions around the particles also have a lower resistance to chemical attack.

A radial temperature gradient was considered as a potential source of structural variations but the maximum temperature decrease from the core surface to the filament surface was estimated to be less than 80 °C for 0.005-in. B/W filaments.

Simple and general analyses of the volume changes brought about by compound formation were made but the lack of information on phase equilibria at temperature and uncertainties in the densities of tungsten borides made it difficult to apply the analyses with certainty. Nonetheless, the formation of a phase between the tungsten core and the two-phase ring next to the boron is likely to require a net circumferential expansion which will crack the boron deposit and initiate the straight radial cracks frequently observed.

3.8 DISCUSSION AND SUMMARY OF GENERAL STRUCTURE OF BORON FILAMENTS

This portion of the program was concerned with characterizing the gross structural features of boron filaments such as the grain and nodule structure, the nature of the core, and the kinds of defects present. Production filaments from Texaco Experiment, Inc., and United Aircraft Research were examined, as were filaments prepared by Astro Research under a variety of conditions. In addition, the development of the boron filament structure was studied by examining a production tailing. Several boron aggregates were examined for comparison with the boron filament structure.

Boron filaments were found to consist of a two-phase core of tungsten borides approximately 0.0007-in. in diameter with a sheath of vapor deposited boron 0.002-in. thick. The core structure could not be resolved by the light microscope, but the x-ray diffraction lines from the borides were consistent with a crystallite size of 0.1μ or greater. The boron sheath consists of a nodular structure with major and minor

nodules typical of surface nucleated, vapor deposited materials. All the boron deposited between 870 and 1260° C has essentially the same crystallographic structure, regardless of substrate, and variations of the deposition parameters within a broad range only vary the morphology.

Metallographic techniques were developed to reveal the core and sheath structure, and standard x-ray methods were employed to observe the boron and boride diffraction patterns. Boron filaments were thinned for transmission electron microscopy studies. As described in the second half of this report, careful indexing was required to identify the various spot patterns. Special techniques were utilized to demonstrate that vapor deposited boron is not a liquid-like amorphous solid, but rather, it consists of a microcrystalline aggregate of α-rhombohedral and tetragonal boron.

The tungsten boride crystal structures were reviewed; their diffraction patterns are similar and it is quite difficult to distinguish between certain borides. The identification and existence of some borides is not well established and there are some uncertainties about the reported phase equilibria in the vicinity of 1150° C.

Boron aggregates prepared by different methods were examined. Boron prepared by growth from the melt consists of the β-rhombohedral structure; β-boron is optically active, twins readily, and does not exhibit cleavage fracture. A high purity polycrystalline sampie fractured conchoidally when struck with a hammer. Boron prepared by gas pyrolysis has a diffraction pattern consisting of only two very diffuse halos indicative of a liquid-like amorphous structure.

Production filaments prepared by Texaco Experiment, Inc., are characterized by:

- A strongly delineated major nodule structure with some filament lengths having a minor nodule structure as well

- A cusped ring structure; the cusps correspond to the major nodule structure and the chamber rings are the result of deposition in several chambers
- A lower resistance to chemical attack at the chamber ring interfaces which is related to the dominant growth mechanism

The surface texture of the United Aircraft Research filament is similar to the Texaco material but there are two chamber rings with different morphologies. The United Aircraft filament is apparently built up in small waves and the entire structure has a chemical reactivity comparable to the chamber ring interfaces of the Texaco material.

All filaments exhibit two fracture modes: the flat longitudinal mode which has the appearance of a cleavage fracture and the conchoidal mode. The flat fracture mode is caused by straight radial cracks which form near the beginning of the deposition process and grow with the filament. These flat, radial cracks are responsible for the longitudinal splitting observed in B/W filaments. The conchoidal mode is simply a typical brittle fracture nucleated by defects such as foreign particles and the core-sheath interface.

Filaments deposited at lower temperatures and shorter times tend to have a minor nodule structure while high temperatures tend to eliminate the minor nodules. The ratio of longitudinal to circumferential dimensions of the major nodules decreases with increasing deposition temperature, ranging from 1:1 to 1:3. This and other features can be incorporated into a nomenclature system for filaments which includes descriptions of the core structure, the sheath structure, and the dominant morphological features of the sheath.

The cores of all B/W filaments react to form various borides, depending upon the time and temperature of deposition. Expansions due to boride formation are probably responsible for the longitudinal cracking described earlier. The borides form by radial diffusion and the expansion reaction probably occurs when the first boride phase to form reacts with the tungsten core to form another boride. Phase identification of the first boride has not been made because a solid state phase transformation must occur on cooling to provide the intimate two-phase mixture of W_2B_5 and τ-$WB_2(WB_4)$ which is observed.

This mixture is present in all the fully reacted B/W filaments examined in this study. The formula τ-$WB_2(WB_4)$ only indicates that the phases τ-WB_2 and WB_4 have essentially the same diffraction patterns and cannot readily be distinguished by x-ray diffraction.

A radial temperature decrease of 80° C from the core-sheath interface to the filament surface was estimated for 0.005-in. filaments. Thus, no structural gradient is likely to exist because of a large temperature difference; however, fluctuations in local temperature can cause the variations in crystallite size and crystal structure which are observed.

During the deposition process, the filaments pass through several mercury seals. Quenching the filament in these seals does not appear to affect the structure of the filament but the area of re-started growth is more susceptible to chemical attack. The radial crack responsible for the flat fracture mode could be initiated by quenching in these seals rather than by expansion due to the formation of borides. Foreign particles are picked up in the radial cracks and can contribute to crack healing and forming renucleated nodules which occur in filaments.

The crystallographic structure of boron filaments deposited under a wide variety of conditions appears to be essentially the same; this structure is discussed in detail in the second half of the report. The morphology of boron filaments is closely related to the deposition conditions and this morphology has been described in the preceding sections.

Section 4 – CRYSTALLOGRAPHIC STRUCTURE OF BORON FILAMENTS

4.1 INTRODUCTION AND REVIEW OF PREVIOUS WORK

4.1.1 Review of Boron Crystal Structure Analyses

Many polymorphs of boron have been reported, and these structures have been reviewed by several authors (Refs. 20, 24, and 25). The boron polymorphs which have been generally accepted are the α-rhombohedral structure (Ref. 26), the tetragonal structure (Ref. 20), and the β-rhombohedral structure; x-ray diffraction studies of these and other structures have been reviewed by Hoard and Newkirk (Ref. 20). β-boron always forms on fusion or by deposition processes which occur above about 1500° C, while the tetragonal structure occurs in the vicinity of 1000 – 1500° C. The α-boron structure is generally found below about 1100° C. Hoard (Refs. 20, 28, and 29) has suggested that only the β-boron form is thermodynamically stable and that all the other forms are the result of variations brought about by kinetic, epitaxial, or impurity factors. These factors have also been suggested by Newkirk to explain the polymorphism of boron (Ref. 28). Peters and Potter (Ref. 30) have shown that vapor deposited α-boron can have an epitaxial relationship with Si single crystals.

Several authors (Refs. 24, 27, and 29) have demonstrated that the boron structure can be described using structural groups of B_{12} icosahedra as can the structure of many of the borides. This concept is of considerable benefit in understanding boron and boride structures and is also useful in discussing the structure of boron filaments. The α-boron structure consists of a rhombohedral arrangement of B_{12} icosahedra ($a = 5.057$ Å, $\alpha = 58.06°$)(Ref. 26) and the tetragonal structure consists of a face-centered tetragonal arrangement of B_{12} units with two interstitial atoms in each unit cell ($a = 8.75$ Å, $c = 5.08$ Å)(Ref. 24). The β-boron structure ($a = 10.12$ Å, $\alpha = 65° 28'$) has been described as an icosahedral arrangement (Refs. 24 and 27) of B_{12} icosahedra with two B_{10} units and a single B atom within the large rhombohedral unit cell. It must be emphasized that in all these structures the B_{12} structural units do not behave as

close packed metal atoms, but rather, have definite orientation relationships and are separated from each other by bond lengths comparable to one-half the B_{12} icosahedron diameter (Refs. 24, 26, and 27).

Because well-defined diffraction evidence is available only for the α-rhombohedral, tetragonal, and β-rhombohedral forms of boron, and because the existence and means of production of the other forms is in some question, the interpretation of the broad diffraction maxima observed from boron filaments was restricted to the well-defined forms. The d-spacings and intensities for the α-rhombohedral from have been published by Decker and Kasper (Ref. 26 – ASTM card 12-377) while Hoard, Sands, and Newkirk (Refs. 20 and 27) have published data on the tetragonal form (ASTM card 12-469) and β-rhombohedral form (ASTM card 11-618). The densities of the various forms of boron are discussed in Appendix C.

4.1.2 Review of Other Investigations on the Structure of Vapor-Deposited Boron

There have been several hypotheses concerning the crystallographic nature of boron filaments. Because early x-ray diffraction data showed two or three broad maxima or halos, the first investigators assumed that boron vapor-deposited at low temperature was "amorphous." Subsequently, as many as seven halos have been observed having intensities which do not decrease monotonically with increasing diffraction angle, proving that vapor-deposited boron cannot have a liquid-like amorphous structure. Lipsitt and co-workers (Ref. 10) at the Aerospace Research Laboratories (ARL) postulated that the halos could result from a highly distorted β-rhombohedral structure but this model was shown to be inconsistent with the positions of the halo maxima as described in Section 4.3.

Later work at ARL (Ref. 31) showed large rel-rod effects in an hexagonal spot pattern obtained from isolated areas of large crystallite size found in ground boron filaments. The same observations were made during this study in thinned as well as ground filaments, and rel-rod effects were noted in other spot patterns as well (see Section 4.4). Otte and Lipsitt (Ref. 31) indexed the hexagonal pattern on the basis of an hexagonal

crystal structure and obtained the same translation vector (5.3 Å) as that obtained from the diffuse maxima indexed on an fcc lattice. From these observations, they postulated an fcc-hcp structure with an ideal c/a ratio and profuse faulting for the structure of vapor deposited boron. The faulting hypothesis was supported by their observation that filament fragments heated by the electron beam recrystallize to a large crystallite size with striations in the image and rel-rod effects in the diffraction patterns.

The Otte-Lipsitt model has been critized for several reasons (Ref. 32), the principal ones being:

- The existence of an fcc structure for elemental boron has not been established
- The postulated correspondence between the halo pattern and the hexagonal pattern was based on rhombohedral cell parameters which are very different from those of the known rhombohedral polymorphs of boron and imply a subunit in the β-rhombohedral structural which, in fact, does not exist (Ref. 33).
- Line broadening due to crystallite size was not considered even though a grain boundary structure with a large crystallite size was not demonstrated
- No image evidence such as stacking fault fringes was presented to demonstrate the existence of stacking faults in the unheated matrix material

In addition to the ARL studies, Wawner has studied the structure of boron filaments (Refs. 8, 14). In a very long exposure Debye-Scherrer pattern of a split and etched filament Wawner found a six halos, as noted in Table 16 (Ref. 14). A tentative indexing scheme showed that the six halos could be indexed on a bcc lattice with a = 6.2Å, but Wawner noted that this scheme has a 25% density discrepancy. Also, the diffraction maxima are very broad, and the calculated lines for various indexing schemes are easily matched to the observed broad peaks. In the same report (Ref. 14), some heat treatment studies were described in which β-boron crystals grew on the surface of boron filaments heated above 1650° C in vacuum. Inert gas suppressed the surface reaction, and the general conclusion was that the transformation was grain growth of a microcrystalline aggregate. Several different substrates were used and no epitaxial effects were noted in the as-deposited or heat treated filaments.

Table 16

X-RAY DIFFRACTION DATA FROM SPLIT AND ETCHED BORON FILAMENT

Observed d(Å)	Calculated [a] d(Å)	Intensity	hkℓ
4.3	4.4	S	110
2.5	2.5	M	211
1.7	1.7	VW	321
1.38	1.4	W	420
1.1	1.1	VVW	440
0.9	0.9	VVW	631

[a] Data taken from Ref. 14, Indexing based on bcc lattice with a = 6.2Å

Galasso and co-workers (Ref. 21) have studied the structure of boron filaments deposited between 700 and 1700° C. Wire substrates of Ta, W, and Mo were used and the boride reactions were examined in all the systems. Boron deposited below about 1400° C was uniform in structure and considered to be amorphous, while deposits above about 1500° C developed a columnar grain structure of β-rhombohedral boron which could be discerned under polarized light. Between 1400 and 1500° C various structures occurred containing both equiaxed and columnar grains of both tetragonal and rhombohedral boron. Heat treatments of 30 seconds duration caused tetragonal boron to form at about 1300° C and β-rhombohedral boron to form above about 1500° C.

4.2 METALLOGRAPHY

4.2.1 Summary of General Observations

In the previous sections, extensive metallographic observations were reported for boron vapor deposited under a variety of conditions. In all the cases examined, the boron had essentially the same appearance except for the macroscopic growth details. The significant features observed were:

- The growth nodules which occur in three general types: major nodules, minor nodules, and renucleated nodules
- The continuity of nodules from one chamber ring to the next
- The increased chemical reactivity at regions of new growth or nucleation
- The complete lack of optical activity under polarized light
- The apparent cleavage and conchoidal modes of fracture

All of the above observations are consistent with a model of vapor-deposited boron in which the boron is either "amorphous" or has a crystallite size smaller than $\sim 1.0\mu$. Some further observations on the structure of vapor deposited boron are given in the following sections.

4.2.2 Optical Anisotropy

The microstructure of large grain size β-rhombohedral boron was presented in Section 3.4 and the structure of the same material observed under polarized light is presented in this section in Fig. 39 where the optical activity of β-boron is clearly demonstrated.

Polarized light photographs of two boron filaments are shown in Fig. 40. The filament in Fig. 40a was deposited by a low temperature electric discharge process (Ref. 34); it exhibits a definite cone structure and strong optical anisotropy. Figures 39 and 40 demonstrate that optical activity can be observed at high magnification if it is present. The filament in Fig. 40b is a production filament, Texaco-σ. Its cone structure can be deduced from the cusps at the chamber ring interfaces, but there is no indication of cone structure revealed by polarized light nor is there any other evidence for optical anisotropy. The variations in brightness around the chamber ring interfaces and across the samples are due to surface roughness and do not indicate true optical activity. Optical activity has been observed in low temperature deposits (Fig 40a) and very high temperature deposits (Ref. 21) but polarized light examinations of various production filaments, the Astro material, and the Texaco tailings all showed that normally deposited boron filaments do not show optical anisotropy.

The nodular structure typical of small crystallite size or small grain size pyrolytically deposited materials has been shown to be the result of surface irregularities in the substrate (Section 3.5). This nodular structure is revealed very clearly in pyrolytic graphite and pyrolytic boron nitride because there is a mutual alignment of crystallites as evidenced by preferred orientation studies in these materials (Refs. 35 and 36). The strong preferred orientation permits large regions to act very much like large single crystals. Vapor deposited boron, on the other hand, has the nodular structure but it is revealed only by etch-relief; therefore, the crystallites in boron must have very little mutual alignment and the crystallite size must be below the resolution of the light microscope; i.e., less than $\sim 1.0\mu$.

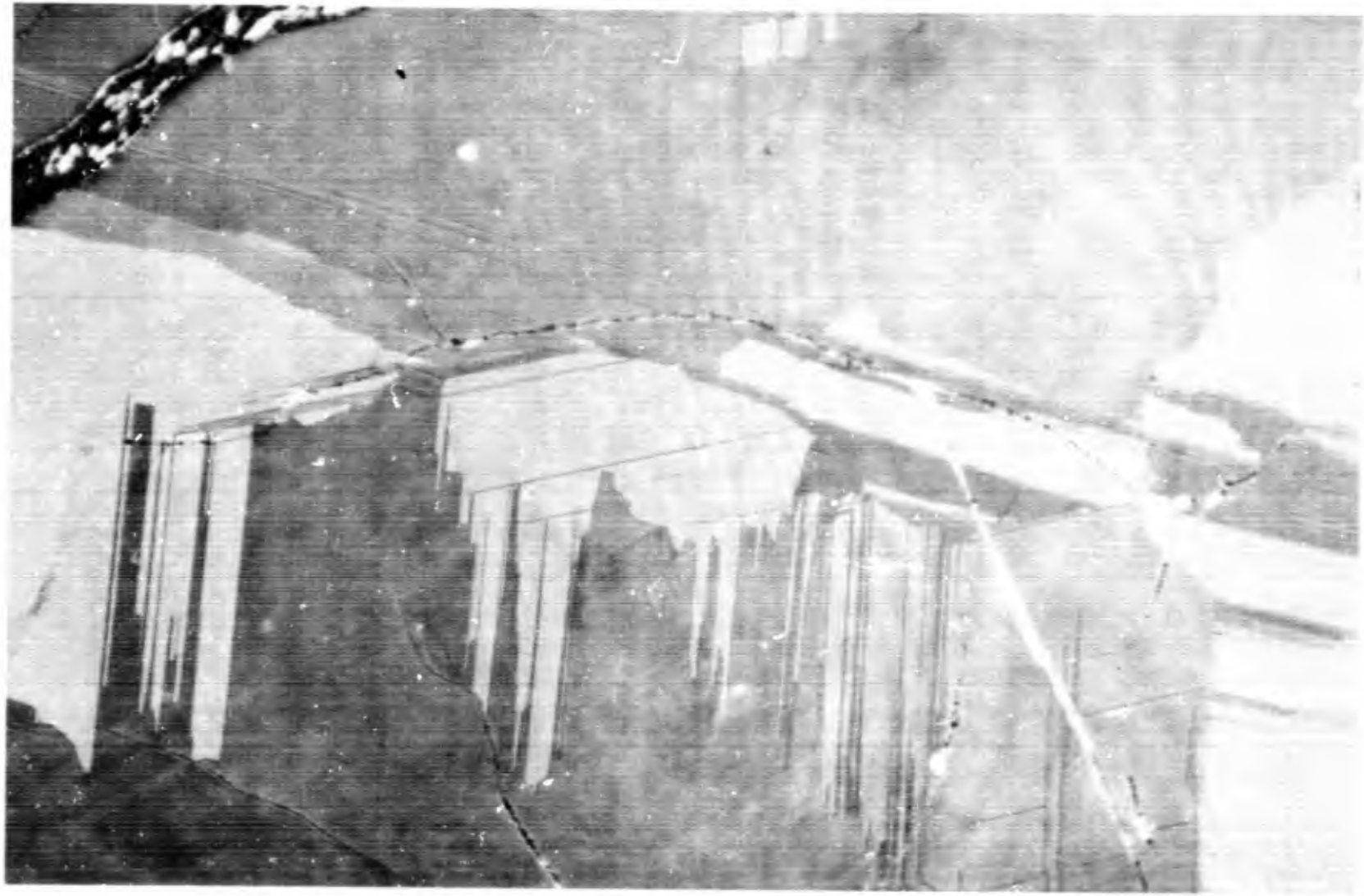

Fig. 39 Bulk, Fractured β-Boron Showing Optical Anisotropy, Twinning, Polycrystallinity, and Cracking. P3641, 500×, Polarized Light

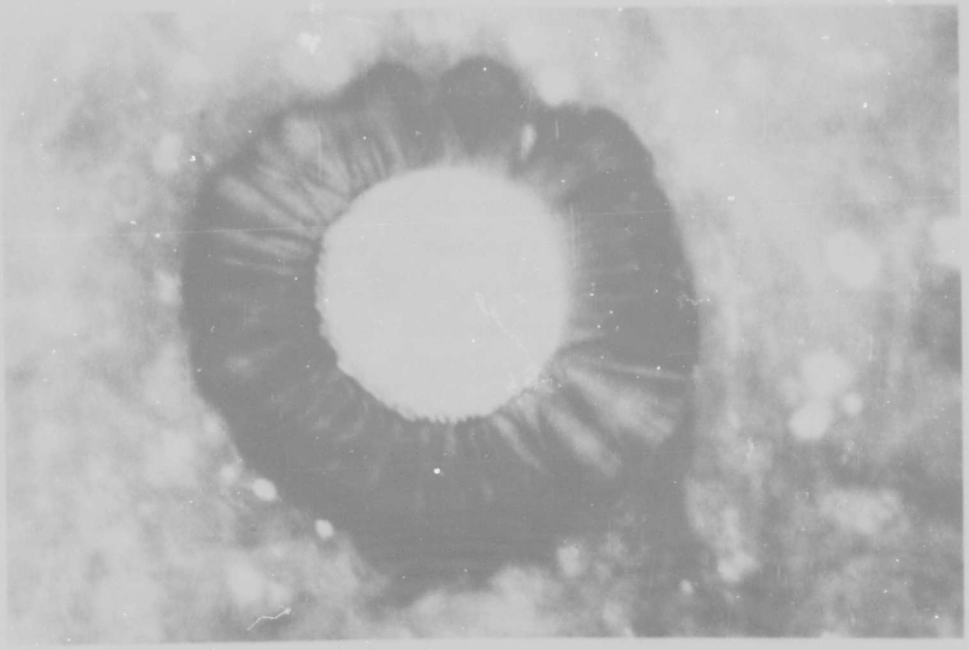

Fig.40(a) Polarized Light Photomicrograph of Boron Filament Deposited at Low Temperature. 3000×

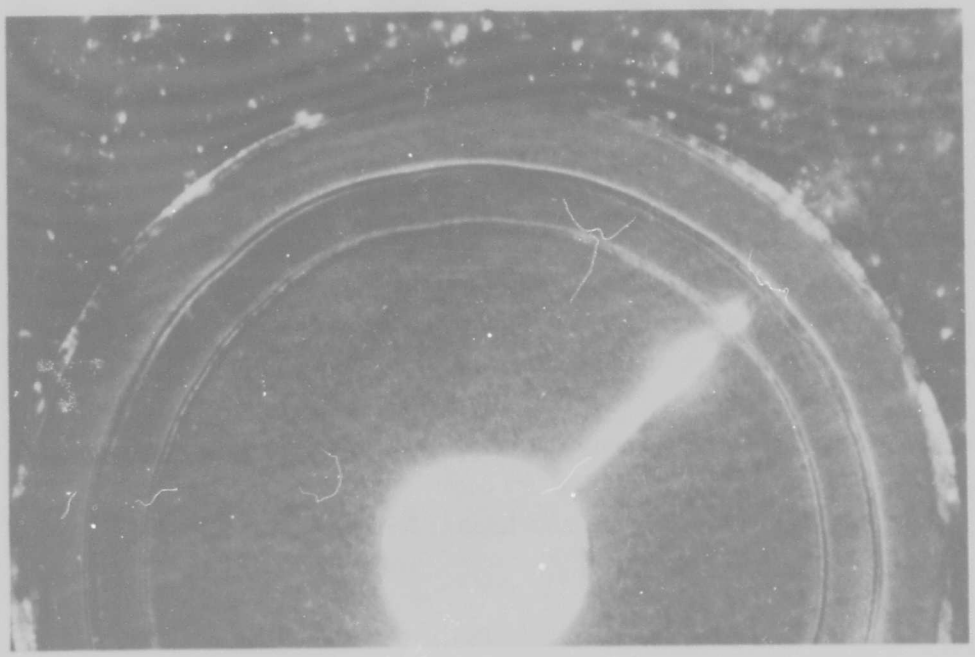

Fig.40(b) Polarized Light Photomicrograph of Texaco-σ Filament. P1270, 1150×

4.2.3 Heat-Treated Filaments

The effect of heat treatment on the structure of boron filaments was examined briefly by heat treating at ~ 1000° C. The heat treatments were done in quartz ampoules evacuated and back filled with high purity argon. To prevent reaction of the filament with the quartz, the ampoules were first lined with Ta foil. Filaments heat treated with this arrangement lost some boron, were kinked into a spiral shape, and demonstrated optical activity under polarized light. Photographs of some filaments heated to 990° C for 48 hours with Ta foil are shown in Fig. 41. At first, the kinking was attributed to stress relief and recrystallization of the filament; however, it was found that boron powder of an unknown purity forms a eutectic with Ta foil at 1000° C, in contradiction to a reported phase diagram (Ref. 37). Changing to a Mo liner resulted in relatively straight filaments after heat treatments as high as 1050° C for 15 hours; but other effects were noted.

Figures 42 and 43 show the structure of some Texaco-3 filaments after a 1050° C-15 hr heat treatment. The filaments were polished on 1μ diamond paste. The filaments are slightly smaller than their original diameter and there are several holes in the boron sheath and at the core-sheath interface. The holes are about 18μ in diameter, are covered inside with a shiny, granular texture, and occur most frequently in the vicinity of the second chamber ring. Longitudinal cross sections of the filaments are shown in Fig. 43. Figure 43a is a section near the outer filament surface while Fig. 43b was taken further into the specimen. The proximity of the holes to the region of the second chamber ring is evident in Fig. 43b. In addition to the holes developing in the heat treated filament, the hardness or abrasion resistance was increased considerably and and sample preparation techniques had to be altered somewhat to cope with the increased hardness. Several days of automatic diamond polishing were required.

Data from two Debye-Scherrer patterns taken from heat treated filaments are given in Table 17. The information is of little use because the borides and boron lines overlap in nearly all cases. The high d-spacing lines of β-boron were not observed, so

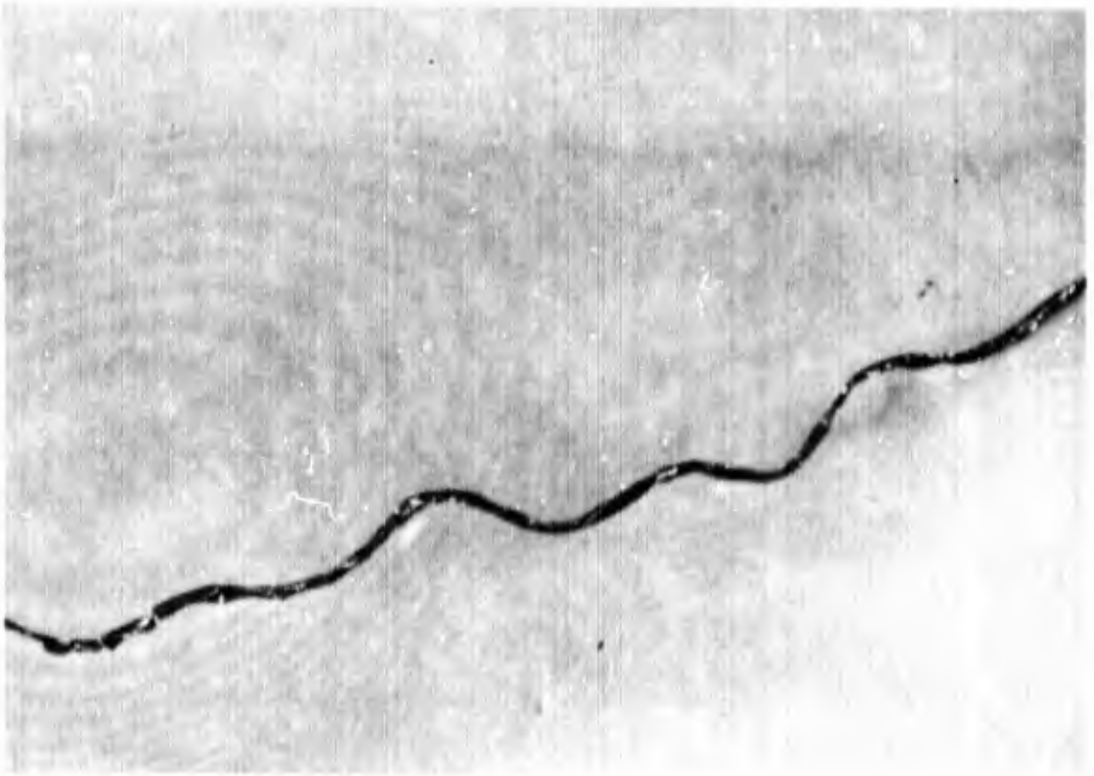

Fig.41a Boron Filament Annealed 990°C for 48 hr. 20×.

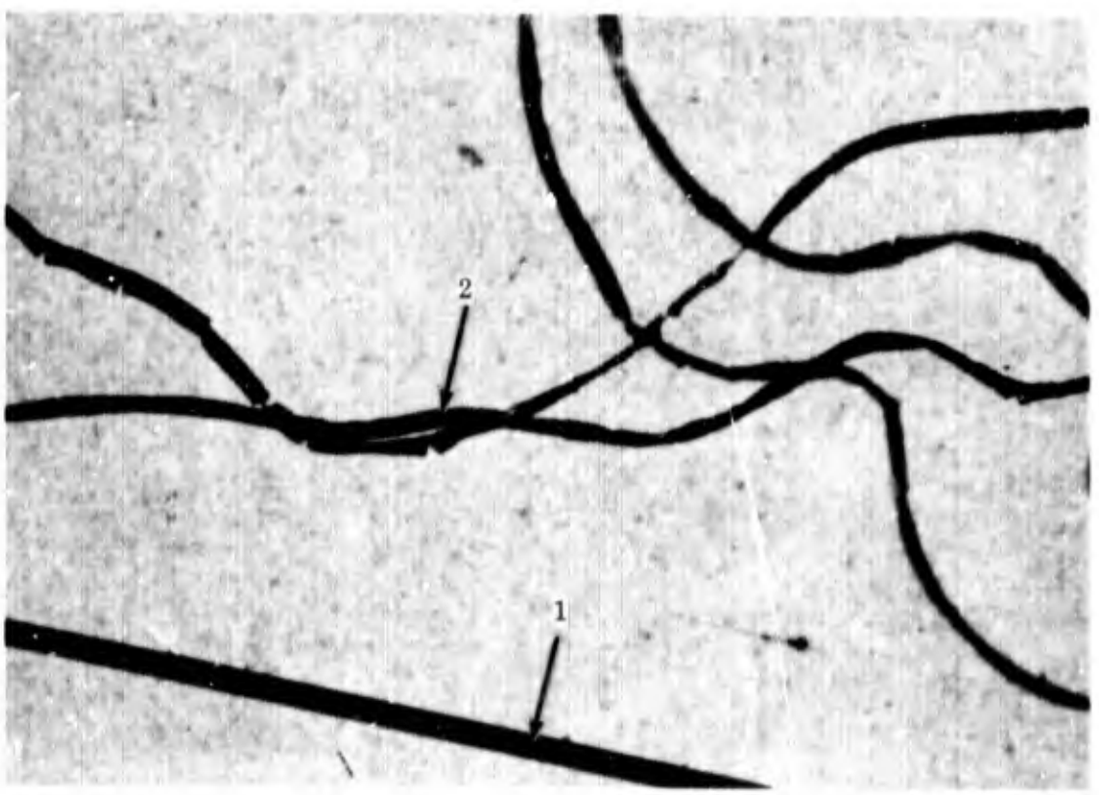

Fig.41b Boron Filament. (1) Annealed 990°C for 48 hr, (2) As-Received. 24×.

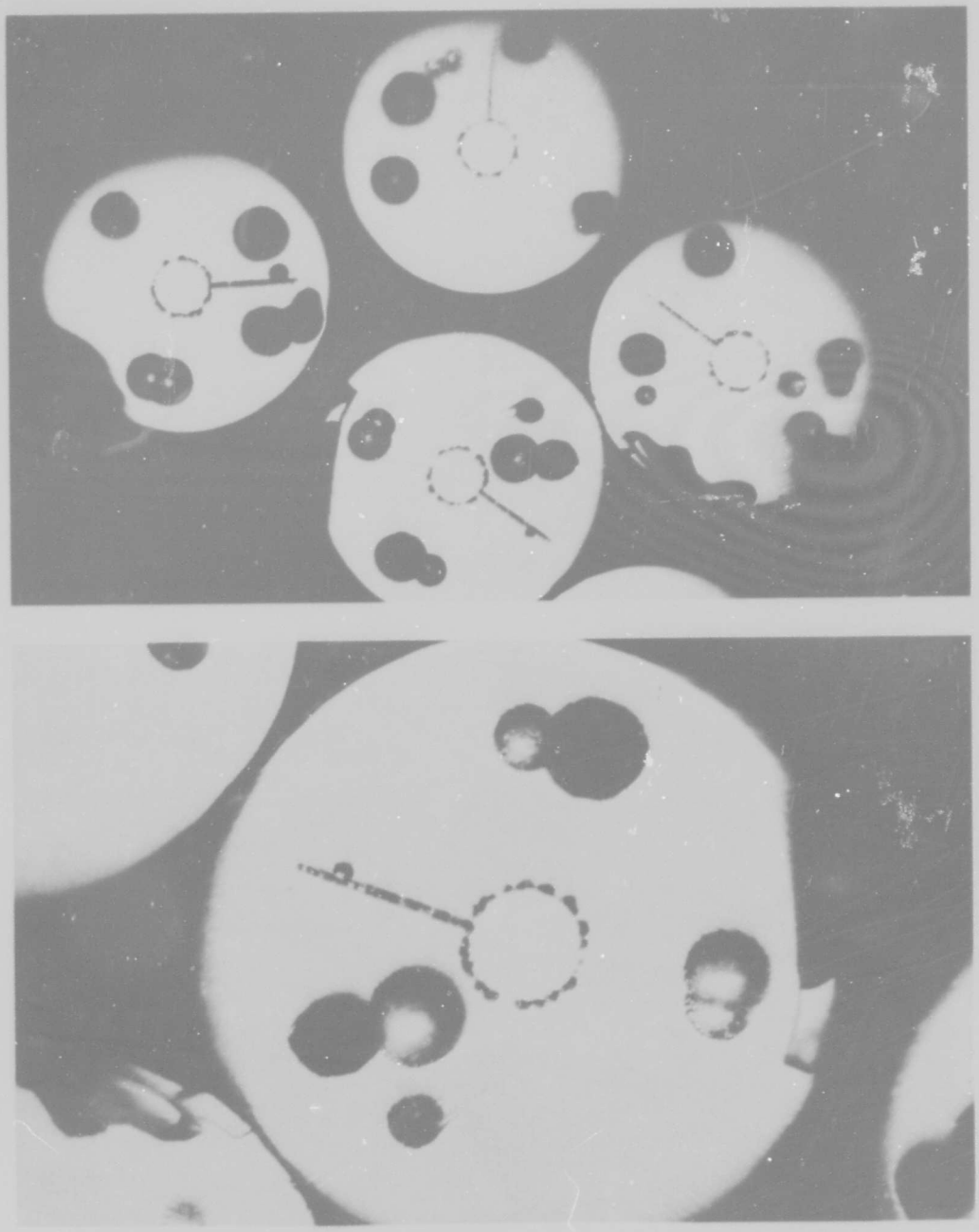

Fig. 42 Transverse Cross Sections of Boron Filaments Heat Treated at 1050°C for 15 hr. (a) P4528, 500×. (b) P4529, 1000×

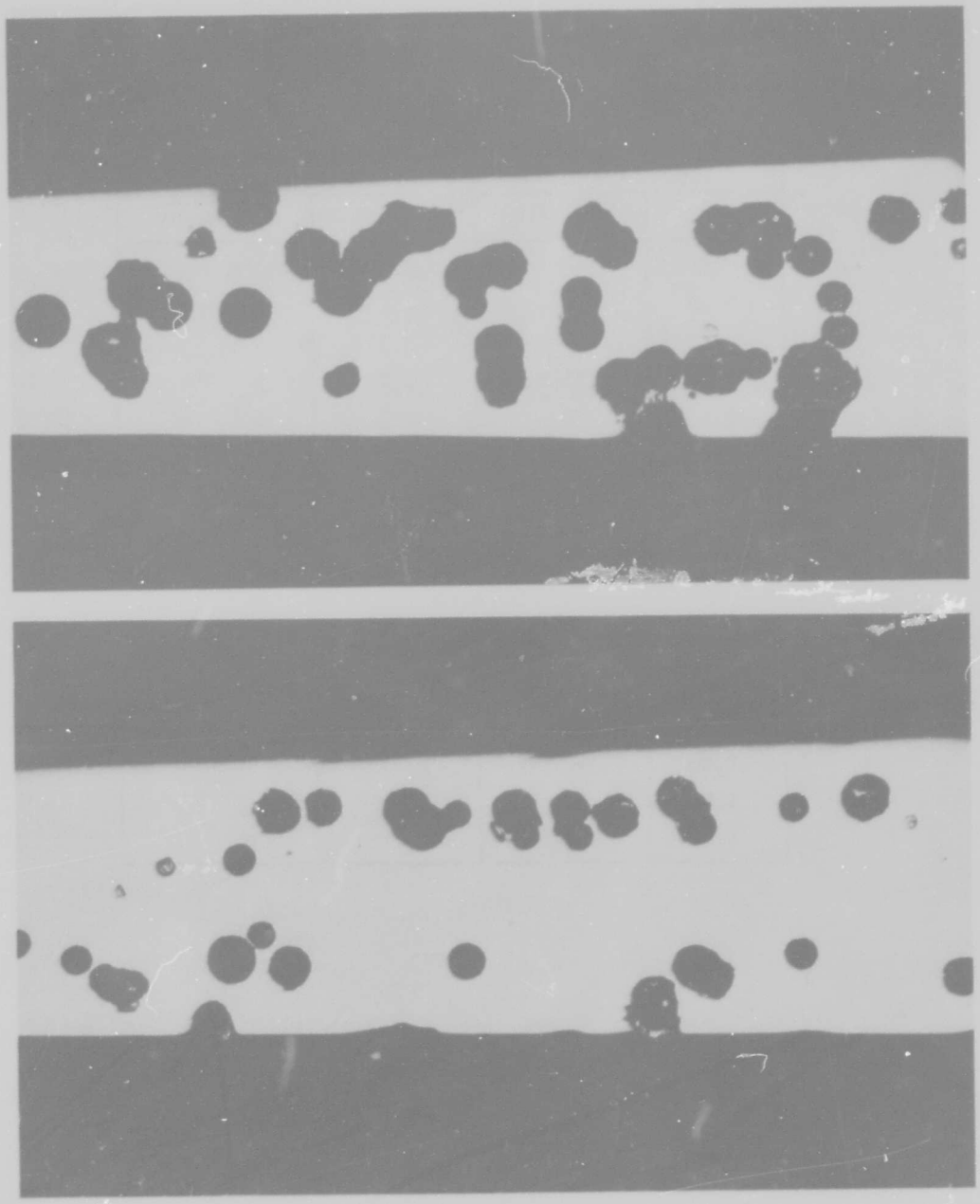

Fig. 43 Longitudinal Sections of Boron Filaments Heat Treated at 1050°C for 15 hr. (a) Near outer surface, P4572, 500×. (b) Further into filament, P4573, 500×

Table 17

DEBYE-SCHERRER PATTERNS OF HEAT-TREATED BORON FILAMENTS

1000° C (24 hr)		980° C (48 hr)	
d(Å)	Intensity	d(Å)	Intensity
4.25	VW	4.20	VW
3.25	M	3.25	M
3.01	W	3.10	VW
2.70	M-Br	2.70	S
2.55	W	2.28	M
2.30	W		
2.25	VW		
2.12	S	2.13	MS
2.08	S	2.05	M
1.90	W	1.93	W
1.73	W	1.73	VW
1.55	W	1.60	VVW
		1.55	M
1.40	W		
1.38	W		
1.34	M		

β-boron is probably not present. The 4.4Å boron halo was always evident, provided that sufficient boron remained on the filament. Diffraction data obtained in the electron microscope is better than x-ray data in this case because of the high degree of sample selectivity in the electron microscope. Electron microscopy of heat treated filaments is discussed in Section 4.4.5.

4.3 X-RAY DIFFRACTION

4.3.1 X-Ray Diffraction – Experimental

Diffraction patterns of boron vapor-deposited between 870 and 1260° C were obtained in Debye-Scherrer cameras, in focusing x-ray diffractometers, and by transmission electron diffraction. The Debye-Scherrer patterns, from whole filaments and filaments ground 30 – 60 minutes in a B_4C mortar and pestle, were obtained with crystal monochromatized and Ni-filtered radiation in both 114.6 and 57.3 mm cameras; the sample for the diffractometer consisted of filaments three layers thick, and the transmission electron diffraction patterns were obtained from thin pieces of boron prepared by grinding or chemical thinning. In all the diffraction geometries and sample preparations, the diffraction patterns of the vapor-deposited boron consisted of broad maxima or halos, whose widths are given by the d-spacing ranges shown in Table 18. Of these halos, the first, second and fifth halos are nearly always seen in the diffraction pattern while the fourth and seventh are frequently seen. The third and sixth halos are very difficult to record and are only rarely observed. Electron and x-ray diffraction relative intensities differ due to differences in the Lorentz factors; the data reported in this section are for x-ray diffraction.

The information in Table 18 is nearly sufficient to indicate the kind of boron present in vapor deposited boron filaments. The β-boron diffraction pattern is very complex with many medium-to-strong lines in the d-spacing range 4.6 – 7.95 Å. (ASTM card 11-618). Because the halos do not extend into this range, it is likely that the amount of β-boron present is rather small. Table 19 lists the major peaks of tetragonal

Table 18

POSITIONS OF HALO MAXIMA IN VAPOR-DEPOSITED BORON

Halo d-Spacing Spread Å	Intensity[b]	Halo Number
4.20 – 4.76	S	1
2.40 – 2.68	M	2
– 2.13 –	VVW	3
1.68 – 1.80	VW	4
1.36 – 1.45	M	5
– 1.1[a] –	VW	6
– 0.94 –	VW	7

[a]Halo observed by Wawner (Ref. 14)

[b]X-ray data

Table 19

MAJOR DIFFRACTION PEAKS FOR TETRAGONAL AND α-RHOMBOHEDRAL BORON

Tetragonal[a]		α-Rhombohedral[b]	
d-Spacing Å	Intensity	d-Spacing Å	Intensity
4.37	100	4.25	45
3.92	75	4.07	100
2.53	25	2.56	70
2.53	10	2.48	10
2.42	75		
2.18	20	2.11	55
1.44	30	1.44	15
1.44	18		
1.38	16	1.36	10
1.38	14	1.35	15
1.37	20	1.26	12
1.32	20		
1.30	14		
1.16	30		

[a]Ref. 20

[b]Ref. 26

(Ref. 20) and α-rhombohedral boron (Ref. 26). Comparing Table 19 with Table 18, there is very little in the broad diffraction maxima of the vapor-deposited boron to distinguish tetragonal from α-rhombohedral boron, but it is evident that the vapor-deposited boron consists of one or the other form. In fact, the final determination of the crystal structure of the as-deposited boron must be inferred from the electron diffraction patterns of vapor-deposited boron filaments which have been beam heated to produce α-boron (see Section 4.4.4). For further discussion of the structure of vapor deposited boron see Section 4.3.2.

The diffraction pattern from a three-filament-thick flat bundle, obtained with Cu Kα radiation at a very slow scanning speed (25 min/deg), is given in Fig. 44 together with some of the α- and β-boron peak positions reported in the ASTM card file and the boron halo patterns as summarized in Table 18. Items to be noted in this figure include:

- The absence of diffracted intensity near 10 deg 2θ where strong β-boron lines would occur
- The discrepancy between the first halo maximum and the position of the most intense β-boron line
- The proximity of halos 1, 2, 3, 5, and 7 to the peak positions of α-boron
- The variation of intensity with increasing angle which corresponds with the data given in Table 18.

Halos 3, 4, and 6 are not evident in this scan and they are very very weak when recorded on x-ray films. As demonstrated in this and the next section, the data given in Fig. 44 are consistent with a model of very small crystallite size tetragonal or α-rhombohedral boron.

To test the distorted β-boron hypothesis (see Section 4.1.2) and to obtain the most reliable data, the diffraction patterns of ground β-boron and whole filaments were

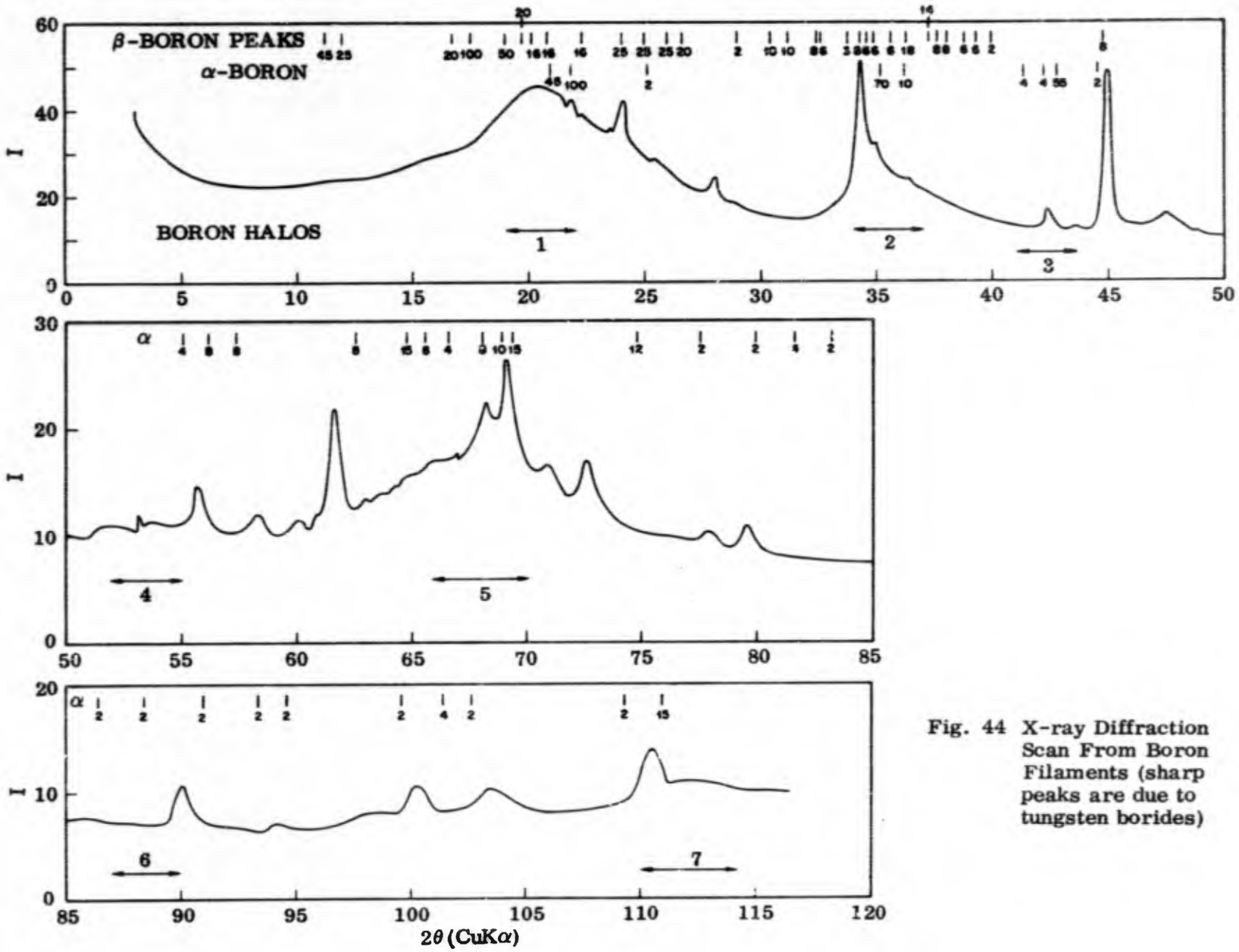

Fig. 44 X-ray Diffraction Scan From Boron Filaments (sharp peaks are due to tungsten borides)

accurately determined in the vicinity of the first boron halo by point counting. To insure maximum resolution of the profiles, chromium radiation was used to determine the pattern. Figure 45 contains the uncorrected boron halo data as well as the halo corrected for background. Also shown are the reported peak positions of α- and tetragonal boron, and the peak positions and observed relative intensities from ground β-boron. The β-boron peaks were 0.1 – 0.2 deg 2θ wide. As may be seen, it would be difficult to conceive of a distortion of the β-boron structure that would result in the first boron halo. However, only a moderate distortion of the two peaks of α-boron or tetragonal boron could produce the observed halo. If the tungsten boride peaks are substracted from the halo, as shown in Fig. 45, then the halo seems asymmetric, with a tail extending away to higher values of 2θ. The shape of this curve is similar to the "hk bands" observed in poorly graphitized carbon and suggests a two-dimensional structure.

The first boron halo can be decomposed into two peaks; a symmetric peak near the (00·3) peak of α-boron and an asymmetric peak near the (10·1). The pairs of curves numbered I, II, III represent different attempts to decompose the halo. Case III gives consistent results for the particle size parameters shown in Fig. 45, as calculated from the theory of diffraction from two-dimensional crystals (Ref. 38, p. 516). In this theory, hk profiles are broadened asymmetrically with a long tail toward high 2θ, and the peak is shifted toward high 2θ values; a crystallite diameter (L_a) can be computed from the line broadening and the peak shift. In addition the (00ℓ) peaks are broadened symmetrically and shifted to lower 2θ values, and a crystallite thickness (L_c) can be computed from the line broadening. Although this interpretation is internally consistent, it is by no means proven. The (200) and (111) peaks of tetragonal boron can be resolved from the halo in the same fashion, and the relative intensities are closer to the reported values than in the case of α-boron. Crystallite sizes computed from the curves in Case II of Fig. 45 – assuming them to be (200) and (111) of tetragonal boron – are presented in Fig. 45. Both curves give a 30 Å crystallite size, which agrees with the data presented in Section 4.4 on electron microscopy. No

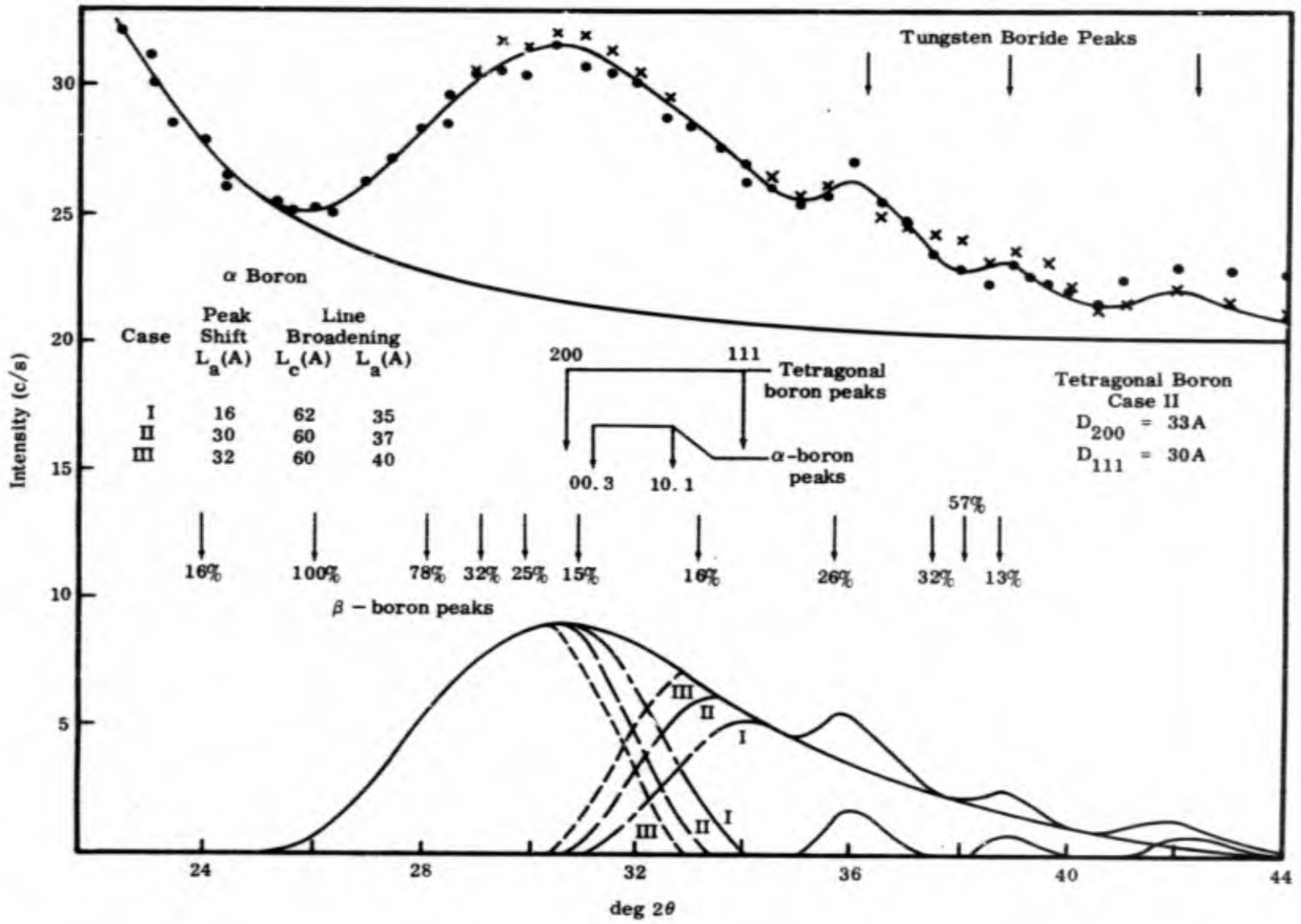

Fig. 45 First Boron Halo, Point Counted in Diffractometer, CrKα Radiation

evidence of a two-dimensional structure has been given, and the crystal structures of the various forms of boron do not strongly suggest a layer structure as do those of carbon and some forms of boron nitride. Thus the x-ray diffraction evidence from vapor-deposited boron found in boron filaments is consistent with a mixture of small crystallite size α-rhombohedral and tetragonal boron. This hypothesis for the structure of boron filaments is discussed further in Section 4.3.2.

The diffraction pattern of Callery boron described in Section 3.4 consists of a very broad halo between 2.4 and 4.4 Å and another halo between 1.35 and 1.45 Å. The first broad maximum corresponds to a merging of the first and second halos listed in Table 18, while the other maximum correspond to the fifth halo listed in that table. Thus, gas pyrolyzed boron powder apparently has the same or similar structure as boron deposited on a hot filament, but it has a smaller crystallite size and may have a higher percentage of misplaced atoms. To account for the line broadening, the crystallite size must approach the unit cell size of α-boron. Crystallite sizes of about 10 Å are consistent with some observations in vapor-deposited boron described Section 4.4.2.

4.3.2 X-Ray Diffraction – Theoretical

The basic structural unit of elemental boron and of many boron compounds is the B_{12} group, which consists of boron atoms located at the vertices of a nearly regular icoshedron. In α-rhombohedral boron, one such icosahedron is located at each lattice point, which gives 12 atoms in the rhombohedral unit cell. The more complex β-rhombohedral form, with 105 atoms in the unit cell, consists of a rhombohedral arrangement of B_{84} groups. In addition, two B_{10} groups and a single boron atom are located along the main diagonal of the rhombohedron (Ref. 27). A B_{84} group is composed of a central B_{12} icosahedron, with 12 half-icosahedra positioned radially on the extended lines through the vertices of the central icosahedron. These half-icosahedra bond to corresponding half-icosahedra from neighboring B_{84} groups along the rhombohedral axes to form complete B_{12} groups.

The "simple" tetragonal polymorph of boron is a face-centered tetragonal arrangement of B_{12} groups, with two single boron atoms per unit cell which occupy tetrahedral interstices (Ref. 39).

In all three of these boron structures, the B_{12} icosahedra have definite orientations with respect to each other in the ideal case. The structure factor for a given "ideal" boron structure is written as

$$F = f(B) \sum_n e^{2\pi i(hu_n + kv_n + \ell w_n)} \tag{5}$$

where the sum is taken over the individual boron atoms in the unit cell. This computation has been carried out for the α-rhombohedral form by Decker and Kasper (Ref. 26) and for the "simple" tetragonal form by Hoard et al. (Ref. 39).

There is another approach to the structure factor calculation for boron structures which is useful in the discussion of vapor-deposited boron. It seems reasonable that the random nature of the deposition process might result in an imperfect or "non-ideal" arrangement of icosahedra, in which the B_{12} groups within a given crystallite are oriented randomly with respect to one another, with slight distortions of the inter-icosahedron bonds. If a large number of randomly oriented structural groups are distributed on a lattice, then a simple statistical argument shows that the average diffracted intensity from this structure is the same as if each lattice point had associated with it a structural group averaged over all possible orientations. The intensity $I(\Omega)$ for a <u>particular</u> random arrangement Ω of structural groups on N lattice sites is given by

$$I(\Omega) = \frac{1}{R^2} \sum_m^N \sum_n^N F_m F_n^* e^{\frac{2\pi i}{\lambda}(\vec{s}-\vec{s}_o)\cdot(\vec{R}_m - \vec{R}_n)} \tag{6}$$

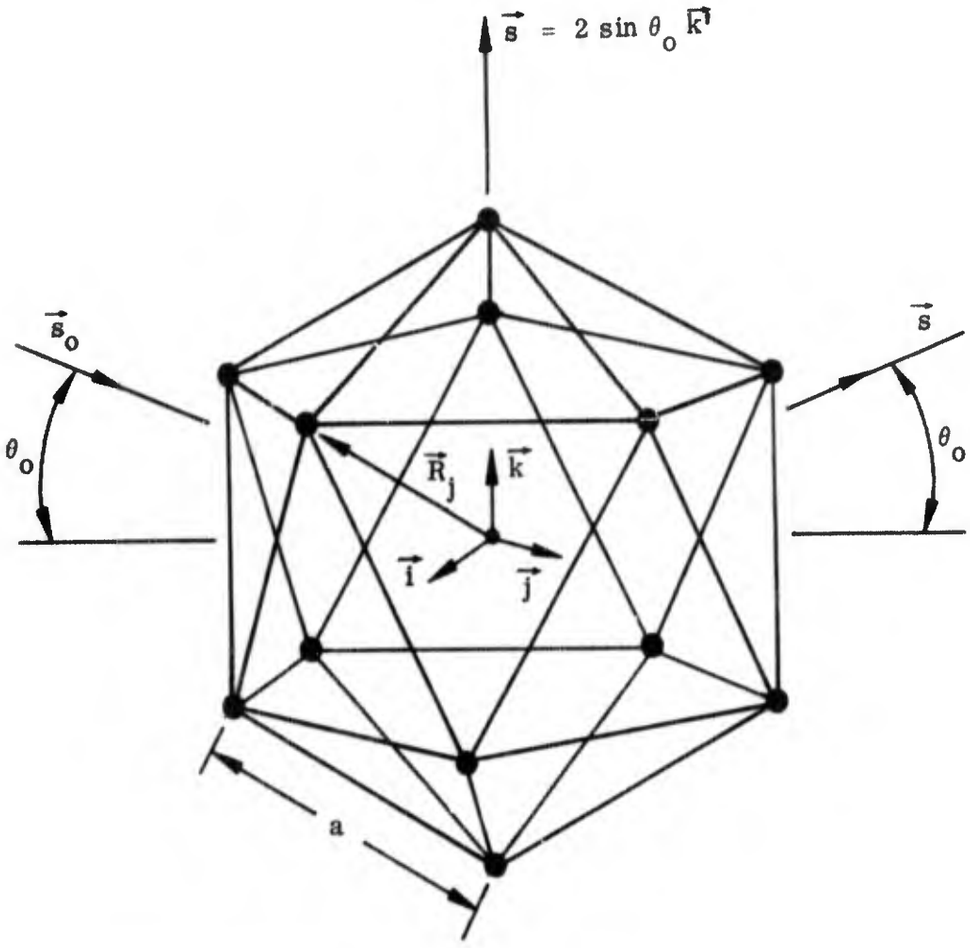

Fig. 46 Geometrical Configuration Used for Calculation of Structure Amplitude of Icosahedron of Boron Atoms

and the intensity averaged over all the possible arrangements Ω is

$$\langle I \rangle = \int_1 \cdots \int_N I(\Omega)\, P(\Omega)\, d\omega_1 \cdots d\omega_N \tag{7}$$

In Eq. (6), F_m and F_n denote the structure amplitudes for the particular orientations of the structural groups located at lattice sites m and n, respectively, and the other symbols have their usual meaning (see, for example, Ref. 40). In Eq. (7), $P(\Omega)$ is the joint probability for the particular configuration Ω, and the integrations are performed over all lattice sites. The end result is that $\langle I \rangle$ can be expressed as

$$\langle I \rangle = \frac{1}{R^2} \langle F \rangle^2 \sum_m \sum_n e^{\frac{2\pi i}{\lambda}(\vec{s}-\vec{s}_0)\cdot(\vec{R}_m-\vec{R}_n)} \tag{8}$$

where

$$\langle F \rangle = \int_m F_m\, P(m)\, d\omega_m \tag{9}$$

and $P(m)$ is the probability of a given orientation on one lattice site.

To obtain $\langle F \rangle$, the "orientation-averaged" structure amplitude, it is necessary to write a general expression for the structure amplitude of the structural group in an arbitrary orientation, and then to average this expression over all orientations. The derivation of $\langle F \rangle$ for the case of a regular icosahedron of boron atoms (Fig. 46) was performed as indicated in the following summary (see, also, Appendix IV):

(1) The regular icosahedron, of edge-length a, is described by a set of 12 vectors $\{\vec{R}_j\}$ from the geometric center to the 12 vertices. The vectors $\{\vec{R}_j\}$ are written in terms of Cartesian basis vectors $\vec{i}$, $\vec{j}$, $\vec{k}$.

(2) A new Cartesian basis $\vec{i}'$, $\vec{j}'$, $\vec{k}'$ is introduced, having the same origin but oriented arbitrarily with respect to the basis vectors $\vec{i}$, $\vec{j}$, $\vec{k}$.

(3) The set of vectors $\{\vec{R}_j\}$ is expressed in terms of the "primed" system, i.e.,

$$\vec{R}'_j = \vec{T}\ \vec{R}_j$$

where $\vec{T}$ is the 3×3 matrix of direction cosines which relates $\vec{i}'$, $\vec{j}'$, $\vec{k}'$ to $\vec{i}$, $\vec{j}$, $\vec{k}$, and has the property $\vec{T}^T = \vec{T}^{-1}$

(4) The set of vectors $\{\vec{R}'_j\} = \{\vec{T}\ \vec{R}_j\}$ describes an arbitrary orientation of the icosahedron with respect to the basis vectors $\vec{i}'$, $\vec{j}'$, $\vec{k}'$.

(5) The diffraction vector is chosen as

$$\vec{s} - \vec{s}_o = 2 \sin \theta_o \vec{k}'$$

This means that the icosahedron is oriented arbitrarily with respect to the plane formed by the directions of propagation of incident and scattered radiation.

(6) The structure amplitude is given by

$$F'(\text{icos.}) = \sum_{j=1}^{12} f(j) \exp\left[\frac{2\pi i}{\lambda} (\vec{s} - \vec{s}_o) \cdot \vec{R}'_j\right] \qquad (10)$$

(7) The final result is

$$F'(\text{icos.}) = 2f(B)\left[\cos(\chi A\cos\gamma_z) + \cos\left\{\chi\left(\frac{\cos\alpha_z}{2\sin 36} + B\cos\gamma_z\right)\right\}\right.$$
$$+ \cos\left\{\chi\left(\frac{1}{2}\cot 36\cos\alpha_z - \frac{1}{2}\cos\beta_z - B\cos\gamma_z\right)\right\}$$
$$+ \cos\left\{\chi\left(\frac{\cos 72}{2\sin 36}\cos\alpha_z - \frac{\sin 72}{2\sin 36}\cos\beta_z + B\cos\gamma_z\right)\right\}$$
$$+ \cos\left\{\chi\left(\frac{\cos 72}{2\sin 36}\cos\alpha_z + \frac{\sin 72}{2\sin 36}\cos\beta_z + B\cos\gamma_z\right)\right\}$$
$$\left. + \cos\left\{\chi\left(\frac{1}{2}\cot 36\cos\alpha_z + \frac{1}{2}\cos\beta_z - B\cos\gamma_z\right)\right\}\right] \qquad (11)$$

where

$$\chi = \frac{4\pi a\sin\theta_o}{\lambda}$$

$$A = \frac{1}{2\sqrt{2}}\left[1 - \cot^2 36 + \cot 36\,(1 + \cot^2 36)^{1/2}\right]^{1/2} + \frac{1}{2}(3 - \cot^2 36)^{1/2}$$

$$= 0.9510$$

$$B = \frac{1}{2\sqrt{2}}\left[1 - \cot^2 36 + \cot 36\,(1 + \cot^2 36)^{1/2}\right]^{1/2}$$

$$= 0.4253$$

and α_z, β_z, and γ_z are the angles between $\vec{k}'$ and $\vec{i}$, $\vec{j}$, and $\vec{k}$, respectively, and f(B) is the atomic scattering factor of boron for x-rays.

If we consider the particular orientation $\alpha_z = \beta_z = \pi/2$, $\gamma_z = 0$, as illustrated in Fig. 46, the above expression simplifies to

$$F'(\text{icos.}) = 2f(B)[\cos \chi A + 5 \cos \chi B] \tag{12}$$

This function is plotted vs. $(\sin \theta_o/\lambda)$ in Fig. 47, using a = 1.76 Å (Ref. 26).

Note that Eq. (11) gives F_m in Eq. (9). The task now is to perform the averaging. At this point it is convenient to make a change of variables from the direction cosines $\cos \alpha_z$, $\cos \beta_z$, and $\cos \gamma_z$ as given in Eq. (11) to Euler angles (θ , ψ) (Ref. 41). The transformation is given by

$$\left.\begin{aligned} \cos \alpha_z &= \sin \theta \sin \psi \\ \cos \beta_z &= \sin \theta \cos \psi \\ \cos \gamma_z &= \cos \theta \end{aligned}\right\} \tag{13}$$

With this substitution, the proper expression for the structure amplitude $\langle F \rangle$ of a "smeared-out" icosahedron becomes

$$\langle F \rangle = \frac{1}{4\pi} \int_{\theta=0}^{\pi} \int_{\psi=0}^{2\pi} F(\theta , \psi) \sin \theta \, d\psi \, d\theta \tag{14}$$

where $F(\theta , \psi)$ is F'(icos.) of Eq. (11), written in terms of Euler angles. When the integration is performed, the final result is

$$\langle F \rangle = 12 f(B) \frac{\sin Z}{Z} \tag{15}$$

where

$$Z = \frac{4\pi r \sin \theta_o}{\lambda}$$

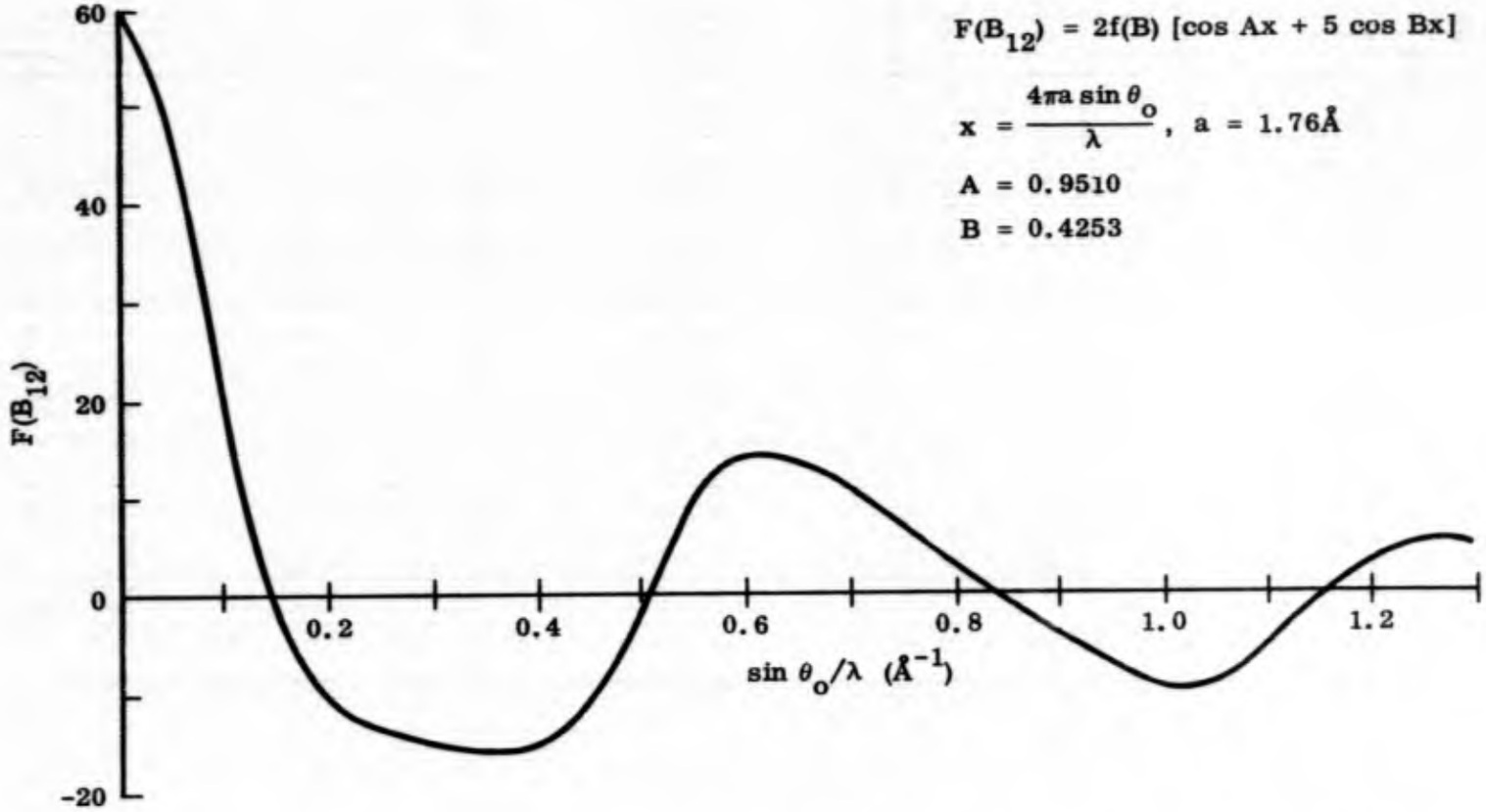

Fig. 47 Structure Amplitude of B_{12} Icosahedron, for Particular Orientation Shown in Fig. 46

f(B) is the atomic scattering factor for boron, r is the radius of the icosahedron (distance from the center to a vertex), and θ_o is the Bragg angle. It may be noted that the result in Eq. (15) is derivable very simply by considering a spherical shell of diffracting material of radius r and scattering power 12 $f(B)/4\pi r^2$ per unit area. This, in fact, is all that the averaging process means.

Equation (15) is plotted in Fig. 48, using the atomic scattering factor of boron for x-rays. (The result for electron scattering is similar, except that f(B) falls off more rapidly with increasing $\sin\theta_o/\lambda$.) Also shown in Fig. 48 are the positions of all the halo maxima observed in electron and x-ray diffraction studies of boron filaments.

Using the function $\langle F \rangle$ in Eq. (15), the structure factors for the various boron structures can now be written in a manner in which the B_{12} groups are treated as large individual "atoms". The results for α-rhombohedral boron and the "simple" tetragonal form of boron are given below.

<u>α-rhombohedral boron</u>. The α-rhombohedral unit cell consists of one B_{12} group at each lattice point. Thus, the only "atomic" coordinate in the unit cell is (000), and therefore,

$$F(\alpha) = \langle F \rangle \tag{16}$$

<u>Tetragonal boron</u>. The unit cell of "simple" tetragonal boron (Ref. 39) contains:

Single boron atoms at $\left(0\,0\,\frac{1}{2}\right)$, $\left(\frac{1}{2}\,\frac{1}{2}\,0\right)$

B_{12} groups at $\left(\frac{1}{4}\,\frac{1}{4}\,\frac{1}{4}\right)$, $\left(\frac{3}{4}\,\frac{3}{4}\,\frac{1}{4}\right)$, $\left(\frac{3}{4}\,\frac{1}{4}\,\frac{3}{4}\right)$, $\left(\frac{1}{4}\,\frac{3}{4}\,\frac{3}{4}\right)$

The structure factor is, therefore,

$$F(T) = f(B)\left[e^{\pi i \ell} + e^{\pi i(h+k)}\right] + \langle F \rangle \left[e^{\frac{\pi i}{2}(h+k+\ell)} + e^{\frac{\pi i}{2}(3h+3k+\ell)} + e^{\frac{\pi i}{2}(3h+k+3\ell)} + e^{\frac{\pi i}{2}(h+3k+3\ell)}\right] \tag{17}$$

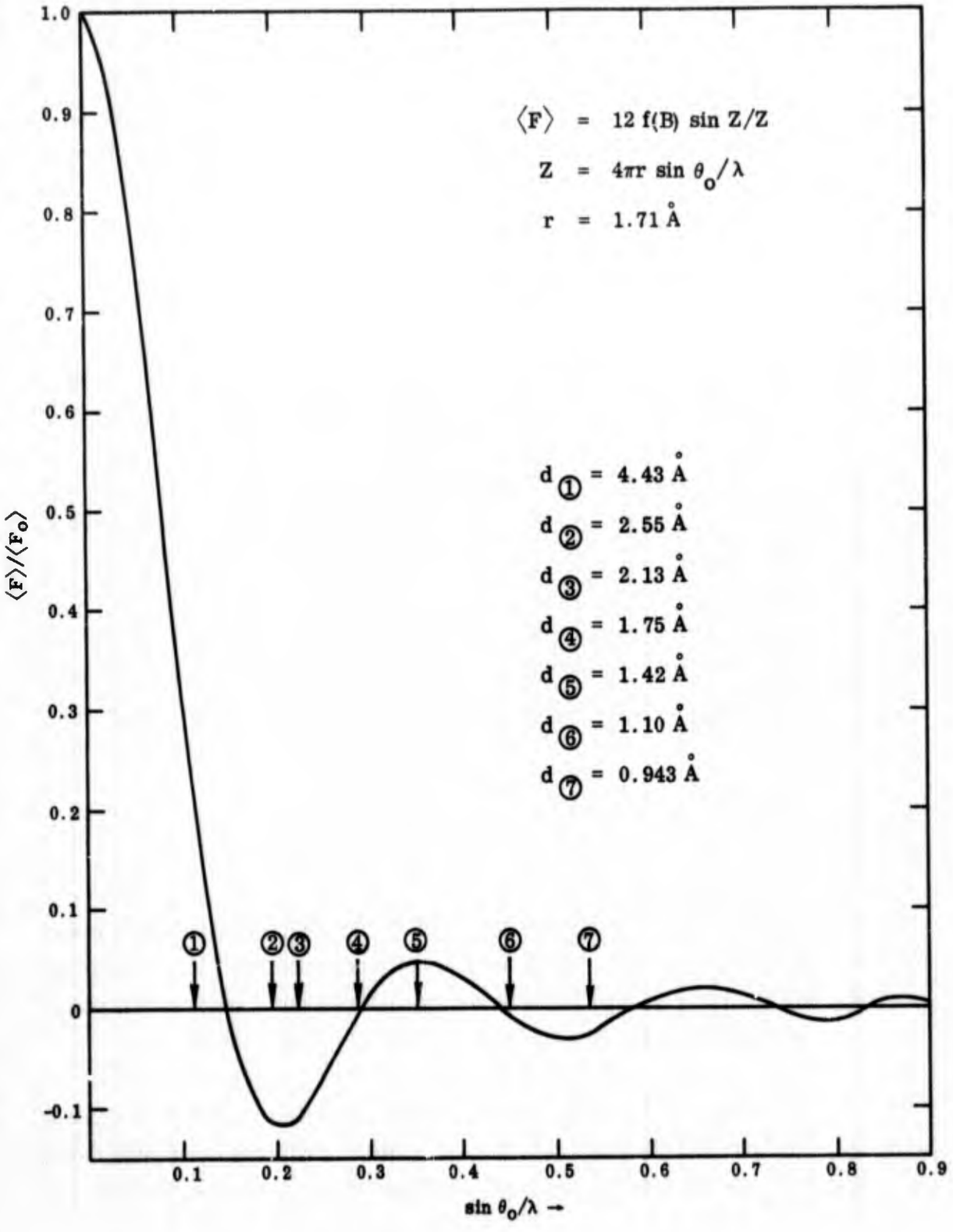

Fig. 48 Normalized, Averaged B_{12} Structure Amplitude, Showing Positions of Halo Maxima

Figure 49 shows the relative integrated intensities of reflections of α-rhombohedral boron, calculated using Eq. (16), plotted against 2θ (Cu Kα). The boundaries of halos 1, 2, 4, and 5 are indicated. These boundaries were obtained from an electron diffraction pattern, and the measured d-spacings were converted to 2θ (CuKα). The third halo was so weak that the boundaries could not be measured accurately on the electron diffraction pattern, and thus only the mean position is indicated. The intensities were calculated as $\langle F \rangle^2 p$, where p is the multiplicity. The Lorentz-polarization factor was not included, so that the intensity distribution shown is essentially that which would be observed on an electron diffraction pattern, in which the Bragg angle, and therefore the L-P factor, is approximately constant. The rapid decrease of the Lorentz-polarization factor with increasing 2θ is the reason why only the strongest halos, 1, 2, and 5 are usually observed on x-ray films (see Table 22, Section 4.4.1) while the weaker halos are more easily recorded in the electron diffraction case. Note that Fig. 49 is for α-boron with randomly oriented icosahedra.

Figure 50 shows the relative integrated intensities of α-boron reflections, for the case of ideally oriented icosahedra. The values shown were obtained from the intensities given in ASTM card 12-377, dividing through by the Lorentz-polarization factor and re-normalizing. The ASTM data are well-founded on single crystal diffraction studies.

Figure 51 shows the calculated intensities for tetragonal boron using $I = \{F(T)\}^2 p$ and F(T) in Eq. (17). This figure is also for randomly oriented icosahedra.

Figure 52 gives the relative integrated intensities for tetragonal boron, for the case of ideally oriented icosahedra. The values were obtained from ASTM card 12-469 by dividing each listed intensity by the Lorentz-polarization factor and re-normalizing. Again, these ASTM data are based on single crystal diffraction studies.

A study of Figs. 49, 50, 51, and 52, together with certain other observations made in connection with the halo diffraction pattern, gives some insight into the probable structure responsible for the halos. Referring to Section 4.3.1, Fig. 45, the first halo

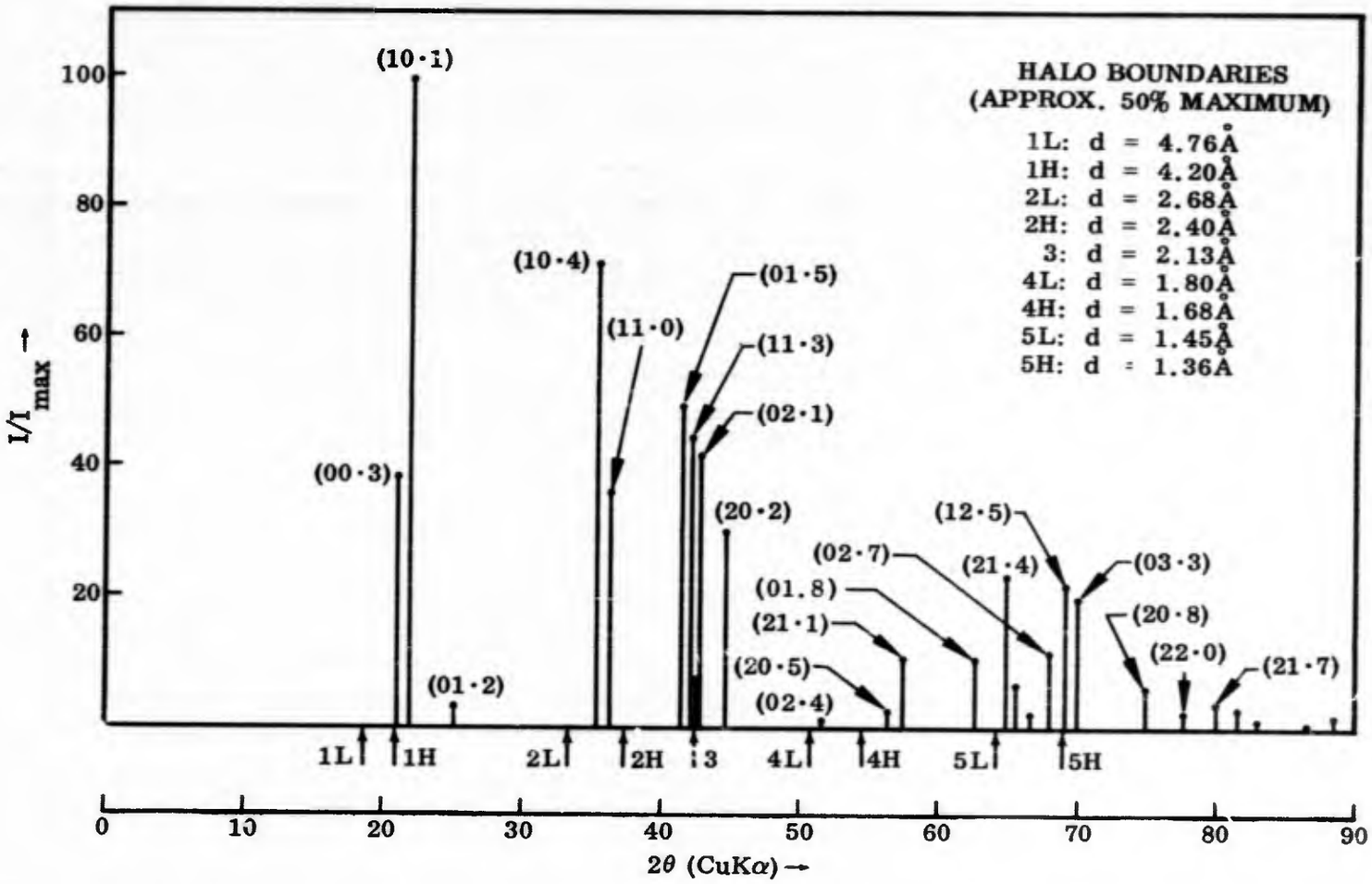

Fig. 49 Relative Integrated Intensities of α-Boron Reflections, Calculated from $\langle F \rangle^2_p$ Versus 2θ(CuKα)

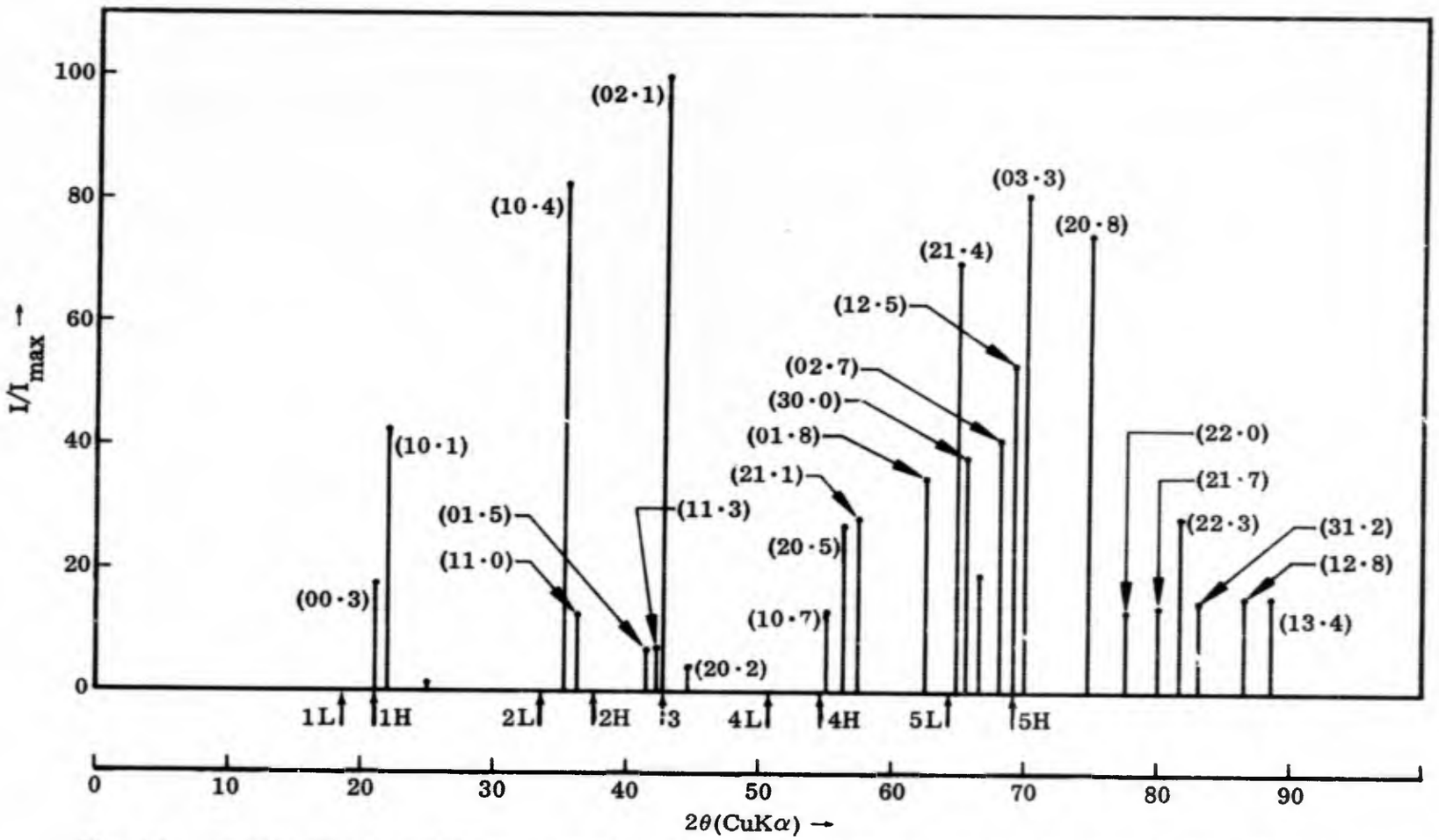

Fig. 50 Relative Integrated Intensities of α-Boron Reflections, From ASTM Card 12-377, With Lorentz-Polarization Factor Divided Out

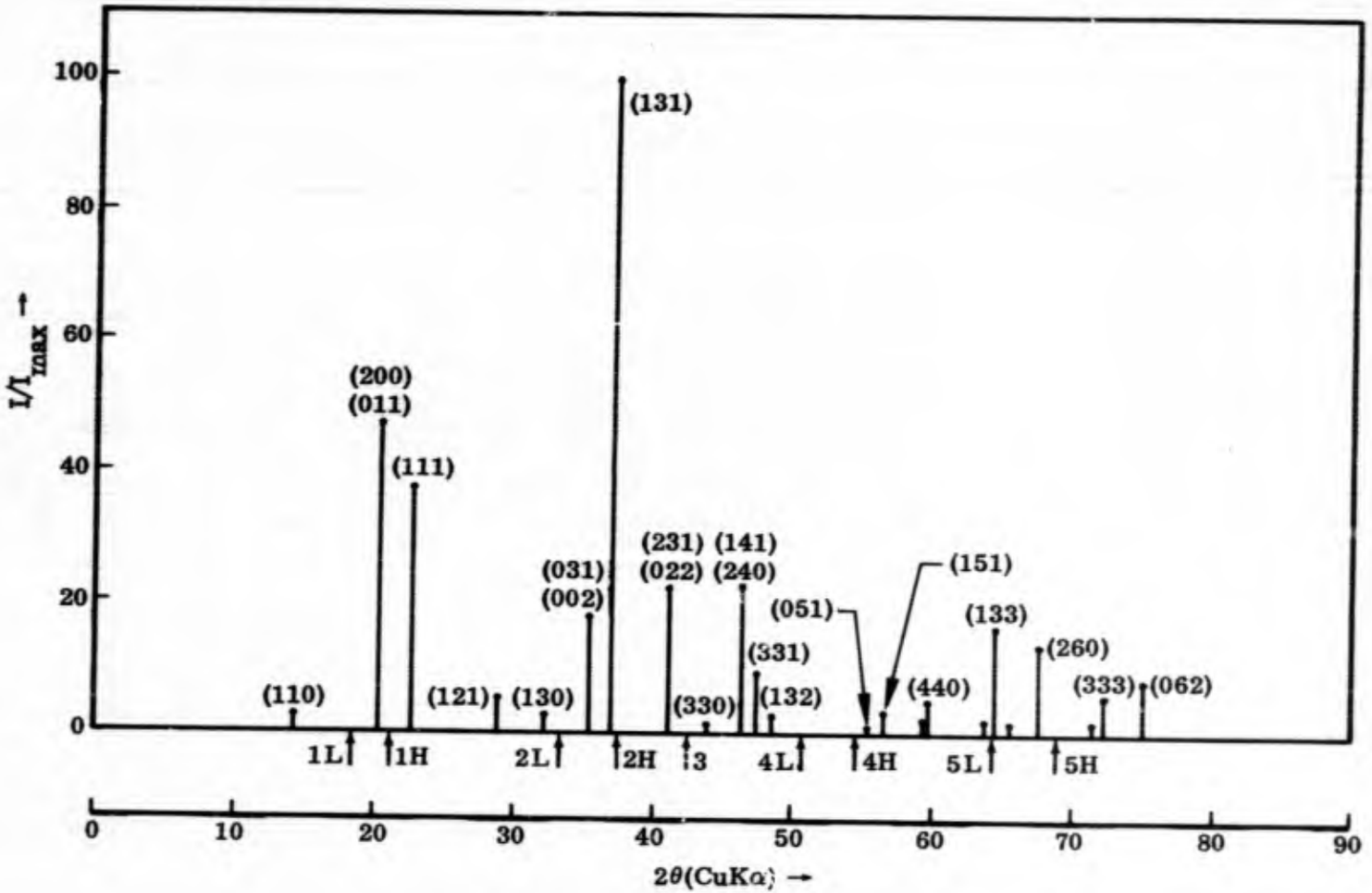

Fig. 51 Relative Integrated Intensities of Tetragonal Boron Reflections, Calculated Using $\langle F \rangle$ Versus $2\theta(CuK\alpha)$

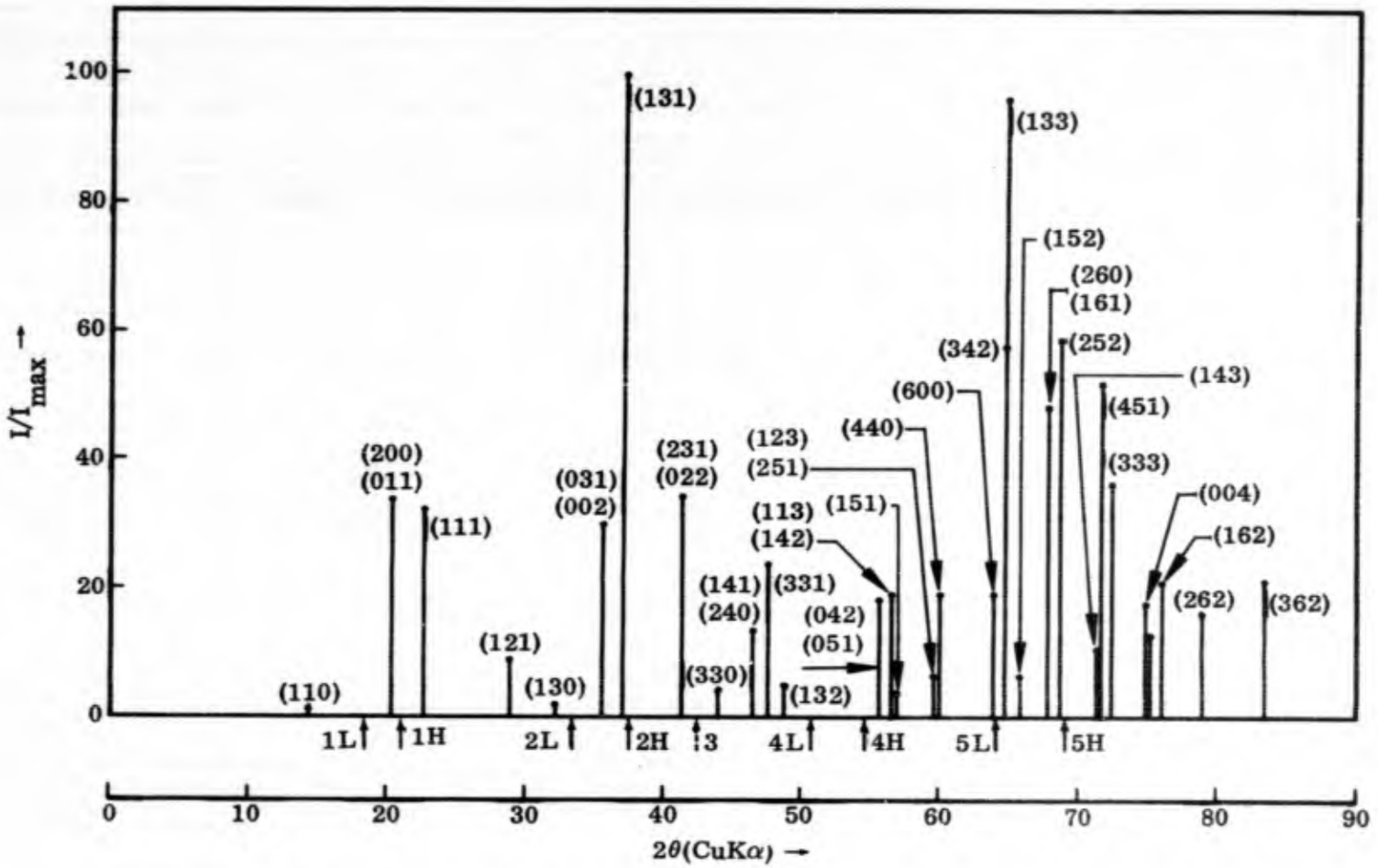

Fig. 52 Relative Integrated Intensities of Tetragonal Boron Reflections, From ASTM Card 12-469, With Lorentz-Polarization Factor Divided Out

profile can be decomposed into two peaks, one corresponding to about 4.35 Å and the other to 3.97 Å. The 3.97 Å peak is of approximately half the intensity of the 4.35 Å peak and these values are in excellent agreement with the data for tetragonal boron – (ASTM card 12-469) d(200) = 4.37 Å, I = 100; d(111) = 3.92 Å, I = 75. The α-boron (00·3) and (10·1) reflections are close, except for the intensity reversal (Figs. 49 and 50). The second halo, d = 2.68 – 2.40 Å, can be interpreted equally well in terms of α:(10·4) + (11·0) or tetragonal: (002) + (131). The third halo, in the vicinity of 2.13 Å, is not so easily explained. This halo is extremely weak as recorded in electron diffraction studies of as-deposited filaments, and has not been observed by x-rays because of the Lorentz-polarization factor and the presence of tungsten boride lines. From Figs. 49 – 52, it is seen that the (11·3) and (02·1) reflections of α-rhombohedral boron are very close to 2.13 Å, whereas the nearest reflections of tetragonal boron are somewhat further away. On the basis of the α-boron structure factor, which is just $\langle F \rangle$ for the random-icosahedron case, one would expect this halo to be about as intense as the second halo (refer to Fig. 48, noting that the intensity goes as $\langle F \rangle^2$). The 2.13 Å halo has been observed to increase in intensity after a 15 hour heat treatment at 1050° C, as discussed in Section 4.4.5. The fourth halo, d = 1.80 – 1.68 Å, is generally observed to be of weak to medium intensity in electron diffraction patterns. No tetragonal boron lines are found in this range, but the α-boron (220) = (02·4) occurs at d = 1.77 Å. This line is so weak, however, that it does not appear on ASTM card 12-377 for α-boron with ideally oriented icosahedra. The intensity is only very slightly increased in the random icosahedron treatment (Fig. 49). The fifth halo, d = 1.45 – 1.36 Å, occurs in the vicinity of five α-boron reflections (Fig. 50) and six tetragonal boron reflections (Fig. 52). In either case, a strong halo could be constructed, as observed. The 1.1 Å halo reported by Wawner (Ref. 14) would appear to agree better with tetragonal boron because its (362) reflection, d = 1.16 Å, is fairly strong (see ASTM card 12-469, and Fig. 52). The α (12·8) is also a possibility (see Fig. 50). The halo at 0.94 Å, observed by Wawner (Ref. 14) and also in this investigation, agrees well with the α-boron ($41\bar{1}$, 542) (ASTM card 12-377), which is the only strong line in this vicinity.

Comparing the ideal-orientation and random-orientation cases for the two boron structures, Figs. 49, 50, 51, and 52, it is seen that the calculated intensities using the random-orientation structure amplitude decrease more rapidly with increasing 2θ than those for the ideal orientation. In some cases, the relative intensities of adjacent reflections are reversed, as in the case of the α (11·3) and (02·1) reflections in Figs. 49 and 50. Also, calculations using the randomized structure amplitude occasionally result in the complete cancellation of reflections which are present in the ideal-orientation case. For example, the (362) reflection of tetragonal boron is quite prominent, as seen from ASTM card 12-469. However, when these indices are substituted into Eq. (17), the result is identically zero. Although the physical reality of the random-orientation model for structures involving the B_{12} groups has not been established, the model appears reasonable in view of the nature of the vapor deposition process. Intensities calculated from the random model usually agree sufficiently well with those obtained from the rigorous, ideal-orientation expression, so the random-orientation method is useful for quick computation in the case of complex structures.

Table 20 below summarizes the analysis of the halo diffraction pattern as discussed in this section.

Table 20

d-SPACINGS OF HALO MAXIMA AND PROBABLE IDENTIFICATION

Halo	d, A	I	Probable Identification
1	4.43	S	Tet. (200)+(111) or α (00·3)+(10·1)
2	2.55	S	α (10·4)+(11·0) or Tet. (002)+(131)
3	2.13	VW	α (02·1) or (11·3)
4	1.74	M	α (02·4)
5	1.42	S	α (21·4)+(30·0)+(00·9)+(02·7)+(12·5) or Tet. (133)+(342)+(152)+(260)+(161)+(252)
6	1.1	VW	Tet. (362) or α (01·11, 13·4)
7	0.94	VW	α (32·4, 12·11)

If halos 3 and 4 are α-boron reflections, as indicated in the table, then an explanation for the intensity reversal must be found. From Fig. 49, the (02·1) and (11·3) reflections are much stronger than the (02·4), and the same holds true in Fig. 50 for the ideal orientation of B_{12} groups. An intensity reversal of this sort must be due to a defect structure, if in fact the choice of ideal structure is the correct one in the first place. For α-rhombohedral boron, such a defect structure might involve interstitial boron atoms or groups of atoms, even though these are not present in the "ideal" α-rhombohedral structure. The structure factor would be modified due to the presence of these interstitials, and the relative intensities of the α-boron lines would be changed.

The only alternative explanation for the halo intensity distribution would be a new structure based on a completely different arrangement of B_{12} icosahedra. The bcc and fcc arrangements of icosahedra proposed by other investigators (Refs. 14 and 31) do not adequately explain the relative halo intensities, however, even though they approximately predict the proper d-spacings. As discussed in Appendix C, the cubic packing arrangements also do not agree with the observed densities.

From the above discussion, it is seen that the choice lies between explaining the observed diffraction data on the basis of defects in the established structures of boron or devising new structures which will explain the observations. The major structural units in boron polymorphs are the B_{12} icosahedra, the B_{10} units in β-boron, and isolated atoms which occur in some of the structures. None of these structural units will behave as single metal atoms having no directionality, so simple packing models, without regard for the established packing arrangements, will be unsatisfactory. The β-rhombohedral structure has been eliminated as an explanation of the halo pattern because of the lack of intensity from 5.0 – 8.0 Å where the strong β-boron lines occur. On the other hand, the halo maxima cannot be adequately explained by a simple mixture of α- and tetragonal-boron because 1) the relative intensities are not correct, as in the case of the α (02·4) compared to the α(02·1) and(11·3), and 2) certain medium-intensity reflections such as the tetragonal (231), (331), (451), and (333) are not observed in the halo pattern (see Figs. 50 and 52). Variations in the relative intensities of diffraction peaks with variations in the degree of order are well known (Ref. 38, p. 380), particularly for layer structures such as partially ordered carbons, and

defects in the α- or tetragonal-boron structure could account for the differences in relative intensity.

The correspondence of the α-boron reflections and the halo positions strongly indicates that the vapor deposited boron examined in this study consists primarily of defective α-boron, but the high intensities of halos 1, 2, and 5 and the easy decomposition of the first halo into the tetragonal (002) and (111) peaks indicates that some tetragonal boron may be present. The variations in relative intensity are likely due to consistently occurring defects in both lattices, and several such defects can be readily conceived. Atoms, atom clusters, or vacancies occurring interstitially between the icosahedra, twinning, imperfect icosahedra consisting possibly of B_{10} groups, and mismatch at crystallite boundaries are some obvious defects which could consistently occur and could affect the relative intensities of the diffraction peaks. The effects of some of these defects can be computed, and suggestions for further studies are made in Section 5.

Structure Factor Calculation for β Rhombohedral Boron. An approximate structure factor for the complex β-rhombohedral form of boron was derived, using the "randomized" structural group approach discussed earlier. The motivation for this calculation was the necessity of explaining the "missing" reflections which arise as a result of the indexing of the $\beta[00\cdot1]$ spot pattern (see Section 4.4.3, Fig. 85). It was noted that many of the reflections which are missing in the electron diffraction pattern (Fig. 85) are also absent from the x-ray powder pattern (ASTM card 11-618). This suggests the possibility of systematic extinctions due to the two B_{10} groups and the single boron atom which lie along the principal diagonal of the rhombohedral cell of β-boron, as described by Hughes et al. (Ref. 27).

Table 21 shows the first eight "missing" β-born reflections, obtained from Fig. 85(d), Section 4.4.3, and indicates which of these are also absent from the x-ray powder pattern.

Table 21

COMPARISON OF "MISSING" β-BORON REFLECTIONS FOR THE ELECTRON AND X-RAY CASES

Reflection Number	(HK·L)	d, Å	Missing, Electron Case	Missing, X-ray Case
1	(10·1)	8.80	Yes	Yes
2	(11·0)	5.47	Yes	No
3	(21·1)	3.54	Yes	No
4	(30·0)	3.16	Yes	Yes
5	(13·1)	2.61	Yes	No
6	(32·1)	2.16	Yes	Yes
7	(14·0)($\bar{1}$5·0)	2.07	Yes	Yes
8	(33·0)	1.82	Yes	No

It should be possible to show from the β-boron crystal structure that the (10·1), (30·0), (32·1) and (14·0) reflections vanish due to destructive interference between waves scattered from the B_{84} groups which reside at the corners of the rhombohedral cell, and those scattered by the B_{10} groups and single boron atom within the cell. Using Hughes' values for the coordinates and dimensions of the B_{84} and B_{10} groups (Ref. 27), the following structure factor for β-boron was derived:

$$F(\beta) = A(B_{84}) + A(B_{10})\, e^{2\pi i[0.385(h+k+\ell)]} + A(B_{10})\, e^{2\pi i[0.615(h+k+\ell)]} + A(B)\, e^{\pi i(h+k+\ell)} \quad (18)$$

where h, k, ℓ are rhombohedral indices, and

$$A(B_{84}) = 12f(B)\left[\frac{\sin\alpha_1}{\alpha_1} + \frac{\sin\alpha_2}{\alpha_2} + 5\frac{\sin\alpha_3}{\alpha_3}\right] \quad (19)$$

$$\alpha_i = \frac{4\pi r_i \sin \theta_o}{\lambda} \quad , \; i = 1,2,3$$

$$r_1 = 1.71 \text{ Å}$$

$$r_2 = 3.41 \text{ Å}$$

$$r_3 = 4.36 \text{ Å}$$

$$A(B_{10}) = f(B)\left(1 + 9\frac{\sin \alpha_1}{\alpha_1}\right) \tag{20}$$

$$A(B) = f(B) \tag{21}$$

The expression for $A(B_{84})$ in Eq. (19) treats the B_{84} group as three concentric spherical shells of scattering material.

Calculation of $F(\beta)$ for the $(30\cdot 0)_H = (2\bar{1}\bar{1})_R$ reflection using Eq. (18) gives a non-zero value. However, this value may be small in comparison to the values for other reflections. Time did not permit extensive calculations using Eq. (18).

Equation (18) should be compared with the rigorous expression for the structure factor, involving the atomic coordinates of all 105 atoms in the unit cell. This expression was not computed due to time limitations.

A question still remains regarding the reflections which are present in the x-ray case but missing in electron diffraction for the indexing scheme used in Fig. 85(d). Because the indexing in Fig. 85(d) appears to be the only one consistent with the published parameters for β-rhombohedral boron, the missing reflections must be caused by a defect structure involving additional boron atoms in the unit cell or distorted arrangements of the interstitial groups already present. Such deviations from the ideal structure might occur in the case of extremely thin crystals such as those which typically yield the hexagonal spot pattern shown in Fig. 85.

4.4 ELECTRON MICROSCOPY

4.4.1 Characteristic Structure of Boron Filaments Observed by Transmission Electron Microscopy

This section discusses typical images and diffraction patterns obtained by transmission electron microscopy of production boron filaments prepared either by electropolishing or by chemical thinning, as described in Section 3.2.3.

4.4.1.1 General Observations

Figure 53 shows one of the first specimens prepared by electropolishing. The image contains a number of dark particles 100 – 200 Å in diameter, the matrix in which these particles are embedded having a fine texture. The irregular boundaries between light and dark regions are indicative of thickness variations. There is no evidence of dislocations, grain boundaries, stacking faults, or other structural features commonly observed in the case of metallic specimens.

The selected area diffraction pattern shown in Fig. 53(b) consists of a pattern of diffuse halos plus some isolated spots; the spots may originate from the embedded particles. In all, six distinct halos were observed on the original plate, although only four are readily distinguished on the print. The average d-spacings of these halos are listed in Table 22 together with those for α-rhombohedral boron shown on card 12-377 in the ASTM x-ray data file.

Table 22

d-SPACINGS OF HALO MAXIMA FROM PLATE 750 (FIG. 53) COMPARED TO α-RHOMBOHEDRAL BORON

Halo No.	Intensity	d, Å at Halo Maximum	α-Rhombohedral Boron		
			d, Å	Intensity	(hkℓ)
1	S	4.43	4.25	45	(111)
2	S	2.55	2.545	70	(211)
3	VW	2.13	2.113	55	$(11\bar{1})$
4	M	1.75	1.77[a]	–	(220)[a]
5	S	1.42	1.424	8	$(2\bar{1}\bar{1})$
6	VW	0.943	0.932	15	$(41\bar{1}, 542)$

[a]Not indicated on ASTM card

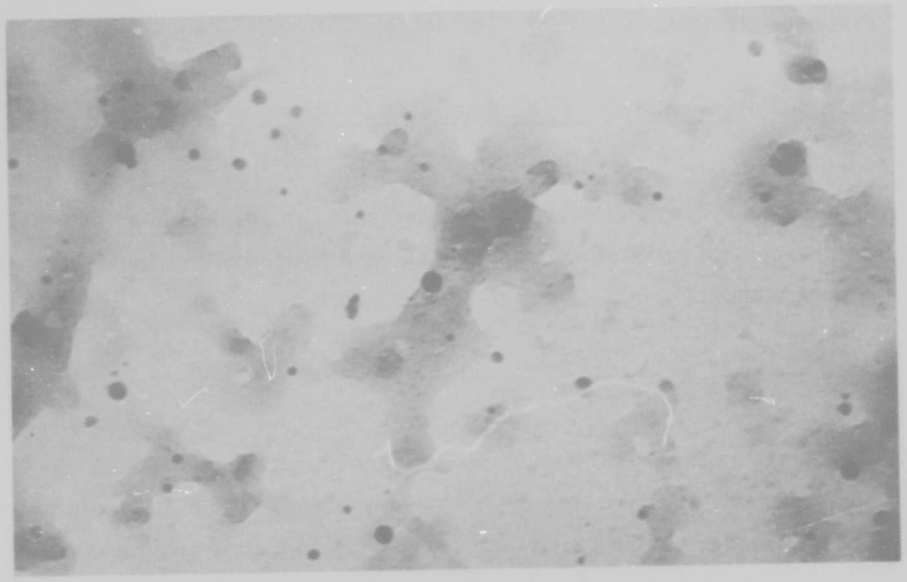

Fig. 53a Electron Transmission Micrograph of Structure of Electro-polished Boron Filament. 140,000×, P750-11a

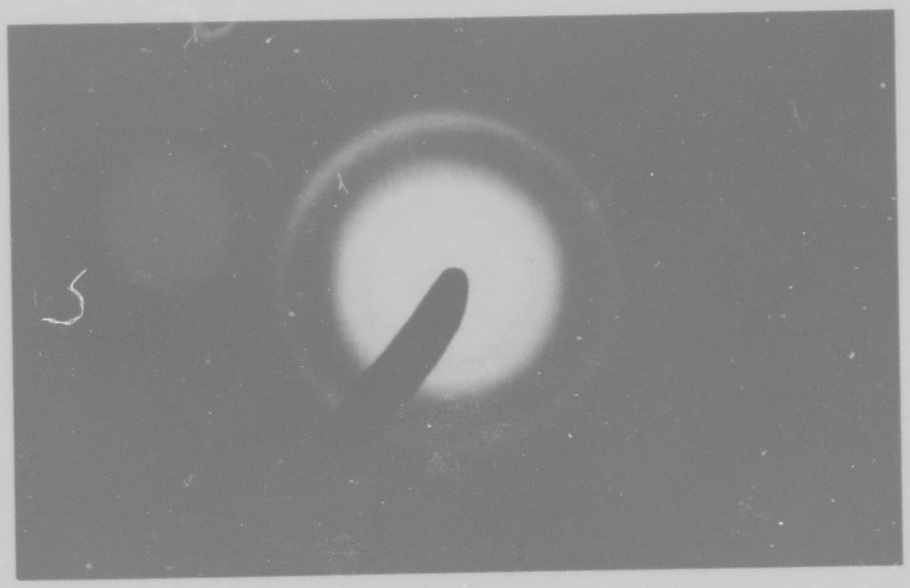

Fig. 53b Characteristic Halo Diffraction Pattern Corresponding to Image in Fig. 53a. 2×, P750-11b

Table 22 shows that the halo maxima lie very close to strong powder pattern reflections of α-rhombohedral boron. A more striking comparison is shown in Section 4.3.2, Fig. 49, which gives the positions of the halo boundaries (at approximately half maximum intensity) in relation to the positions of all the α-rhombohedral boron reflections taken from the ASTM card plus the $\alpha(220) \equiv (02 \cdot 4)$ which is not listed on the card.

A careful examination of the halo pattern of Fig. 53(b) reveals two isolated spots lying just outside the fifth halo, which correspond to a d-spacing of 1.1 Å. A complete halo of this d-spacing has been reported by Wawner (Ref. 14), using a Debye-Scherrer x-ray camera. A halo of very nearly this spacing has been observed in this laboratory in the case of filaments heat treated for long times at "low" temperatures (see Section 4.4.5).

It is of interest to establish quantitatively the correspondence between the halos as observed in electron diffraction and in x-ray diffraction. In a Debye-Scherrer film of whole boron filaments, only the three strongest halos, i.e., numbers 1, 2, and 5 in Table 22, can be easily observed. In Table 23, below, the d-spacings corresponding to the low and high angle boundaries of each of the three halos are shown, along with the quantity $\Delta 2\theta/\tan \hat{\theta}$ for each halo, where $\hat{\theta}$ is the average value of the Bragg angle of the halo. This quantity, derived by differentiating Bragg's law, permits a direct comparison of the breadths of the halos in the x-ray and the electron cases. (The halo boundaries were determined by eye on both the x-ray film and the electron diffraction plate. It was established that the boundaries observed by eye correspond very nearly to the half-height line breadth determined from densitometer traces of the halos on a Debye-Scherrer film.)

The results in Table 23 compare very well and they definitely establish the similarity of the x-ray and electron diffraction patterns.

Table 23

COMPARISON OF POSITIONS AND BREADTHS OF DIFFRACTION HALOS OBTAINED FROM WHOLE PRODUCTION-RUN BORON FILAMENTS MEASURED BY X-RAY AND ELECTRON DIFFRACTION

Measured Quantity	Halo 1		Halo 2		Halo 5	
	X-ray	ED	X-ray	ED	X-ray	ED
d(low θ), Å	4.576	4.755	2.674	2.679	1.427	1.449
d(high θ), Å	4.077	4.201	2.385	2.400	1.306	1.355
$\Delta 2\theta/\tan\hat{\theta}$, deg	13.22	14.32	13.12	12.62	10.18	7.68

Figure 54 contains several examples of the structure and characteristic halo diffraction patterns from a chemically thinned filament specimen. The halo patterns are identical to those shown in Fig. 53(b), except that no isolated spots are present. The structure shown in the images is somewhat different from that shown in Fig. 53(a), even taking into account the lower magnification in Fig. 54. The images do not show the light-to-dark variations present in Fig. 53(a), nor do they show the high density of embedded particles. Rather, the surface appears very smooth, and, again, no evidence of dislocations, boundaries, or stacking faults is apparent. Figure 54(a) shows that near the edge there are several overlapping layers, while in Fig. 54(c), the projection has a pleated appearance which also is frequently observed in filament grindings (see Section 4.4.3). In all three images, isolated small inclusions can be seen, which, when corrected for magnification differences, are considerably larger than the particles shown in Fig. 53(a). However, no effect of these inclusions is evident in the diffraction patterns shown.

A close inspection of the images of Fig. 54 shows that the thinned boron has a very fine, grainy texture. This structure is indicative of a very small crystallite size which is qualitatively consistent with the broad halo diffraction pattern. This question is discussed quantitatively in Section 4.4.2.

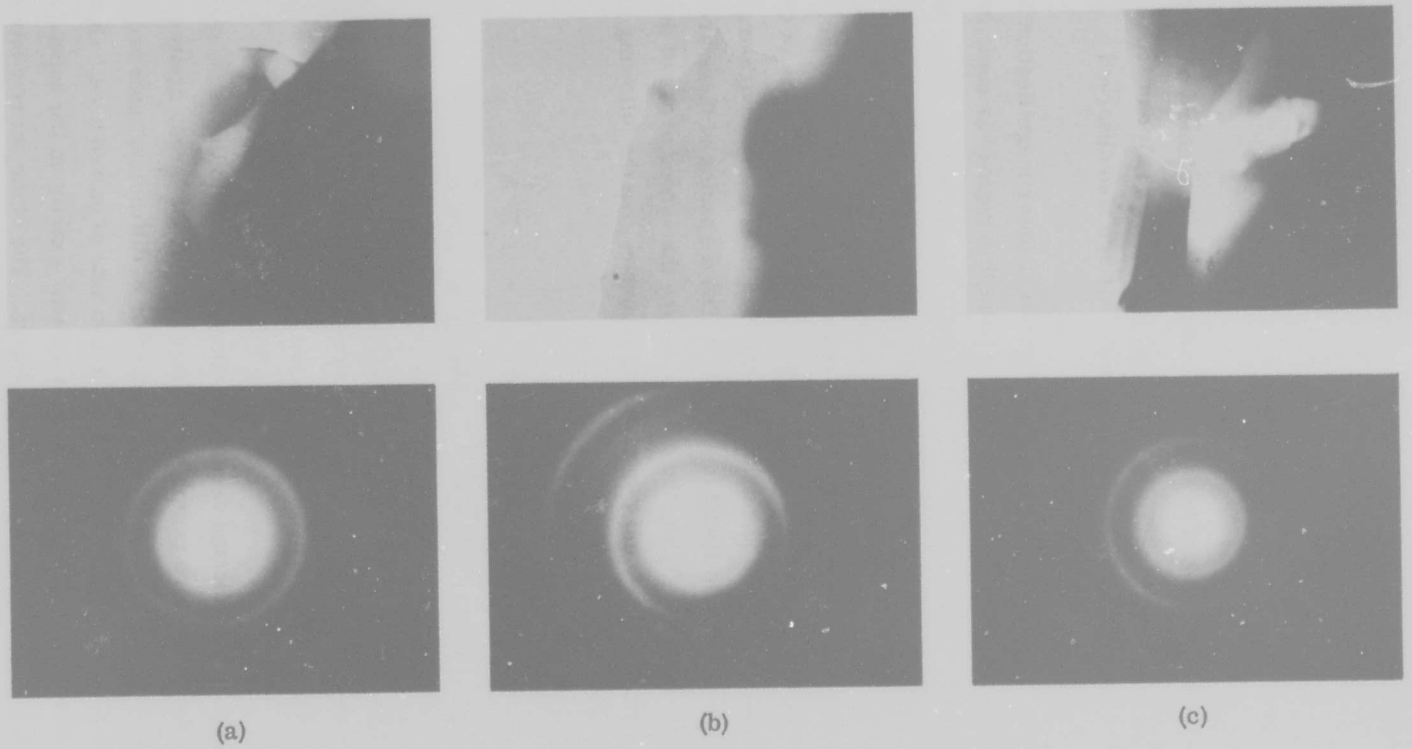

Fig. 54 Three Examples of the Typical Structure of Chemically Thinned Boron Filament, Each Showing the Characteristic Halo Diffraction Pattern. Images at 13,500×. (a) P1103. (b) P1104. (c) P1105

4.4.1.2 "Inclusions" in Boron Filaments

Figure 55 shows another specimen of chemically thinned boron filament at 49,500×. This structure resembles more closely the one shown in Fig. 53(a); numerous "inclusions" are present, and the light-to-dark transitions are also observed.

The unusual boundary seen in Fig. 55(a) (top) is shown at lower magnification in Fig. 56(a). The selected area diffraction pattern from this region has some interesting features: the usual diffuse halo pattern is present, but in addition, there are some spots and arcs. The four spots inside the first halo, as well as several of the spots just outside the second halo, correspond to reflections of potassium ferricyanide, indicating incomplete rinsing of the specimen. Just outside the first halo, six arcs can be seen, which correspond to a d-spacing of 3.63 Å. If lines are drawn through opposed arcs and extended, it is found that the extended lines pass through arcs located just inside the fourth halo listed in Table 22. The d-spacing of these arcs is 1.81 Å, just half of 3.63 Å. Thus, the outer arcs are the second order of the first arcs. The ASTM cards for α- and β-rhombohedral boron give the following information:

$$\alpha: \quad d(01\cdot 2) = 3.544\ \text{Å}, \quad d(02\cdot 4) = 1.77\ \text{Å}$$

$$\beta: \quad d(02\cdot 4) = 3.71\ \text{Å}, \quad d(04\cdot 8) = 1.86\ \text{Å}$$

Because the uncertainty in the camera constant of the microscope is sufficiently large to encompass both these values, the identification cannot be positive on the basis of this pattern alone and more information is required.

Figure 56(b) shows another selected area diffraction pattern from the same specimen, this time with the aperture more completely filled by one of the large, spotty areas as indicated in the accompanying image. A large number of diffraction spots and arcs are present in this pattern. Attention is drawn to two sets of paired arcs. One set consists of the pair just inside the first halo and the pair exactly on the second halo; these arcs lie on a nearly horizontal line in the figure. The other set consists of the pair just outside the first halo and the pair just inside the fourth halo listed in Table 22

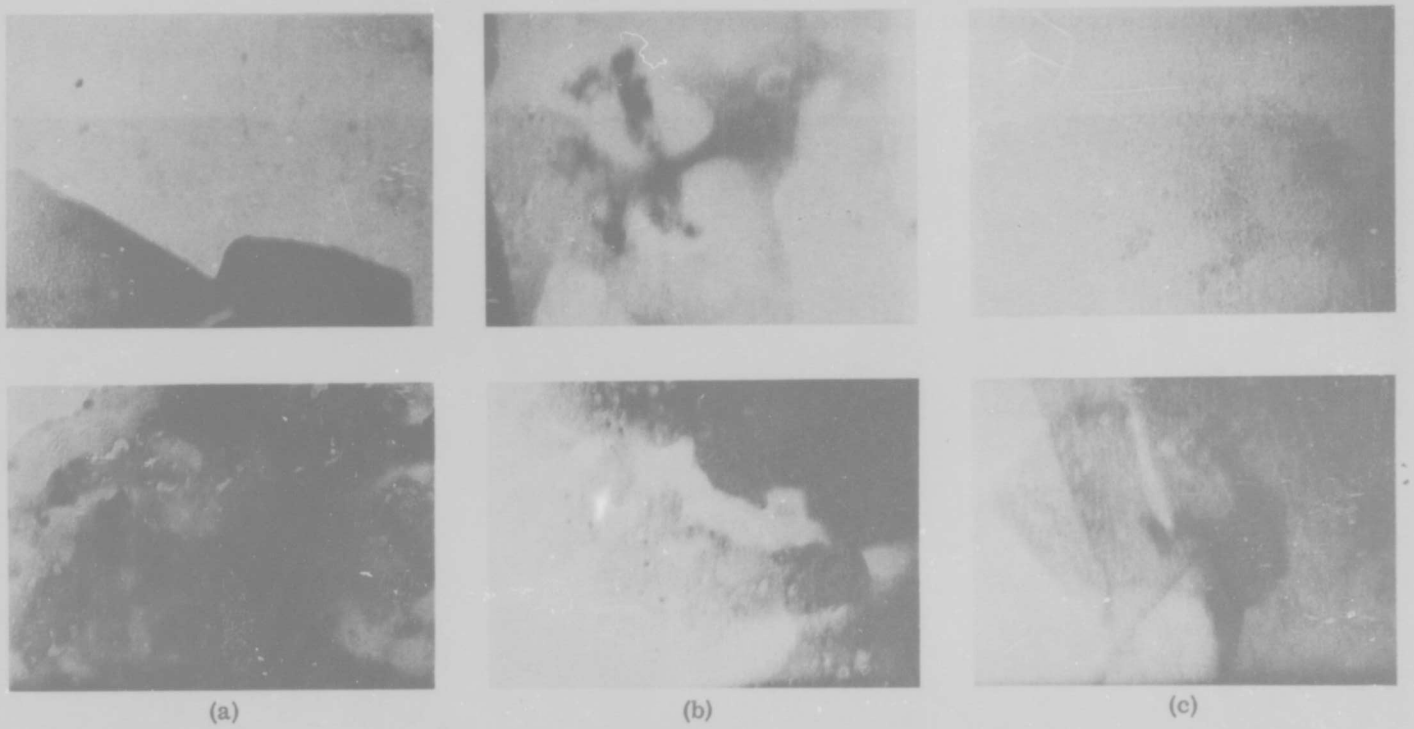

(a) (b) (c)

Fig. 55 Further Examples of the Structure of Chemically Thinned Boron Filament. All images at 49,500×. (a) P1340. (b) P1341. (c) P1342

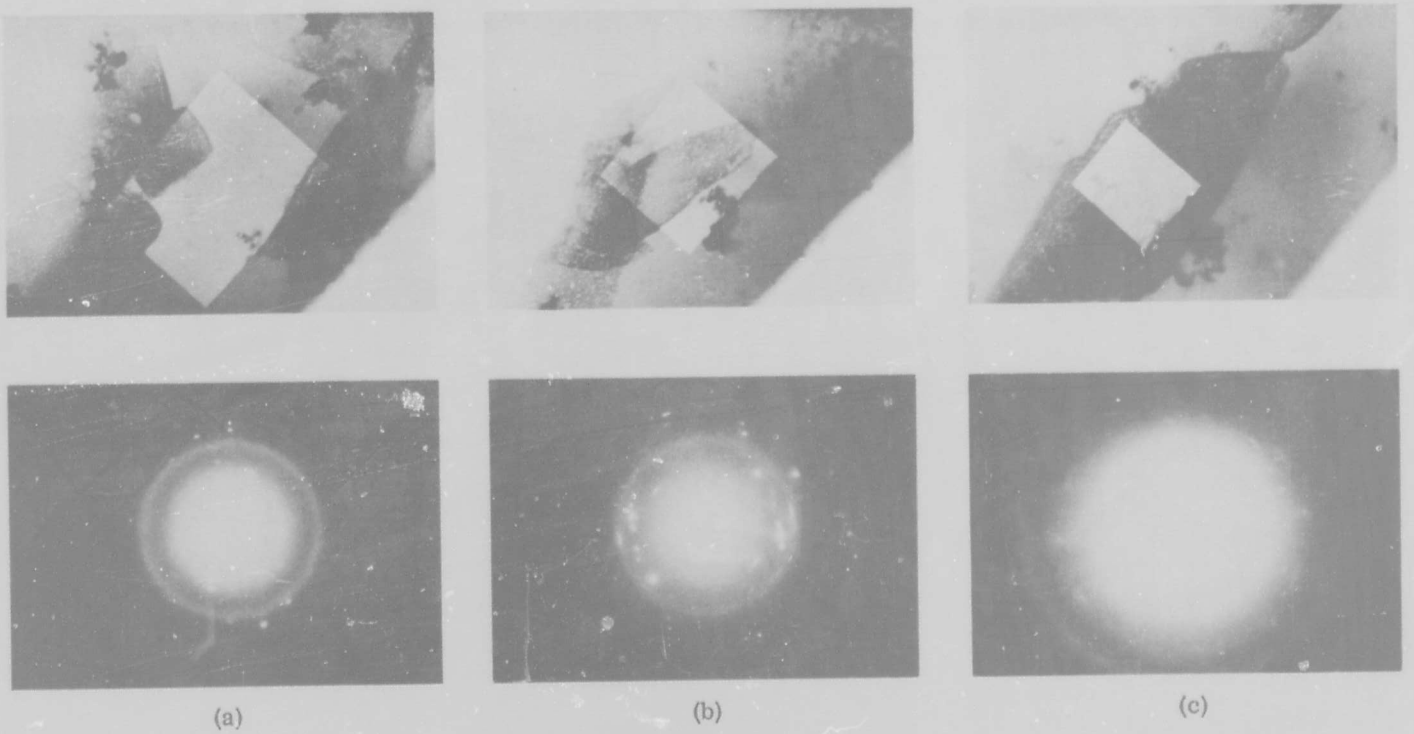

(a) (b) (c)

Fig. 56 Same Specimen as in Fig. 55. Images at 12,500×. Selected-area diffraction patterns indicate the presence of crystalline β-rhombohedral boron. (a) P1344. (b) P1345. (c) P1346

(the third and fourth halos are invisible in Fig. 56). This set lies on a line approximately 30 deg from the horizontal, proceeding from upper left to lower right. The first set of arcs has d-spacings of 5.15 Å and 2.576 Å, while the second set has d-spacings of 3.65 Å and 1.825 Å. This second set is identical to that described in the discussion of Fig. 56(a) in the preceding paragraph. Because there is no α-rhombohedral boron reflection with d-spacing of 5 Å or higher, the first set of arcs must be the (10·4) and (20·8) reflections of β-rhombohedral boron. If the second set is also due to the same β crystal or small group of crystals, it must be the (02·4) and (04·8) reflections. This indexing is easily proved by checking the angle between the (10·4) and (02·4) planes of β-rhombohedral boron. The calculated angle is 42°33', using the formula

$$\cos\theta = \frac{H_1H_2 + K_1K_2 + \frac{1}{2}(H_1K_2 + H_2K_1) + \left(\frac{3a^2}{4c^2}\right) L_1L_2}{\sqrt{H_1^2 + K_1^2 + H_1K_1 + \left(\frac{3a^2}{4c^2}\right) L_1^2}\ \sqrt{H_2^2 + K_2^2 + H_2K_2 + \left(\frac{3a^2}{4c^2}\right) L_2^2}} \qquad (22)$$

The angle measured from the plate is 45 deg. The agreement is within 3 deg, showing that the arcs arise from a small cluster of β-rhombohedral boron crystals near the orientation $[20\cdot\bar{1}]$. Judging from the accompanying image showing the area corresponding to this diffraction pattern, it would appear that the large spotty areas are probably crystalline β-rhombohedral boron lying on the surface and giving rise to the numerous diffractions spots and arcs. The underlying smooth area gives the usual continuous halo pattern.

Figure 56(c) contains another example of the presence of β-rhombohedral boron, indicated by the paired arcs. Calculation of interplanar angles shows that the two pairs of arcs just outside the first halo must correspond to two different groups of β crystals, even though no such division is apparent in the image. The two pairs of arcs lie 60 deg apart, and no two permutations of (02·4) give this interplanar angle. Thus, from Fig. 56 it is apparent that the presence of β-rhombohedral boron can make a contribution to the halo pattern intensity: the (20·8) type reflections contribute to the second halo, and the (04·8) type reflections contribute to the third halo.

Figure 57 gives more evidence for the presence of β-rhombohedral boron in as-produced boron filaments. This specimen, which was electropolished, has a number of precipitate-like particles in a textured matrix [Fig. 57(a)]. The measured d-spacings of the spotty rings shown in the diffraction pattern, Fig. 57(b), are given in Table 24.

Figure 58 shows another example of the structure of a chemically thinned filament. Numerous angular particles are embedded in a smooth (at this magnification) matrix. The diffraction pattern shows the four strongest halos, as usual, but in addition, two discontinuous, sharp rings can be observed between the first and second halos, and two opposed spots can be seen just inside the first halo. Table 25 gives the d-spacings obtained from this pattern. ("H" indicates "halo"-compare with halo d-spacings given in Table 22.) The sharp lines, presumably originating from the angular particles, are clearly identified as β-rhombohedral boron.

To study these particles further, attention was focused on a single particle. Figure 59 shows the selected area aperture outlining a single particle, along with the resulting diffraction pattern; this pattern has considerable spottiness. The outlined particle is evidently composed of a number of crystallites which give rise to the spots, whereas the surrounding matrix material produces the usual halos. Table 26 lists the various d-spacings obtained from this pattern and compares the ones not indicated by "H" (for halo) with reflections of β-rhombohedral boron.

Figure 60 shows a selected area diffraction pattern from another particle. In this case even less of the matrix material is included within the boundaries of the selected area aperture; consequently, the halo pattern is weaker and the contributions from the polycrystalline particle are more intense. Table 27 lists the measured d-spacings and their identification.

The fourth halo (numbering according to Table 22) is completely broken up in this pattern and three orders of the $\beta(10\cdot4)$ reflection are visible.

Fig. 57a Electron Transmission Micrograph of Electropolished Boron Filament Showing Clusters of Crystalline Material. 75,000×. P818-7a

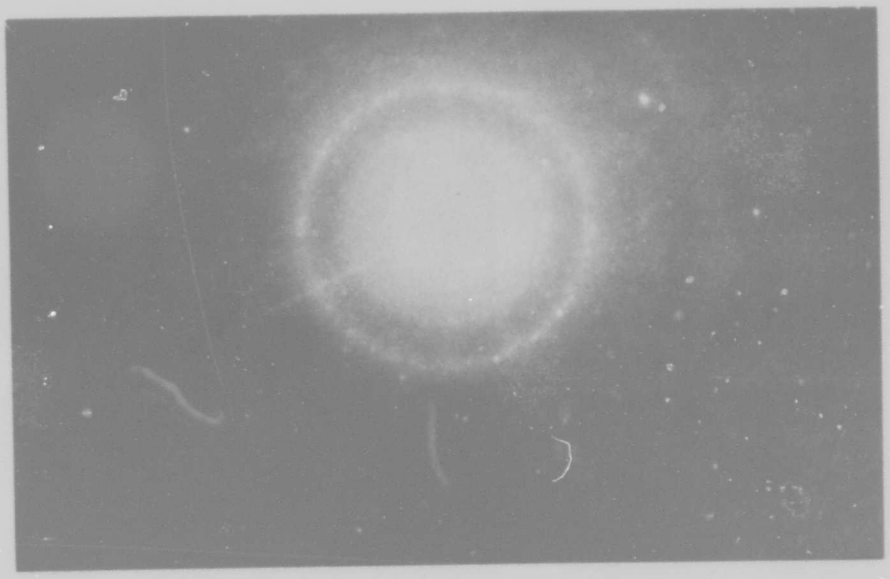

Fig. 57b Diffraction Pattern From Area Shown in Fig. 57a. Note decomposition of halos into spotty rings. 2×. P818-7b

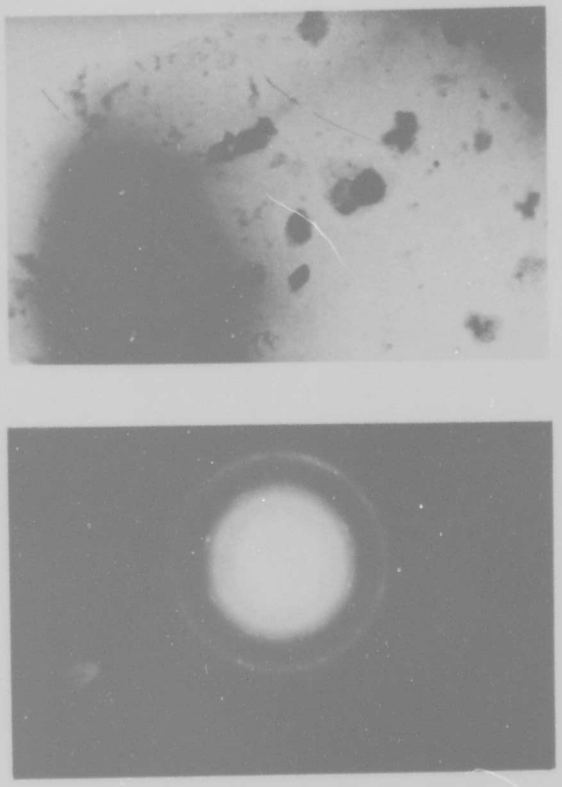

Fig. 58 Chemically Thinned Boron Filament Showing Crystalline Regions Distributed Throughout the Matrix. 15,000×. Diffraction pattern shows arced rings in addition to halos. 1.2×. P1465

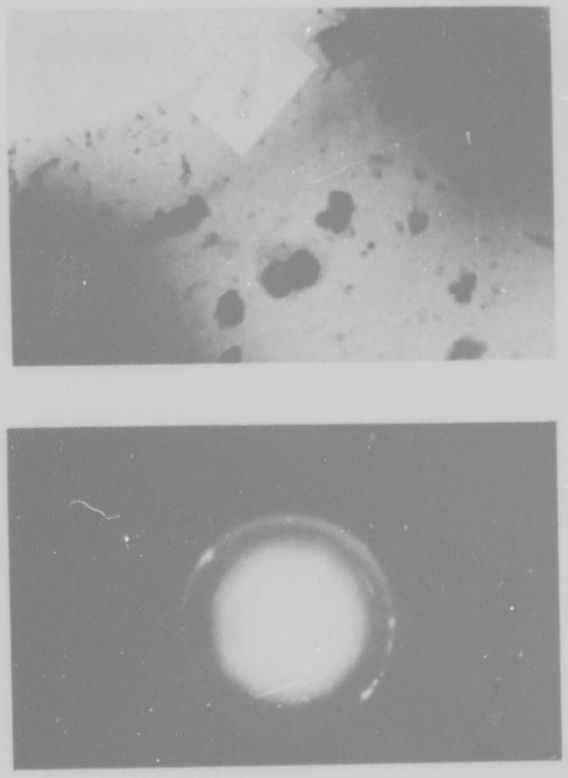

Fig. 59 Same Area Shown in Fig. 58, Also at 15,000×. Selected area diffraction from one of the crystalline regions produces well-defined arcs and spots superimposed on halo pattern. 1.2×. P1466

Table 24

d-SPACINGS FROM DIFFRACTION PATTERN SHOWN IN FIG. 57(b)

Number	Measured d, Å	β-boron	
		d, Å	(HK·L)
1	4.95	5.06	(10·4)
2	4.36	4.41	(20·2)
3	2.87	2.86	(12·5)
4	2.43	2.41	(13·4)
5	2.14	–	–
6	1.91	–	–
7	1.58	–	–

Table 25

d-SPACINGS FROM DIFFRACTION PATTERN SHOWN IN FIG. 58

Number	Measured d, Å	β-boron	
		d, Å	(HK·L)
1	5.15	5.06	(10·4)
2 (H)	4.37		
3	3.58	3.55	(21·1)
4	2.93	2.94	(30·3)
5 (H)	2.53		
6 (H)	1.72		
7 (H)	1.38		

Table 26

d-SPACINGS FROM DIFFRACTION PATTERN SHOWN IN FIG. 59

Number	Measured d, Å	β-boron	
		d, Å	(HK·L)
1	5.15	5.06	(10·4)
2 (H)	4.37		
3	3.58	3.55	(21·1)
4	2.93	2.94	(30·3)
5	2.59	2.52	(20·8)
6	2.55		
7 (H)	2.53		
8	2.06	2.06	(23·5)
9	1.98	–[a]	–
10 (H)	1.72		
11	1.62	–	–
12 (H)	1.39		
13 (H)	0.925		

[a] ASTM card 11-618 for β-rhombohedral boron does not go below 2.02 Å

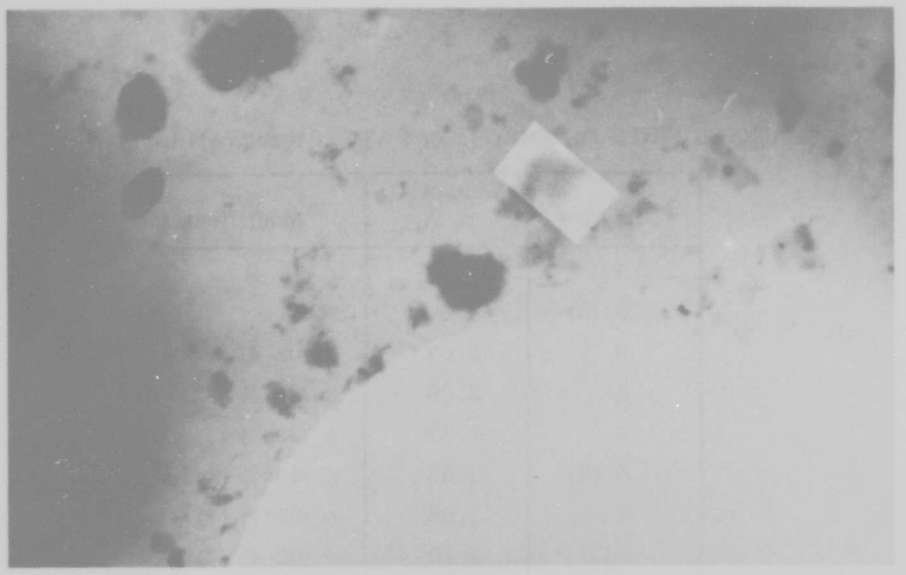

Fig. 60a Same specimen as in Figs. 58 and 59. Note outline of selected area aperture over one of the crystalline regions. 25,000×. P1467-14b

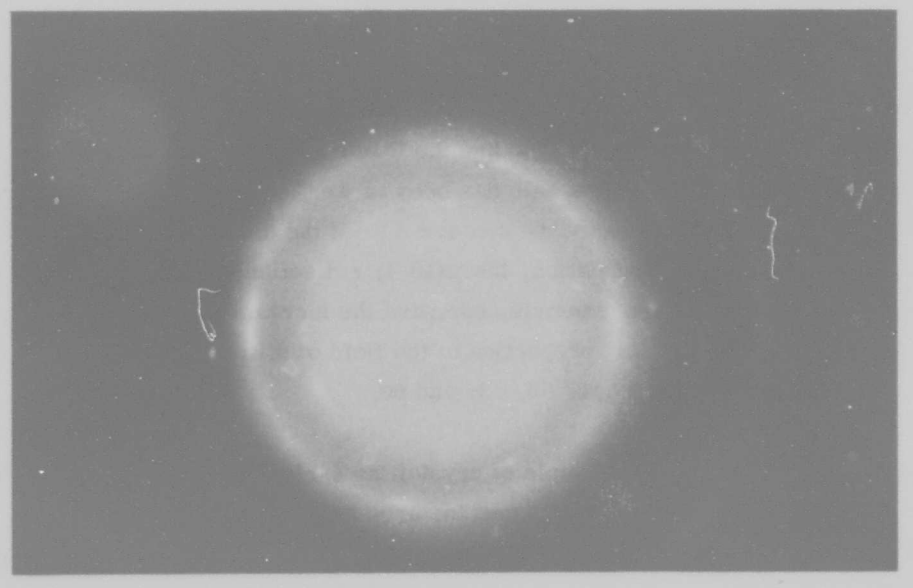

Fig. 60b Selected Area Diffraction Pattern From Region Shown in Fig. 60a. Three orders of the (10·4) reflection of β-rhombohedral boron can be distinguished. 2×. P1467-14a

Table 27

d-SPACINGS FROM DIFFRACTION PATTERN SHOWN IN FIG. 60

Number	Measured d, Å	Identification
1	5.10	β (10·4)
2 (H)	4.37	
3	3.63	β (02·4) or (21·1)
4	3.06	β (21·4)
5	2.93	β (30·3)
6 (H)	2.53	β (20·8) (2nd order)
7	2.09	α (02·1) (?)
8	1.80	α (02·4) (?)
9 (H)	1.70	β (30·12) (3rd order)
10	1.60	α (21·1) or (11·6)
11 (H)	1.39	
12 (H)	0.925	

In the examples considered thus far, the preferred orientation of the polycrystalline particles of β-rhombohedral boron has been such that the second halo has had superimposed upon it the β(20·8) reflection and the fourth halo the β(30·12). No examples have been found in which the first halo has been broken up, even though there are some strong β reflections in this range (4.2 – 4.8 Å). If the β-rhombohedral boron is present in any significant proportion, the β(10·4) reflections, which fall inside the first halo, will be seen. For example, compare the increasing intensity of these reflections with the increasing proportion of the field of diffraction occupied by the β particles in the sequence of Figs. 58, 59, and 60.

Figure 61 shows yet another example of crystalline β-rhombohedral boron embedded in the filament material. The position of the arcs again identifies β positively, as in the previous cases. Note how the individual particles appear to blend into the "matrix." The diffraction pattern contains a number of parallel streaks which indicate a planar defect in certain of the crystallites.

Fig. 61a High Magnification View of Crystalline Regions in Chemically Thinned Boron Filament. 92,000×. P1459-6a

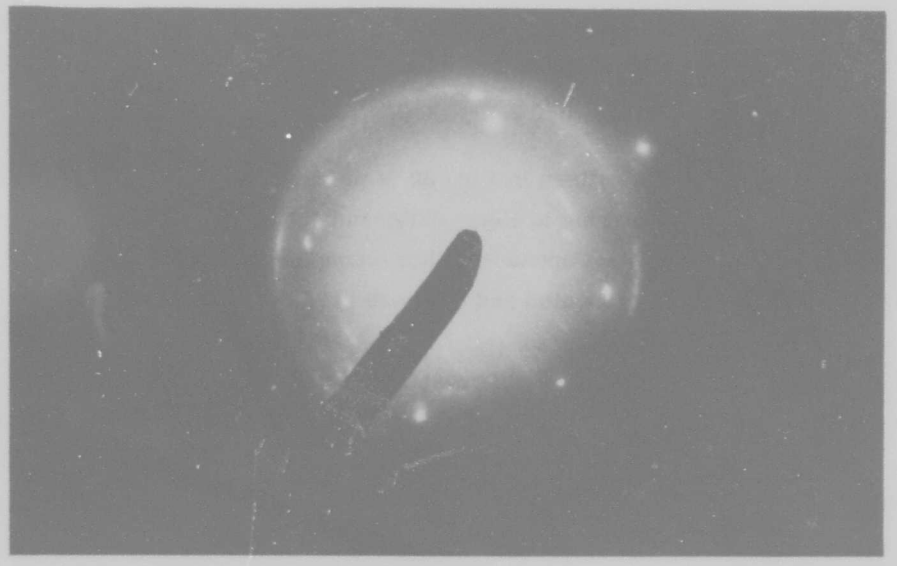

Fig. 61b Diffraction Pattern Obtained From Area Shown in Fig. 61a. Crystalline regions are identified as β-rhombohedral boron. Streaks in the diffraction pattern indicate that the crystalline regions contain planar defects. 2×. P1459-6b

Up to this point, the examples of isolated crystalline regions embedded in the boron "matrix" have all been polycrystalline. On occasion, single-crystal regions yielding well-defined spot patterns are observed. Figure 62 shows one such spot pattern obtained from the crystallite outlined by the edges of the selected area aperture; the diagram in Fig. 62(c) shows the indexing of the pattern. By a careful check of d-spacings and interplanar angles, the pattern was identified as β-rhombohedral boron in the $[7\bar{4}\cdot\bar{4}]$ orientation.

One might be tempted to assign two permutations of the same indices to the spots indexed as $(3\bar{2}\cdot 8)$ and $(2\bar{4}\cdot 6)$, since the measured d-spacings are very nearly the same; however, trial and error computation shows that this is impossible and that two different reflections with nearly the same d-spacings are involved. The correctness of the assigned indices can be verified only by checking the interplanar angles. The d-spacings alone are unreliable for indexing a spot pattern of a substance with many closely spaced lines as in the case of β-boron, since slight variations in the camera constant and derivations from exact pattern orientation can result in slight errors in the observed d-spacings. Table 28 compares measured and calculated d-spacings and angles for this pattern.

An interesting feature of the pattern in Fig. 62 is the fact that certain reflections are missing. For example, referring to Figs. 62(b) and (c), the $(20\cdot 5)$ is present but the $(1\bar{2}\cdot 3)$ and the $(04\cdot\bar{1})$ do not appear. Other examples of this phenomenon of missing reflections will be presented and discussed in later sections.

Figure 63 shows another β-boron single crystal spot pattern observed in a specimen of chemically thinned boron filament. The diagram in Fig. 63(c) shows the indexed pattern. This pattern also shows missing reflections, e.g., $(\bar{1}1\cdot 1)$, $(02\cdot 1)$, $(13\cdot 1)$ etc. Note also that the intensities of the $(11\cdot 0)$ and $(33\cdot 0)$ reflections are very low. This point is important to the interpretation of the $\beta[00\cdot 1]$ spot pattern (see Sections 4.3.2 and 4.4.3).

Measured and calculated d-spacings and angles for the pattern in Fig. 63(c) are presented in Table 29.

(a)

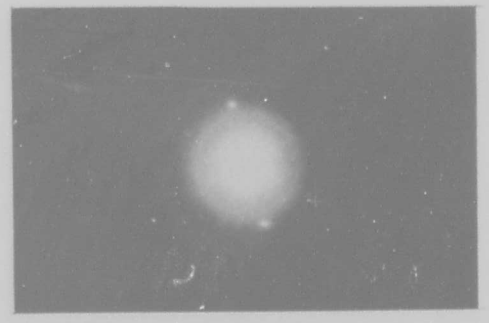

(b)

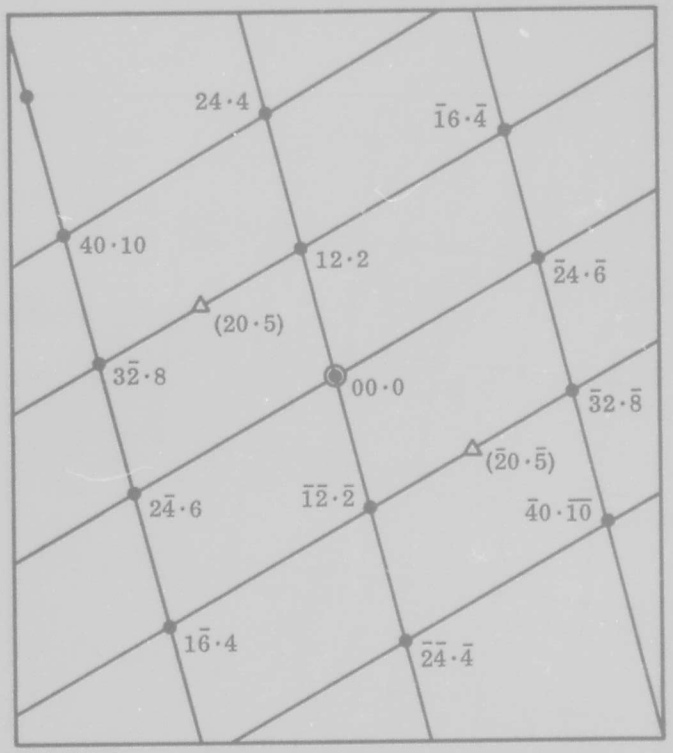

(c)

Fig. 62 Analysis of Spot Pattern Obtained From Crystalline Region of Chemically Thinned Boron Filament. (a) Image at 12,500×, showing outline of selected-area aperture. (b) Diffraction pattern obtained from crystalline region outlined in (a). (c) Indexed diffraction pattern: β-rhombohedral boron, zone axis $[7\bar{4}\cdot\bar{4}]$. P1377

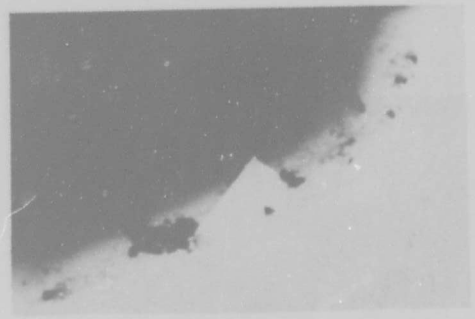

(a)

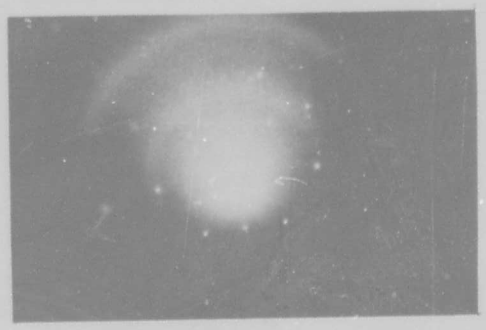

(b)

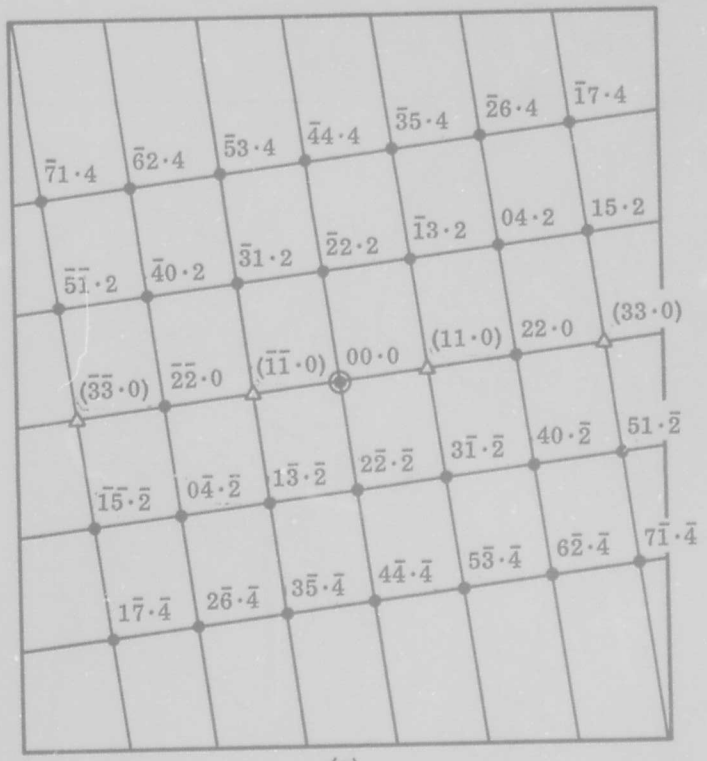

(c)

Fig. 63 Another Single Crystal Spot Pattern Observed in a Specimen of Chemically Thinned Boron Filament. (a) Image at 13,000×. (b) Diffraction pattern obtained from small crystal outlined in (a). (c) Indexed diffraction pattern: β-rhombohedral boron, zone axis $[2\bar{2}\cdot4]$. P1393

Table 28

COMPARISON OF MEASURED AND CALCULATED d-SPACINGS AND ANGLES FOR DIFFRACTION PATTERN SHOWN IN FIG. 62(c)

Quantity	Measured Value	Calculated Value[a]
β d $(3\bar{2}\cdot 8)$	2.09 Å	2.28 Å
β d $(2\bar{4}\cdot 6)$	2.07 Å	2.25 Å
β d $(12\cdot 2)$	3.65 Å	3.43 Å
β d $(40\cdot 10)$	1.63 Å	1.67 Å
β d $(1\bar{6}\cdot 4)$	1.60 Å	1.64 Å
$\measuredangle$ $(3\bar{2}\cdot 8)$, $(2\bar{4}\cdot 6)$	39.5°	38° 34'
$\measuredangle$ $(12\cdot 2)$, $(3\bar{2}\cdot 8)$	73.0°	71° 56'
$\measuredangle$ $(12\cdot 2)$, $(\bar{2}4\cdot\bar{6})$	74.0°	69° 30'
$\measuredangle$ $(40\cdot 10)$, $(2\bar{4}\cdot 6)$	58.0°	66° 15'

[a] Using $a_o = 10.944$ Å, $c_o = 23.715$ Å, corresponding to $a_R = 10.12$ Å, $\alpha = 65°\ 28'$

Table 29

COMPARISON OF MEASURED AND CALCULATED d-SPACINGS AND ANGLES FOR DIFFRACTION PATTERN SHOWN IN FIG. 63(c)

Quantity	Measured Value	Calculated Value
β d $(\bar{2}2\cdot 2)$	4.46 Å	4.40 Å
β d $(22\cdot 0)$	2.81 Å	2.74 Å
β d $(3\bar{1}\cdot\bar{2})$	3.49 Å	3.43 Å
β d $(04\cdot 2)$	2.38 Å	2.32 Å
$\measuredangle$ $(\bar{2}2\cdot 2)$, $(\bar{1}3\cdot 2)$	38.5°	38° 48'
$\measuredangle$ $(\bar{1}3\cdot 2)$, $(40\cdot\bar{2})$	84.0°	83° 4'
$\measuredangle$ $(\bar{3}1\cdot 2)$, $(\bar{3}5\cdot 4)$	60.0°	60° 42'
$\measuredangle$ $(04\cdot 2)$, $(51\cdot\bar{2})$	56.0°	54° 23'

(a)

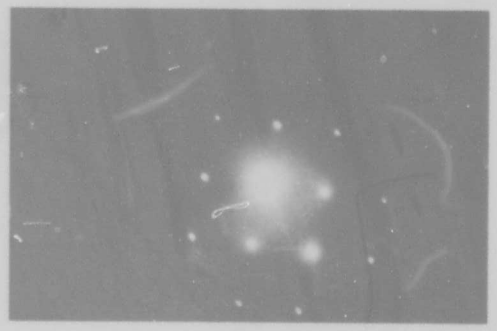

(b)

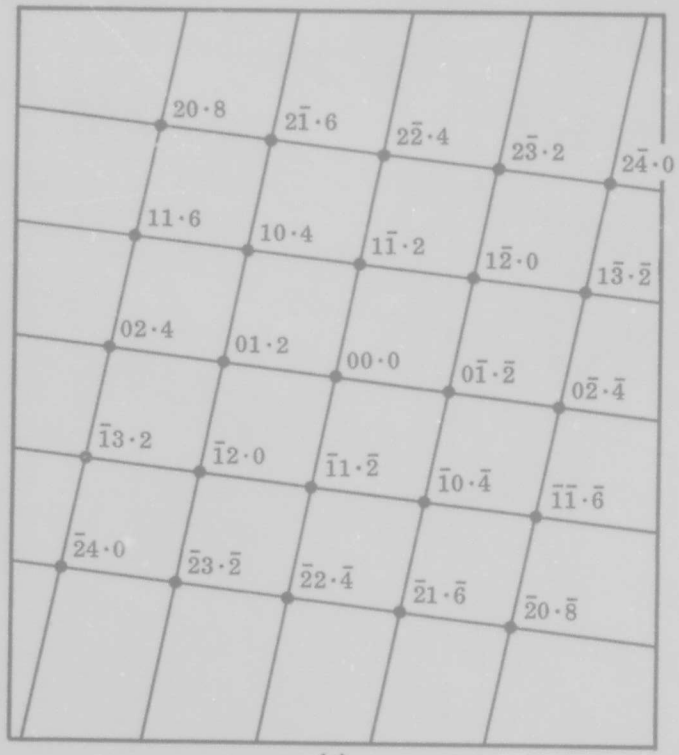

(c)

Fig. 64 A Single Crystal Spot Pattern Obtained From a Projection on a Specimen of Electropolished Boron Filament. (a) Image of projection, at 17,500×. (b) Diffraction pattern obtained from edge of projection. (c) Indexed diffraction pattern: α-rhombohedral boron, zone axis [$\bar{2}$0·1]. P749

Figure 64, a complete single-crystal spot pattern of α-rhombohedral boron obtained from a specimen of electropolished filament, is another example of the necessity of measuring interplanar angles. On the basis of d-spacings alone, the pattern would appear to be β-rhomobohedral boron. Figure 64(c) gives the complete indexing of the pattern, and Table 30 compares the measured and calculated d-spacings and angles. There are no missing reflections in this pattern.

Table 30

COMPARISON OF MEASURED AND CALCULATED d-SPACINGS AND ANGLES FOR DIFFRACTION PATTERN SHOWN IN FIG. 64(c)

Quantity	Measured Value	Calculated Value
α d $(01\cdot 2)$	3.39 Å	3.52 Å
α d $(1\bar{1}\cdot 2)$	3.44 Å	3.52 Å
α d $(10\cdot 4)$	2.53 Å	2.53 Å
α d $(1\bar{2}\cdot 0)$	2.31 Å	2.45 Å
α d $(1\bar{3}\cdot 2)$	1.47 Å	1.56 Å
$\measuredangle$ $(01\cdot 2)$, $(1\bar{1}\cdot 2)$	94.0°	91° 40'
$\measuredangle$ $(01\cdot 2)$, $(1\bar{3}\cdot 2)$	26.0°	26° 14'
$\measuredangle$ $(10\cdot 4)$, $(1\bar{2}\cdot 0)$	90.0°	90° 0'
$\measuredangle$ $(10\cdot 4)$, $(\bar{2}3\cdot \bar{2})$	106.0°	107° 57'
$\measuredangle$ $(01\cdot 2)$, $(\bar{2}3\cdot \bar{2})$	59.0°	62° 6'

4.4.1.3 Summary of Characteristic Structure of Boron Filaments Observed by Transmission Electron Microscopy

The observations of thinned, production on boron filaments by transmission electron microscopy may be summarized as follows: Overall, the bulk of the thinned material has a fine-textured surface with gradual thickness variations (Fig. 54). No contrast due to dislocations, subgrain boundaries, stacking faults, or other defects can be observed. This structure produces a diffraction pattern consisting of six diffuse halos which correspond closely to reflections of α-rhombohedral boron. The images and halo diffraction pattern of this material suggest that it is composed primarily of α-rhombohedral boron of extremely small crystallite size with possibly some tetragonal

boron present. Isolated regions consisting of polycrystalline or single crystal α- or β-rhombohedral boron can frequently be found embedded in the matrix. These regions are typically of the order of 1000 Å in diameter, but may range from 100 – 10,000 Å.

Most of these crystalline regions are found to consist of β-rhombohedral boron. Many different specimens of production filament were prepared and examined, and no exceptions to the above observations were found, nor were systematic variations observed from one filament to another. All the specimens examined in this study were deposited in the vicinity of 1150°C.

4.4.2 Crystallite Size Determination by Electron Microscopy

In the previous section, the structure of thinned boron filaments was shown to consist of a matrix of very finely textured material in which numerous particles of crystalline α- or β-rhombohedral boron are embedded. The matrix material gives rise to the halo diffraction pattern which is characteristic of vapor deposited boron. In this section, experiments are described and evidence is presented which show that the textured matrix consists mainly of α-rhombohedral boron of extremely small crystallite size. Moreover, the small crystallite size adequately accounts for the broadening of the α-boron lines to produce the halo pattern.

4.4.2.1 Textural Observations and Line Broadening Experiments

Figures 65 – 68 show high-magnification electron micrographs of the matrix structure, in a region relatively free from crystalline inclusions. The textured appearance is very obvious in these photographs, all of which were obtained from the same specimen.

The mean dimension of the texture as measured from the photographs in Figs. 65 to 68 is approximately 70 Å. This texture effect could be due either to thickness variations on a very small scale, perhaps produced by chemical thinning, or to diffraction contrast. If the latter is the case, then the texture is indeed due to individual crystallites oriented more or less at random, the dark areas arising from those crystallites which are oriented properly for diffraction. For diffraction contrast to be sharp, the specimen must be no more than several crystallite diameters in thickness; otherwise, contrast is lost due to multiple diffraction. Indeed, Fig. 65 shows a distinct diminution of contrast with increasing distance from the edge.

Other features to note in examining Figs. 65 to 68 are the extremely jagged edges and the absence of thickness contours near the edges. These effects are also indications of a small crystallite size material.

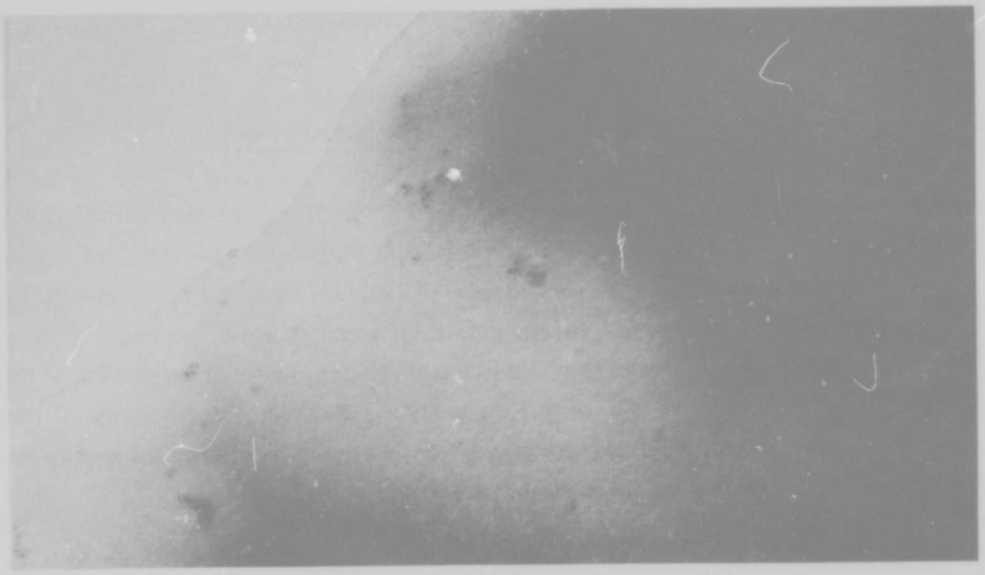

Fig. 65 Structure of Chemically Thinned Boron Filament, Showing Texture Effect. 44,000×. P1499-10a

Fig. 66 Same Area as in Fig. 65, at Higher Magnification. 183,000×. P1499-10b

Fig. 67 Another Example of the Textured Appearance of Thinned Boron Filament. 183,000×. P1493-4a

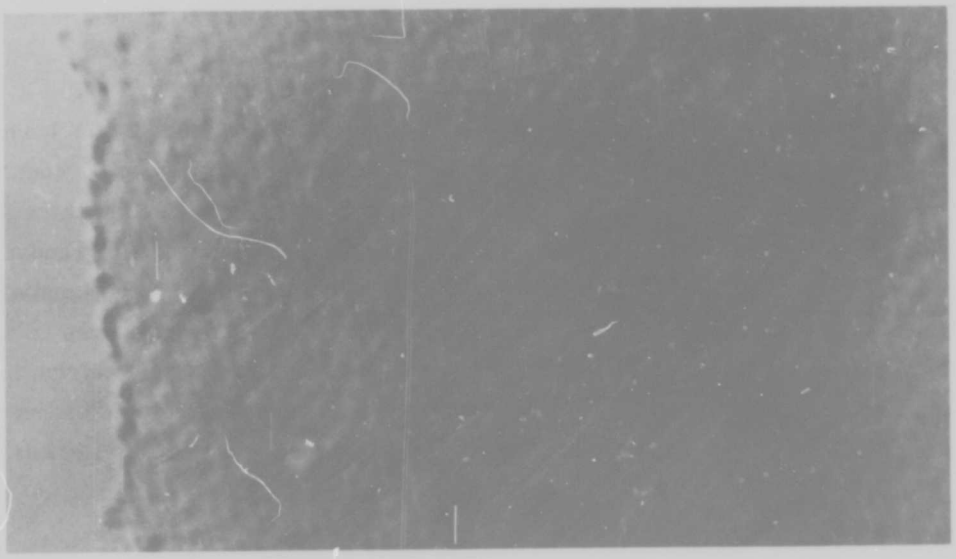

Fig. 68 Another Area of the Same Specimen, Near That of Fig. 67. 183,000×. P1493-4b

To establish that the texture represents true diffraction contrast, two approaches are possible:

(1) Study and compare the granular detail in the image at different tilt angles
(2) Study the broadening of the halo diffraction pattern to ascertain whether a consistent result is obtained between the directly measured texture dimensions and the crystallite size required to produce the observed broadening.

These two approaches are discussed below:

(1) Tilting Experiment

If an image in the electron microscope shows a granular texture, it is possible to establish whether the texture is produced by diffraction contrast by tilting a selected region through 5° or more and comparing the granular detail in the two micrographs. If crystalline regions are responsible for the texture, the tilt will change the diffraction conditions for many of the crystallites, and a change in granular detail will be produced (Ref. 42). If the texture is due to thickness variations, there will be essentially no change in appearance.

This experiment was performed several times by preparing a suitably thin boron filament specimen, locating an area with some distinguishing feature, and photographing it at two different angles of tilt at least 5° apart. Figures 69 to 71 show three pairs of images at different tilts. It is apparent that there is some change in granular detail at the different tilts, but these micrographs are not considered to be conclusive evidence by themselves. Specimen motion and vibration during the exposures as well as slight differences in focusing conditions could also have been factors contributing to the slight differences in appearance. It was found that a comparable difference in detail was sometimes obtained with two different exposure times at the same tilt (Fig. 72).

(2) Analysis of Line Broadening

The characteristic halo pattern arising from the textured material shown in Figs. 65 to 68 provides the most insight into the nature of the structure of vapor-deposited boron.

(a)

(b)

Fig. 69 Tilting Experiment 1. 183,000×. (a) 0° Tilt. (b) +6° Tilt. P1580-1a and 1581-2a

(a)

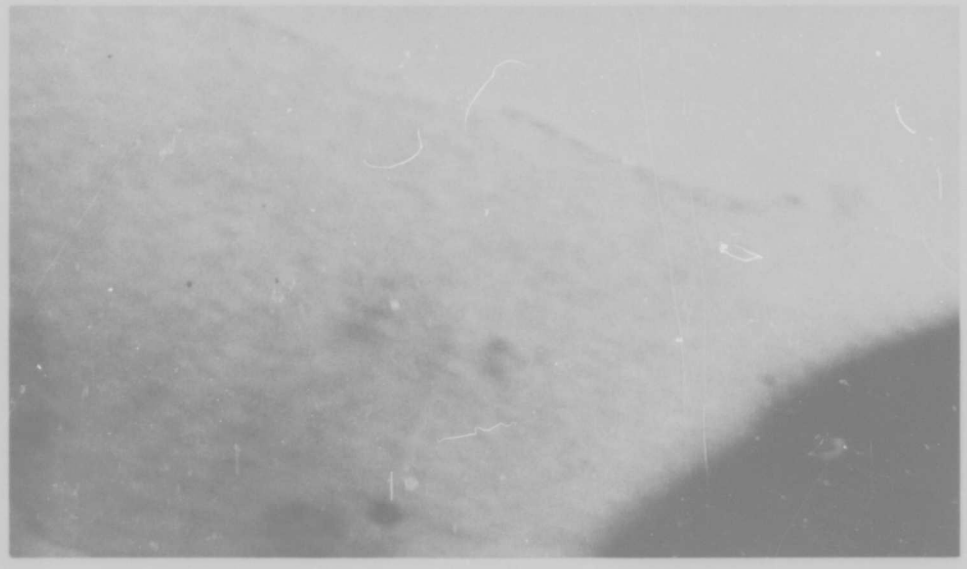

(b)

Fig. 70 Tilting Experiment 2. 183,000×. (a) -4° Tilt. (b) +2° Tilt. P1589-10a, and 1590-11a

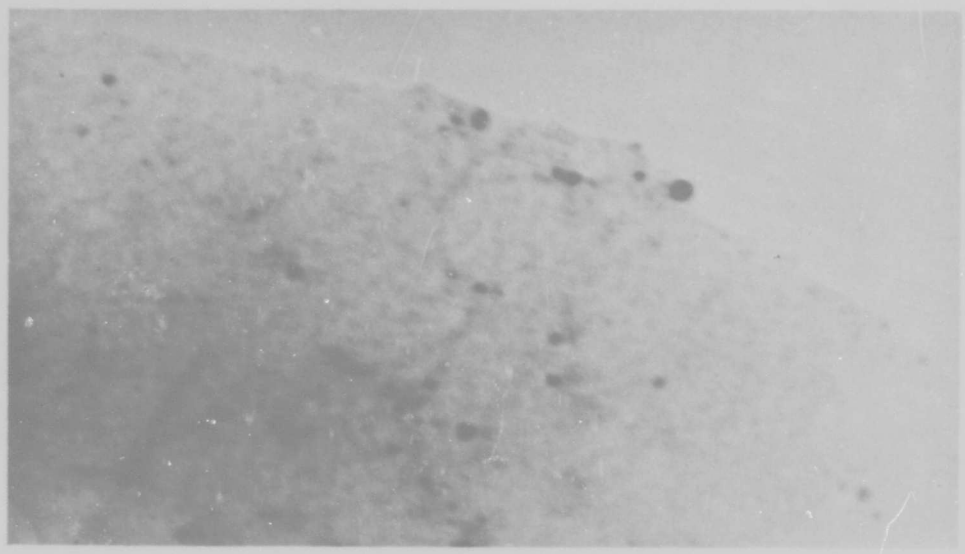

(a)

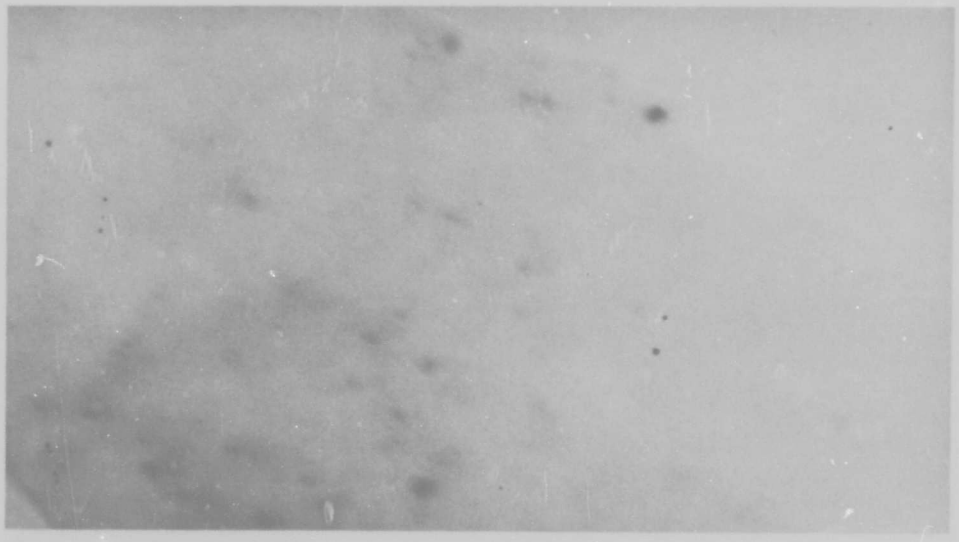

(b)

Fig. 71 Tilting Experiment 3. 183,000×. (a) +2° Tilt. (b) -4° Tilt. P1591-12a and 1592-13a

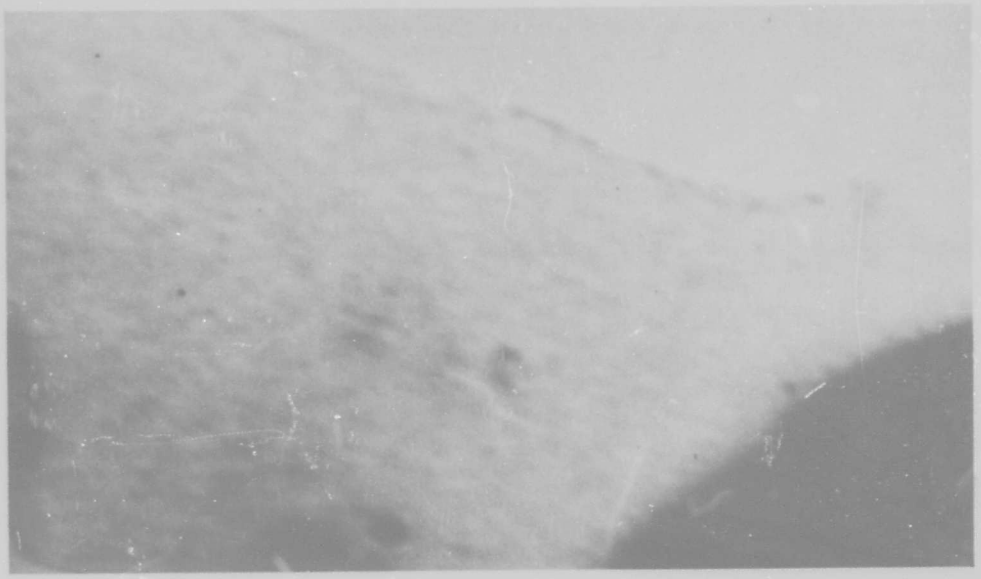

(a)

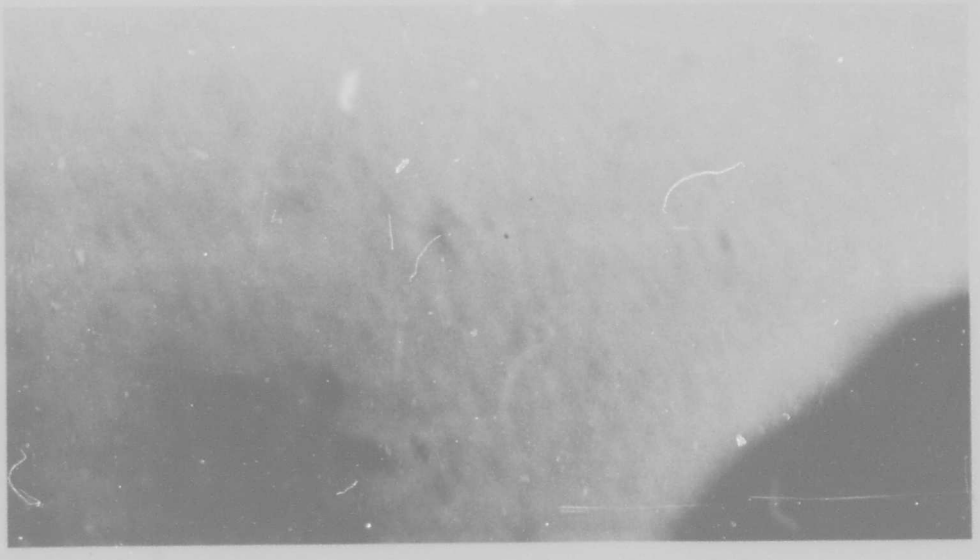

(b)

Fig. 72 Illustration of Change in Granular Detail With Exposure Time at Constant Tilt (+2°). 183,000×. (a) Long exposure. (b) Short exposure. P1590

If one considers the intensity variation of successive halos (Table 22, Section 4.4.1) it becomes immediately apparent that the material is not "liquid-like" amorphous. If it were, each successive halo would, of necessity, be less intense then the preceding one, and in any event six well-developed halos would never be observed (Ref. 43). The presence of several maxima is a clear indication that the material is actually crystalline, with its diffraction lines broadened by one or another of several causes which will now be discussed.

In general, the broadening of a diffraction line may be due to any or all of the following causes:

(a) Non-uniform strain
(b) Stacking faults
(c) Small size of the diffracting crystallites

The probable magnitudes of each of these contributions are considered below for the case of the boron filament halo pattern.

(a) Strain. Strain broadening can be estimated from the maximum residual strain

$$e_{max} = \frac{\sigma_R}{E} \tag{23}$$

where σ_R is the maximum residual stress, tensile or compressive, and E is Young's modulus.

For boron filaments, $\sigma_R \approx 3 \times 10^5$ psi (Ref. 13) and $E \approx 6 \times 10^7$ psi. These values yield

$$e_{max} \approx 5 \times 10^{-3}$$

The strain broadening of a diffraction line, in radians, is given by

$$\beta \text{ (strain)} = \Delta(2\theta) = -2 \frac{\Delta d}{d} \tan \theta \tag{24}$$

where $\Delta d/d$ is the strain expressed as a fractional change in interplanar spacing. To obtain the maximum tensile (or compressive) strain alone, the value of $\Delta d/d$ must be divided by two. Thus

$$\beta \text{ (strain)} = 4\, e_{max} \tan \theta \qquad (25)$$

where θ is the Bragg angle (Ref. 44).

Referring to Fig. 49, $\theta \approx 10°$ for the first halo, measured with CuKα radiation. Because $\tan 10° = 0.176$,

$$\beta \text{ (strain)} = \Delta(2\theta) = 4 \times (5 \times 10^{-3}) \times (0.176) \times 57.3$$

$$\approx 0.2°(2\theta)$$

From Fig. 49, the measured breadth is approximately $2.5°\ 2\theta$, much larger than that due to strain alone. It should be noted that the halo boundaries indicated in Fig. 49 were determined by eye from the electron microscope plate, and the d-spacings corresponding to the boundaries were converted to 2θ (CuKα). These measurements agree well with the half-maximum line breadth determined from a densitometer trace of the halos on a Debye-Scherrer x-ray film; thus, the halo boundaries shown may be considered to give the breadth of the halos at half maximum intensity. The above analysis clearly shows that strain alone cannot account for the observed broadening. Even if the first halo consists of more than one reflection, the breadth of each individual line would still have to be much larger than 0.2° to result in the continuous distribution of intensity observed in the halos.

(b) Faulting. Stacking fault contrast or stacking fault fringes have never been observed in thinned filament material which gives the characteristic halo pattern. Light microscopy and x-ray diffraction studies have shown that vapor-deposited boron has no preferred orientation; therefore, evidence of stacking faults should be apparent in the

electron microscope images if the crystallite size is considerably larger than 100 Å and if stacking faults are a common occurrence in vapor-deposited boron. If the crystallite size is smaller than 100 Å, the line broadening will be dominated by the crystallite size contribution. Stacking faults could contribute to the line breadths but there must be some independent evidence of their existence.

(c) Crystallite Size Determination. To calculate the broadening due to small crystallite size, an estimate of the average dimensions of the crystallites must be obtained.

One estimate can be made on the basis of the texture shown in Figs. 65 – 68, i.e., the 70 Å value reported previously. The broadening due to crystallites of this size may be calculated from the Scherrer equation

$$\beta = \Delta(2\theta) = \frac{\lambda}{D \cos\theta} \tag{26}$$

where D is the mean crystallite size, λ is the wavelength of the radiation used, and θ is the Bragg angle. Referring to Fig. 49, the first halo, measured with CuKα radiation, has $\theta \approx 10°$, $\cos\theta = 0.985$. Using λ(CuKα) = 1.542 Å and D = 70 Å, we obtain

$$\beta = \frac{1.542 \times 57.3}{70 \times 0.985}$$

$$= 1.3°$$

Thus, a 70 Å crystallite size is too large to account for the observed broadening (2.5°). Again referring to Fig. 49, it may be argued that the first halo is actually a doublet, consisting of either the (00·3) and (10·1) reflections of α-boron, or the (200) and (111) reflections of "simple" tetragonal boron. If a composite peak is constructed from the two α peaks, each taken with its maximum at the theoretical Bragg angle

and each broadened by a 70 Å crystallite size, i.e., each broadened by 1.3°, then the composite breadth is actually only 1.7°. If a composite peak is constructed using instead the two tetragonal peaks, the peak separation is so great that the doublet is well-resolved for 1.3° broadening.

If all the observed broadening is due to small crystallite size, the above analysis may be inverted so as to calculate the crystallite size necessary to produce the observed broadening. In the x-ray case, using CuKα radiation, the breadth of the first halo is approximately 2.5°. Thus, neglecting the effect of the doublet,

$$D = \frac{\lambda \times 57.3}{\beta \cos \theta} = \frac{1.542 \times 57.3}{2.5 \times 0.985} = 36 \text{ Å}$$

Using CrKα radiation, the breadth of the (00·3) component of the first halo is about 4° (see Fig. 4[illegible]. Ignoring any two-dimensional lattice effects and taking λ(CrKα) = 2.29 Å, $\theta = 15°$, $\cos \theta = 0.966$,

$$D = \frac{2.29 \times 57.3}{4 \times 0.966} = 34 \text{ Å}$$

[If the halo is considered to be due to the (200) and (111) reflections of tetragonal boron, as discussed in Section 4.3.2, similar results are obtained.]

The same calculation can be made in the electron diffraction case. By measuring the width ΔD of the second halo (d = 2.55 Å) on the diffraction plate, and using the value of the microscope effective camera length L (see Fig. 76), the breadth of the second halo is found to be

$$\beta = \frac{\Delta D}{L} = \frac{1.5 \text{ mm}}{928 \text{ mm}} = 1.6 \times 10^{-3} \text{ rad}$$

$$= 0.093°$$

Taking $\lambda = 0.037$ Å for 100 kV electrons and $\cos\theta = 1.0$,

$$D \approx \frac{\lambda}{\beta} = \frac{0.037}{1.6 \times 10^{-3}}$$

$$= 23 \text{ Å}$$

This value is slightly small because the second halo is also a doublet, consisting of either the α-boron (10·4) and (11·0) reflections (see Fig. 49), or the (002) and (131) reflections of tetragonal boron (Fig. 51).

As a final check, refer to the fourth halo in Fig. 49. This is a singlet, consisting of the α-boron (02·4) reflection (d = 1.77 Å). The measured breadth is 4°, and the Bragg angle $\theta = 26.1°$, $\cos\theta = 0.898$. Thus

$$D = \frac{1.542 \times 57.3}{4.0 \times 0.898}$$

$$= 25 \text{ Å}$$

The results of these measurements are summarized in Table 31.

Table 31

CRYSTALLITE SIZE VALUES CALCULATED FROM HALO LINE BREADTHS

Halo	Doublet	Method	Calculated D, Å
1	Yes	ED converted to CuKα	36
1	Yes (resolved)	XRD CrKα	34
2	Yes	ED	23
4	No	ED converted to CuKα	25

Thus an average crystallite size of about 30 Å is necessary to produce the observed broadening, if it is assumed that in fact all the broadening is due to small crystallite size.

4.4.2.2 Small Beam Diffraction Experiments

To obtain a more direct measure of the size of the diffracting crystallites, the following experiment was performed. A suitably thin region of a specimen of chemically thinned boron filament was located in the electron microscope, and a series of halo patterns were photographed using smaller and smaller openings of the selected area aperture and exposing for long times (0.5 - 1 hour). When the projected aperture dimensions were reduced to give a diffracting area of about 250 Å × 250 Å, a diffraction pattern was obtained which showed distinct arcing of the second halo: three distinct arcs were observed, superimposed on a faint continuous halo background (Fig. 73). The halo appeared to be as broad as the same halo photographed under normal conditions; however, the breadths of weak, broad lines are very difficult to measure accurately.

At a somewhat larger projected aperture opening, approximately 600 Å × 600 Å, only continuous halos were observed (Fig. 74). For comparison, a diffraction pattern from a specimen of vapor deposited gold is shown in Fig. 75. In this case, the projected aperture size is 0.5μ × 0.5μ, and the diffraction rings are discontinuous, indicating a much larger crystallite size. (The large crystallite size is also indicated by the very small size of the individual diffraction spots.)

Figure 76 shows the measurements made on the discontinuous halo pattern of Fig. 73. Each of the three distinct arcs found on the second halo had a breadth β equal to that of the halo itself i.e., about 0.09°, and an angular width of about 12°. Because the circumferential width of each arc was approximately twice its radial breadth, it is possible that each arc was due to diffraction from two or more crystallites having very nearly the same orientation.

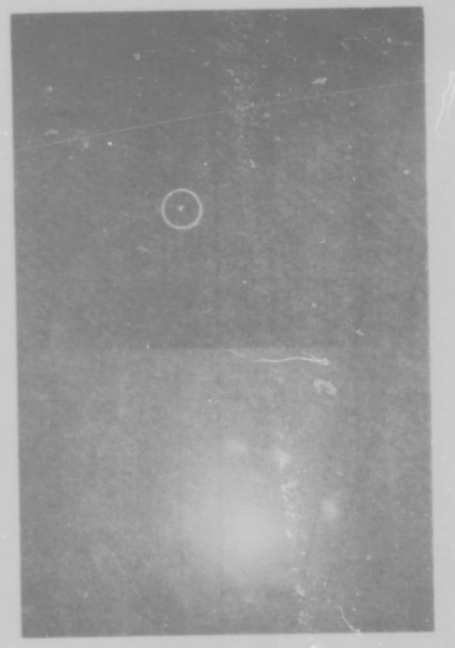

Fig. 73 Three Maxima Superimposed on Second Halo. Projected aperture dimensions 250 Å × 250 Å. 12,500×. P1219

Fig. 74 Continuous Halo Pattern. Projected aperture dimensions 600 Å × 600 Å. One hour exposure. 12,500×. P1220

Fig. 75 Spotty Ring Pattern From Vapor Deposited Gold. Projected aperture dimensions 0.5 μ × 0.5 μ. 12,500×. P1216

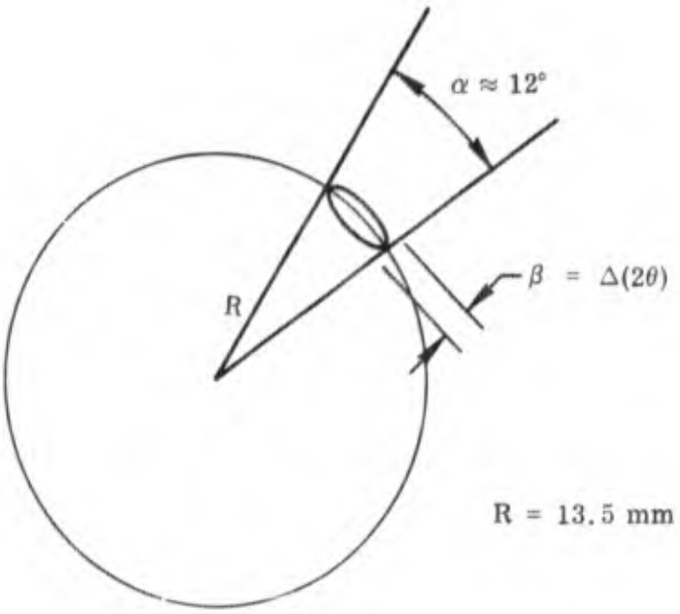

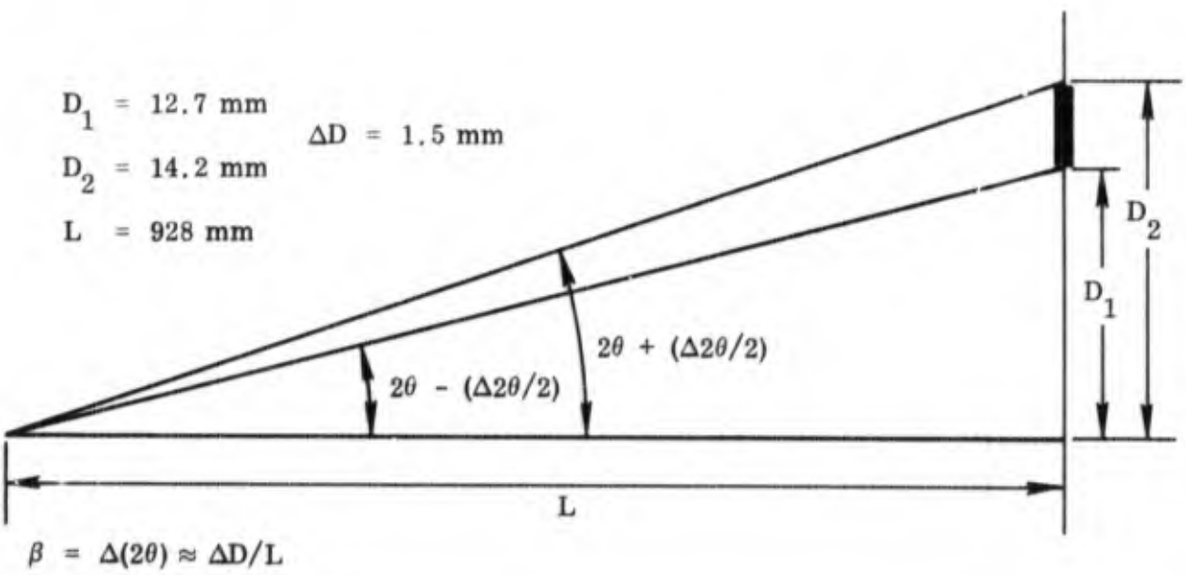

Fig. 76 Measurements Taken From Halo Pattern With Maxima, Shown in Fig. 73

An estimate of the size of the crystallites producing the discrete diffraction spots can be made as follows. Consider a diffracting volume of area A, bounded by the projected edges of the selected area aperture, and specimen thickness T. The number of crystallites in this volume, assuming uniform size and isotropy, is simply

$$N = \frac{AT}{D^3} \tag{27}$$

Now consider diffraction from one isolated crystallite. The probability $P(\theta_B)\,\Delta\theta$ that this crystallite is oriented properly for diffraction at Bragg angle θ_B is given (Ref. 44, p. 127) by

$$P(\theta_B)\,\Delta\theta = \frac{1}{2}\cos\theta_B\,\Delta\theta \tag{28}$$

The term $\Delta\theta$ involves the beam divergence, α_o, and also the breadth β associated with the reflection itself; thus, we can write, approximately,

$$\Delta\theta = \alpha_o + \beta \tag{29}$$

Then, the number, n, of crystallites oriented properly for diffraction at Bragg angle θ_B is given by

$$n = NP(\theta_B)\,\Delta\theta = \left(\frac{AT}{D^3}\right)\cdot\frac{\cos\theta_B}{2}(\alpha_o + \beta) \tag{30}$$

Now, n is exactly the number of diffraction spots observable on a particular ring of the diffraction pattern. Solving Eq. (30) for the crystallite size D yields

$$D = \left[\frac{AT\cos\theta_B}{2n}(\alpha_o + \beta)\right]^{1/3} \tag{31}$$

For the case shown in Fig. 73, $n = 3$, assuming each arc is due to only one crystallite. Typically, $\alpha_o \approx 4 \times 10^{-3}$ radian for a 500μ condenser aperture (Ref. 45). From Fig. 76, $\beta = \Delta D/L = 1.5/928 = 1.6 \times 10^{-3}$ rad. $A = 250 \times 250 = 6.25 \times 10^4$ $(\mathring{A})^2$. Then, assuming $T = 500$ Å, $\cos \theta_B \approx 1$, one obtains

$$D \approx 30 \text{ Å}$$

This is the correct magnitude to give the observed broadening. However, if the crystallites are of uniform size, the foil is $500/30 \approx 17$ crystallites thick which is certainly too many layers to permit good diffraction contrast. Also, the above analysis provides no explanation for the continuous, faint halo background.

Suppose, instead, that the crystallites are not of uniform size, but vary from unit cell dimensions (~5 Å) up to about 100 Å. Then the larger crystallites, in the range 50–100 Å, are the ones which produce the textured appearance of the images. With this assumption, consider again the same diffracting volume, i.e.,

$$A = 250 \times 250 \ (\mathring{A})^2 = 6.25 \times 10^4 \ (\mathring{A})^2$$

$$T = 500 \text{ Å}$$

For this thickness, crystallites of the order of 100 Å should be distinguishable by diffraction contrast, since only 5 layers of this size crystallite are involved. In this diffracting volume, the maximum number of 100 Å crystallites would be

$$N = \frac{AT}{D^3} = \frac{6.25 \times 5 \times 10^6}{10^6} \approx 30$$

Now, since

$$P(\theta_B) \, \Delta\theta \approx \frac{1}{2} \times 5.6 \times 10^{-3},$$

it is obvious that

$$n = NP(\theta_R)\,\Delta\theta << 1$$

Physically, this means that the probability is very small that any of the 30 or so large crystallites are oriented correctly for diffraction. This small probability of diffraction by the larger crystallites explains the fact that, although the experiment in Fig. 73 was duplicated many times, only occasionally was any arcing observed in the halos (see Figs. 77, 78, and 79). In all cases, however, a continuous halo pattern was observed, even for the smallest selected area aperture size. To obtain a continuous halo, complete overlapping of individual diffraction spots must occur. If we assume that each diffraction spot is symmetrical, i.e., its radial and circumferential dimensions are equal, then the minimum number required to form a completely continuous ring (assuming no preferred orientation) can be estimated as

$$n_o = \frac{2\pi R}{\beta L} = \frac{2\pi RD \cos\theta_B}{L\lambda} \qquad (32)$$

where R is the radius of the diffraction ring, L is the camera length, and βL is the mean dimension of a diffraction spot (equal to the breadth of the ring). Suppose that the continuous faint halos originate from very small crystallites, say D = 10 Å. Then, from Eq. (32), taking R = 13.5 mm as in Fig. 76 (second halo), λL = 35 Å-mm, and $\cos\theta_B = 1$,

$$n_o = \frac{2\pi \times 13.5 \times 10}{35} \approx 25$$

From Eq. (29),

$$\Delta\theta = \alpha_o + \beta$$

$$= \alpha_o + \frac{\lambda}{D}$$

Fig. 77 Thirty Minute Exposure, Projected Aperture Size 200 Å × 200 Å. Only continuous halos are visible. Diffraction pattern shown at 2×, image of aperture (circled)at 24,000×. P1502

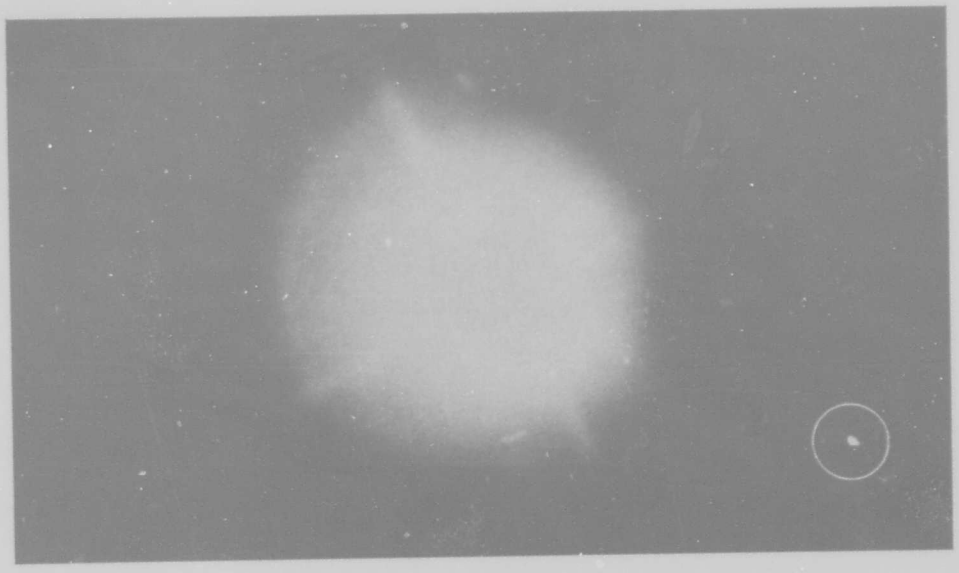

Fig. 78 Seventy Minute Exposure, Projected Aperture Size 500 Å × 500 Å. Some maxima are visible on second halo. Diffraction pattern shown at 2×, image of aperture (circled) at 24,500×. P1394

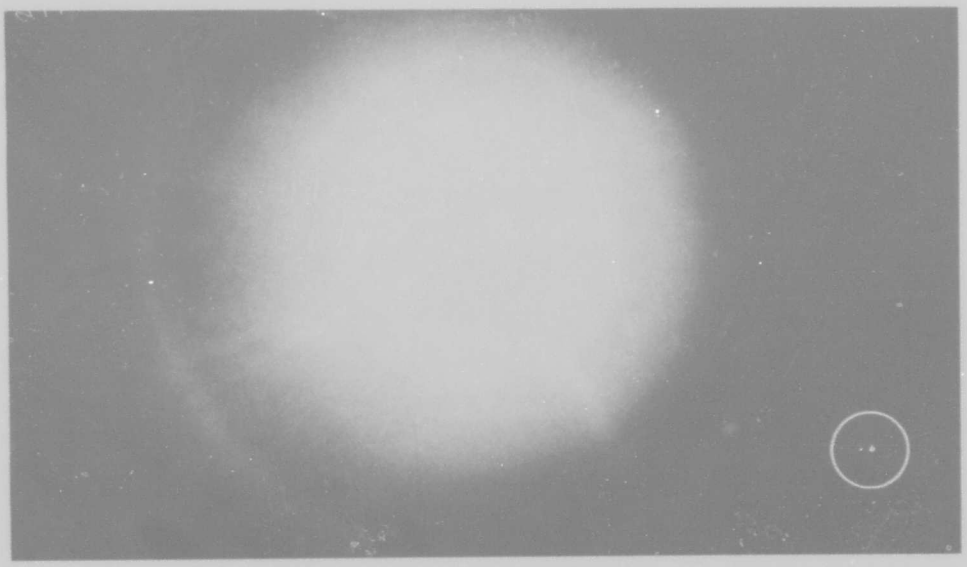

Fig. 79 Thirty-Five Minute Exposure, Projected Aperture Size 300 Å × 300 Å. Only continuous halos are visible. Diffraction pattern shown at 2×, image of aperture (circled) at 24,000×. P1464

Using $\lambda = 0.037$ Å for 100 kV electrons and $\alpha_o = 4 \times 10^{-3}$ as before,

$$\Delta\theta = 4 \times 10^{-3} + 3.7 \times 10^{-3}$$

$$\approx 8 \times 10^{-3} \text{ rad}$$

Now note that if a halo consists of M different, closely spaced reflections, then the total probability of scattering into the halo is just the sum of the probabilities for scattering by each component reflection. Thus

$$P(\hat{\theta}_{halo})\,\Delta\theta = \Delta\theta \sum_{i=1}^{M} P(\theta_i) \tag{33}$$

$$= \frac{1}{2}\Delta\theta \sum_{i} \cos\theta_i$$

In the electron diffraction case, all the Bragg angles are very small and nearly equal.

$$\therefore\ P(\hat{\theta}_{halo})\,\Delta\theta \approx \frac{M}{2}\Delta\theta$$

Taking $M = 2$, which is exact for the first two halos (see Fig. 49),

$$P(\hat{\theta}_{halo})\,\Delta\theta \approx \Delta\theta = 8 \times 10^{-3}$$

Thus from Eq. (30), the total number of 10Å crystallites required to produce a single continuous diffraction ring must be

$$N = \frac{n_o}{P(\hat{\theta}_{halo})\,\Delta\theta} = \frac{25}{8 \times 10^{-3}} \approx 3 \times 10^{3}$$

Because approximately the same number would be required for each halo, the total number of crystallites for the entire pattern of 5 or so halos is

$$N_T = 5 \times 3 \times 10^3 \approx 10^4$$

The smallest diffracting volume used in these experiments was estimated to be

$$AT = 200 \times 200 \times 500 \ (\text{Å})^3$$

$$= 2 \times 10^7 \ (\text{Å})^3$$

The volume occupied by 10^4 crystallites of mean dimension 10 Å is about half of this, which would leave room for about $10^7/10^6 = 10$ crystallites of 100 Å dimensions, and these crystallites account for the texture visible in the images.

The fact that extensive broadening of the faint continuous halo pattern is not observed for very small diffracting volumes, as would be expected if the pattern is due to extremely small crystallites, may be explained by the following: the halo pattern in the small aperture experiments is so weak that it is completely invisible on the fluorescent screen. The 1-hour exposures used were probably only sufficient to produce blackening of the plate near the maxima of the halos, so the entire breadth was not recorded.

4.4.2.3 Summary of Crystallite Size Determinations

In this section, evidence has been presented to show that the structure of vapor-deposited boron, exclusive of the large crystalline inclusions, consists of extremely small crystallites with a size distribution in the range 10−100 Å. The main points may be summaried as follows:

(1) High magnification images of the matrix structure consistently show a uniform texture having a mean dimension of about 70 Å. Tilting experiments suggest

that the texture is possibly due to diffraction contrast, indicating that actual crystallites of this dimension are being imaged.

(2) An average crystallite size of about 30Å accounts adequately for the observed broadening of the halos.

(3) Diffraction patterns obtained from extremely small volumes show occasional isolated spots superimposed on a continuous halo pattern. For the small-aperture case, the appearance of continuous halos requires that the majority of the diffracting crystallites have dimensions on the order of 10Å. The larger crystallites have much smaller probabilities of being oriented correctly for diffraction.

(4) The structure cannot be liquid-like amorphous because of the numerous well-defined halos and their intensity distribution.

(5) A size distribution of crystallites from 10 – 100 Å explains all the experimental observations:

   (a) The large crystallites, near 100 Å, are imaged directly.

   (b) The average crystallite size, integrating over the entire distribution, is about 30 Å.

   (c) The diffraction pattern obtained for "large" (micron-size) selected areas arises from a random sampling of the entire distribution. Thus, the broadening can be calculated exactly from the average crystallite size.

   (d) The diffraction pattern obtained for small (~100 Å size) selected areas arises from a preferential sampling of the small (~10 Å) crystallites. Occasional, favorably oriented, larger crystallites (~100 Å) can produce isolated arcs on the halo pattern.

4.4.3 Grinding Experiments

A number of samples of ground boron filaments and crystalline β-rhombohedral boron were examined in the electron microscope. The samples were ground in a boron carbide mortar and pestle. The grindings were suspended in ethanol and picked up on evaporated carbon substrates for examination. These experiments were initially motivated by observations of investigators at Aerospace Research Laboratories (Ref. 10) who noted that grindings of filaments and β-rhombohedral boron gave similar single crystal spot patterns, especially the [00·1]. These investigators postulated that the diffuse halos observed in x-ray diffraction studies of whole filaments were caused by groups of strain-broadened reflections of β-rhombohedral boron, and that grinding the filaments relieved the residual stresses, causing single-crystal spot patterns of crystalline β-boron to be observed in the microscope. In Section 4.3, this hypothesis is shown to be incorrect.

The electron microscope observations of grindings made during the course of this work are presented in the following sections.

4.4.3.1 Ground β-rhombohedral Boron

A number of different crystallographic orientations were observed in addition to the [00·1], which was actually observed very infrequently. Figures 80 –84 show samples of five indexed patterns. It will be noted that the patterns in Figs. 80, 82, and 83 are missing certain reflections. Thus, in Fig. 80, the $(\bar{2}1\cdot 0)$ and $(2\bar{1}\cdot 0)$ reflections, as well as all those obtained by adding the (02·1), (04·2), (06·3), etc. to these reflections, are missing. Figure 82 is the same as Fig. 85, to be discussed presently. In Fig. 83, the $(01\cdot\bar{1})$ and $(0\bar{1}\cdot 1)$ reflections, as well as all those obtained by adding the (00·3), (00·6), etc. to these reflections, are missing. Table 32 shows some of the measured and calculated d-spacings and angles for the pattern of Fig. 83; the good agreement indicates the correctness of the indexing.

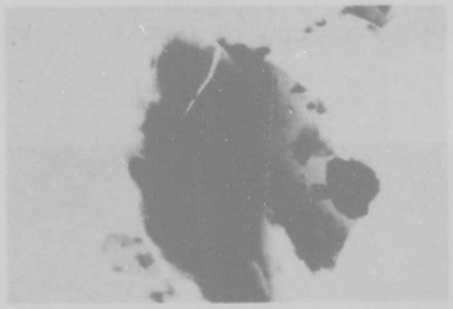

(a)

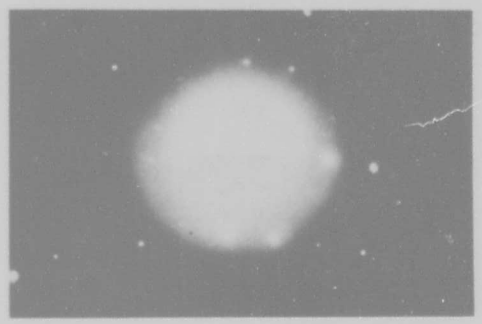

(b)

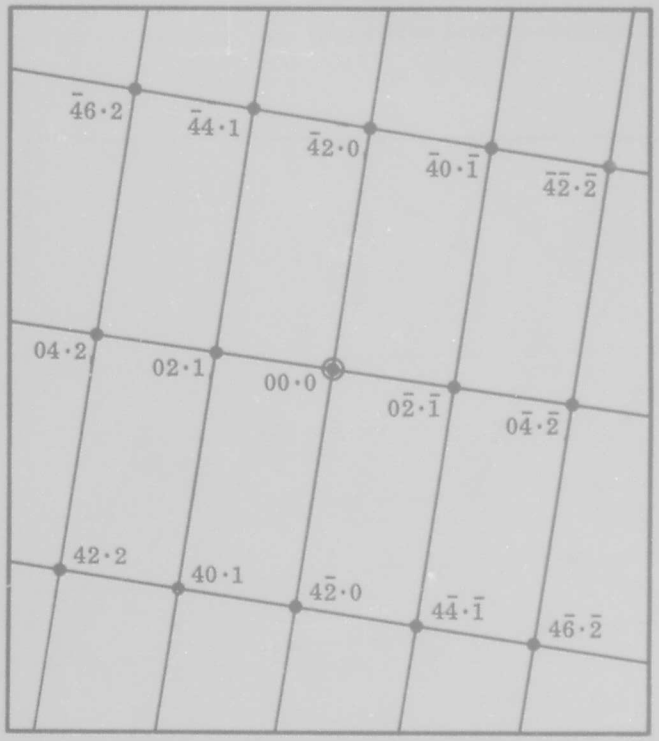

(c)

Fig. 80 Ground β-Rhombohedral Boron, Example 1. (a) Image 17,000×. (b) Diffraction pattern obtained from particle in (a). (c) Indexed pattern: β $[01\cdot\bar{4}]$; P694

(a)

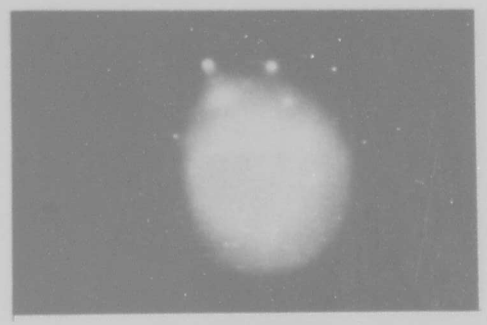

(b)

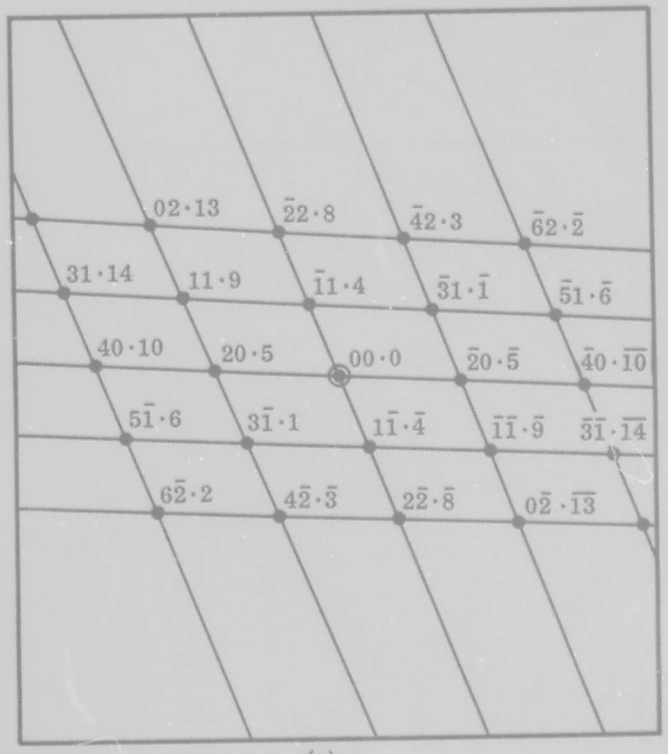

(c)

Fig. 81 Ground β-Rhombohedral Boron, Example 2. (a) Image 19,500×. (b) Diffraction pattern obtained from particle in (a). (c) Indexed pattern: β $[\bar{1}7\cdot\bar{2}]$; P696

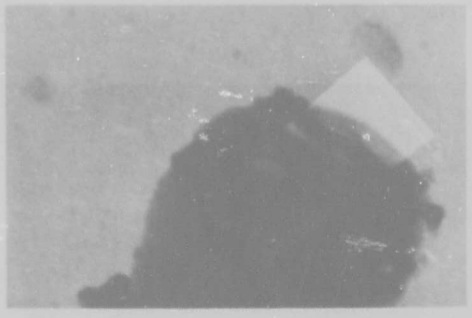

(a)

(b)

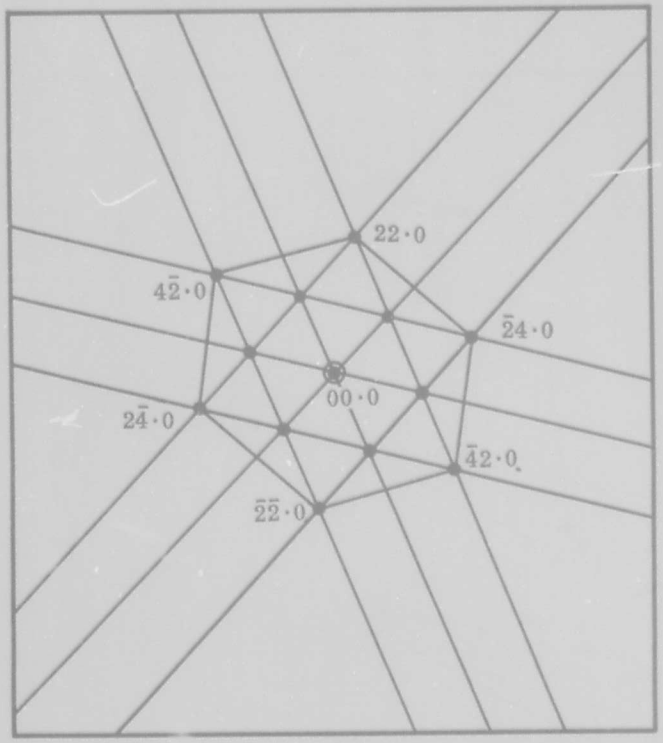

(c)

Fig. 82 Ground β-Rhombohedral Boron, Example 3. (a) Image 15,750×. Note bend contours. (b) Diffraction pattern obtained from area shown in (a). (c) Indexed pattern: β [00·1]; P931

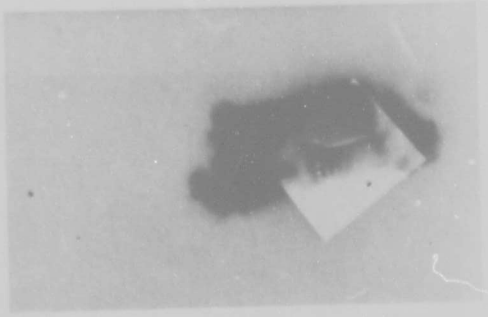

(a)

(b)

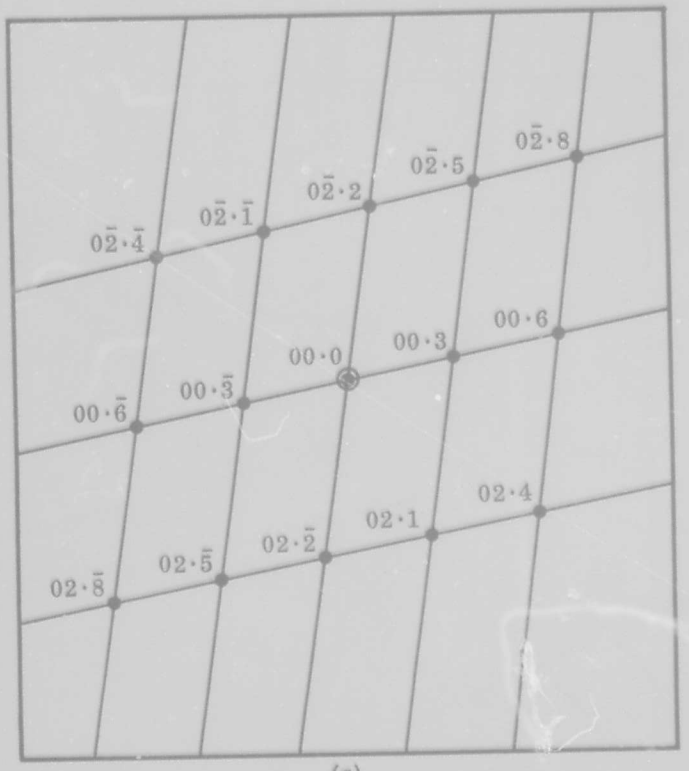

(c)

Fig. 83 Ground β-Rhombohedral Boron, Example 4. (a) Image 16,500×. (b) Diffraction pattern from area shown in (a). (c) Indexed pattern: β $[2\bar{1}\cdot 0]$; P926

(a)

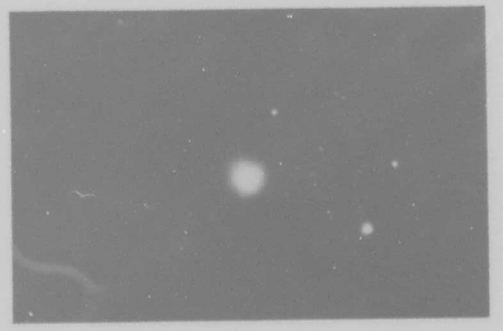

(b)

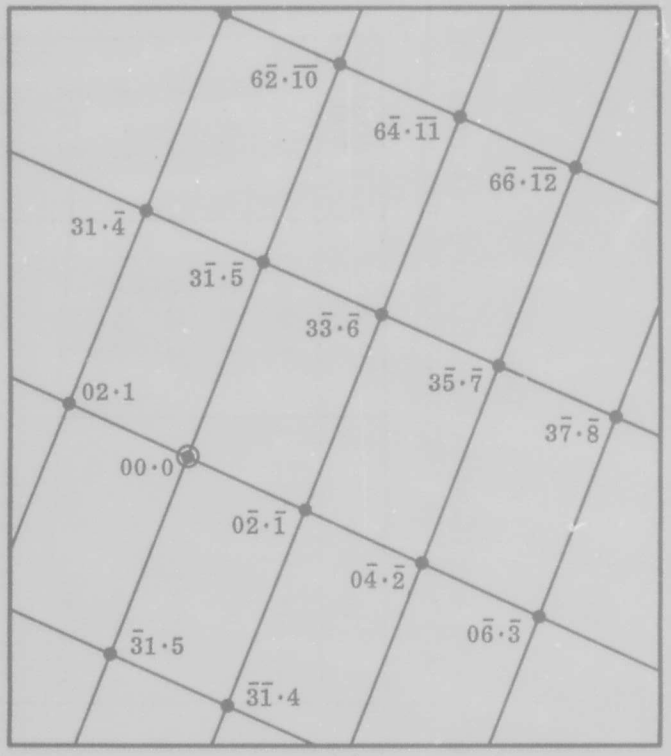

(c)

Fig. 84 Ground β-Rhombohedral Boron, Example 5. (a) Image 15,750×. (b) Diffraction pattern from area shown in (a). (c) Indexed pattern: β [$7\bar{5}\cdot6$]; P929, and P930

Table 32

COMPARISON OF MEASURED AND CALCULATED d-SPACINGS AND ANGLES FOR DIFFRACTION PATTERN SHOWN IN FIG. 83(c)

Quantity	Measured Value	Calculated Value
β d (00·3)	7.66 Å	7.90 Å
β d (02·$\bar{2}$)	4.68 Å	4.40 Å
β d (02·1)	4.82 Å	4.65 Å
β d (02·4)	3.66 Å	3.70 Å
β d (00·6)	3.83 Å	3.95 Å
$\measuredangle$ (00·3), (0$\bar{2}$·2)	69.5°	68°12'
$\measuredangle$ (00·3), (0$\bar{2}$·5)	45.0°	45°0'
$\measuredangle$ (02·1), (0$\bar{2}$·8)	104.5°	110°42'
$\measuredangle$ (02·4), (00·3)	46.5°	51°20'
$\measuredangle$ (02·$\bar{5}$), (02·4)	89.5°	83°40'

Figure 85(a) shows another example of the [00·1] β-boron spot pattern, this time in more nearly exact orientation. Although this particular pattern was obtained from a sample of pure β-rhombohedral boron (ground for 30 minutes in a B_4C mortar), the same pattern has been observed in filament grindings (see Fig. 92). However, in both situations, this pattern is observed infrequently. It is of interest to discuss this pattern in some detail, since it has been the source of considerable controversy in the interpretation of the structure of boron filaments. A paper was recently published in which this pattern, observed in a sample of ground filament, was offered as the principal evidence for the existence of profuse faulting in the boron filament structure (Ref. 31). The authors of this paper observed that the hexagonal pattern remained essentially unchanged when the specimen was tilted through ±30° in the microscope, indicating long rel-rods normal to the plane of the pattern. They indexed the pattern as fcc [111], with rel-rods through certain reflections from neighboring planes of the reciprocal lattice. These rel-rods intersect the central plane at points which can be indexed on a hexagonal axis system. Although the authors presented a self-consistent indexing scheme, several difficulties were found to exist in their overall interpretation and a paper has since been written discussing these points (Ref. 32). Because this hexagonal pattern has been observed in grindings of pure β-rhombohedral boron, it must be indexed using the known β-boron parameters.

Figure 85(c) presents the proper indexing which accounts for all the observed diffraction spots in terms of d-spacings and interplanar angles of β-rhombohedral boron. The pattern includes contributions from three adjacent reciprocal lattice planes.

Figure 85(b) indicates the d-spacing measurements made on the diffraction pattern shown in Fig. 85(a), and Table 33 shows the measured d-spacings, the assigned indices, and the spacings calculated from these indices using the published (rhombohedral) parameters for β-boron, i.e., $a_R = 10.12\,\text{Å}$, $\alpha = 65°28'$ (Ref. 33). The corresponding hexagonal parameters are

$$a_o = a_R\sqrt{2(1 - \cos\alpha)} = 10.944\,\text{Å}$$

$$c_o = a_R\sqrt{3(1 + 2\cos\alpha)} = 23.715\,\text{Å}$$

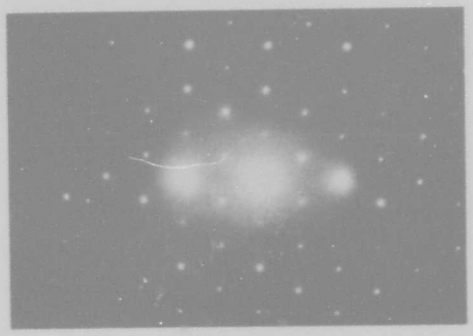

Fig. 85a Hexagonal Spot Pattern From Grindings of β-Rhombohedral Boron. β [00·1], exact orientation; P879

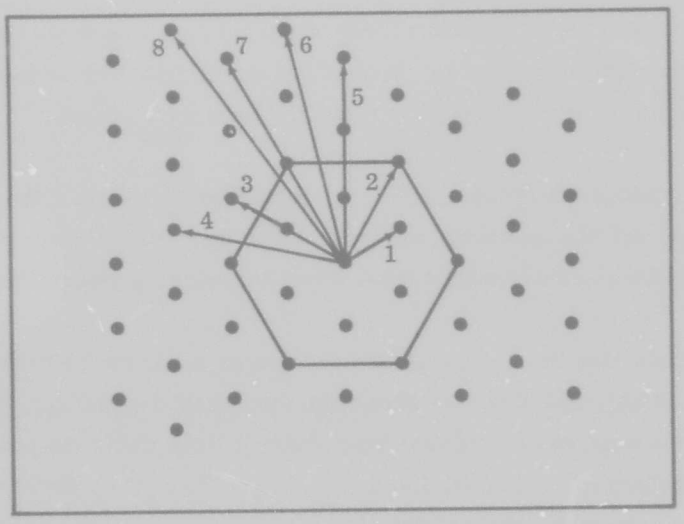

Fig. 85b Diagram of Diffraction Pattern Shown in (a), Indicating Succession of d-Spacing Measurements. Outlined hexagon is formed by six (22·0) type reflections.

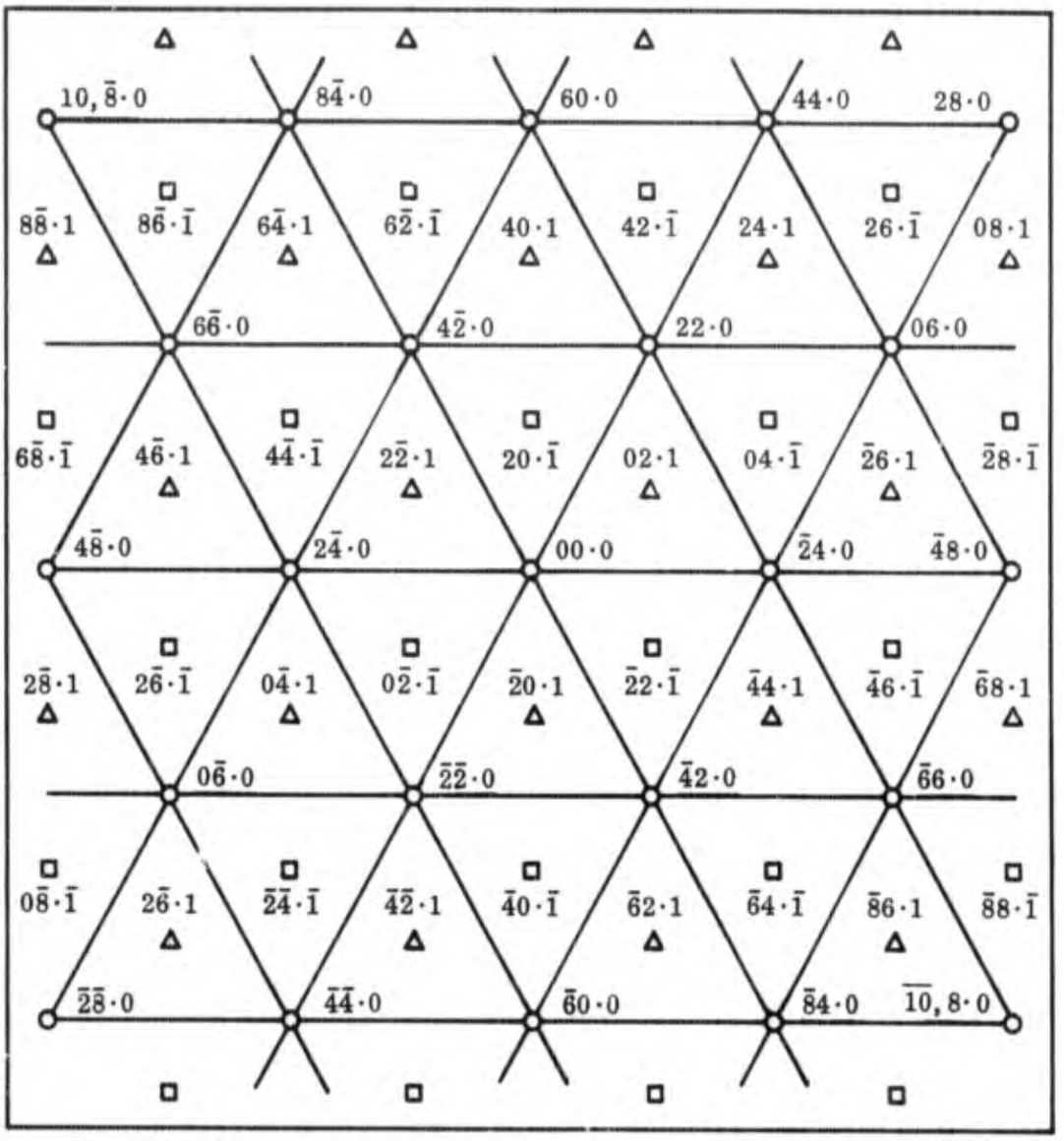

△ REFLECTION FROM PLANE ABOVE

□ REFLECTION FROM PLANE BELOW

Fig. 85c Complete Indexing of Hexagonal Spot Pattern. [Contributions from three layers of reciprocal lattice are observed; inner hexagon, formed by long rel-rods from reciprocal lattice points above and below central plane, gives projected d-spacings which correspond to "forbidden" reflections of the form (20·0)]

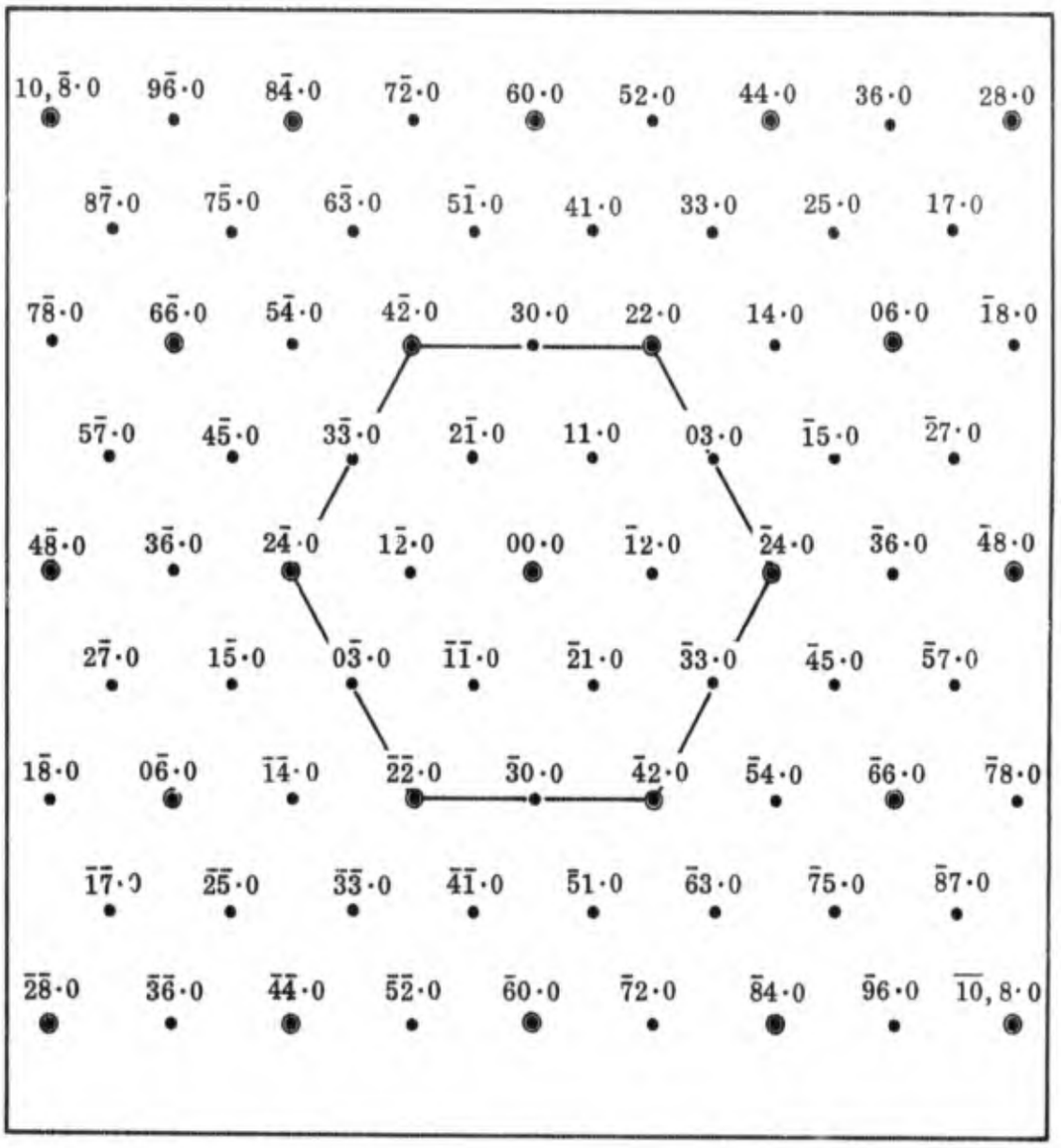

Fig. 85d One Complete Reciprocal Lattice Plane of β-Rhombohedral Boron, Normal to Main Diagonal. [Only reflections observed in pattern are those whose indices are even multiples of basis vectors (11·0) and (1$\bar{2}$·0)]

Note that the spots nearest the center of the pattern give d-spacings which correspond to reflections of the form $(20\cdot 0)$. These reflections are "forbidden," since they do not correspond to integral indices in the rhombohedral system. If we consider the adjacent reciprocal lattice planes positioned $1/c_o$ above and below the plane containing reciprocal lattice vectors of the form $(HK\cdot 0)$, i.e., planes having vectors of the form $(HK\cdot 1)$ and $(HK\cdot \bar{1})$, it becomes apparent that the innermost hexagon is formed by extensions of the reciprocal lattice points $(02\cdot 1)$, $(2\bar{2}\cdot 1)$, and $(\bar{2}0\cdot 1)$ from the plane above, and $(20\cdot \bar{1})$, $(0\bar{2}\cdot \bar{1})$, and $(\bar{2}2\cdot \bar{1})$ from the plane below. It is easily verified that

$$\left(\frac{1}{d_{02\cdot 1}}\right)^2 = \left(\frac{1}{d_{20\cdot 0}}\right)^2 + \left(\frac{1}{c_o}\right)^2$$

With the innermost hexagon indexed in this manner and the $(HK\cdot 0)$ reflections as in Table 33, the pattern is completely indexed [Fig. 85 (c)]. (The fact that the measured d-spacings shown in Table 33 are all slightly smaller than the corresponding calculated values is attributed to a slight error in the camera constant.)

The observed pattern thus consists of contributions from three planes of the reciprocal lattice superimposed, indicating very long rel-rods parallel to the c_o axis, as stated by the other investigators (Ref. 31). This indexing scheme is the only one possible using the parameters of β-rhombohedral boron; however, with this indexing, there exist a number of "missing" reflections. Examples of this have been cited earlier (Section 4.4.1, Figs. 62 and 63; Section 4.4.3, Figs. 80, 82,and 83), but the phenomenon was first noted in connection with the β [00·1]. The fact that this phenomenon has been observed in a number of different single crystal spot patterns of both α- and β-rhombohedral boron, all properly indexed, proves that the effect is a real one, not previously encountered. Figure 85(d) shows that if just one of the three reciprocal lattice planes contributing to the hexagonal pattern is considered, e.g., the $(HK\cdot 0)$, the only reflections observed are those which correspond to even multiples of the basis vectors $(11\cdot 0)$ and $(1\bar{2}\cdot 0)$. In Fig. 85(d), the complete reciprocal lattice plane $(HK\cdot 0)$ is shown, with the reflections actually observed indicated by circles. For further examples and discussion of the missing reflections problem, the reader should refer to Sections 4.3.2 and 4.4.4.

Table 33

MEASURED AND CALCULATED d-SPACINGS FROM HEXAGONAL SPOT PATTERN, FIG. 85 (b)

Number	Measured d, Å	β-Boron (HK·L)	Calculated[(a)] d, Å
1	4.68	(20·0)	4.74
2	2.69	(22·0)	2.74
3	2.34	($\bar{4}$4·0)	2.37
4	1.75	($\bar{6}$4·0)	1.79
5	1.56	(06·0)	1.58
6	1.29	($\bar{2}$8·0)	1.32
7	1.33	($\bar{4}$8·0)	1.37
8	1.06	($\bar{6}$,10·0)	1.09

[(a)]Using a_o = 10.944 Å, c_o = 23.715 Å, corresponding to a_R = 10.12 Å, $\alpha = 65°28'$.

Another problem associated with the pattern of Fig. 85 is the origin of the rel-rods. At first it was thought that they were produced by extreme thinness of the ground boron particles. This idea seemed to be in agreement with the ARL observation that the hexagonal spot pattern was most frequently observed in the case of extremely thin particles which could scarcely be distinguished from the carbon substrate. To obtain a direct measurement of the particle thickness, a sample of β-boron grindings (grinding time approximately 1 hour) was placed on a carbon substrate and shadowed with chromium. The shadowed particles were then examined in the microscope and their thicknesses were calculated from the measured lengths of the shadows. The measurements were complicated by the fact that the boron particles tended to agglomerate. The calculated thicknesses ranged from 100 to 1000 Å, with most near 1000 Å. However, even 100 Å is too thick to produce rel-rods of the required length. Figure 86 shows three examples of the shadowed particles of β-boron; note the pleated appearance of the particle in Fig. 86(c).

With crystal thickness apparently eliminated as a possible cause of the long rel-rods, attempts were made to obtain evidence for planar defects in the small β-boron crystallites. Figure 87(a) shows a particle with a set of parallel striations, which become strongly illuminated in dark field [Fig. 87(b)]. The corresponding diffraction pattern is shown in Fig. 87(c) and indexed in Fig. 87(d). The dark field image in (b) was taken with the objective aperture over the $(1\bar{4}\cdot\bar{4})$ reflection. Although several Kikuchi lines are visible in the diffraction pattern, no streaking of the diffraction spots can be seen to aid in identifying the crystallographic plane of the defects responsible for the striations. It is known that β-boron twins readily (see Section 3.4); thus, the striations are probably due to thin twins.

Figure 88 is an extremely thin particle of β-boron. The diffraction pattern shows fine structure in the diffraction spots, as discussed by Amelinckx (Ref. 46). By measuring the reciprocal distance ΔS between two successive minima in the fine structure, an estimate of the crystal thickness can be obtained. The result for the case shown is approximately 20 Å. This dimension is much thinner than the shadowing experiments indicated, and a crystal this thin could result in long rel-rods normal

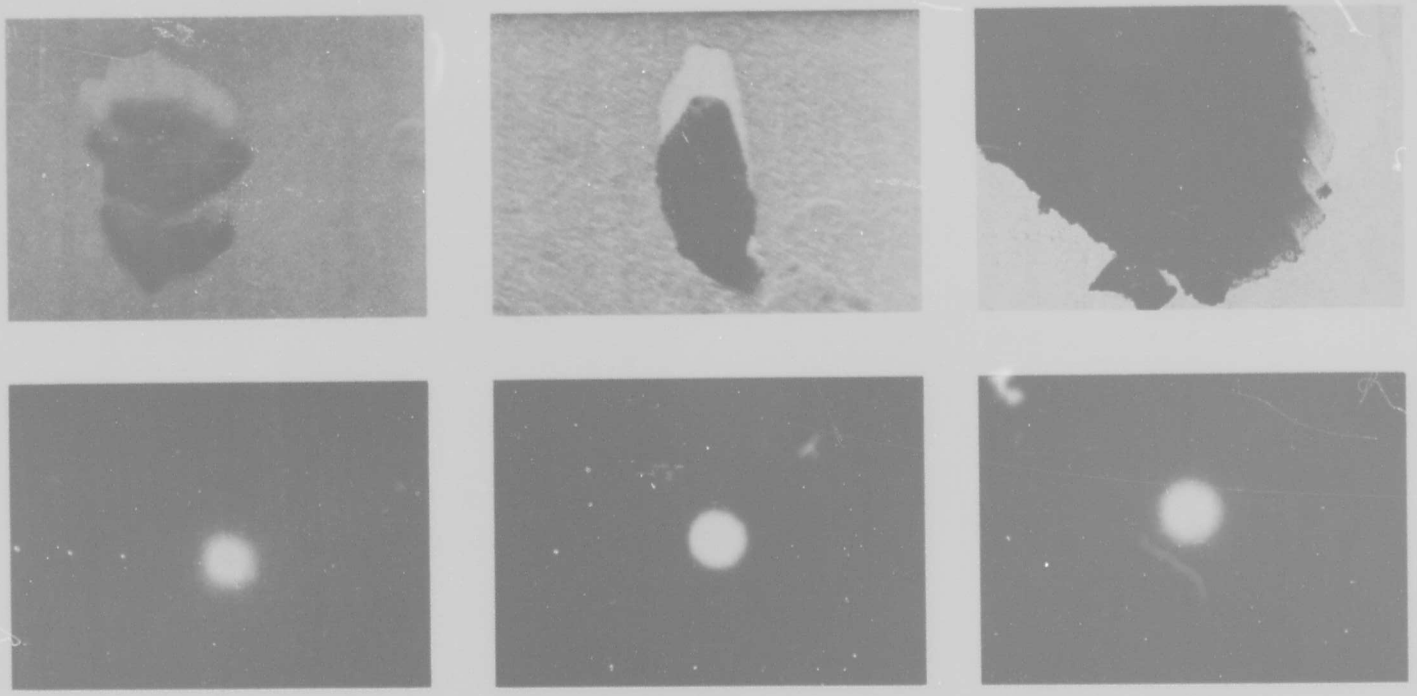

(a) (b) (c)

Fig. 86 Three Examples of Particles of Ground β-Rhombohedral Boron Shadowed With Chromium for Thickness Measurements. (a) 71,000×, measured thickness 515 Å, P1023. (b) 53,000×, measured thickness 890 Å, P1024. (c) 7,500×, P1025

Fig. 87a Bright Field Image of Edge of Particle of Ground β-Rhombohedral Boron, Showing Faint Parallel Striations. 31,500×, P923

Fig. 87b Dark Field Image of Same Area, Showing Illuminated Striations. 31,500×, P923

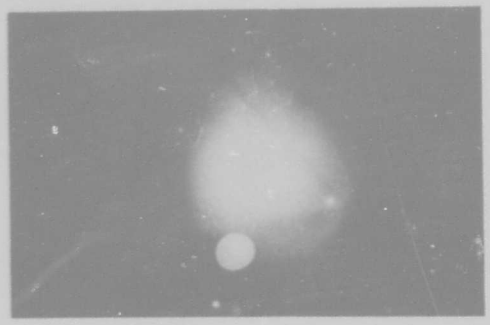

Fig. 87c Diffraction Pattern From Area Shown in (a) and (b). Objective aperture is placed over the reflection operating in (b), P924

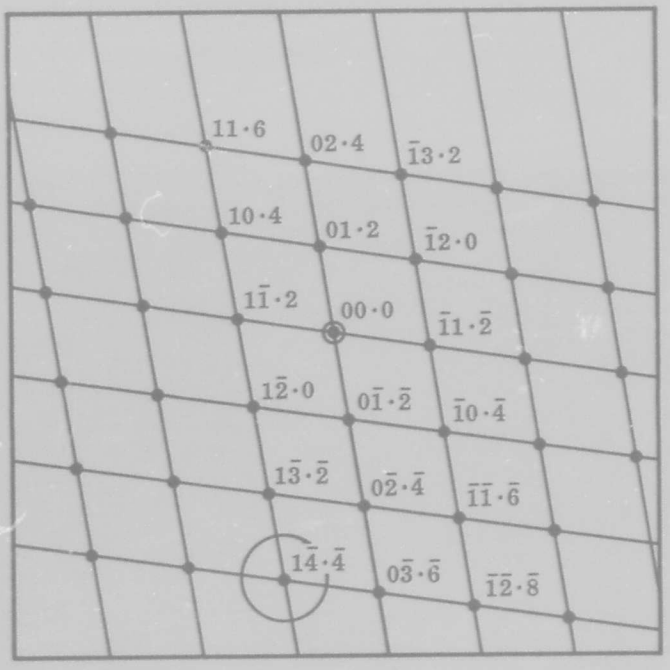

Fig. 87d Indexed Diffraction Pattern: $\beta[20\cdot\bar{1}]$

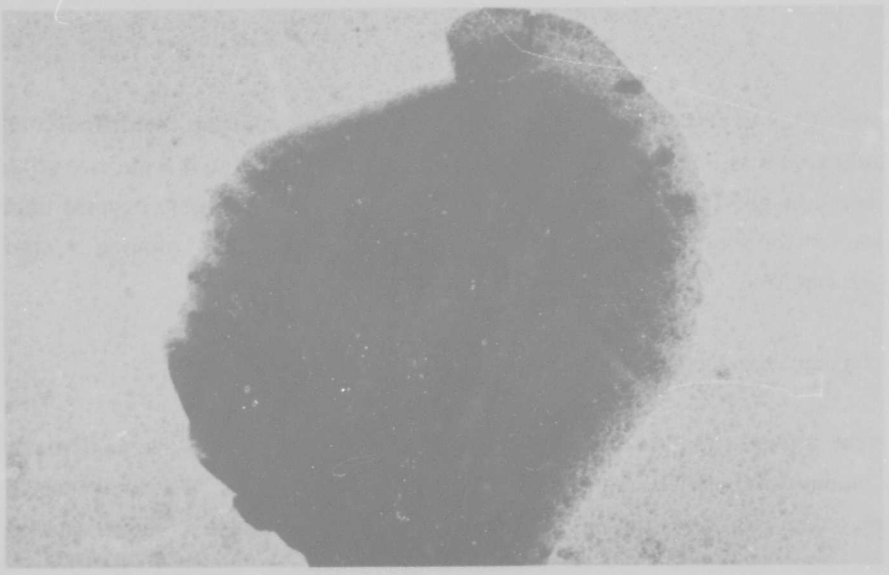

Fig. 88a Extremely Thin Particle of Ground β-Rhombohedral Boron. 31,500×, P862

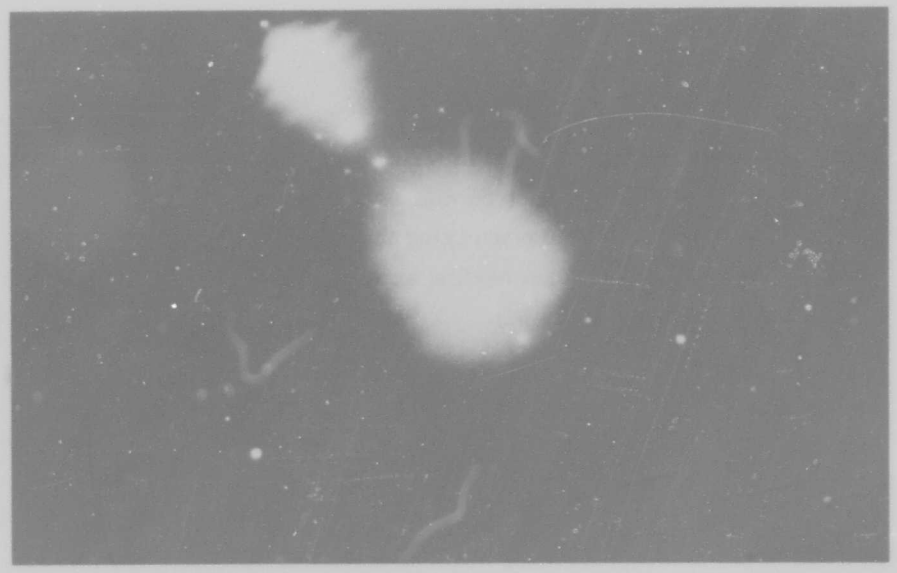

Fig. 88b Diffraction Pattern From Thin Particle Shown in (a), Showing Fine Structure of Diffraction Spots. 2×, P862

to the plane of the crystal. The very close spacing of the spots in the diffraction pattern indicates a rel-rod effect because the d-spacing calculated from two adjacent spots is much larger than the highest spacing for β-boron. Thus the crystal thickness explanation for the long rel-rods probably has some validity, but twinning is also a possible explanation.

4.4.3.2 Ground Production Boron Filaments

The electron microscope observations of ground boron filaments were essentially the same as those of thinned filaments, discussed in Section 4.4.1. The characteristic diffraction pattern is again the halo pattern, an example of which is shown in Fig. 89 which may be compared to Fig. 53, Section 4.4.1. As in the case of the thinned filaments, occasional single crystal spot patterns are observed. Figures 90 and 91 show two indexed α-boron spot patterns, and Figs. 92 and 93 show two β-boron spot patterns. Figure 92 is the same pattern as that in Fig. 85, and Fig. 93 is the same pattern as that shown in Fig. 84.

4.4.4 Beam Heating Experiments

A number of experiments were performed in which specimens of chemically thinned boron filaments were heated in the electron microscope for various time periods by removing the condenser aperture and converging the electron beam on the specimen with the second condenser lens. Beam heating experiments of this type were first done on boron filaments at ARL (Ref. 31).

Figure 94 shows a beam heating sequence. The structure before heating is smooth and gives the typical halo diffraction pattern, Fig. 94(a). After heating in the electron beam for several seconds, Fig. 94(b), the structure coarsens near the edge, and the halo pattern begins to decompose into spotty rings. Very little change is observed in either the image or the diffraction pattern with additional heating [Figs. 94(c) and (d)].

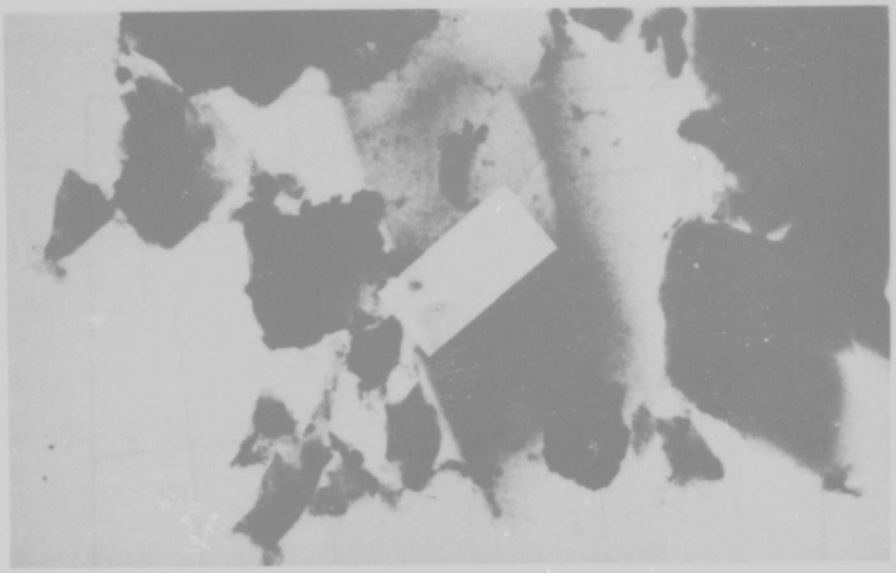

Fig. 89a Particles of Ground Production-Run Boron Filament. 31,500×, P811

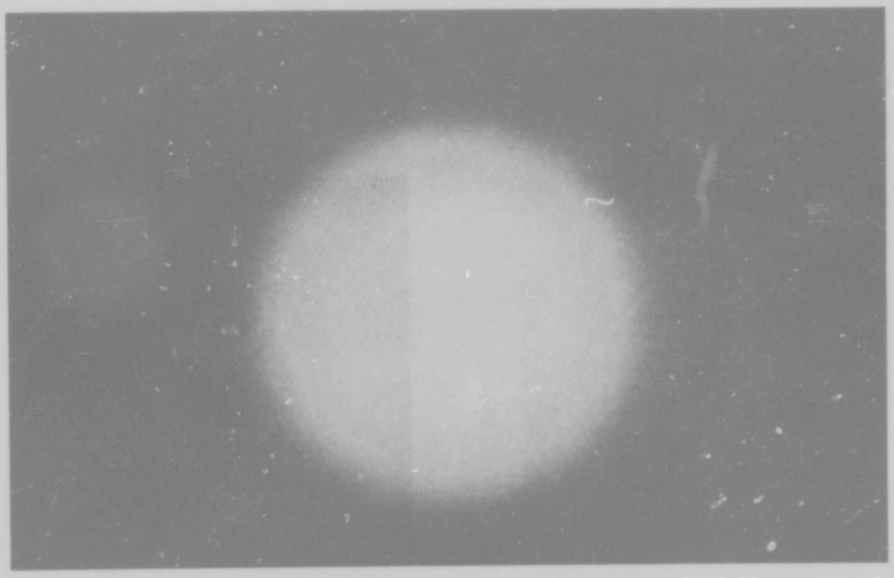

Fig. 89b Halo Pattern Obtained From Area Shown in (a). 2×, P811

(a)

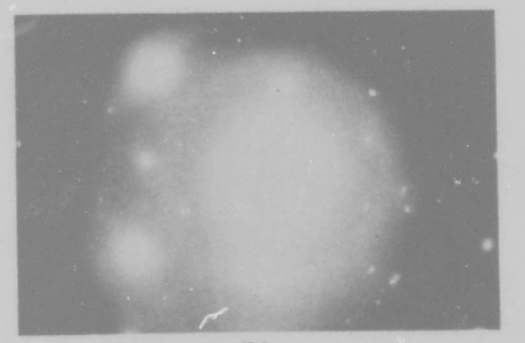

(b)

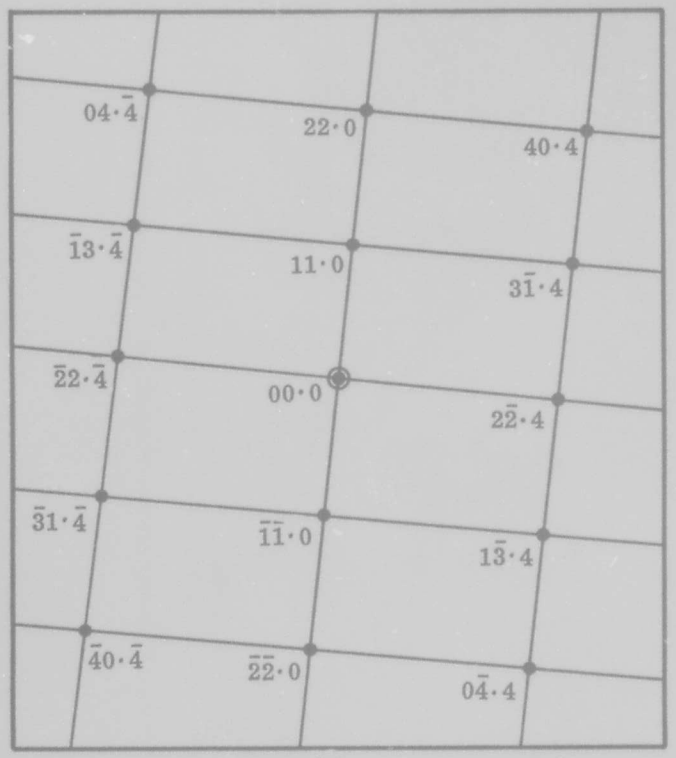

(c)

Fig. 90 Spot Pattern From Boron Filament Grindings, Example 1. (a) Image 46,000×. (b) Diffraction pattern obtained from particle shown in (a). (c) Indexed pattern: $\alpha[\bar{1}1\cdot 1]$; P1237

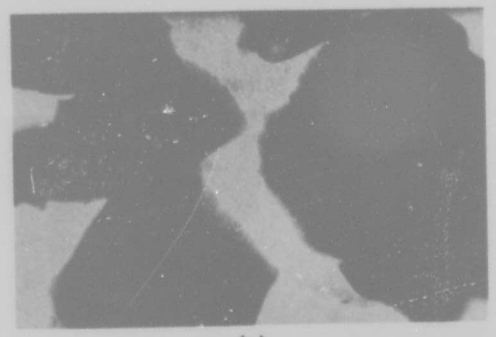

(a)

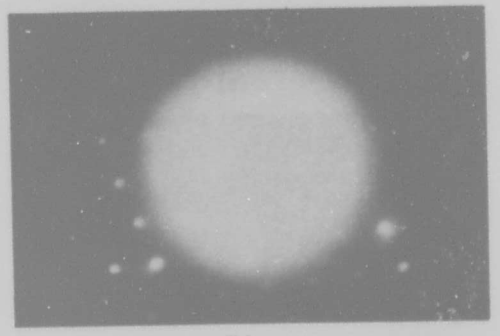

(b)

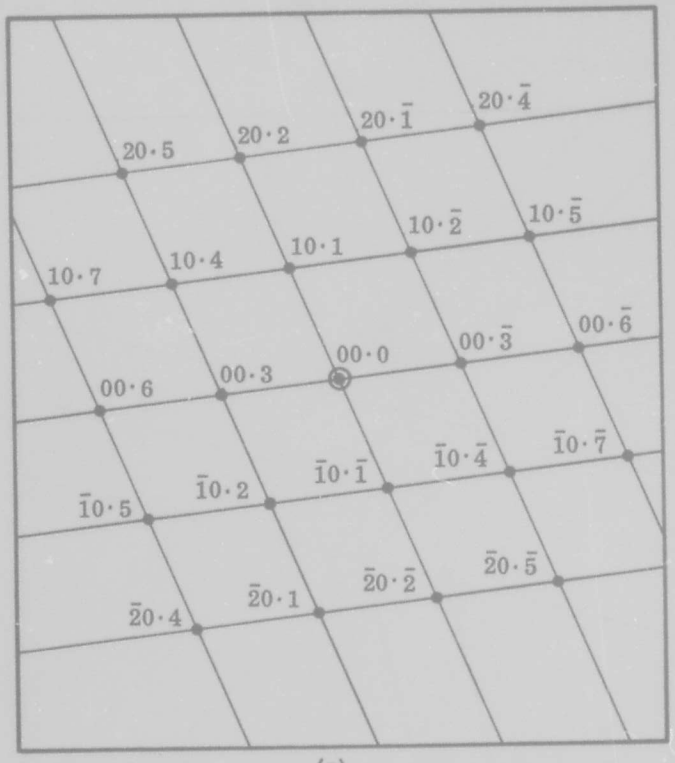

(c)

Fig. 91 Spot Pattern From Boron Filament Grindings, Example 2. (a) Image 45,000×. (b) Diffraction pattern obtained from area shown in (a). (c) Indexed pattern: $\alpha[1\bar{2}\cdot 0]$; P702

(a)

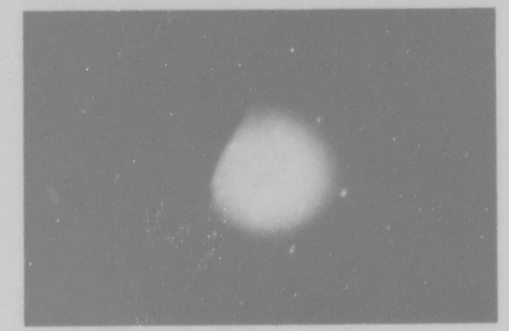

(b)

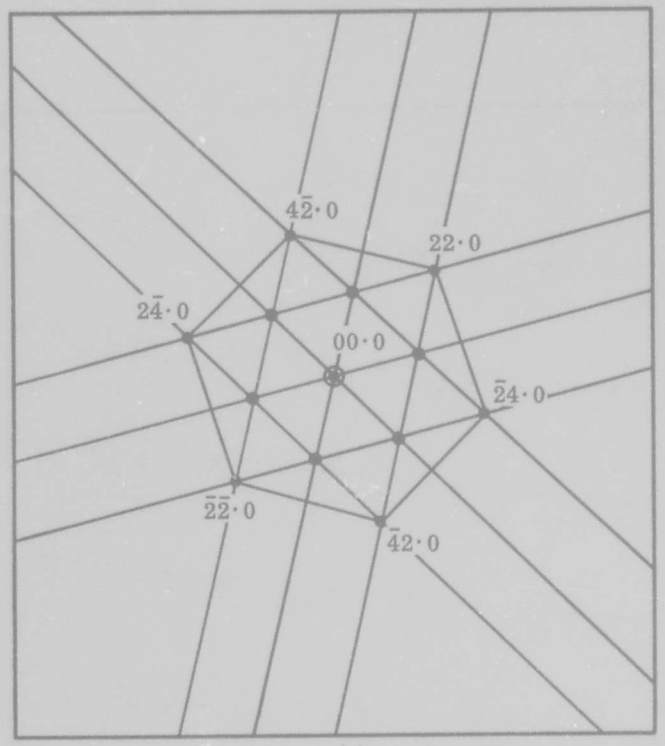

(c)

Fig. 92 Spot Pattern From Boron Filament Grindings, Example 3. (a) Image 17,000×. (b) Diffraction pattern obtained from area outlined in (a). (c) Indexed pattern: $\beta[00\cdot1]$; P886

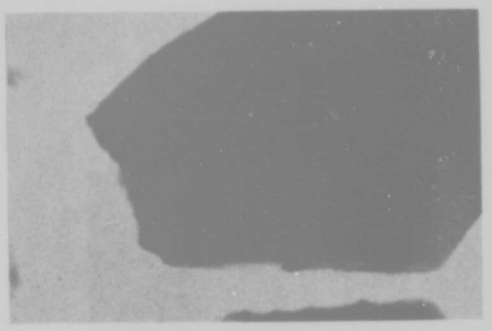

(a)

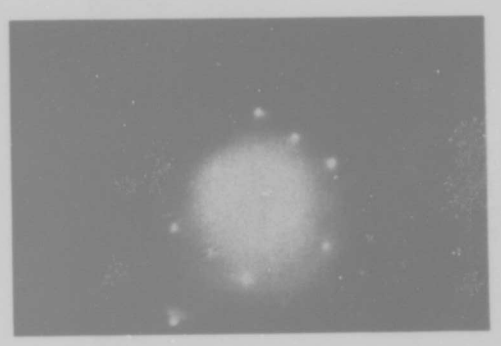

(b)

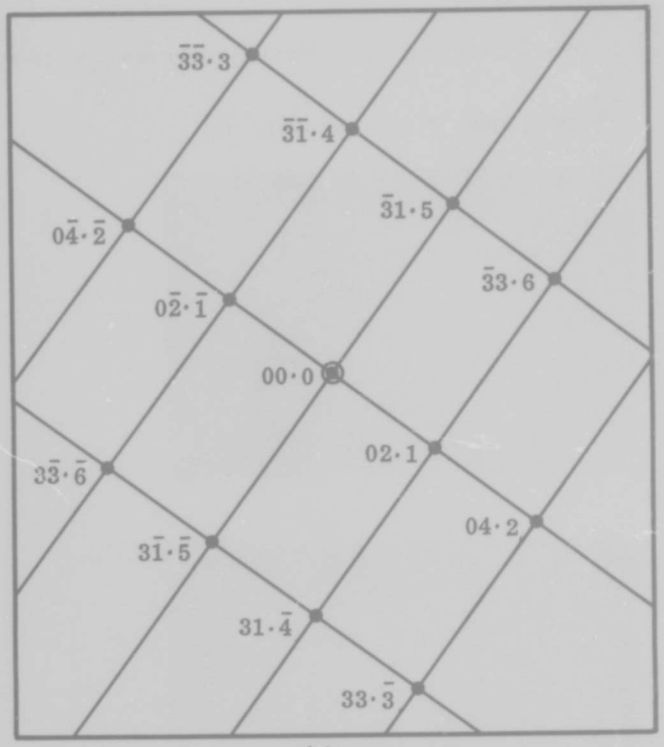

(c)

Fig. 93 Spot Pattern From Boron Filament Grindings, Example 4. (a) Image 15,750×. (b) Diffraction pattern obtained from particle shown in (a). (c) Indexed pattern: $\beta[7\bar{5}\cdot 6]$; P884

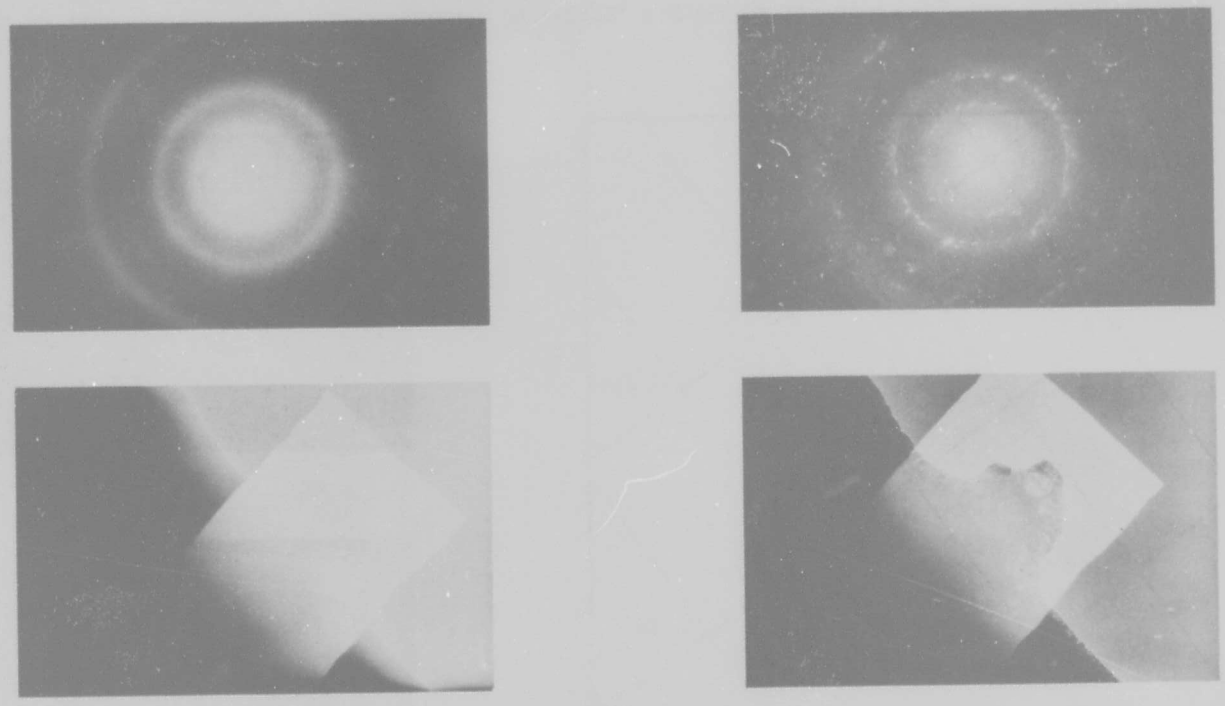

(a) Before Heating

(b) After Several Seconds Heating

Fig. 94 Sequence of Micrographs Showing the Effect of Continued Heating in the Electron Beam. All images at 12,500×. P1180-1183

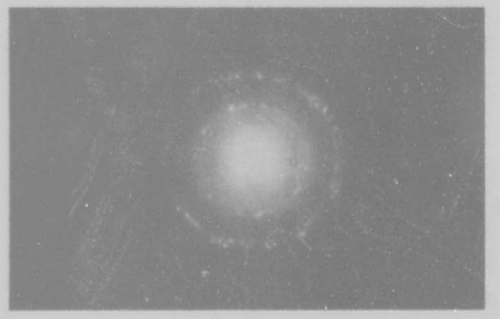

(c) After Further Heating

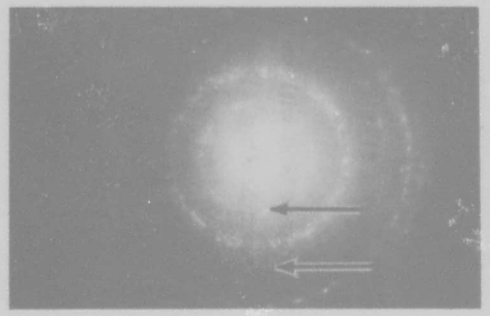

(d) After 1 Minute Heating

Fig. 94 Concluded

This stability is typical of the behavior observed for relatively thick specimens such as the one shown. Table 34 gives an analysis of the diffraction pattern shown in Fig. 94(d). The observed d-spacings are compared with those of the four known crystalline forms of boron: α-rhombohedral (ASTM card 12-377), β-rhombohedral (ASTM card 11-618), and the two tetragonal forms (ASTM cards 11-617 and 12-469).

On first examination, the observed d-spacings appear to agree best with those of β-boron, which might be expected in the case of severe beam heating. However, the first five lines of the β-boron powder pattern are absent, including the strongest line at 5.06 Å. Also, major lines of the two tetragonal forms are absent. These observations led to the consideration of a slightly distorted α-boron structure having the $(00 \cdot 3)$ spacing increased from the theoretical 4.25 Å to about 4.55 Å. Careful inspection of the diffraction pattern reveals two parallel streaks, indicated by arrows, one of which is twice as far from the center of the pattern as the other. The corresponding measured d-spacings are 4.04 and 2.02 Å. These d-spacings can only be two orders of the same reflection. Because the 2.02 Å reflection of β-boron and the 2.06 Å reflection of tetragonal boron are not second-order-type reflections, the only possibility is that the two streaks are the $(10 \cdot 1)$ and $(20 \cdot 2)$ reflections of α-boron [(100) and (200) in terms of rhombohedral indices]. This observation strongly suggests that the halo pattern does in fact originate from α-boron reflections broadened primarily by small crystallite size. A comparison of the line positions and intensities in Fig. 94(d) with Fig. 49 illustrates this very well.

Figure 95 gives another example of the effects of beam heating. The circular regions, which are thinner than the surrounding areas, were observed to grow rapidly during electron beam heating. The diffraction pattern shown in Fig. 95(a) was obtained from one of these thin regions (note outline of selected area aperture). The pattern is essentially identical to that of Fig. 94(d), showing the breakup of the halo pattern into α-boron reflections. The numerous streaks in the pattern are rel-rods, which indicate that the growing particles contain planar defects. Figure 95(b) shows a selected area diffraction pattern taken from an adjacent thick region of the specimen. Here, the breakup is not so distinct, and evidence of continuous halos can still be seen.

Table 34

COMPARISON OF d-SPACINGS FROM FIG. 94(d)
WITH THOSE OF THE KNOWN FORMS OF BORON

Number		Measured d, Å	α-Boron d, Å	β-Boron d, Å	11-617 Tetragonal d, Å	12-469 Tetragonal d, Å
Halo 1[a]	1	4.54	4.25	4.51	4.52	4.38
	2	→ 4.04	4.07	3.98	3.93	3.92
Halo 2	3	2.60	2.545	2.59	2.61	2.534
	4	2.42	2.479	2.41	2.41	2.426
	5	→ 2.02	2.03	2.02	–	2.060
Halo 4	6	1.74	1.77	1.75[b]	–	–
	7	1.65	1.666	1.65	–	1.653
	8	1.54	1.603	1.54	–	1.545
Halo 5	9	1.46	1.482	1.46	–	1.457
	10	1.36	1.359	1.36	–	1.367

(a)Halos numbered in accordance with Fig. 53, Section 4.4.1.
(b)d-Spacings for β-boron below 2.02 Å obtained from Debye-Scherrer X-ray film (Ref. 10).

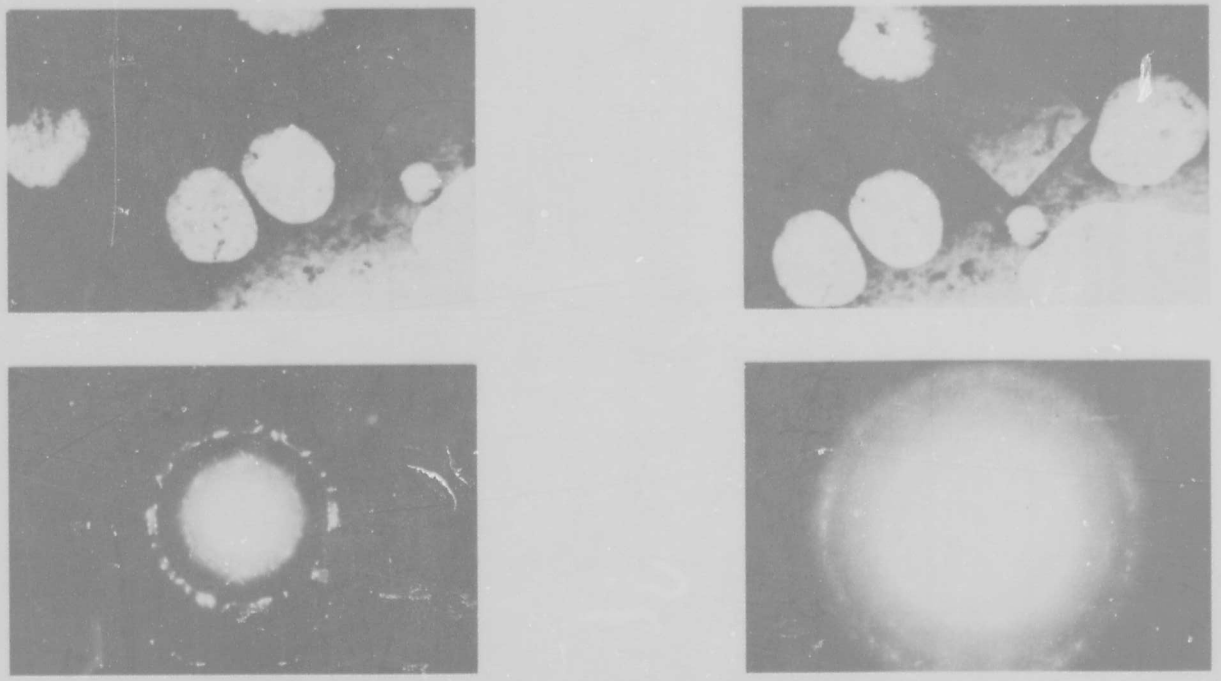

(a) (b)

Fig. 95 Structure Produced by Several Seconds of Heating in the Electron Beam. (a) Selected area diffraction from thin, circular region. (b) Selected area diffraction from thicker area. Images at 12,000×. P1482 and P1483

Figure 96 shows the structure of a thinned filament subjected to 8 seconds of beam heating and Table 35 gives an analysis of the diffraction pattern. The measurements are grouped according to successive orders of streaked spots, which helped to identify the pattern as α-rhombohedral boron. The two arced rings in the position of the second halo are the (10·4) and (11·0) reflections of α-boron. Note that these two reflections are spread apart, the (10·4) being shifted to a higher d-spacing and the (11·0) to a lower d-spacing. The 4.66 Å d-spacing was obtained from two diametrically opposed arcs of very weak intensity just inside the first halo position; these weak arcs indicate the presence of a small amount of β-rhombohedral boron.

Figure 97 gives an example of the structure produced by heating a thinned filament for a very short time (~ 1 sec) in the electron beam, and Fig. 98 (a different specimen) shows the structure at some distance away from an intensely heated area. These structures are identical, and consist of 1500 Å crystallites in a matrix of small (<100 Å) crystallites as described in Section 4.4.2. Table 36 presents a number of d-spacings corresponding to the spots on the diffraction pattern in Fig. 98; the table identifies the large crystallites as either α-rhombohedral or tetragonal boron. Although certain of the d-spacings can also be identified with reflections of β-rhombohedral boron, the absence of any spots of d-spacing greater than 4 Å tends to eliminate this possibility.

Figure 99 shows the structure produced as a result of strong beam heating. Note the holes in the structure (cf. Fig. 95) and the clustering of the crystallites. Measurements of the d-spacings for a number of the spots in the diffraction pattern indicate the presence of α and possibly some tetragonal boron.

Figure 100 is another example of the beam heated structure at some distance away from the strongly heated area. As in Figs. 97 and 98, numerous crystallites of about 1000 Å size are embedded in the matrix of small-crystallite material. Careful examination of the selected-area diffraction pattern revealed the single-crystal spot pattern, shown in Fig. 100(c), superimposed upon the halos. This pattern was

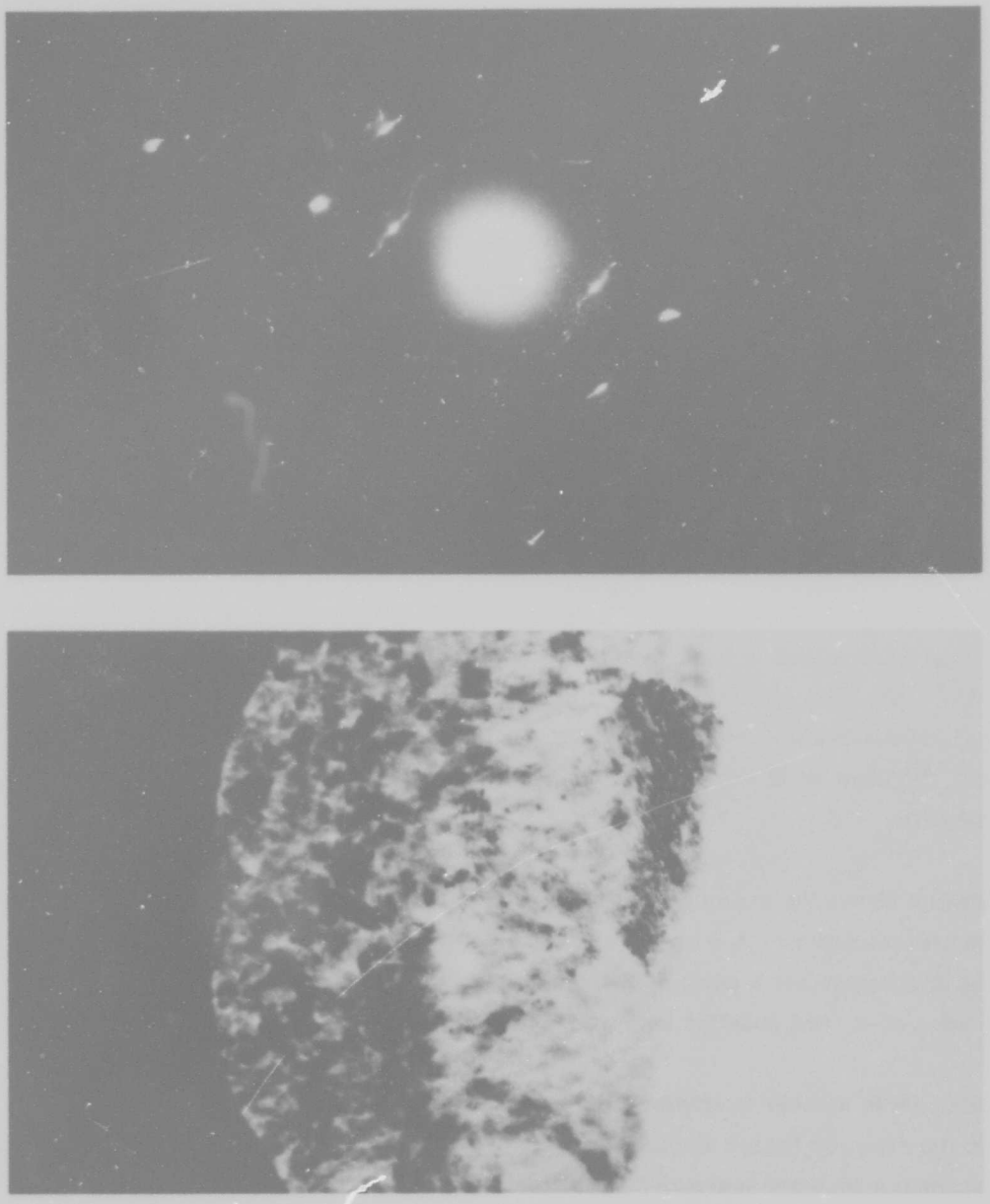

Fig. 96 The Effect of Beam Heating for 8 Seconds. The diffraction pattern shows the transformation from halos to discrete reflections of α-rhombohedral boron. Image at 27,000×, pattern at 2×. P1108

Table 35

MEASURED d-SPACINGS FROM DIFFRACTION PATTERN SHOWN IN FIG. 96

Number	Measured d, Å	d, Å	α-Boron (hkℓ)	(HK·L)
1 (1st order)	4.32	4.25	(111)	(00·3)
2 (2nd order)	2.16	2.086	(222)	(00·6)
3 (3rd order)	1.44	1.403	(333)	(00·9)
4 (1st order)	2.68	2.545	(211)	(10·4)
5 (2nd order)	1.34	1.268	(422)	(20·8)
C	1.77	1.77	(220)	(02·4)
7	1.68	1.666	(322)	(10·7)
8 (1st order)	2.46	2.479	$(10\bar{1})$	(11·0)
9 (2nd order)	1.23	1.230	$(20\bar{2})$	(22·0)
10	1.49	1.482	(332)	(01·8)
11	4.66			β (02·1)

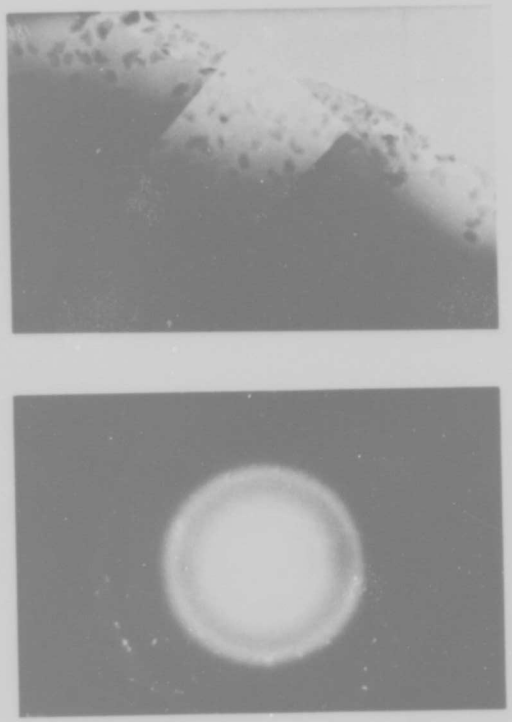

Fig. 97 Crystallites of α-Rhombohedral Boron Produced by Beam Heating for About 1 Sec. 12,000×. P1399

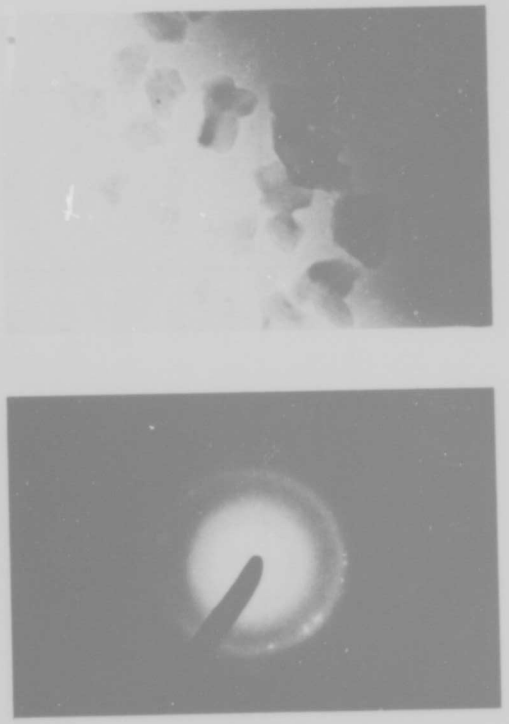

Fig. 98 Crystallites of α-Rhombohedral Boron at the Outer Edge of the Heat Affected Zone of an Intensely Heated Specimen. 46,000×. P1247

Table 36

MEASURED d-SPACINGS FROM DIFFRACTION PATTERN SHOWN IN FIG. 98

Number	Measured d, Å	α-Boron[a]			Tetragonal Boron[b]	
		d, Å	(hkℓ)	(HK·L)	d, Å	(hkℓ)
1	3.97	4.07	(100)	(10·1)	3.92	(111)
2	2.50	2.545	(211)	(10·4)	2.526	(031)
3	2.37	–	–	–	2.426	(131)
4	1.90	–	–	–	1.908	(331)
5	1.69	1.666	(322)	(10·7)	1.655	(042)
6	1.61	1.603	$(20\bar{1})$	(21·1)	1.624	(151)
7	1.45	1.438	(310)	(21·4)	1.457	(600)
8	1.41	1.403	(333)	(00·9)	1.420	(152)
9	1.34	1.346	(300)	(30·3)	1.321	(143)
10	1.29	1.268	(422)	(20·8)	1.306	(333)
11	1.22	1.230	$(20\bar{2})$	(22·0)	1.217	(024)
12	1.175	1.178	$(31\bar{1})$	(22·3)	1.172	(224)
13	1.048	1.048	$(22\bar{2})$	(04·2)	–	–
14	0.932	0.932	$(41\bar{1})$	(32·4)	–	–
15	0.814	–	–	–	–	–

[a]ASTM Card 12-377.
[b]ASTM Card 12-469.

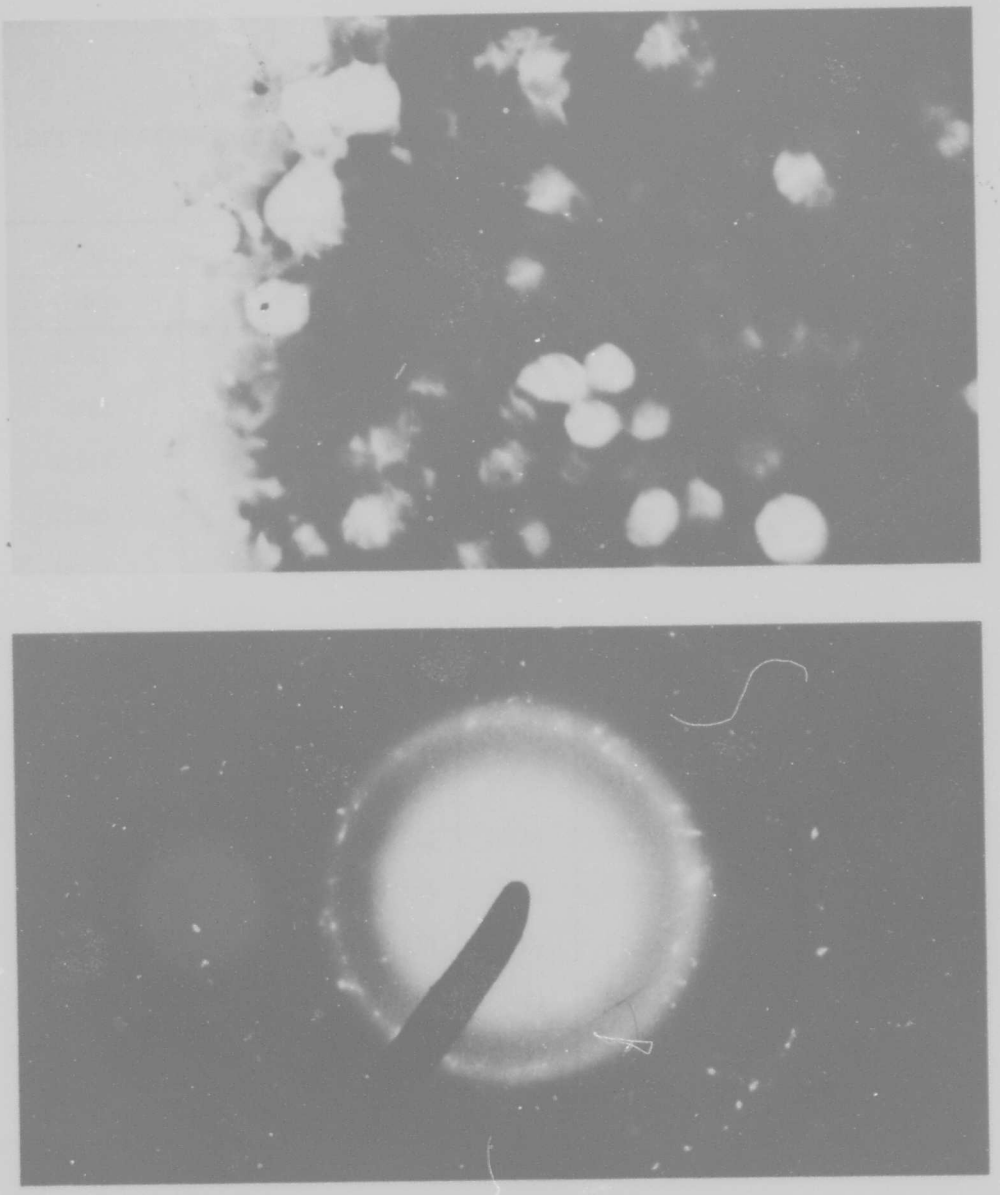

Fig. 99 Structure Produced by Intense Beam Heating. 25,000×. P1243

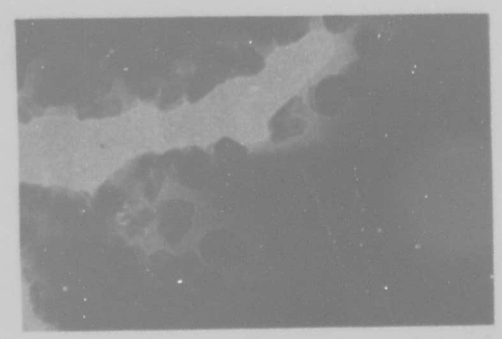

(a)

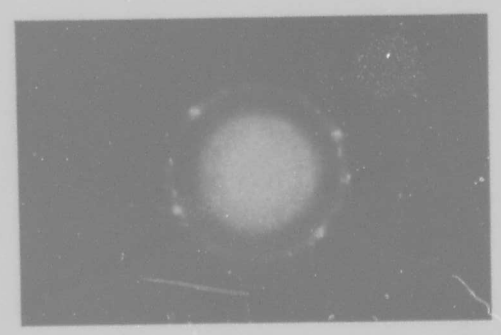

(b)

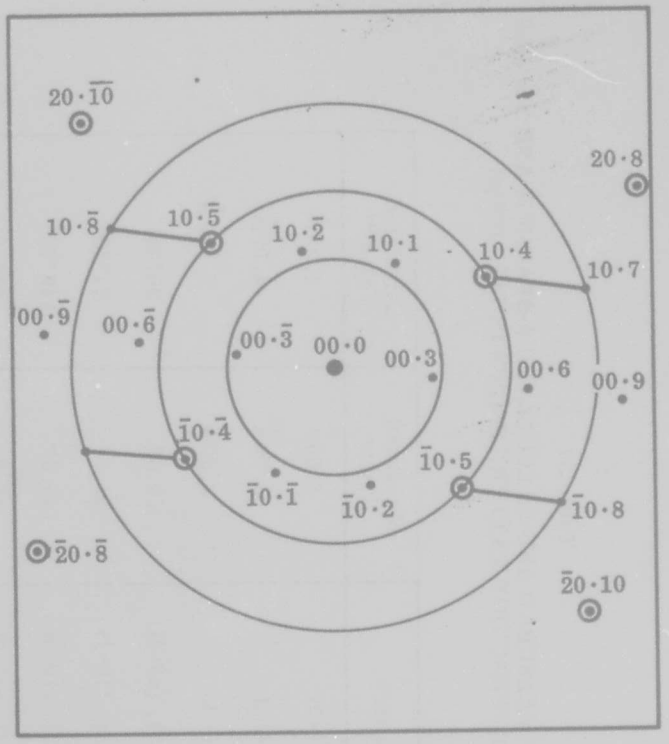

(c)

Fig. 100 Another Example of the Beam-Heated Structure at the Edge of the Heat-Affected Zone. (a) 1000 Å crystallites of α-rhombohedral boron embedded in the matrix, 46,000×. (b) Diffraction pattern consisting of a streaked single crystal pattern superimposed on the matrix halos. (c) Indexed spot pattern: α-boron [$\bar{1}$2·0], with streaks normal to (00·3) planes. P1112

Table 37

COMPARISON OF MEASURED AND CALCULATED d-SPACINGS AND ANGLES FOR DIFFRACTION PATTERN SHOWN IN FIG. 100 (c)

Quantity	Measured Value	Calculated Value[a]
α d (00·3)	4.60 Å	4.25 Å
α d (10·1)	3.86 Å	4.07 Å
α d (10·4)	2.50 Å	2.545 Å
$\measuredangle$ (00·3), (10·4)	34.5°	36°28'
$\measuredangle$ (00·3), (10·1)	67.0°	71°19'
$\measuredangle$ (00·3), (10·$\bar{5}$)	145.5°	149°25'
$\measuredangle$ (10·4), (10·$\bar{2}$)	81.0°	87°36'
$\measuredangle$ (10·1), (10·$\bar{5}$)	78.0°	78°5'

[a]Using a_o = 4.908 Å, c_o = 12.567 Å (ASTM Card 12-377).

indexed as α-boron in the $[\bar{1}2\cdot 0]$ orientation. Table 37 compares some measured and calculated d-spacings and angles for this pattern. The four prominent streaks in the pattern shown in Fig. 100(c) are in the $[00\cdot 3]$ direction, indicating possible growth faults on the basal planes of the large α crystallites.

Figure 101 shows a specimen subjected to intense heating in the electron beam. A single crystal spot pattern can be distinguished, superimposed upon the decomposed halo pattern. This spot pattern has been indexed as β-rhombohedral boron in the $[4\bar{1}\cdot\bar{4}]$ orientation. There are rel-rod streaks through the spots in the direction $[2\bar{5}\cdot 1]$ on the diagram, which corresponds to the $(0\bar{2}3)$ type planes in the rhombohedral axis system.

Figure 102 is another example of strong beam heating. Very faint striations can be seen within the boundaries of the selected area aperture, parallel to the short edges. When rotation of the image with respect to the diffraction pattern is taken into account, these striations are perpendicular to the continuous rel-rods shown in the diffraction pattern. The last vestiges of the halo pattern can still be seen. Careful examination of the intense spots reveals a single-crystal pattern which can be indexed as β-boron $[\bar{5}4\cdot 0]$. The rel-rods are in the direction $[12\cdot\bar{1}]$ in reciprocal space, indicating faulting on the $(12\cdot\bar{1})_H = (10\bar{2})_R$ planes. The faulted structure is probably due to the incomplete transformation from α- to β-boron, i.e., the individual B_{12} groups have not completely oriented themselves to form the constituent B_{84} units of the β structure. In view of the complex structural groups of boron, and the unusual crystallographic planes showing rel-rod effects, the faulting is undoubtedly much more difficult to describe than in the case of metals.

Figure 103 shows another specimen subjected to intense beam heating. Striations can be seen in the individual crystallites; these striations are shown at high magnification in Fig. 104. The single-crystal spot pattern shown in Fig. 103(b) was obtained from the fingerlike projection encircled in Fig. 103(a). The pattern, identified as α-boron $[1\bar{2}\cdot 0]$, is indexed in Fig. 103(c). This pattern may be compared with that shown in Fig. 100(c).

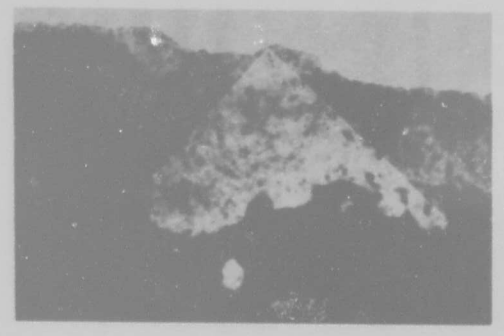

(a)

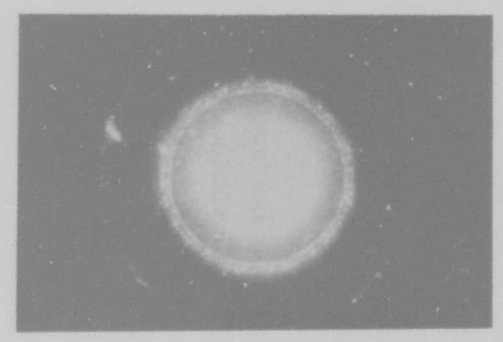

(b)

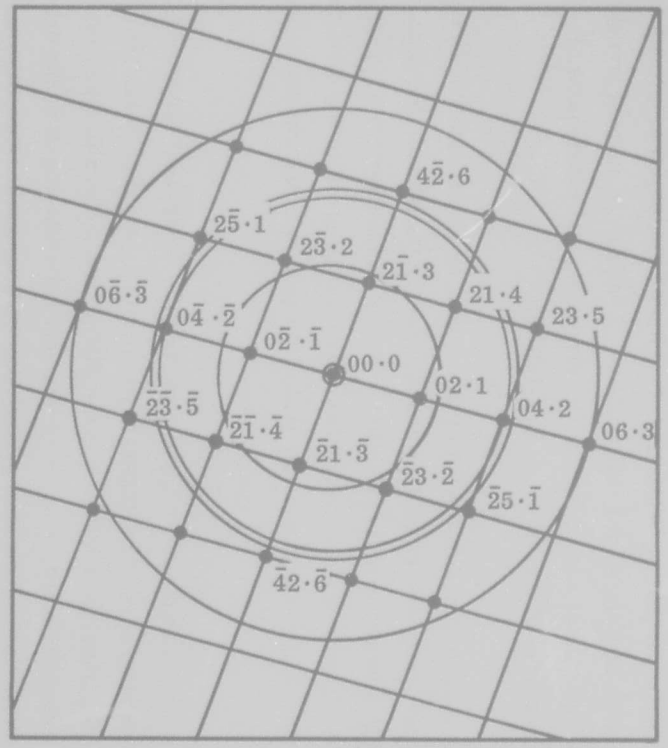

(c)

Fig. 101 Another Example of the Effect of Strong Beam Heating. (a) Image, showing mass of crystallites, 12,000×. (b) Selected area diffraction pattern, showing a spot pattern superimposed upon the rings. (c) Indexed spot pattern: $\beta\,[4\bar{1}\cdot\bar{4}]$. P1480

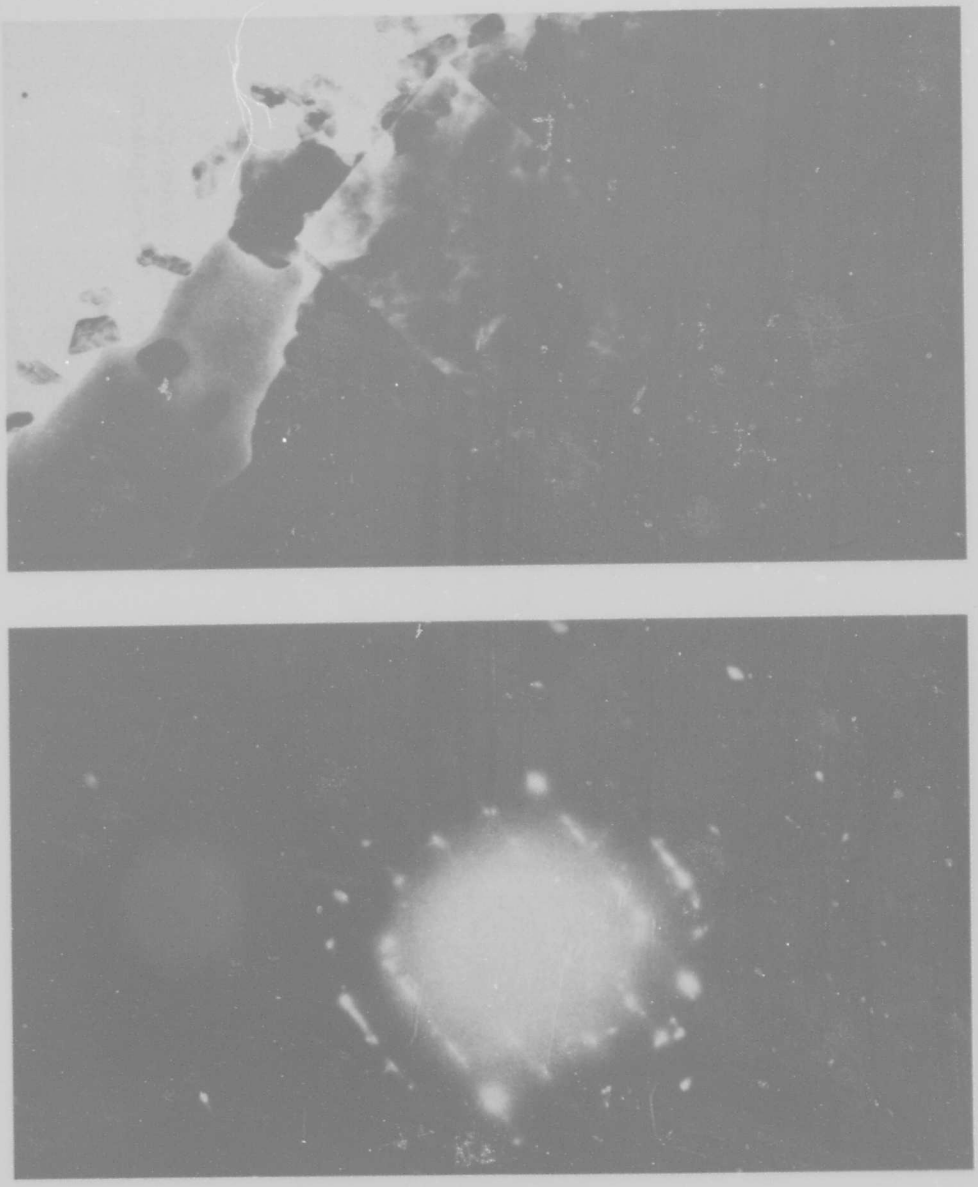

Fig. 102 Strong Beam Heating. (a) Image at 24,000×. Note striated crystallites. (b) Selected area diffraction pattern, 2×. The location of the halos can still be seen. Streaks are perpendicular to striations in the image. P1503

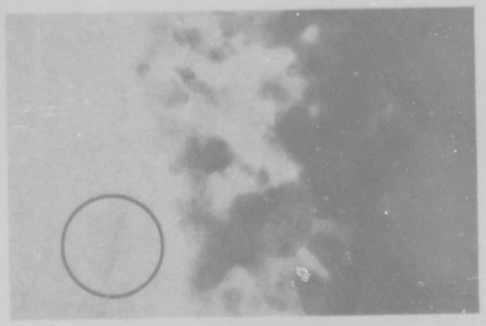

(a)

(b)

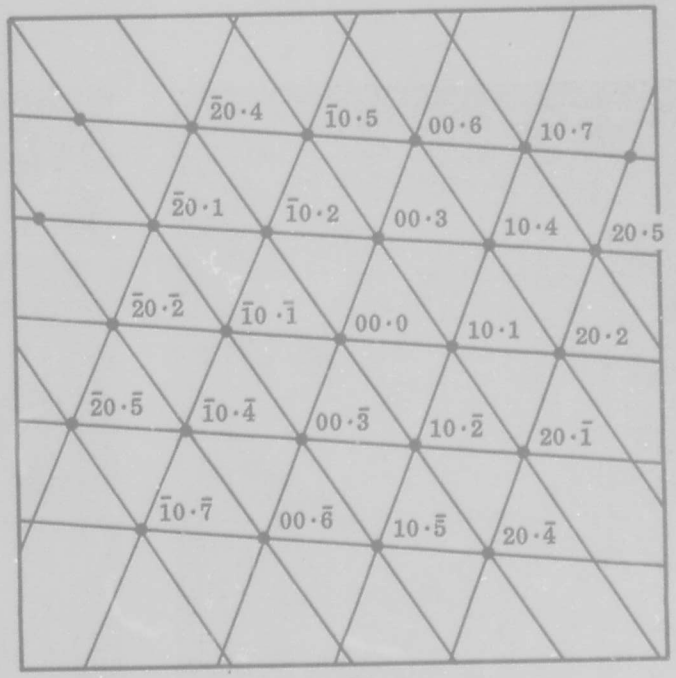

(c)

Fig. 103 Another Region Subjected to Strong Beam Heating. (a) Image showing striated crystallites, 13,500×. (b) Single crystal spot pattern obtained from area circled in (a). Indexed pattern: $\alpha[1\bar{2}\cdot0]$. (Compare with Fig. 100). P1110

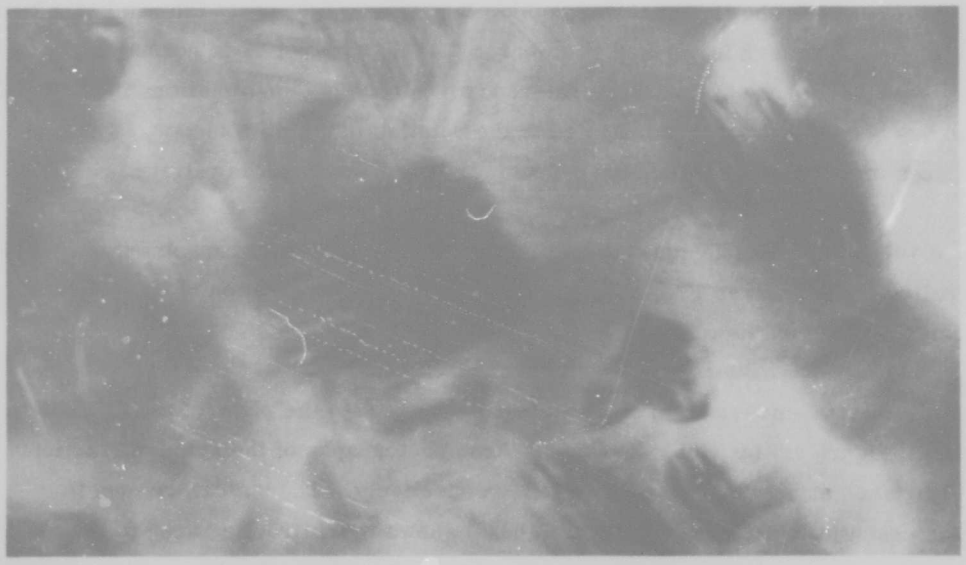

Fig. 104 High-Magnification View of Beam Heated Area Shown in Fig. 103(a). 94,000×. P1111

Figure 105 gives another α-boron spot pattern obtained in the same vicinity as that in Fig. 103. Both of these α-boron spot patterns are perfect, i.e., no rel-rod effects are visible.

Figure 106 shows a high-magnification image of a striated crystallite and its corresponding selected-area diffraction pattern. This crystallite can also be seen near the left edge of Fig. 102, which shows that it was outside the region of the most intense beam heating. The diffraction pattern is indexed as α-boron $[0\bar{4}\cdot 1]$, with rel-rods normal to the $(01\cdot 8)$ type planes. Note that these rel-rods are normal to the striations in the image, which has been rotated to compensate for the rotation in the microscope. Table 38 compares measured and calculated d-spacings and angles for this pattern.

Figure 107 shows a single-crystal spot pattern obtained from the specimen of Fig. 94. The pattern is indexed in Fig. 107(c) as $\beta[\bar{3}7\cdot\bar{4}]$. The direction of the rel-rods indicates faulting on the $(51\cdot 4)_H = (50\bar{1})_R$ planes.

Figure 108 is a demonstration of long rel-rods normal to the plane of the diffraction pattern. Figure 108(a), (b), and (c) are three photographs of the same diffraction pattern, taken at +10°, 0°, and -10° tilt, respectively. The pattern is seen to remain essentially unchanged. Figure 108(d) shows the diffracting area of the electropolished filament specimen which gave the pattern after beam heating. Figure 108(e) shows the indexing of the pattern. This pattern is identical to those shown in Figs. 84(c) and 93(c) (Section 4.4.3), except for the extra spots indicated by "Δ". Table 39 compares the measured d-spacings with those of β-rhombohedral boron.

Figure 109 is another β-boron spot pattern produced by intense beam heating. The pattern is indexed as $[\bar{2}1\cdot 0]$ in Fig. 109(c). The long rel-rods are in the direction $[02\cdot 4]$ in reciprocal space, indicating faulting on these planes.

Figure 110 contains another streaked spot pattern obtained from the same area. This is the most significant pattern observed, because it was taken during the phase transformation from α- to β-rhombohedral boron. It was found that this pattern consists

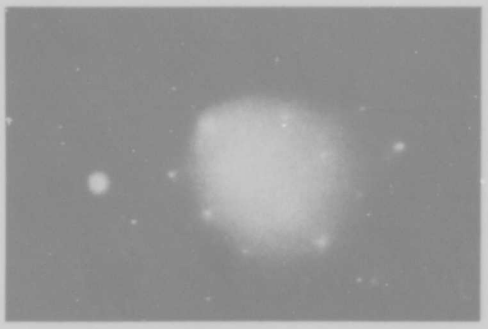

(a)

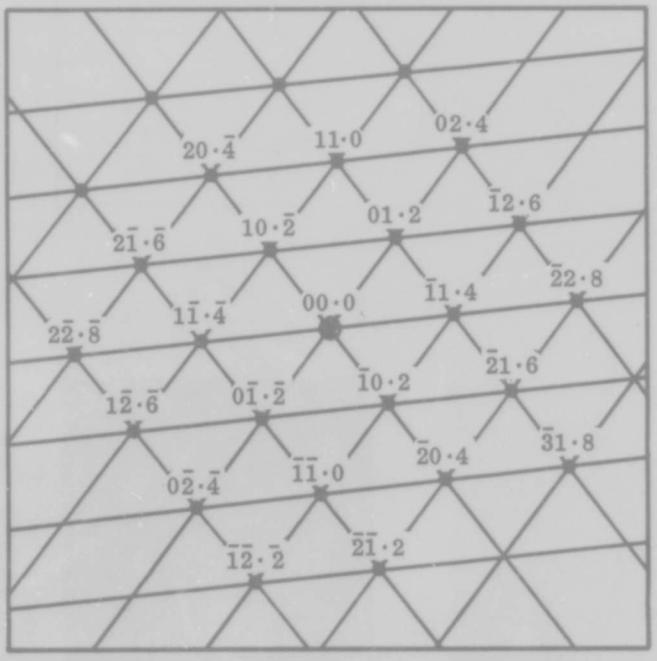

(b)

Fig. 105 Another Single-Crystal Spot Pattern Obtained From Area Shown in Fig. 103(a). Indexed as $\alpha[\bar{2}2\cdot\bar{1}]$. P1110

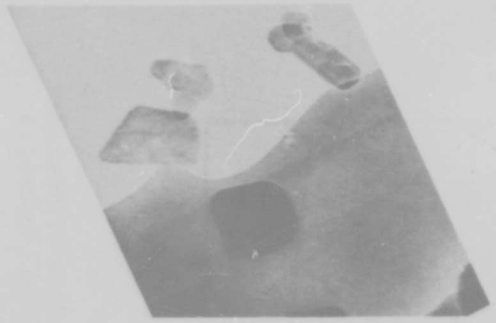

(a)

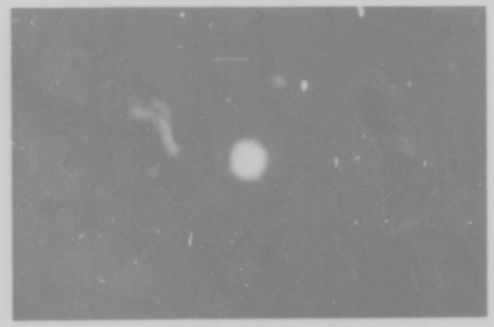

(b)

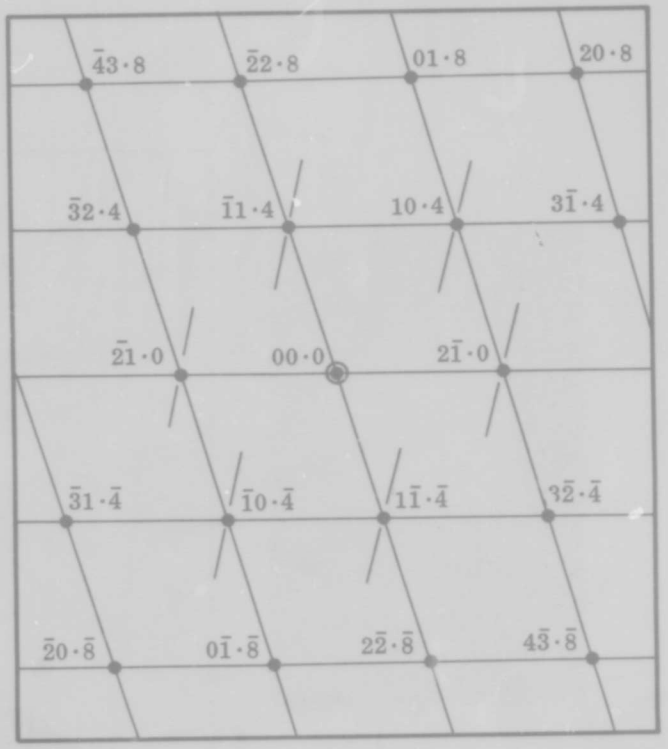

(c)

Fig. 106 A Single Striated Crystallite of α-Rhombohedral Boron at Edge of Intensely Heated Area Shown in Fig. 102. (a) Image at 49,500×. (b) Streaked diffraction pattern from trapezoidal-shaped crystal in (a). (c) Indexed diffraction pattern: $\alpha[0\bar{4}\cdot 1]$. P1504

Table 38

COMPARISON OF MEASURED AND CALCULATED d-SPACINGS AND ANGLES FOR DIFFRACTION PATTERN SHOWN IN FIG. 106(c)

Quantity	Measured Value	Calculated Value[a]
α d $(\bar{2}1\cdot 0)$	2.49 Å	2.45 Å
α d $(\bar{1}1\cdot 4)$	2.71 Å	2.53 Å
α d $(10\cdot 4)$	2.37 Å	2.53 Å
α d $(\bar{3}2\cdot 4)$	1.53 Å	1.43 Å
α d $(01\cdot 8)$	1.47 Å	1.47 Å
α d $(\bar{4}3\cdot 8)$	1.03 Å	0.943 Å
$\measuredangle (10\cdot 4), (2\bar{1}\cdot 0)$	52.5°	59°1'
$\measuredangle (\bar{1}1\cdot 4), (2\bar{1}\cdot 0)$	112.5°	120°59'
$\measuredangle (01\cdot 8), (3\bar{2}\cdot \bar{4})$	113.5°	119°2'
$\measuredangle (\bar{3}2\cdot 4), (3\bar{1}\cdot 4)$	120.5°	121°55'
$\measuredangle (3\bar{2}\cdot \bar{4}), (10\cdot 4)$	85.0°	88°3'
$\measuredangle (\bar{1}1\cdot 4), (3\bar{2}\cdot \bar{4})$	147.0°	150°1'

[a] Using $a_o = 4.908$ Å, $c_o = 12.567$ Å (ASTM Card 12-377).

(a)

(b)

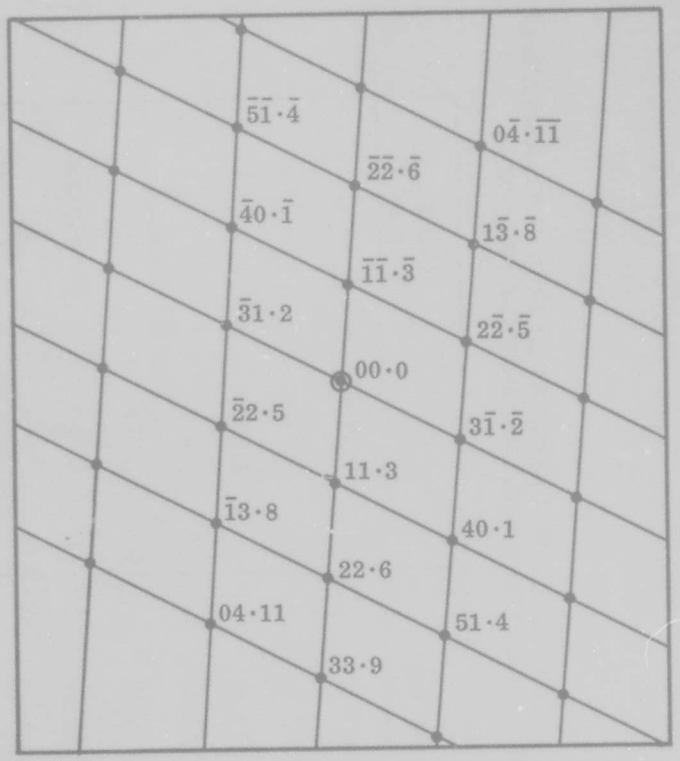

(c)

Fig. 107 A Streaked Single Crystal Pattern Obtained From Specimen Shown in Fig. 94. (a) Image, 12,500×. (b) Spot pattern obtained from projection outlined in (a). (c) Indexed pattern: $\beta[\bar{3}7\cdot\bar{4}]$. P1179

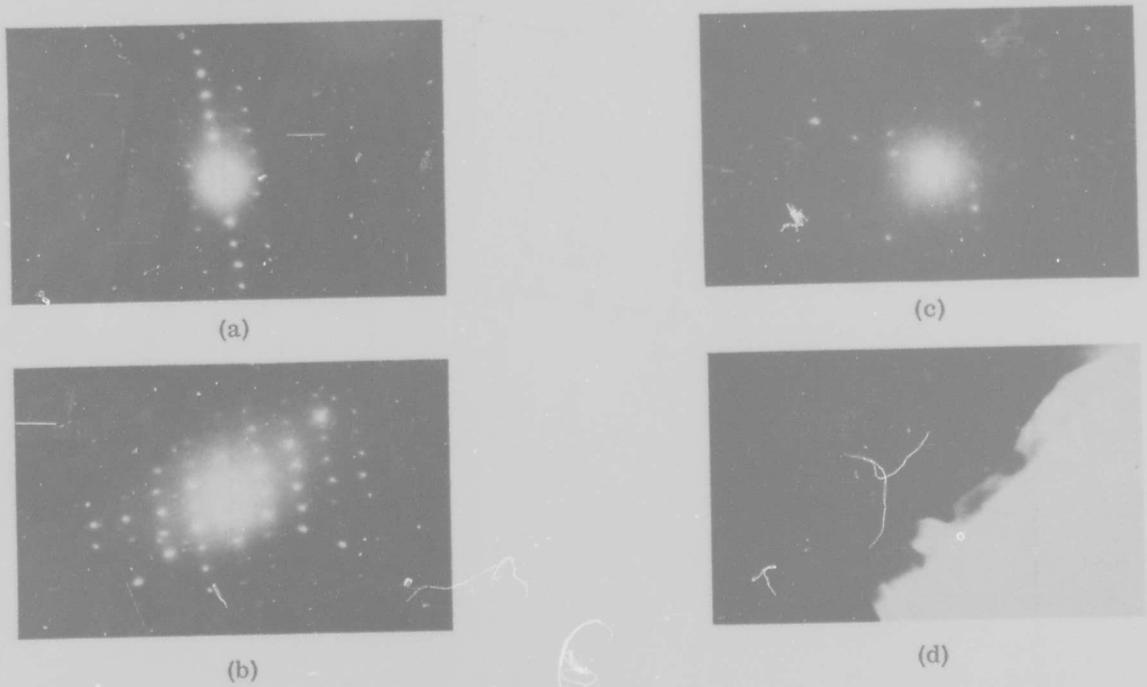

Fig. 108 Diffraction Pattern Obtained From Edge of an Electropolished Filament Specimen. Pattern remains unchanged over large tilt angles. (a) +10° Tilt. (b) 0° Tilt. (c) -10° Tilt. (d) Diffracting area, 15,750×. P949, 950 and 951

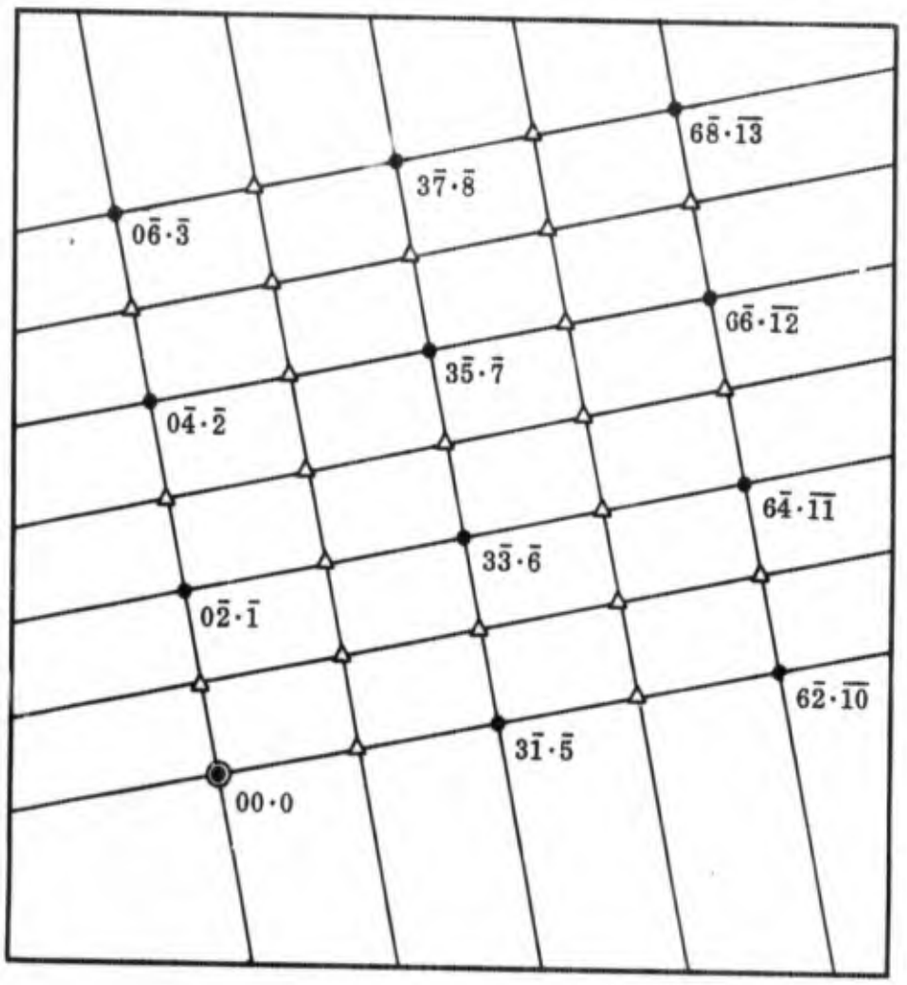

Fig. 108e Indexing of Diffraction Pattern Shown in Fig. 108(a) - (c): $\beta[\bar{7}5\cdot\bar{6}]$

Table 39

MEASURED AND CALCULATED d-SPACINGS FROM DIFFRACTION PATTERN SHOWN IN FIG. 108(e)

Number	Measured d, Å	β-Boron	
		d, Å	(HK·L)
1	4.77	4.65	$(0\bar{2}\cdot\bar{1})$
2	2.90	2.86	$(3\bar{1}\cdot\bar{5})$
3	2.48	2.47	$(3\bar{3}\cdot\bar{6})$
4	2.34	2.32	$(0\bar{4}\cdot\bar{2})$
5	1.86	1.83	$(3\bar{5}\cdot\bar{7})$
6	1.47	1.43	$(6\bar{2}\cdot\bar{10})$
7	1.60	1.55	$(0\bar{6}\cdot\bar{3})$
8	1.38	1.38	$(3\bar{7}\cdot\bar{8})$
9	1.11	1.07	$(6\bar{8}\cdot\bar{13})$

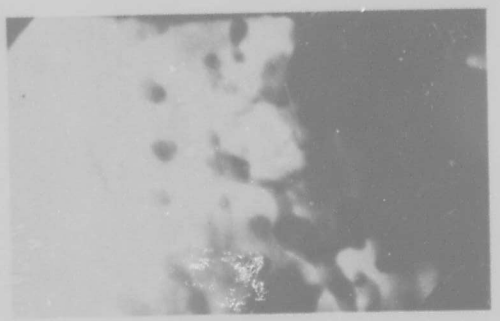

(a)

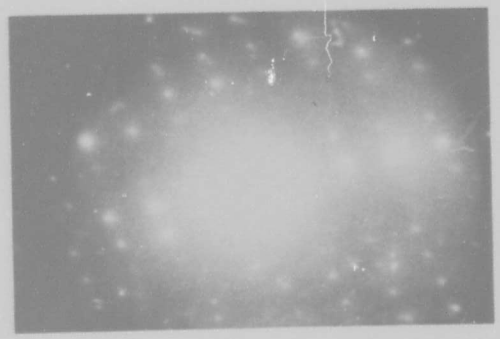

(b)

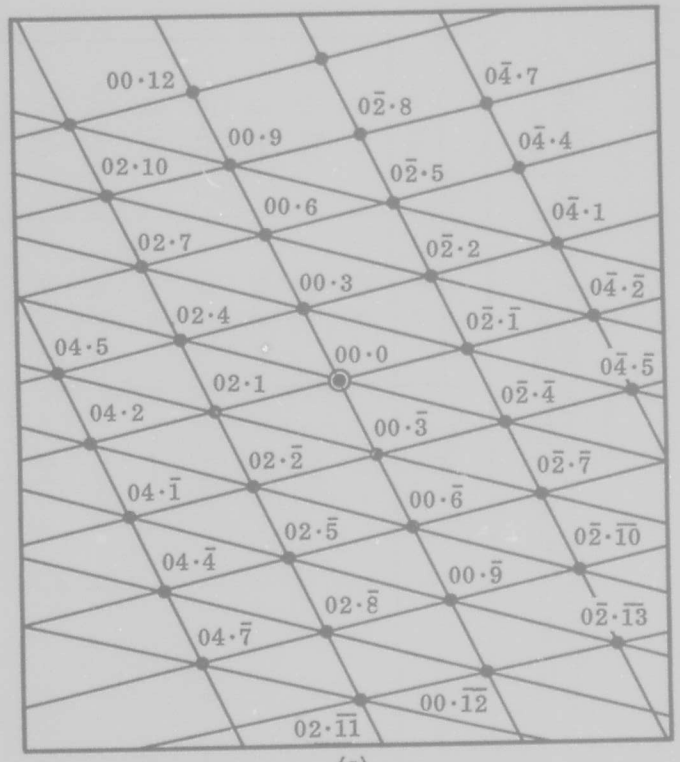

(c)

Fig. 109 Another Example of Severe Beam Heating. (a) Image, showing network of crystallites, 12,500×. (b) Streaked diffraction pattern from area shown in (a). (c) Indexed pattern: $\beta[\bar{2}1\cdot 0]$. P1249

(a)

(b)

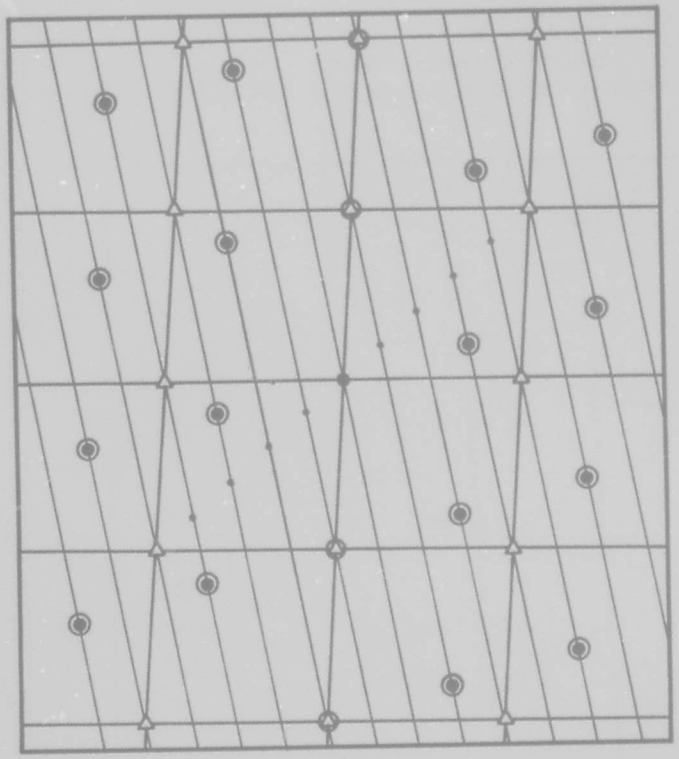

(c)

Fig. 110 Streaked Spot Pattern Obtained From Severely Heated Area Shown in Fig. 109. (a) Image, 12,500×. (b) Streaked diffraction pattern. (c) Diagram of diffraction pattern: $\alpha[20\cdot\bar{1}]$ and $\beta[3\bar{1}\cdot\bar{2}]$ superimposed

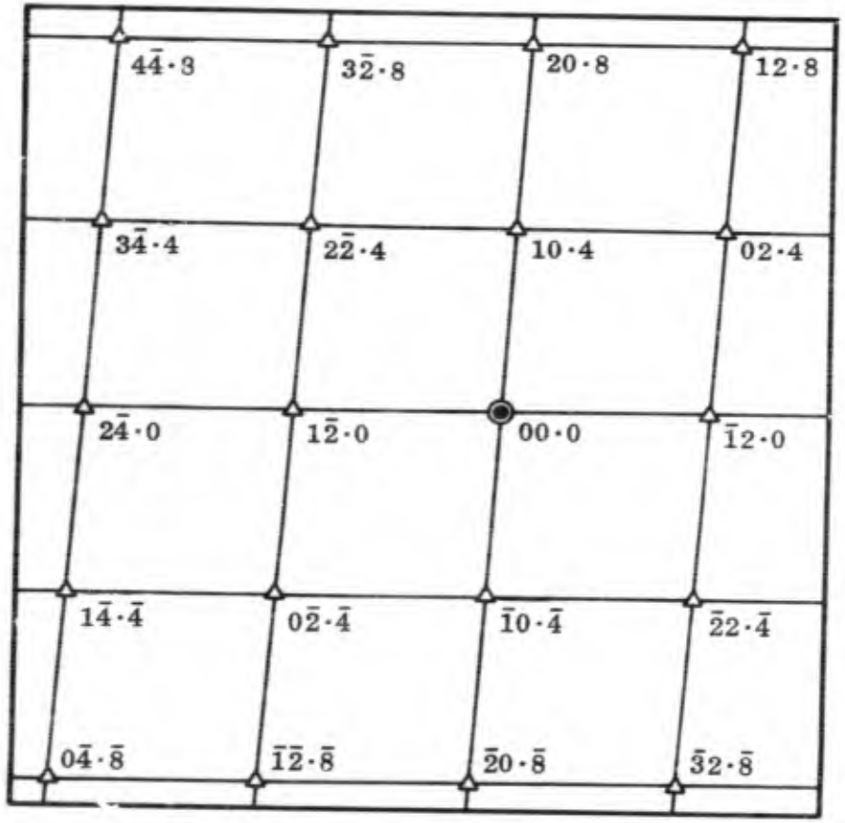

Fig. 110d α-Rhombohedral [$20\cdot\bar{1}$] Spot Pattern Obtained From Fig. 110c

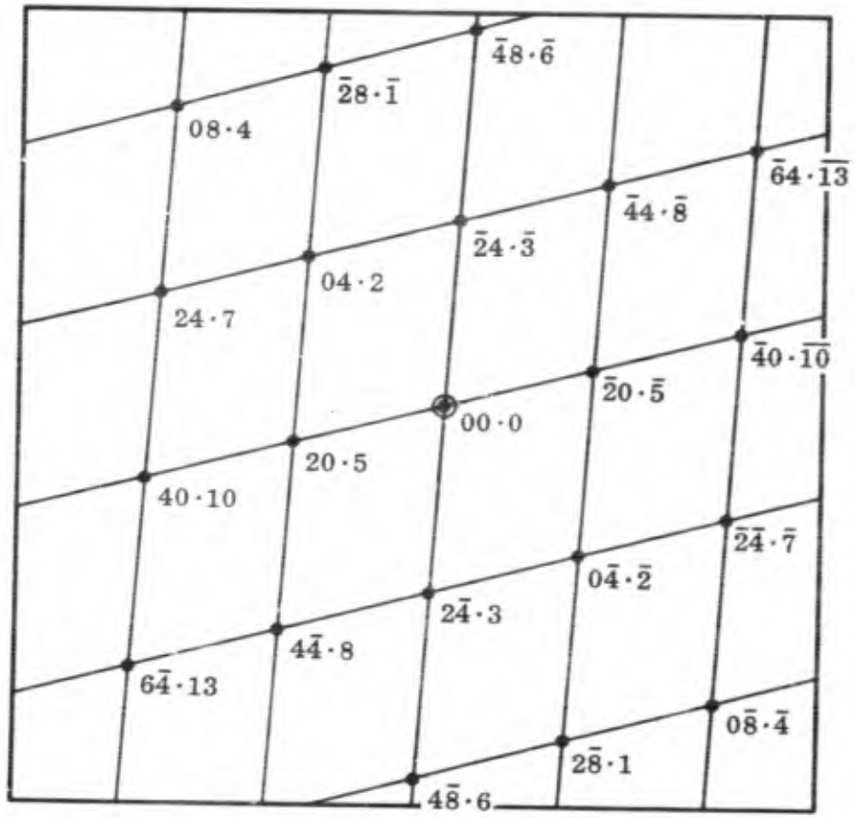

Fig. 110e β-Rhombohedral [$3\bar{1}\cdot\bar{2}$] Spot Pattern Obtained From Fig. 110c

of two well-defined, overlapping single crystal patterns, one of α and the other of β. Moreover, the patterns are definitely related because the streaks pass through reflections of both patterns, and certain reflections of the two patterns coincide. Figure 110(c) gives the complete pattern, as obtained directly from the plate [Fig. 110(b)], while (d) and (e) show the two component patterns, the $[20\cdot\bar{1}]\alpha$ and the $[3\bar{1}\cdot\bar{2}]\beta$. Tables 40 and 41 show measured and calculated d-spacings and angles for the α and β patterns, respectively.

Comparison of Figs. 110(c), (d), and (e) indicates that the following orientation relationships exist:

$$(10\cdot4)_\alpha \parallel (\bar{2}4\cdot\bar{3})_\beta$$
$$(02\cdot4)_\alpha \parallel (\bar{6}4\cdot\overline{13})_\beta$$

Also, the direction of the rel-rod streaks in the plane of the pattern shows that planar disorder exists on the $(5\bar{2}\cdot16)$ planes in α and the $(13\cdot1)$ planes in β. The meaning of this relationship is not clear, since the d-spacing of $(5\bar{2}\cdot16)$ in α-boron is about 0.6 Å, or only one-third of the interatomic distance within a B_{12} group. The spacing corresponding to the reciprocal distance between the streaked lines in Fig. 110(c) is 10.2 Å, which is about twice the β $(10\cdot4)$ spacing. This large spacing would seem to indicate rel-rod effects normal to the plane of the pattern as well. The diagonal row of spots parallel to the α $(02\cdot4)$ is also unexplained.

An examination of the $\alpha[20\cdot\bar{1}]$ pattern, Fig. 110(d), reveals that certain reflections are missing – the $(01\cdot2)$ and $(1\bar{1}\cdot2)$ and all those formed by linear combinations of these in which the sum of the coefficients is an odd integer. Figure 64(c), Section 4.4.1, showed an example of the $\alpha[\bar{2}0\cdot1]$ pattern, with no missing reflections, obtained from an electropolished filament specimen. Figure 111 gives this pattern again, with the pattern of Fig. 110(d) inverted and superimposed upon it. This superposition demonstrates which reflections are missing. Because there is no doubt about the

Table 40

COMPARISON OF MEASURED AND CALCULATED d-SPACINGS AND ANGLES FOR α $[20\cdot\bar{1}]$ PATTERN SHOWN IN FIG. 110(d)

Quantity	Measured Value	Calculated[a] Value
α d $(10\cdot4)$	2.55 Å	2.526 Å
α d $(1\bar{2}\cdot0)$	2.43 Å	2.454 Å
α d $(2\bar{2}\cdot4)$	1.81 Å	1.760 Å
α d $(0\bar{2}\cdot\bar{4})$	1.72 Å	1.760 Å
α d $(3\bar{4}\cdot4)$	1.12 Å	1.104 Å
α d $(3\bar{2}\cdot8)$	1.16 Å	1.123 Å
α d $(1\bar{4}\cdot\bar{4})$	1.08 Å	1.104 Å
$\measuredangle(10\cdot4), (3\bar{2}\cdot8)$	27.5°	27°15'
$\measuredangle(3\bar{2}\cdot8), (1\bar{2}\cdot0)$	65.0°	62°46'
$\measuredangle(2\bar{2}\cdot4), (1\bar{2}\cdot0)$	45.0°	44°10'
$\measuredangle(2\bar{2}\cdot4), (3\bar{4}\cdot4)$	19.5°	18°16'
$\measuredangle(3\bar{4}\cdot4), (\bar{1}0\cdot\bar{4})$	113.5°	115°54'
$\measuredangle(3\bar{4}\cdot4), (1\bar{4}\cdot\bar{4})$	51.0°	51°48'
$\measuredangle(1\bar{4}\cdot\bar{4}), (\bar{1}0\cdot\bar{4})$	62.0°	64°6'
$\measuredangle(3\bar{4}\cdot4), (0\bar{2}\cdot\bar{4})$	68.5°	70°4'

[a] Using $a_o = 4.908$ Å, $c_o = 12.567$ Å (ASTM Card 12-377).

Table 41

COMPARISON OF MEASURED AND CALCULATED d-SPACINGS AND ANGLES FOR β $[3\bar{1}\cdot\bar{2}]$ PATTERN SHOWN IN FIG. 110(e)

Quantity	Measured Value	Calculated[a] Value
β d $(\bar{2}4\cdot\bar{3})$	2.55 Å	2.586 Å
β d $(04\cdot2)$	2.35 Å	2.324 Å
β d $(24\cdot7)$	1.62 Å	1.583 Å
β d $(20\cdot5)$	3.32 Å	3.352 Å
β d $(6\bar{4}\cdot13)$	1.24 Å	1.278 Å
β d $(4\bar{4}\cdot8)$	1.80 Å	1.851 Å
$\measuredangle(\bar{2}4\cdot\bar{3}), (04\cdot2)$	43.5°	42°25'
$\measuredangle(\bar{2}4\cdot\bar{3}), (24\cdot7)$	71.0°	66°49'
$\measuredangle(04\cdot2), (20\cdot5)$	64.5°	60°58'
$\measuredangle(04\cdot2), (6\bar{4}\cdot13)$	92.0°	89°42'
$\measuredangle(20\cdot5), (6\bar{4}\cdot13)$	26.5°	28°44'
$\measuredangle(20\cdot5), (4\bar{4}\cdot8)$	41.0°	44°8'
$\measuredangle(4\bar{4}\cdot8), (6\bar{4}\cdot13)$	14.0°	15°24'

[a] Using $a_o = 10.944$ Å, $c_o = 23.715$ Å (ASTM Card 11-618).

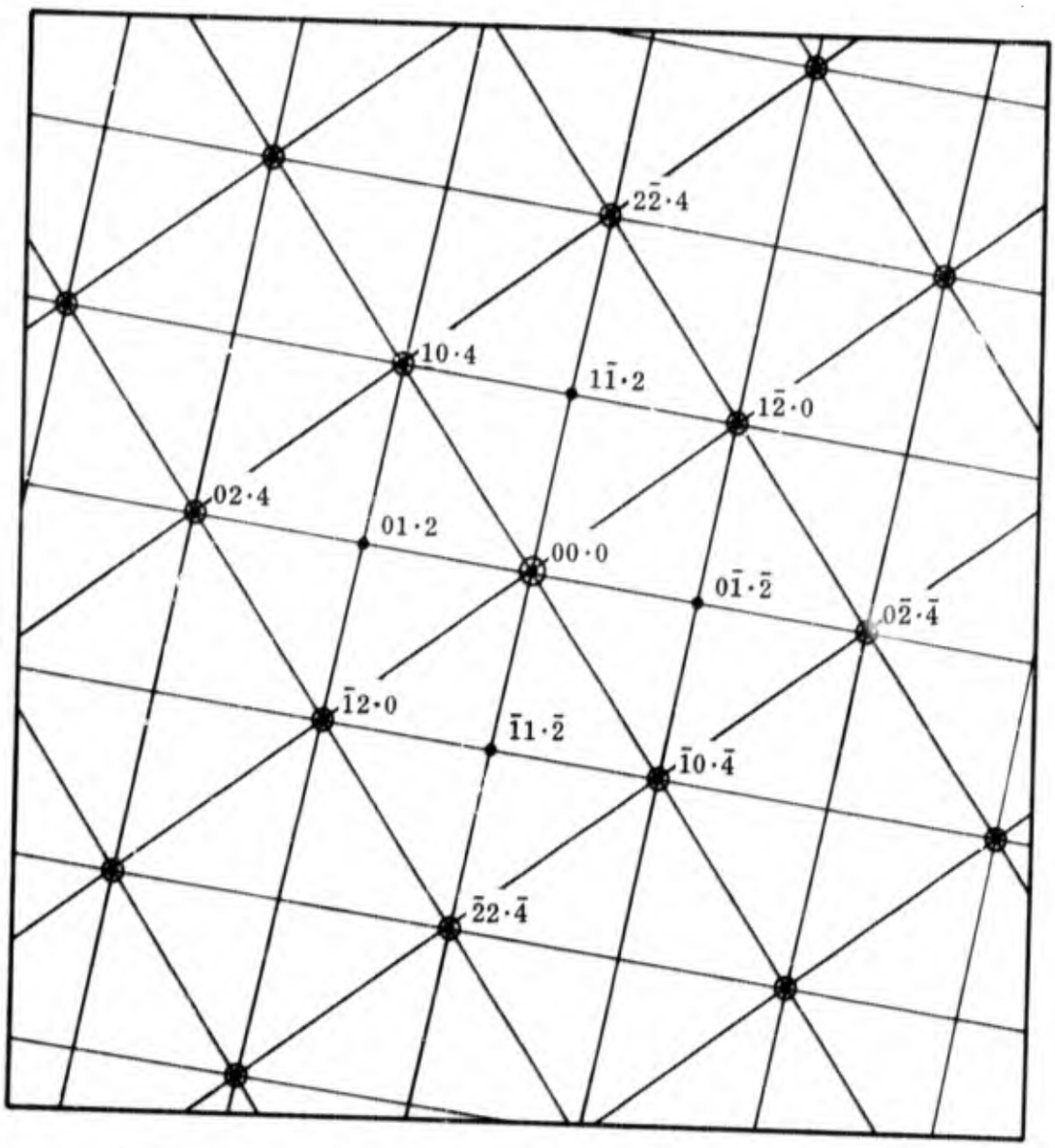

Fig. 111 Illustration of the Missing Reflections of the α-Boron Spot Pattern Shown in Fig. 110d. The fine grid is the $\alpha[\bar{2}0\cdot1]$ pattern with all reflections present. The coarse grid shows the reflections present in the pattern of Fig. 110d

indexing of these patterns, it is apparent that the missing reflections are in some way related to defects in the rhombohedral boron structures.

In summary, beam heating experiments have clearly shown the growth of large, striated crystallites of α-rhombohedral boron from the matrix of small-crystallite α-boron, accompanied by the decomposition of the characteristic halo pattern of the matrix into discrete rings corresponding to reflections of α-rhombohedral boron. More intense beam heating results in the transformation of some of the α- to β-rhombohedral boron. Analysis of the streaked single-crystal diffraction patterns of the beam-heated material indicates that planar defects exist on a variety of crystallographic planes, most of which are of high indices. Some of the spot patterns are missing certain reflections and their absence indicates a deviation from the "theoretical" structure. This effect was also noted in spot patterns obtained from grindings of pure β-rhombohedral boron and also ground filament, Section 4.4.3.

4.4.5 Heat Treated Filaments

Samples of production-run boron filaments were wrapped in molybdenum foil, sealed in evacuated quartz ampules, and annealed at several different temperatures for various lengths of time. Some of the filaments which were annealed at 1050°C for 15 hours were ground in a boron carbide mortar and pestle and examined in the electron microscope.

Figure 112 shows one of these particles and the halo diffraction pattern obtained from it. Five distinct halos were distinguished. The average d-spacings of these halos are listed in Table 42 and compared with those measured from the as-deposited filament sample shown in Fig. 113 (same as Fig. 53, Section 4.4.1).

Table 42 shows that the 1050°C heat treatment resulted in a significant increase in the intensity of the 2.12 Å halo. If the halos are interpreted as broadened α-rhombohedral boron reflections, then from Fig. 48, Section 4.3.2, a halo at 2.12 Å should have an

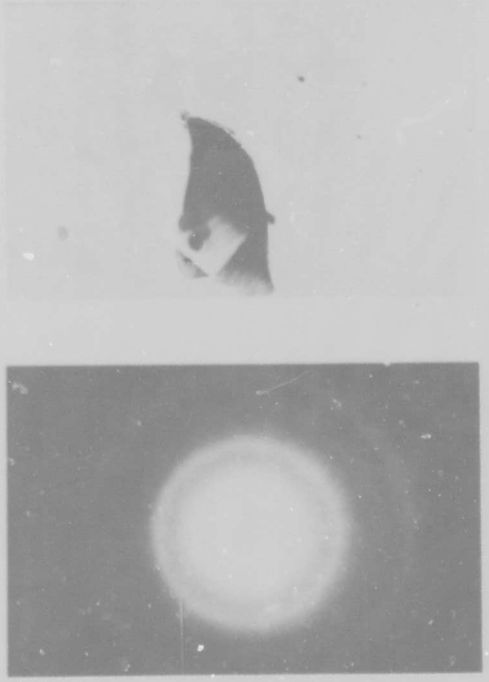

Fig. 112 Particle of Ground Boron Filament, Heat Treated 15 hr at 1050°C in Vacuum. 12,500×. Halo pattern shows increase in intensity of third halo (d = 2.12 Å). P1265

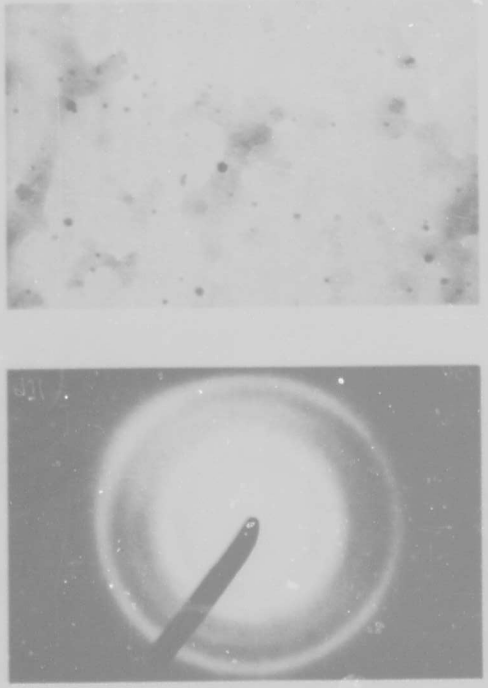

Fig. 113 Electropolished, As-Deposited Boron Filament Specimen, Showing Typical Halo Pattern. Third halo is nearly invisible on print. P750

Table 42

COMPARISON OF HALO d-SPACINGS FROM HEAT-TREATED AND AS-DEPOSITED BORON FILAMENTS

Number	Heat Treated[a]		As Deposited[b]	
	d, Å	I	d, Å	I
1	4.41	S	4.43	S
2	2.51	S	2.55	S
3	2.12	M	2.13	VW
4	1.69	M	1.75	M
5	1.40	S	1.42	S

(a) 1050°C, 15 hours in vacuum.
(b) Section 4.4.1, Table 22. Electropolished, as-deposited filament.

intensity comparable to that of the second halo at 2.55 Å, because the values of $\langle F \rangle$ are very nearly the same. From Fig. 49, it is seen that the 2.12 Å halo occurs in the vicinity of four reflections of α-rhombohedral boron, ranging from 2.03 to 2.18 Å. Thus, the 1050°C heat treatment brought the intensity distribution of the halos into closer agreement with that predicted for the α-rhombohedral boron structure. If some sort of defect α structure is responsible for the halo intensity distribution observed in the case of as-deposited filaments (see discussion in Section 4.3.2), then the heat treatment apparently tends to produce a more nearly ideal α structure.

It should be noted that 2.13 Å is the d-spacing of the $(10\bar{1}0)$ reflection of carbon, and therefore the possibility of the carbon substrate contributing to the halo intensity must be considered. The $(10\bar{1}0)$ prism planes will diffract strongly only if there is considerable preferred orientation in the carbon substrate, with the basal planes parallel to the plane of the substrate. Because, in preparing carbon substrates for transmission electron microscopy, the object is to have as little preferred orientation as possible, it is believed that the carbon contribution to the increased halo intensity is negligible.

Figure 114 shows an example of increased intensity of the third halo in a chemically thinned specimen of as-deposited filament. This specimen was beam heated slightly at a point outside the field of view, but the structure in the region where the diffraction pattern was taken showed no effects of heating. The spots in the pattern presumably come from the particle within the boundaries of the selected area aperture, while the halos come from the surrounding matrix. Table 43 gives the measured d-spacings of the halo maxima compared to those from Fig. 53, Section 4.4.1.

Note that all the halos are shifted to lower d-spacings. The 1.19 Å halo is close to that reported by Wawner (Ref. 14) and was not observed previously in this investigation. The d-spacing shift is greater than can be accounted for by the uncertainty in the camera constant, and this shift may reflect a change in lattice parameter of the

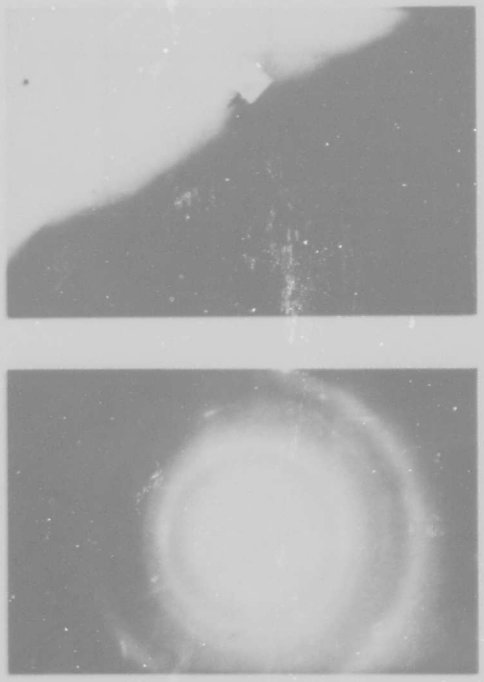

Fig. 114 Chemically Thinned, As-Deposited Boron Filament Specimen, Near a Beam Heated Area. Note distinct third halo. All halo maxima shifted slightly to lower d-spacings. Image at 12,000×. P1506

Table 43

d-SPACINGS OF HALO MAXIMA FROM FIG. 114, COMPARED WITH THOSE OF FIG. 53, SECTION 4.4.1

Number	Intensity	d, Å	As-Deposited d, Å
1	S	4.06	4.43
2	S	2.42	2.55
3	M	2.03	2.13
4	W	1.64	1.75
5	S	1.33	1.42
6	W	1.19	–

crystallites in the matrix. Figure 115 shows the halo boundaries compared to the positions of α-boron reflections. The agreement with α-boron is good for intensities as well as for d-spacings in this case.

No evidence of crystallite growth due to heat treatment, such as sharpening of the halos, was found in this investigation. Precise measurements of halo breadths in electron diffraction would require close control of exposure time and also of the second condenser lens current, which determines the instrumental broadening in electron diffraction patterns.

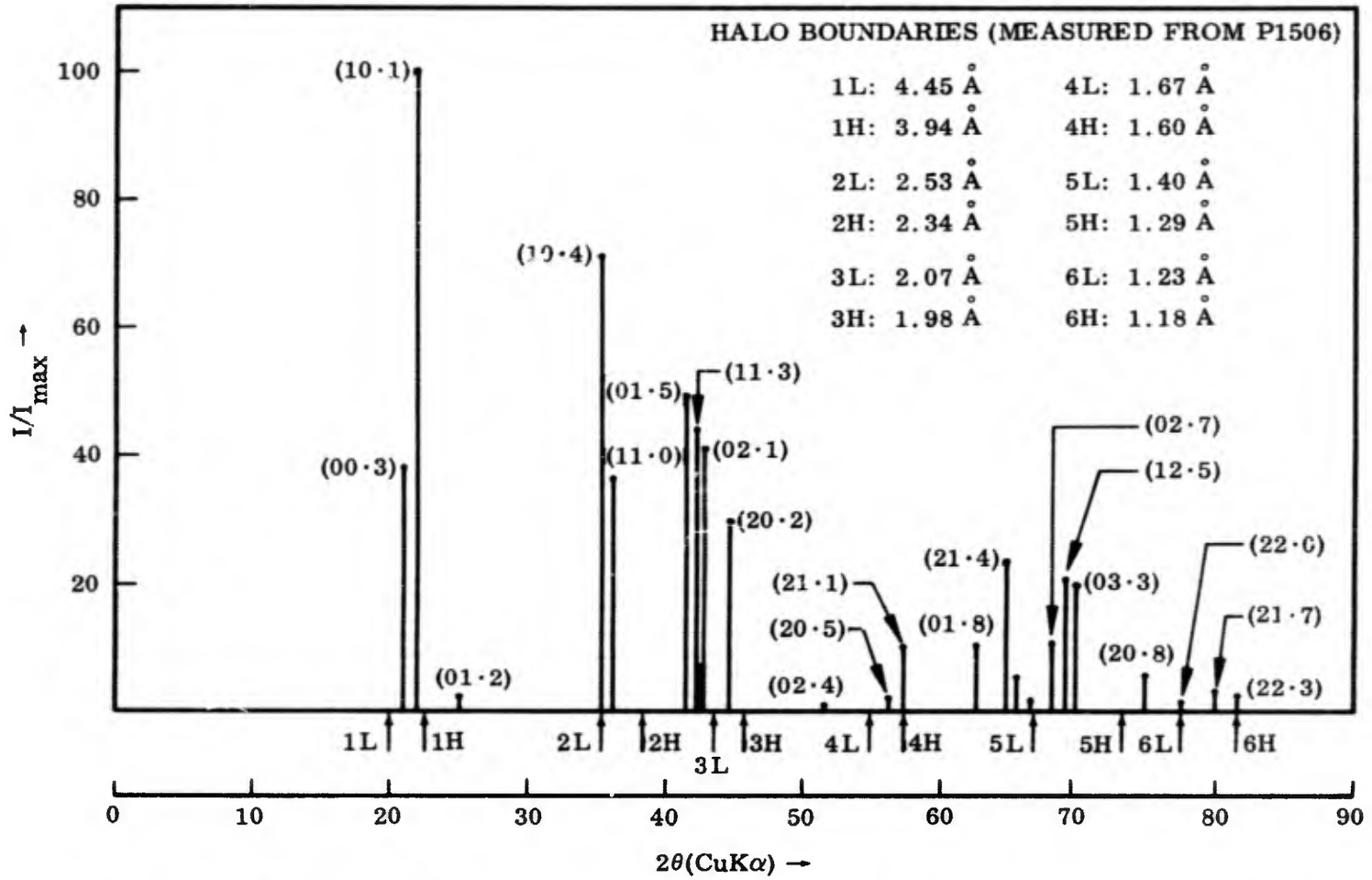

Fig. 115 Comparison of Halo Boundaries From Area Subjected to Slight Beam Heating With α-Boron Line Positions

4.4.6 Summary of Electron Microscope Results

The transmission electron microscopy study of thinned, vapor-deposited boron filaments has shown that the characteristic structure consists of a finely textured matrix with occasional embedded particles ranging in size from 1μ down to about 100 Å. The matrix yields a diffraction pattern consisting of 6 or 7 broad halos. The isolated particles are usually identifiable as single crystal or polycrystalline α- or β- rhombohedral boron. The matrix shows no evidence of dislocations or stacking faults.

High-magnification micrographs of the matrix structure have shown that the typical dimension of the texture is about 70 – 100 Å. Tilting experiments indicate that the textured appearance is due to diffraction contrast from small crystallites, and analysis of line broadening of the halos, as observed in both x-ray and electron diffraction, yields an average crystallite size of about 30 Å. Experiments using a very small selected area aperture have been interpreted to indicate a range of crystallite sizes from 10 – 100 Å, with an overall average size in agreement with the estimate from line broadening. The largest crystallites in the distribution are imaged in the microscope and produce the textured appearance of the matrix. Analysis of the halo pattern has established the probable identity of the crystallites as α-rhombohedral boron, although some evidence suggests the presence of the "simple" tetragonal form also. The halo intensity distribution definitely rules out a liquid-like amorphous structure.

Examination of ground β-rhombohedral boron has shown many different single crystal spot patterns. The [00·1] spot pattern shows forbidden reflections caused by long rel-rods normal to the (00·1) planes. The rel-rods are caused either by planar disorder or extreme thinness of the diffracting crystallite, or both. In addition, certain reflections which are allowed by the space group are missing from the pattern, some of which are also missing from the x-ray powder data. Many of the same reflections were found to be absent from other single-crystal spot patterns of β-boron. Grindings of

as-deposited boron filament were also examined. The observations were essentially the same as those for thinned filaments, i.e., the characteristic halo pattern and occasional single crystal spot patterns of α- or β-rhombohedral boron. Some of these patterns also had certain reflections missing. The correctness of the indexing of each spot pattern was verified by checking both d-spacings and interplanar angles.

A number of beam heating experiments were performed on specimens of thinned, as deposited filament. Heating the thinned filaments in the electron beam for a very short time results in the growth of large (1500 Å) striated crystallites of α-rhombohedral boron from the small-crystallite matrix. The growth of these new crystallites is accompanied by the decomposition of the halo pattern into discrete rings corresponding to reflections of α-rhombohedral boron. Some evidence of the "simple" tetragonal form of boron was also found in the partially decomposed halo patterns. With further beam heating, numerous spot patterns appear. All of the patterns studied were indexed either as α- or β-rhombohedral boron. Many of these patterns contained streaks indicating a structure containing planar defects. Several of the patterns also showed missing reflections, as observed in the grinding experiments.

When the as-deposited filaments were heat treated at 1050°C for 15 hours and examined in the electron microscope, the intensity of the third halo, at 2.12 Å, was found to be much greater than in the as-deposited filament samples. The halo intensity distribution from these heat-treated filaments was in better agreement with that predicted by the structure factor for α-rhombohedral boron.

Table 44 summarizes the observations of streaked diffraction patterns, indicating the crystallographic planes which are normal to the streaks. From this table it is apparent that the planar disorder which results in long rel-rods can occur on a great variety of crystallographic planes. The situation is therefore much more complex than in the case of metals, which typically show stacking faults on only one family of planes.

Table 45 summarizes the occurrences of missing reflections in spot patterns of α- and β-rhombohedral boron.

Table 44

SUMMARY OF REL-ROD EFFECTS IN ELECTRON DIFFRACTION PATTERNS OF BORON

Figure	Plate	Pattern Identification	Source	(hkℓ) Plane Normal to Rel-Rods
85	879	$\beta[00\cdot 1]$	β Grindings	(111)
88	862	$\beta[01\cdot \bar{1}]$	β Grindings	$(00\bar{1})$
100	1112	$\alpha[\bar{1}2\cdot 0]$	Beam-heated	(111)
101	1480	$\beta[4\bar{1}\cdot \bar{4}]$	Beam-heated	$(0\bar{2}3)$
102	1503	$\beta[\bar{5}4\cdot 0]$	Beam-heated	$(10\bar{2})$
106	1504	$\alpha[0\bar{4}\cdot 1]$	Beam-heated	(332)
107	1179	$\beta[\bar{3}7\cdot \bar{4}]$	Beam-Heated	$(50\bar{1})$
108	949-951	$\beta[\bar{7}5\cdot \bar{6}]$	Beam-heated	$(7\bar{2}1)$
109	1249	$\beta[\bar{2}1\cdot 0]$	Beam-heated	(220)
110	1251	$\alpha[20\cdot \bar{1}]$ $\beta[3\bar{1}\cdot \bar{2}]$	Beam-heated	(835) $(21\bar{2})$

Table 45

SUMMARY OF MISSING REFLECTIONS IN ELECTRON DIFFRACTION PATTERNS OF BORON

Figure	Plate	Pattern Identification	Source	Reflections Missing
85	879	$\beta[00\cdot 1]$	β Grindings	$(10\cdot 1), (11\cdot 0), (21\cdot 1), (30\cdot 0), \ldots$
62	1377	$\beta[7\bar{4}\cdot \bar{4}]$	Thinned filament	$(1\bar{2}\cdot 3), (0\bar{4}\cdot 1), \ldots$
63	1393	$\beta[2\bar{2}\cdot 4]$	Thinned filament	$(\bar{1}1\cdot 1), (02\cdot 1), (13\cdot 1), \ldots$ [$(11\cdot 0), (33\cdot 0)$ very weak]
80	694	$\beta[01\cdot \bar{4}]$	β Grindings	$(2\bar{1}\cdot 0), (21\cdot 1), \ldots$
83	926	$\beta[2\bar{1}\cdot 0]$	β Grindings	$(01\cdot \bar{1}), (01\cdot 2), (01\cdot 5), (01\cdot \bar{4}), \ldots$
90	1237	$\alpha[\bar{1}1\cdot 1]$	Filament grindings	$(1\bar{1}\cdot 2), (20\cdot 2), \ldots$
92	886	$\beta[00\cdot 1]$	Filament grindings	$(10\cdot 1), (11\cdot 0), (21\cdot 1), (30\cdot 0), \ldots$
109	1249	$\beta[\bar{2}1\cdot 0]$	Beam-heated	$(01\cdot \bar{1}), (01\cdot 2), (01\cdot 5), (01\cdot \bar{4}), \ldots$
110	1251	$\alpha[20\cdot \bar{1}]$ $\beta[3\bar{1}\cdot \bar{2}]$	Beam-heated	$(1\bar{1}\cdot 2), (01\cdot 2), \ldots$ $(02\cdot 1), (2\bar{2}\cdot 4), \ldots$

The table shows clearly that in β-boron, for example, the $(11\cdot 0)$ type reflections are absent from the $[00\cdot 1]$ and $[01\cdot\bar{4}]$ patterns, and are present, but very weak, in the $[2\bar{2}\cdot 4]$ pattern. This reflection is present in the x-ray powder pattern (see Table 21, Section 4.3.2). For α-boron, the $(01\cdot 2)_H = (110)_R$ reflection is missing in two different patterns, i.e. the $[\bar{1}1\cdot 1]$ and the $[20\cdot\bar{1}]$. Note that in Fig. 64(c), section 4.4.1, the $\alpha[\bar{2}0\cdot 1]$ pattern contains all reflections. These examples indicate that the missing reflections are due to various defect structures, i.e., departures from the ideal crystalline structures.

A knowledge of the atomic arrangements in the defect α-rhombohedral structures would permit the calculation of the observed halo diffraction pattern. From Fig. 49, the α-boron reflections near the third halo are the $(01\cdot 5)$, $(11\cdot 3)$, $(02\cdot 1)$, and $(20\cdot 2)$. The absence of one or more of these reflections due to a defect structure would cause the intensity of the third halo to be anomalously low, as observed. Table 45 indicates that the $(20\cdot 2)$ is missing from one of the α-boron spot patterns, the $\alpha[\bar{1}1\cdot 1]$. Note also that the $(01\cdot 2)$-type reflections are missing from both of the α-boron spot patterns as well as from the $\beta[2\bar{1}\cdot 0]$ pattern (Figs. 83, 109). Further examination of Table 45 reveals that:

- the $(02\cdot 1)$ is missing from $\beta[2\bar{2}\cdot 4]$ and $\beta[3\bar{1}\cdot\bar{2}]$
- the $(11\cdot 3)$ is missing from $\beta[7\bar{4}\cdot\bar{4}]$
- the $(01\cdot 5)$ is missing in $\beta[2\bar{1}\cdot 0]$

Other β-boron spot patterns shown in the text do contain the reflections noted above. Since it has already been shown that one reflection, the $(01\cdot 2)$, is frequently missing from both β and α spot patterns, it might be expected that, if the $\alpha[2\bar{2}\cdot 4]$, $[3\bar{1}\cdot\bar{2}]$, $[7\bar{4}\cdot\bar{4}]$ etc., patterns had been observed, then the $(02\cdot 1)$, $(11\cdot 3)$ and $(01\cdot 5)$ reflections might also be missing.

A greater number of α-boron single crystal spot patterns, in a variety of orientations, must be observed and indexed in order to verify this hypothesis. Unfortunately, there were relatively few large crystallites of α-boron in the vapor deposited boron filaments examined in this study.

4.5 DISCUSSION AND SUMMARY OF CRYSTALLOGRAPHIC STRUCTURE OF BORON FILAMENTS

The crystallographic structure of the vapor-deposited boron sheath of continuous boron filaments has been studied by polarized light microscopy, transmission electron microscopy, x-ray diffraction, and electron diffraction. Other aggregates of boron were also examined for comparison .

Boron filaments produced in the range 1600° to 2300° F (870° – 1260° C) do not exhibit optical anisotropy, and there is no indication of preferred orientation of the boron in the diffraction patterns. Filaments deposited by electrical discharge near 300° C do show optical anisotropy typical of small-crystallite, vapor-deposited materials with preferred orientation, and filaments deposited above 1600° C have a columnar grain structure which is optically active. Large grain size β-rhombohedral boron prepared by solidification from the melt is optically active, has a strong tendency to twin, and fractures conchoidally. There is no evidence of easy cleavage on a particular plane in β-rhombohedral boron. Vapor-deposited boron filaments have a nodular structure comparable to that of other vapor-deposited materials. The absence of both optical anisotropy and preferred orientation suggests that the vapor-deposited boron consists of randomly oriented crystallites which are too small to be resolved by light microscopy. A similar situation is found in pyrolytic carbons deposited at sufficiently low temperatures.

The characteristic diffraction pattern from vapor-deposited boron consists of at least six broad but well-defined halos. Because the successive halo maxima do not decrease in intensity, the possibility of a liquid-like amorphous structure is immediately eliminated. The complete halo pattern can usually be observed by transmission electron diffraction, but in general only the three most intense halos are readily seen by x-ray diffraction because of the greater effect of the Lorentz-polarization factor in the x-ray case. Electron diffraction is therefore a more convenient tool for studying the structure of vapor-deposited boron; it also permits the study of isolated small areas. Both the x-ray and electron diffraction studies of the halo pattern predict a crystallite size

of about 30 Å to account for the observed broadening. Comparison of the positions of the halo boundaries with the positions of the reflections of the known crystallographic forms of boron shows that the halo pattern is best interpreted as a mixture of the α-rhombohedral and "simple" tetragonal polymorphs. The intensity distribution of the halos suggests the presence of systmatic defects in the ideal α or tetragonal structures. The same halo pattern is observed in both thinned and ground specimens of boron filament. Density observations (Appendix C) are also consistent with a mixture of α- and tetragonal boron.

The persistence of the halo pattern down to a selected area size of 200 Å × 200 Å, together with the textured appearance of the vapor-deposited boron in high-magnification electron micrographs, suggests a distribution of crystallite sizes from 10 – 100 Å. The 30 Å crystallite size calculated from the broadening represents the average size obtained by integrating over the distribution.

No evidence of stacking faults or dislocations was found in transmission electron micrographs of vapor-deposited boron, but inclusions ranging in size from 100 – 10,000 Å were frequently seen. These inclusions produce either single crystal spot patterns or discontinuous rings, and are usually identifiable as either α-rhombohedral or β-rhombohedral boron.

Many different single crystal spot patterns of α- and β-rhombohedral boron, obtained from both thinned and ground samples of boron filament, were observed and indexed in this study, but no single cyrstal patterns of tetragonal boron were found. Moreover, the majority of the crystalline inclusions in as-deposited filament specimens were identified as β, while α was found to occur relatively infrequently.

Beam heating in the electron microscope causes the growth of 1500 Å crystallites of α-rhombohedral boron from the small-crystallite matrix. Many of these large crystallites have striations which correlate with streaks in the corresponding diffraction patterns. More intense beam heating causes the formation of β-rhombohedral boron as well as

the α form. In the early stages of beam heating, the halo pattern is found to decompose into discrete reflections of α-rhombohedral boron. A number of single crystal patterns from the beam heated material were indexed.

Many of the indexed single crystal spot patterns of both α- and β-rhombohedral boron contain missing reflections. In the case of β-boron, some of the reflections which are missing in the electron diffraction patterns are also absent from the x-ray powder data, and are systematic extinctions caused by the interstitial groups in the large rhombohedral cell of β-boron. The other reflections, which are missing from the electron diffraction patterns but present in the x-ray powder data, are due to deviations from the ideal structures of α- and β-boron.

The absence of certain reflections due to a defect α-boron structure is suggested as the probable explanation of the anomalous intensity distribution of the halo pattern.

The single-crystal spot patterns of α- and β-rhombohedral boron also show rel-rod effects in a number of different directions in reciprocal space. These observations demonstrate that in boron there exists no simple family of crystallographic planes on which faults occur, as in the case of many metals.

Section 5 – FUTURE WORK

Exclusive of production difficulties and the elimination of defects which reduce the overall strength, four major problem areas were defined in this investigation and remain to be studied:

- The first is to acquire more accurate and more complete information on the properties of the core compounds.
- The second is to obtain a better description of the defect α-rhombohedral/tetragonal model proposed for the structure of vapor deposited boron.
- The third is to obtain more information on the effect of thermal treatment in various environments.
- The fourth is to explain the missing reflections found in large crystallite cast and vapor-deposited β-rhombohedral boron as well as large crystallite vapor-deposited α-rhombohedral boron.

Phase equilibria at the deposition temperature would be best studied during deposition in a high temperature x-ray camera; the volume expansion could be monitored by observing the flexure of flat plate substrates as they react with the deposited material. Because other materials are now being used as cores for boron filaments, these materials should also be examined.

An improved description of the α-rhombohedral/tetragonal boron model might be derived from more precise determinations of the halo shapes and relative intensities. These data are best obtained using a microphotometer on carefully controlled electron diffraction photographs. Various models could then be tested against the improved intensity data using theoretical structure factor calculations. Unfortunately, the diffraction halos cannot be interpreted exactly, and several defect structures will probably fit the data equally well. One possible solution to the problem is to obtain better diffraction data from deposits prepared over a wider temperature range and to examine these deposits extensively, observing variations in amount and kinds of large crystallite size material as well as variations in the halo structure. Infrared absorption measurements may also help determine the nature of bonding in vapor deposited boron.

Several unusual effects of heat treatment were left unexplained. The possible halo shifts may provide some information on the model of vapor-deposited boron but the formation of voids in the filament and the unusual reaction with Ta are not understood. The anelasticity and plastic deformation of boron filaments are also unexplained as are the strength losses due to heat treatment.

Although the missing reflections in both α- and β-rhombohedral boron have been well demonstrated, the reasons for their absence are not fully understood. Systematic defects such as missing structural groups, or misplaced atoms or atom clusters are probably responsible, but these ideas must be checked by making structure factor calculations and comparing the calculated intensities to better relative intensity data.

Section 6 – REFERENCES

1. R. C. Ellis, Jr., "Some Etching Studies on Boron", Boron-Synthesis, Structure and Properties, p. 135, Plenum Press, Inc. 1960
2. Claude P. Talley, et al., "Preparation and Properties of Massive Amorphous Elemental Boron", Boron-Synthesis, Structure and Properties, p. 94, Plenum Press, Inc. 1960
3. R. Kiessling, Acta Chem. Scand. 3, 1949, p. 595
4. G. V. Samsonov and Ya. S. Umanskiy, Hard Compounds of Refractory Materials, NASA Technical Transl. TTF-102, June 1962
5. G. V. Samsonov, I. Ya. Markovskii, A. F. Zhigach, and M. G. Valyashko, Boron, Its Compounds and Alloys, Atomic Energy Commission Translation, AEC-tr-5032(Book 2), 1960
6. Aerojet General Corp., "Ternary Phase Equilibria, Part I, Vol. III, Systems Mo-B and W-B," E. Rudy and St. Windisch, Tech. Report AFML-TR-65-2, Part 1, Vol. III, Sept. 1965
7. B. Post, p. 301 in Boron, Metallo-Boranes, Compounds, and Boranes, R. Adams, Ed., John Wiley and Sons, Interscience, 1964
8. Texaco Experiment Inc., "Boron Reinforcements for Structural Composites", C. P. Talley, W. J. Clark, K. M. Gunn, F. E. Wawner, Jr., and J. E. Schultz, ASD-TDR-62-257, Part II, Apr 1963
9. H. P. Woods, F. E. Wawner, Jr., and B. G. Fox, Science, 151, n3706, 7 Jan 1966 p. 75
10. Aerospace Research Laboratories, H. A. Lipsitt, "A Study of Boron Filaments", Metallurgy and Ceramics Research Laboratory (research initiated 28 Oct 1964)
11. A. Chretien and J. Helgorsky, Compts Rendus, 252, 1961, p. 742
12. R. Kieffer, R. Benesovsky, and E. R. Honak, Z. Anorg. Chemie, 268, 1952, p. 191

13. General Electric Company, "Research on Improved High-Modulus, High-Strength Filaments and Composites Thereof", Tech. Report AFML-TR-65-319, Sept. 1965

14. Texaco Experiment, Inc., "High-Modulus, High-Strength Reinforcements for Structural Components", C. P. Talley, Tech. Report ML-TDR-64-88, Part III, Aug 1965

15. F. E. Wawner, Jr., p. 283 in Boron, Vol. 2, Edited by G. K. Gaulé, Plenum Press, New York, 1966

16. L. F. Coffin, Jr., J. Amer. Ceram. Soc., 47, n. 10, 1964, p. 473

17. R. J. Diefendorf, p. 313 in High Temperature Technology, Butterworths Pub. Co. for International Union of Pure and Applied Chemistry, 1964

18. J. C. Bokros, Carbon, 3, n2, Oct. 1965, p. 201

19. M. L. Hammond, to be published in Communications, J. Amer. Ceram. Soc.

20. J. L. Hoard and A. E. Newkirk, J. Amer. Chem. Soc., 82, 1960, p. 70

21. United Aircraft Corporation, "Improved High Modulus, High Strength Filaments and Composites", R. Fanti, R. D. Schile, and F. S. Galasso et al., Tech Report AFML-TR-65-380, Nov. 1965

22. T. A. Dolton and P. J. Schneider, Orgn. 55-24, Bldg. 104, Lockheed Missiles & Space Company, Private Communication to M. L. Hammond, 1966

23. R. F. Karlak, Orgn. 52-30, Bldg. 201, Lockheed Missiles and Space Co., Private Communication to M. L. Hammond, 1966

24. V. I. Matkovich, R. F. Giese, Jr., and J. Economy, "Packing of B_{12} Groups in Boron and Boride Structures", ONR Technical Report No. 3, July 1964

25. H. J. Becker, p. 89 in Boron, Vol. 2, Edited by G. K. Gaulé, Plenum Press, New York, 1966

26. B. F. Decker and J. S. Kasper, Acta Cryst. 12, 1959, p. 503

27. R. E. Hughes et al., J. Amer. Chem. Soc. 85, 1963, p. 361

28. J. L. Hoard, p. 51 in Borax to Boranes, Advances in Chemistry Series, Number 32, American Chemical Society, Washington, D.C., 1961

29. J. L. Hoard and R. E. Hughes, p. 89 of Boron, Vol. 2, Edited by G. K. Gaulé, Plenum Press, New York, 1966

30. E. T. Peters and W. D. Potter, Trans. AIME, 233, 1965, p. 473

31. H. A. Lipsitt and H. M. Otte, phys. stat. solidi, 13, 1966, p. 439

32. P. F. Lindquist, M. L. Hammond, and R. H. Bragg, to be published in phys. stat. solidi 13, Sept. 1966

33. D. E. Sands and J. L. Hoard, J. Amer. Chem. Soc. 79, 1957, p. 5582

34. Lockheed Missiles & Space Co., "Formation of Boron Filaments by Electrical Discharge Processes", M. E. Sibert, R. D. Wales, A. E. Hultquist, Technical Report AFML-TR-66-93, April 1966

35. R. H. Bragg and C. M. Packer, Nature, 195, 1962, p. 1080

36. R. H. Bragg, D. D. Crooks, R. W. Fenn, Jr., and M. L. Hammond, Carbon, 1, 1964, p. 171

37. Aerojet General Corp., "Ternary Phase Equilibria, Part I, Vol. X, Systems V-B, Nb-B, and Ta-B", Tech. Report AFML-TR-65-2, Part I, Vol. X, March 1966

38. H. P. Klug and L. E. Alexander, X-ray Diffraction Procedures for Polycrystalline and Amorphous Materials, John Wiley and Sons, New York, 1956

39. J. L. Hoard, R. E. Hughes, and D. E. Sands, J. Amer. Chem. Soc., 80, 1958, p. 4507

40. R. W. James, The Crystalline State - Vol. II, The Optical Principles of the Diffraction of X-rays, G. Bell & Sons, London, 1948

41. H. Goldstein, Classical Mechanics, Addison-Wesley, 1950, p. 107

42. R. D. Heidenreich, Fundamentals of Transmission Electron Microscopy, Interscience, New York, 1964, p. 45

43. A. Guinier, X-ray Diffraction, Freeman & Co., London, 1963, p. 72

44. B. D. Cullity, Elements of X-ray Diffraction, Addison-Wesley, 1956, p. 265

45. G. Thomas, Transmission Electron Microscopy of Metals, Wiley, New York, 1962, p. 111

46. S. Amelinckx, The Direct Observation of Dislocations, Supplement 6 of Solid State Physics, Academic Press, New York, 1964, p. 193

47. J. L. Hoard, S. Geller, and R. E. Hughes, J. Amer. Chem. Soc., 73, 1951, p. 1892

48. Texaco Experiment, Inc., "Boron Reinforcements for Structural Composites," C. P. Talley et al., ASD-TDR-62-257 (Pt. I) March 1952

Appendix I

RADIAL TEMPERATURE GRADIENTS IN COMPOSITE CYLINDERS

Boron filaments are concentric composite cylinders with an inner core of borides and an outer sheath or mantle of vapor deposited boron. The filaments are often prepared by resistively heating a wire to cause the thermal decomposition of a boron-containing gas on the surface. The borides and boron have different thermal characteristics and there exists the possibility of a radial temperature gradient which could result in a radial structure gradient. Dolton and Schneider (Ref. 22) have derived the expressions for temperature gradients in composite cylinders, both of which generate heat. Their analysis is given in this appendix.

The general form of the differential equation for transient radial heat conduction, including a heat source is:

$$\frac{\partial}{\partial r}\left(K\frac{\partial t}{\partial r}\right) + \frac{1}{r}\frac{\partial}{\partial r}(Kt) + \dot{q}_o = \rho C_p \frac{\partial t}{\partial \theta} \qquad \text{(A-1)}$$

If steady state exists and thermal properties are assumed constant, (Eq. A-1) reduces to:

$$\frac{d^2t}{dr^2} + \frac{1}{r}\frac{dt}{dr} + \frac{\dot{q}_o}{K} = 0 \qquad \text{(A-2)}$$

The general solution of (A-2) is readily found to be:

$$t = C_1 \ln r - \frac{\dot{q}_o}{4K} r^2 + C_2 \qquad \text{(A-3)}$$

Now, consider the system with a cylindrical core, c , surrounded by a mantle, m , both of which generate heat at rates $\dot{q}_c$ and $\dot{q}_m$ respectively and which have conductivities K_c and K_m , as shown in Fig. 116 .

The temperature at the inner core surface is designated $t_{c,s}$, the temperature at the outer surface of the mantle by $t_{m,s}$.

General expressions (one for the core, and one for the mantle) for the temperatures may be obtained with the following boundary conditions:

(1) $\frac{dt_c}{dr} = 0$; @ $r = 0$ (geometrical symmetry)

(2) $K_c \frac{dt_c}{dr} = K_m \frac{dt_m}{dr}$; @ $r = r_c$ (continuity of heat flux)

(3) $h (t_{m,s} - t_a) = - K_m \frac{dt_m}{dr}$; @ $r = r_c$ (surface convection)

(4) $t_m = t_c$; @ $r = r_c$ (continuity of temperature)

These boundary conditions are then used to find the constants in Eq. (A-3), written for core and mantle temperatures:

$$t_c = C_1 \ln r + \frac{\dot{q}_c}{4K_c} r^2 + C_2 \qquad 0 \le r \le r_c \qquad \text{(A-3a)}$$

$$t_m = C_3 \ln r - \frac{\dot{q}_m}{4K_m} r^2 + C_4 \qquad r_c \le r \le r_m \qquad \text{(A-3b)}$$

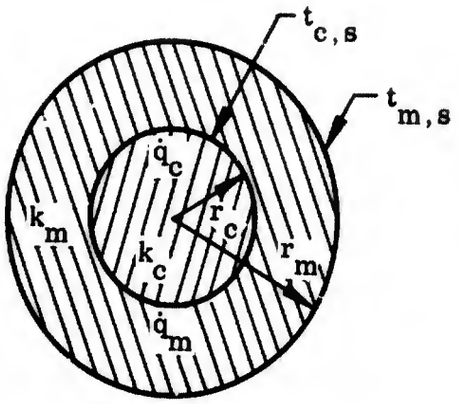

Fig. 116 Model for Radial Temperature Gradient Calculation

The resulting expressions are:

$$\frac{4K_m (t_c - t_a)}{\dot{q}_m r_m^2} = 2\left(\frac{r_c}{r_m}\right)^2 \left(\ln \frac{r_m}{r_c} + \frac{1}{B_i}\right)\left(\frac{\dot{q}_c}{\dot{q}_m} - 1\right) - \left(\frac{r_c}{r_m}^2 + \frac{2}{B_i} + 1\right)$$

$$- \frac{\dot{q}_c}{\dot{q}_m} \frac{K_m}{K_c}\left[\left(\frac{r}{r_m}\right)^2 - \left(\frac{r_c}{r_m}\right)^2\right] \qquad 0 \le r \le r_c$$

and

$$\frac{4K_m}{\dot{q}_m r_m^2}(t_m - t_a) = 2\left(\frac{r_c}{r_m}\right)^2 \left(\ln \frac{r_m}{r} + \frac{1}{B_i}\right)\left(\frac{\dot{q}_c}{\dot{q}_m} - 1\right) - \left(\frac{r}{r_m}\right)^2 + \frac{2}{B_i} + 1 \qquad r_c \le r \le r_m$$

where B_i = Biot No. $= hr_m/K_m$

For the particular case of a known outer surface temperature, $h \to \infty$, $B_i \to \infty$ and $t_{m,s} \to t_a$. The expressions then become

$$\frac{4K_m (t_c - t_{m,s})}{\dot{q}_m r_m^2} = 2\left(\frac{r_c}{r_m}\right)^2 \left(\ln \frac{r_m}{r_c}\right)\left(\frac{\dot{q}_c}{\dot{q}_m} - 1\right) - \left(\frac{r_c}{r_m}\right)^2 + 1$$

$$- \frac{\dot{q}_c}{\dot{q}_m} \frac{K_c}{K_m}\left[\left(\frac{r}{r_m}\right)^2 - \left(\frac{r_c}{r_m}\right)^2\right] \qquad 0 \le r \le r_c$$

and

$$\frac{4K_m (t_m - t_{m,s})}{\dot{q}_m r_m^2} = 2\left(\frac{r_c}{r_m}\right)^2 \left(\ln \frac{r_m}{r}\right)\left(\frac{\dot{q}_c}{\dot{q}_m} - 1\right) - \left(\frac{r}{r_m}\right)^2 + 1 \qquad r_c \le r \le r_m$$

Be letting $r = r_c$ the temperature drop across the mantle becomes:

$$\frac{4K_m (t_{c,s} - t_{m,s})}{q_m r_m^2} = 2\left(\frac{r_c}{r_m}\right)^2 \left(\ln \frac{r_m}{r_c}\right)\left(\frac{q_c}{q_m} - 1\right) - \left(\frac{r_c}{r_m}\right)^2 + 1 \qquad \text{(A-4)}$$

Equation (A-4) is used in Section 3.7.4 to compute the temperature difference between the core-mantle interface and the outer filament surface. The temperature difference is only 8 – 80° C; therefore, radial temperature gradients do not seem to be important in determining the structure of boron filaments.

Appendix II

CALCULATION OF THE REACTANTS-TO-PRODUCTS VOLUME RATIO WHEN TWO SUBSTANCES COMBINE CHEMICALLY TO FORM TWO DISTINCT COMPOUNDS

When boron is deposited on tungsten in the vicinity of 1000° C, the boron reacts with the tungsten to form tungsten borides. Boron filaments are usually prepared by depositing boron on hot tungsten wires and it is important to consider the possibility of volume changes during the formation of new phases. A simple analysis of the problem is presented in Section 3.7.5; the more general treatment by Karlak (Ref. 23) is presented in this appendix.

The type of reaction considered is of the form

$$aA + bB \rightarrow c_1 A_{x_1} B_{y_1} + c_2 A_{x_2} B_{y_2} = c_1 C_1 + c_2 C_2 \qquad \text{(B-1)}$$

in terms of molar quantities. In terms of mass and volume the equations are respectively

$$(a M_A) A + (b M_B) B \rightarrow \left(c_1 M_{C_1}\right) C_1 + \left(c_2 M_{C_2}\right) C_2 \quad \text{(mass)} \qquad \text{(B-2)}$$

$$\left(\frac{a M_A}{\rho_A}\right) A + \left(\frac{b M_b}{\rho_B}\right) B \rightarrow \left(\frac{c_1 M_{C_1}}{\rho_{C_1}}\right) C_1 + \left(\frac{c_2 M_{C_2}}{\rho_{C_2}}\right) C_2 \quad \text{(volume)} \qquad \text{(B-3)}$$

The M_i's are the molecular weights and the ρ_i's the specific gravities or densities. Equation (B-3) can be abbreviated as

$$\gamma_A A + \gamma_B B \rightarrow \gamma_{C_1} C_1 + \gamma_{C_2} C_2 \qquad \text{(B-3a)}$$

From (B-1) we can write

$$a = c_1 x_1 + c_2 x_2$$

$$b = c_1 y_1 + c_2 y_2$$

So that

$$\gamma_A = \frac{a M_A}{\rho_A} = (c_1 x_1 + c_2 x_2) \frac{M_A}{\rho_A} \qquad \text{(B-4a)}$$

$$\gamma_B = \frac{b M_B}{\rho_B} = (c_1 y_1 + c_2 y_2) \frac{M_B}{\rho_B} \qquad \text{(B-4b)}$$

The definitions of γ_{C_1} and γ_{C_2} can be used to give

$$c_1 = \frac{\gamma_{C_1} \rho_{C_1}}{M_{C_1}}$$

$$c_2 = \frac{\gamma_{C_2} \rho_{C_2}}{M_{C_2}} \qquad \text{(B-5b)}$$

Substituting these into 4a, -b yields

$$\gamma_A = \left(\frac{\gamma_{C_1} \rho_{C_1}}{M_{C_1}} x_1 + \frac{\gamma_{C_2} \rho_{C_2}}{M_{C_2}} x_2 \right) \frac{M_A}{\rho_A} \qquad \text{(B-6a)}$$

$$\gamma_B = \left(\frac{\gamma_{C_1} \rho_{C_1}}{M_{C_1}} y_1 + \frac{\gamma_{C_2} \rho_{C_2}}{M_{C_2}} y_2 \right) \frac{M_B}{\rho_B} \qquad \text{(B-6b)}$$

Because the volumes of C_1 and C_2 formed are arbitrary, they must be determined from the specific case considered. For cylindrical symmetry with substance A extending from the axis to radius r_A, substance C_1 extending from $r_A \rightarrow r_{C_1}$, substance C_2 extending from $r_{C_1} \rightarrow r_{C_2}$, and substance B from r_{C_2} outward, the volumes of C_1 and C_2 are given by

$$V_{C_1} = \pi\left(r_{C_1}^2 - r_A^2\right) \tag{B-7a}$$

$$V_{C_2} = \pi\left(r_{C_2}^2 - r_{C_1}^2\right) \tag{B-7b}$$

Equations (B-6a, -b) relate arbitrary volumes of C_1 and C_2 to the corresponding volumes of A and B. Thus substitution of Eqs. (A-7a, -b) into Eqs. (B-6a, -b) will result in expressions for the volumes of A and B which reacted to form the measured volumes of C_1 and C_2 (per unit length of cylinder). Thus,

$$V_A = \left[\frac{\pi\left(r_{C_1}^2 - r_A^2\right)\rho_{C_1}}{M_{C_1}} x_1 + \frac{\pi\left(r_{C_2}^2 - r_{C_1}^2\right)\rho_{C_2}}{M_{C_2}} x_2\right] \frac{M_A}{\rho_A} \tag{B-8a}$$

$$V_B = \left[\frac{\pi\left(r_{C_1}^2 - r_A^2\right)\rho_{C_1}}{M_{C_1}} y_1 + \frac{\pi\left(r_{C_2}^2 - r_{C_1}^2\right)\rho_{C_2}}{M_{C_2}} y_2\right] \frac{M_B}{\rho_B} \tag{B-8b}$$

The desired expression for the volume ratio is

$$R = \frac{V_A + V_B}{V_{C_1} + V_{C_2}} = \frac{V_A + V_B}{V_C} \tag{B-9}$$

Substituting Eqs. (B-8a, -b) into (B-9) and simplifying yields the required equation.

$$R = \frac{\left(r_{C_1}^2 - r_A^2\right)\frac{\rho_{C_1}}{M_{C_1}}\left(\frac{M_A}{\rho_A}x_1 + \frac{M_B}{\rho_B}y_1\right) + \left(r_{C_2}^2 - r_{C_1}^2\right)\frac{\rho_{C_2}}{M_{C_2}}\left(\frac{M_A}{\rho_A}x_2 + \frac{M_B}{\rho_B}y_2\right)}{\left(r_{C_2}^2 - r_A^2\right)} \qquad \text{(B-10)}$$

If only one compound is formed, say $C_1 = C$, and $rC_2 = rC_1$, the last term in the numerator of (Eq. B-10) vanishes. Also the difference of the radii squared cancel in the remaining form to give

$$R = \frac{\rho_C}{M_C}\left(\frac{M_A}{\rho_A}x + \frac{M_B}{\rho_B}y\right) \qquad \text{(B-11)}$$

Now $a = cx$ and $b = cy$ can be used to eliminate x and y, in terms of a, b, and c, and Eq. (B-11) becomes

$$R = \frac{\rho_C}{cM_C}\left(\frac{aM_A}{\rho_A} + \frac{bM_B}{\rho_B}\right) = \frac{\gamma_A + \gamma_B}{\gamma_C} \qquad \text{(B-12)}$$

which can be obtained directly from basic principles.

Equations (B-10) can be generalized for two reactants combining to form n products. The result is

$$R = \frac{1}{r_{C_n}^2 - r_{C_o}^2}\sum_{i=1}^{n}\left(r_{C_i}^2 - r_{C_{i-1}}^2\right)\frac{\rho_{C_i}}{M_{C_i}}\left(\frac{M_A}{\rho_A}x_i + \frac{M_B}{\rho_B}y_i\right) \qquad \text{(B-13)}$$

where $r_{C_o} \equiv r_A$ in the previous notation.

Obviously, an increase in volume will correspond to $R > 1$, no change to $R = 1$. and a shrinkage to $R < 1$.

Equation (B-12) is used in Section 3.7.5 to estimate the volume changes brought about by the formation of various tungsten borides.

Appendix III
DENSITY CONSIDERATIONS

A crystallographic model must be consistent with the observed densities, and densities have been determined for the three best-established boron polymorphs and for the vapor-deposited boron found in boron filaments. Table 46 lists the observed densities of various forms of boron, together with their respective references. The α form is the most dense, followed by the β and "simple" tetragonal forms. The density of vapor-deposited boron is closest to that of β-boron, but the close agreement leaves no room for microporosity and defect structures which might be expected to form during vapor deposition. Evidence for several kinds of defects is presented in the main text, and it is reasonable to expect a 1 to 5% discrepancy in the density of vapor-deposited materials.

Table 46
REPORTED DENSITIES FOR CERTAIN FORMS OF BORON

Polymorph	Observed Density (gm/cm^3)	Reference
α-rhombohedral	2.46	26
β-rhombohedral	2.35	26, 33
"Simple" tetragonal	2.31	26, 47
Vapor-deposited boron in filaments	2.37	14, 48

Table 47 lists some calculated densities based on various models. The bcc and fcc models refer to bcc and fcc arrangements of B_{12} icosahedra which have been postulated by various authors (Refs. 14 and 21). The bcc arrangement has a density discrepancy of about 25% relative to the observed density of vapor-deposited boron;

Table 47

CALCULATED DENSITY FOR VARIOUS MODELS OF BORON

Model	Calculated Density (gm/cm^3)	Calculation Basis
B_{12} icosahedra in fcc packing	2.04	a_o = 7.5 Å, 48 B atoms/unit cell
B_{12} icosahedra in bcc packing	1.81	a_o = 6.2 Å, 24 B atoms/unit cell
Mixture 40% α-60% tetragonal-boron	2.37	α- and tetragonal boron at theoretical density
Mixture 49% α-50% tetragonal-1% porosity	2.37	α- and tetragonal boron at theoretical density
Mixture 74% α-24% tetragonal-2% porosity	2.37	α- and tetragonal boron at theoretical density

the fcc arrangement differs by 15%. These density differences, and the fact that the fcc and bcc arrangements do not explain the observed diffraction intensities, tend to eliminate these packing arrangements from consideration.

If the vapor-deposited boron consisted entirely of α-rhombohedral boron, there would be a 6% density discrepancy and the halo pattern described in Section 4.3.2 could not be adequately explained. The diffraction data are consistent with a model of α- and "simple" tetragonal boron, and the densities of several such mixtures are considered in Table 47 . Neglecting microporosity, density considerations predict a 40% α-60% tetragonal boron mixture. When porosity is taken into account, mixtures of 49% α-50% tetragonal-1% porosity and 74% α-24% tetragonal-2% porosity fit the observed density. Further refinement of the nature of the mixture cannot be made because the densities of defect α- and tetragonal boron are not known.

Appendix IV

NOTE ON THE STRUCTURE AMPLITUDE CALCULATION FOR A REGULAR ICOSAHEDRON OF BORON ATOMS

In the calculation of $\langle F \rangle$ in section 4.3.2, an approximation was made implicitly which is justified here.

Beginning with Eq. (7) (section 4.3.2, p. 129) and substituting for $I(\Omega)$ according to Eq. (6), one obtains

$$\langle I \rangle = \int_1 \cdots \int_N \frac{1}{R^2} \sum_m \sum_n F_m F_n^* e^{\frac{2\pi i}{\lambda} (\vec{s} - \vec{s}_o) \cdot (\vec{R}_m - \vec{R}_n)} \prod_{i=1}^{N} P(\theta_i, \psi_i, \phi_i) \, d\omega_i \quad \text{(IV-1)}$$

where

$$\prod_{i=1}^{N} P(\theta_i, \psi_i, \phi_i) = P(\Omega) \quad \text{(IV-2)}$$

This expression gives two types of terms: those in which $m = n$, and those in which $m \neq n$. For $m = n$, a typical term is

$$\frac{1}{R^2} \int_m F_m F_m^* P(m) \, d\omega_m = \frac{1}{R^2} \langle F^2 \rangle \quad \text{(IV-3)}$$

whereas for $m \neq n$, the typical term is

$$\frac{1}{R^2} \int_m F_m P(m) \, d\omega_m \int_n F_n^* P(n) \, d\omega_n = \frac{1}{R^2} \langle F \rangle^2 \quad \text{(IV-4)}$$

Mathematically, for the case of the boron icosahedron of edge length 1.80 Å, Eq. (IV-5) becomes

$$\left\langle F^2 \right\rangle = 12\, f^2 \left[1 + \frac{\sin sr_1}{sr_1} + 5 \left(\frac{\sin sr_2}{sr_2} + \frac{\sin sr_3}{sr_3} \right) \right] \qquad \text{(IV-7)}$$

where

$$r_1 = 3.42\ \text{Å},\ r_2 = 1.80\ \text{Å},\ \text{and}\ r_3 = 2.91\ \text{Å}$$

Also, Eq. (IV-6) becomes

$$\left\langle F \right\rangle^2 = 144\, f^2 \frac{\sin^2 sr}{(sr)^2} \qquad \text{(IV-8)}$$

where

$$r = 1.71\ \text{Å}$$

The accompanying figure is a plot of $\left\langle F^2 \right\rangle / 144\, f^2$ and $\left\langle F \right\rangle^2 / 144\, f^2$ as a function of $\sin \theta/\lambda$. The two curves are in good agreement out to about $\sin \theta/\lambda = 0.25$, or $d = 2$ Å. For lower d-spacings, intensities fall off more rapidly than normal with increasing $\sin \theta/\lambda$ when $\left\langle F \right\rangle^2$ is used as in Eq. (8), section 4.3.2.

REFERENCES

IV-1 R. W. James, The Optical Principles of the Diffraction of X-Rays, G. Bell and Sons, 1958, p. 494 ff.

IV-2 H. C. Longuet-Higgins and M. deV. Roberts, Proc. Roy. Soc. (London), 230A, 110 (1955)

IV-3 F. Herman and S. Skiilman, Atomic Structure Calculations, Prentice-Hall, 1963.

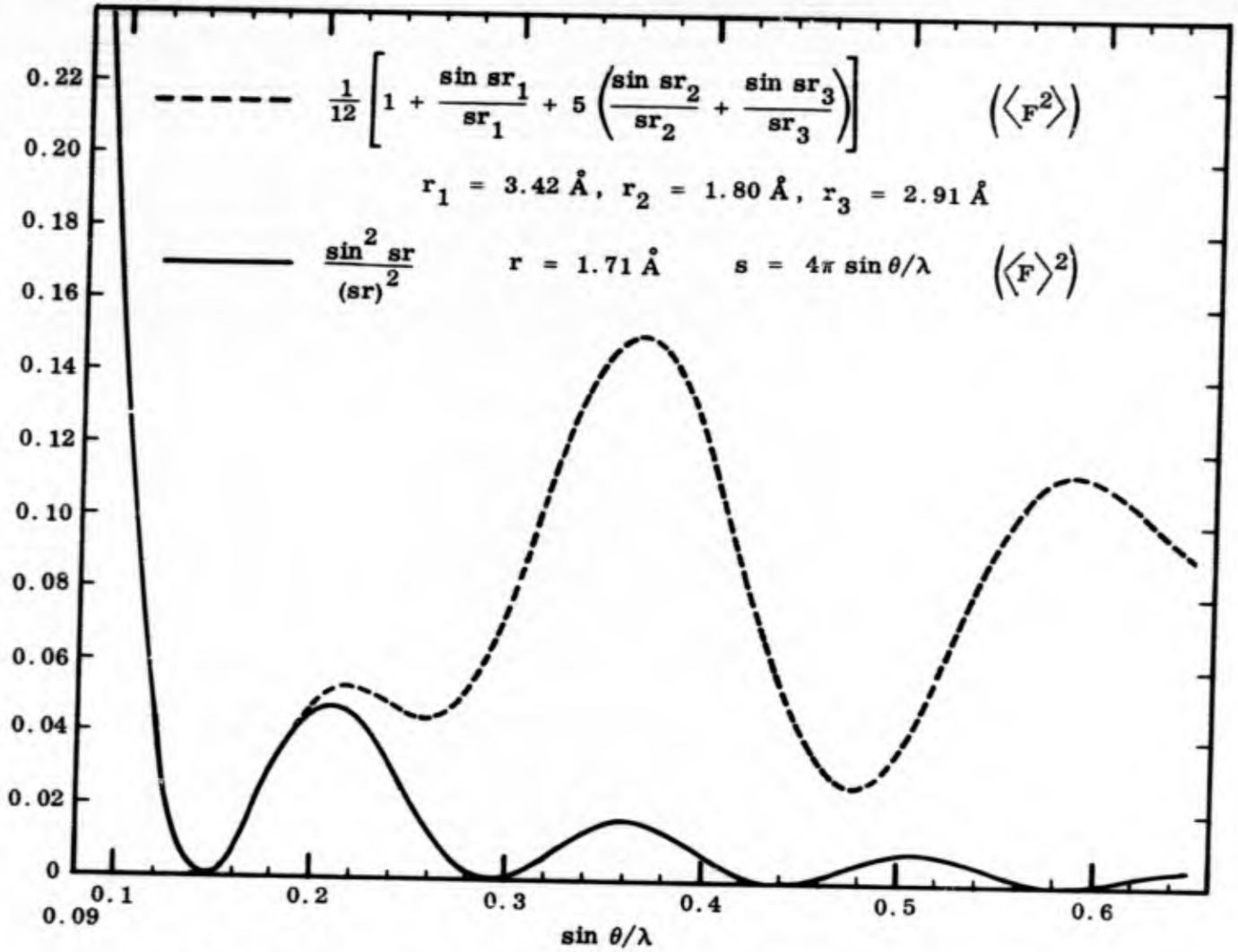

Fig. 117 Comparison of $\langle F^2 \rangle$ and $\langle F \rangle^2$ for boron icosahedron

UNCLASSIFIED
Security Classification

DOCUMENT CONTROL DATA - R&D

(Security classification of title, body of abstract and indexing annotation must be entered when the overall report is classified)

1. ORIGINATING ACTIVITY (Corporate author) Lockheed Missiles & Space Company Materials Sciences Laboratory Palo Alto, California	2a. REPORT SECURITY CLASSIFICATION Unclassified 2b. GROUP None

3. REPORT TITLE

STRUCTURE OF VAPOR-DEPOSITED BORON FILAMENTS

4. DESCRIPTIVE NOTES (Type of report and inclusive dates)

Summary Technical Report

5. AUTHOR(S) (Last name, first name, initial)

Hammond, M. L.
Lindquist, P. F.
Bragg, R. H.

6. REPORT DATE	7a. TOTAL NO. OF PAGES	7b. NO. OF REFS
November 1966	316	51

8a. CONTRACT OR GRANT NO.	9a. ORIGINATOR'S REPORT NUMBER(S)
AF 33(615)-3140 new b. PROJECT NO. 7351 c. Task No. d. 735107	9b. OTHER REPORT NO(S) (Any other numbers that may be assigned this report)

10. AVAILABILITY/LIMITATION NOTICES This document is subject to special export controls and each transmittal to foreign governments or foreign nationals may be made only with prior approval of the Metals and Ceramics Division (MAM), Air Force Materials Laboratory, Wright-Patterson AFB, Ohio

11. SUPPLEMENTARY NOTES	12. SPONSORING MILITARY ACTIVITY
	AFML (MAMS) Wright-Patterson AFB, Ohio 45433

13. ABSTRACT

This report describes the structure of boron filaments vapor-deposited at ~1000°C on a tungsten wire substrate. Production and specially prepared filaments were examined as were samples taken from the deposition chambers after a filament length was cooled there in place. Both the morphology and crystallographic structure of boron filaments are described.

This document is subject to special export controls and each transmittal to foreign governments or foreign nations may be made only with prior approval of the Metals and Ceramics Division (MAMS) of the Air Force Materials Laboratory, Wright-Patterson Air Force Base, Ohio 45433.

→ APPROXIMATELY

DD FORM 1 JAN 64 1473

UNCLASSIFIED
Security Classification

14. KEY WORDS	LINK A		LINK B		LINK C	
	ROLE	WT	ROLE	WT	ROLE	WT

INSTRUCTIONS

1. ORIGINATING ACTIVITY: Enter the name and address of the contractor, subcontractor, grantee, Department of Defense activity or other organization *(corporate author)* issuing the report.

2a. REPORT SECURITY CLASSIFICATION: Enter the overall security classification of the report. Indicate whether "Restricted Data" is included. Marking is to be in accordance with appropriate security regulations.

2b. GROUP: Automatic downgrading is specified in DoD Directive 5200.10 and Armed Forces Industrial Manual. Enter the group number. Also, when applicable, show that optional markings have been used for Group 3 and Group 4 as authorized.

3. REPORT TITLE: Enter the complete report title in all capital letters. Titles in all cases should be unclassified. If a meaningful title cannot be selected without classification, show title classification in all capitals in parenthesis immediately following the title.

4. DESCRIPTIVE NOTES: If appropriate, enter the type of report, e.g., interim, progress, summary, annual, or final. Give the inclusive dates when a specific reporting period is covered.

5. AUTHOR(S): Enter the name(s) of author(s) as shown on or in the report. Enter last name, first name, middle initial. If military, show rank and branch of service. The name of the principal author is an absolute minimum requirement.

6. REPORT DATE: Enter the date of the report as day, month, year, or month, year. If more than one date appears on the report, use date of publication.

7a. TOTAL NUMBER OF PAGES: The total page count should follow normal pagination procedures, i.e., enter the number of pages containing information.

7b. NUMBER OF REFERENCES: Enter the total number of references cited in the report.

8a. CONTRACT OR GRANT NUMBER: If appropriate, enter the applicable number of the contract or grant under which the report was written.

8b, 8c, & 8d. PROJECT NUMBER: Enter the appropriate military department identification, such as project number, subproject number, system numbers, task number, etc.

9a. ORIGINATOR'S REPORT NUMBER(S): Enter the official report number by which the document will be identified and controlled by the originating activity. This number must be unique to this report.

9b. OTHER REPORT NUMBER(S): If the report has been assigned any other report numbers *(either by the originator or by the sponsor)*, also enter this number(s).

10. AVAILABILITY/LIMITATION NOTICES: Enter any limitations on further dissemination of the report, other than those imposed by security classification, using standard statements such as:

(1) "Qualified requesters may obtain copies of this report from DDC."

(2) "Foreign announcement and dissemination of this report by DDC is not authorized."

(3) "U. S. Government agencies may obtain copies of this report directly from DDC. Other qualified DDC users shall request through _____."

(4) "U. S. military agencies may obtain copies of this report directly from DDC. Other qualified users shall request through _____."

(5) "All distribution of this report is controlled. Qualified DDC users shall request through _____."

If the report has been furnished to the Office of Technical Services, Department of Commerce, for sale to the public, indicate this fact and enter the price, if known.

11. SUPPLEMENTARY NOTES: Use for additional explanatory notes.

12. SPONSORING MILITARY ACTIVITY: Enter the name of the departmental project office or laboratory sponsoring *(paying for)* the research and development. Include address.

13. ABSTRACT: Enter an abstract giving a brief and factual summary of the document indicative of the report, even though it may also appear elsewhere in the body of the technical report. If additional space is required, a continuation sheet shall be attached.

It is highly desirable that the abstract of classified reports be unclassified. Each paragraph of the abstract shall end with an indication of the military security classification of the information in the paragraph, represented as *(TS)*, *(S)*, *(C)*, or *(U)*.

There is no limitation on the length of the abstract. However, the suggested length is from 150 to 225 words.

14. KEY WORDS: Key words are technically meaningful terms or short phrases that characterize a report and may be used as index entries for cataloging the report. Key words must be selected so that no security classification is required. Identifiers, such as equipment model designation, trade name, military project code name, geographic location, may be used as key words but will be followed by an indication of technical context. The assignment of links, rules, and weights is optional.